CRANFIELD UNIVERSITY

GAVIN SUTTON

THE DEVELOPMENT OF A COMBUSTION TEMPERATURE STANDARD FOR THE CALIBRATION OF OPTICAL DIAGNOSTIC TECHNIQUES

SCHOOL OF ENGINEERING

PHD

CRANFIELD UNIVERSITY

SCHOOL OF ENGINEERING

DEPARTMENT OF AUTOMOTIVE MECHANICAL AND
STRUCTURES ENGINEERING
(OPTICAL DIAGNOSTICS GROUP)

PHD

1998

GAVIN SUTTON

THE DEVELOPMENT OF A COMBUSTION TEMPERATURE STANDARD FOR THE CALIBRATION OF OPTICAL DIAGNOSTIC TECHNIQUES

PROF. DOUG GREENHALGH

NOV 2005

THE DEVELOPMENT OF A COMBUSTION TEMPERATURE STANDARD FOR THE CALIBRATION OF OPTICAL DIAGNOSTIC TECHNIQUES

ABSTRACT

This thesis describes the development and evaluation of a high-temperature combustion standard. This comprises a *McKenna* burner premixed flame, together with a full assessment of its temperature, stability and reproducibility. I have evaluated three techniques for high-accuracy flame thermometry: Modulated Emission in Gases (MEG), Rayleigh scattering thermometry and photo-acoustic thermometry.

MEG: Analysis shows that MEG is not usable in this application because the sharp spectral features of the absorption coefficient of gases are represented within MEG theory as an average absorption coefficient over the optical detection bandwidth. A secondary difficulty arises from the lack of high power lasers operating at wavelengths that coincides with molecular absorption lines in the hot gas.

Rayleigh Scattering: Applying corrections for the temperature-dependence of the scattering cross-section, it has been possible to determine the temperature of the combustion standard with an uncertainty of approximately 1%. The temperature dependence of the scattering cross-section arises from changes in the mean molecular polarisability and anisotropy and can amount to 2% between flame and room temperatures. Using a pulse Nd-YAG laser operating at 532 nm and high linearity silicon detectors, the Rayleigh scattering experimental system has been optimised. Temperatures measured over a three-month interval are shown to be reproducible to better than 0.4% demonstrating the suitability of the McKenna burner as a combustion standard.

Photo-Acoustic: By measuring the transit time of a spark-induced sound wave past two parallel probe beams, the temperature has been determined with an uncertainty of approximate 1%.

Flame temperatures measured by the photo-acoustic and Rayleigh scattering thermometry system show good agreement. For high airflow rates the agreement is better than 1% of temperature, but for low airflow rates, photo-acoustic temperatures are approximately 3.6% higher than the Rayleigh temperatures. Further work is needed to understand this discrepancy.

THE DEVELOPMENT OF A COMBUSTION TEMPERATURE STANDARD FOR THE CALIBRATION OF OPTICAL DIAGNOSTIC TECHNIQUES

THE DEVELOPMENT OF A COMBUSTION TEMPERATURE STANDARD FOR THE CALIBRATION OF OPTICAL DIAGNOSTIC TECHNIQUES

1. INTRODUCTION

The high temperatures generated by combustion processes have a direct influence on a variety of factors including chemical reaction rates, process efficiency, pollutant levels, product quality and rate of failure mechanisms. It is therefore of great importance that the temperature is determined to the best possible accuracy. Conventional contact probes such as the thermocouple are still widely used in high temperature applications due to their relative simplicity of use and low cost and a large proportion of traceability in the combustion industry is via corrected thermocouples [1]. However, thermocouple gas thermometry is subject to numerous errors resulting from the complex interaction between the thermocouple and its environment, leading to an equilibrium that depends on the following factors:

- Convective heat transfer across the boundary layer from flame to thermocouple, which in turn depends on many factors including the velocity of the gas.
- Radiative heat exchange between the thermocouple, the gas, the particulate matter and the surrounding walls.
- The recovery factor from the transfer of gas kinetic energy to thermal energy within the boundary layer of the hot junction.
- Heat transfer along the thermocouple due to conduction.
- Catalytic enhancement of chemical reaction rates.

Non-contact laser diagnostic techniques avoid the problems associated with the perturbative nature of physical probes but are generally expensive to implement and many commonly-used laser diagnostic techniques are in themselves technically complex and assumptions made in applying the techniques and the data reductions often result in poor uncertainty.

High-temperature combustion standards are designed to address these issues by giving direct traceability to the fundamental definition of the temperature scale, ITS-90 [2], providing a stable, reproducible region of known temperature and composition. Laser diagnostic systems can then be calibrated by measuring in this region. Developing the combustion standard is a twofold process in which a stable and reproducible high-temperature source must be complemented by a high-accuracy traceable temperature measurement technique.

After reviewing extant work on high temperature transfer standards and assessing temperature calibration techniques (§1.1), this thesis describes the development and validation of a high-temperature combustion standard. This includes evaluation of the novel Modulated Emission in Gases (MEG) thermometry technique (Chapter 3). In light of technical difficulties applying the MEG thermometry technique to real flames, two additional techniques, Rayleigh scattering and photo-acoustic thermometry are investigated.

Previous Rayleigh and photo-acoustic thermometry systems offer an accuracy of approximately 2 - 5% of temperature. By identifying the sources of uncertainty in the two techniques and developing corrections, it has been possible to determine the temperature of a stabilised, pre-mixed flat-flame with an uncertainty of approximately 1% of temperature.

To achieve 1% uncertainty with Rayleigh scattering thermometry, the key assumption that the elastic scattering of light by a molecule (proportional to its Rayleigh scattering cross-section) is not temperature dependent is investigated. We find that a temperature-dependence of the order of a few percent exists due to change in a molecule's mean polarizability [4] and mean anisotropy. Therefore, to obtain accurate temperatures we need to determine not only the species concentrations in the flame region but also the change with temperature of the scattering cross-section. A detailed analysis of this procedure is given in Chapter 4.

For photo-acoustic thermometry, we use the beam-deflection technique which measures the *transit time* of a spark-induced sound wave passing two fixed parallel probe laser beams to determine the speed of sound, and hence temperature. The blast wave from a laser-induced spark does not travel at the speed of sound in the gas, except in the limit of large distances from the spark when normal sound wave propagation returns. By modelling the excitation produced by the spark as a cylindrical blast wave, it has been possible to extrapolate to the speed of sound in the limit of large *spark to probe beam* distances and hence determine the flame temperature to higher accuracy.

Chapter 5 contains a detailed comparison of the flame temperatures measured by the Rayleigh and photo-acoustic thermometry systems.

1.1 EXTANT WORK ON HIGH TEMPERATURE TRANSFER STANDARDS

The survey of extant work on transfer standards is somewhat limited. The majority of optical diagnostic systems presented to date are more concerned with temperature reproducibility and the determination of the frequently large errors in the measurement process. Some encouraging work has been published in the areas of stabilised flames, gas cells and high temperature lamps, indicating that there is a need for such artefacts.

1.1.1 HIGH PURITY GAS CELLS

A substantial amount of work has been carried out regarding a transfer standard for gas temperature measurements at the National Physical Laboratory [3]. The system comprises a high temperature furnace that can be operated over the temperature range 300 °C to 1600 °C, containing a central pure gas sample with suitable optical access. The furnace temperature is monitored by calibrated thermocouples, *Accufiber*^{TM} optical-fibre probes and a radiation thermometer inserted into the housing block of the gas sample. Agreement between the three probes, each calibrated to ITS-90, was of order 0.3% (of temperature). No detailed calculations were made as to the temperature gradients across the gas sample, such errors were assumed to be within the uncertainty of the measuring instruments. The equipment was later used as part of EC project *MAT1-CT-940051* "*Development of a transfer standard for laser thermometry*", in which Coherent Anti Stokes Raman scattering (CARS) measurements, amongst others, were performed and found to be in good agreement with the sample temperature with typical differences of 20 °C between the CARS temperatures and those of the gas cell at the top of the operational range of the furnace, although it is worthy of note that some measurements gave more significant discrepancies . A report on the feasibility of extending the gas temperature standard furnace to 2000 °C has also been produced [4], the main conclusion being that the present time, suitable materials to contain the hot gas samples were very limited. It also suggests that a stabilised flame may provide a route forward. Other disadvantages may result from degradation of the thermocouples or fibre-optic probes but it should be possible to identify problems efficiently by comparison with the other temperature probes used. The main advantages of such hot gas volumes are firstly, that a wide range of experimental temperatures can be investigated and secondly, that the system is moderately simple to implement with a range of different sample gases.

A standard high temperature furnace containing a sealed cell of N_2 has also been reported [5] for the calibration of a modeless dye laser CARS system. The temperature is traceable to ITS-90 via a calibrated radiation pyrometer. Differences of as little as 2% are reported between the CARS and Pyrometer temperatures up to 2100 °C at 20 atmospheres. It does therefore seem feasible to construct a high temperature furnace as a calibration source, providing that an inert gas cell is used. This is appropriate for the calibration of an N_2 CARS system but is still not suitable for measurements on other constituents of a typical combustion process.

1.1.2 CHARACTERISED STABILISED FLAMES

Characterised standard flames can be used as a source of calibration and verification of a number of optical temperature and concentration measurement techniques. One such artefact [6] employs a commercially available flat flame burner [7] with a sintered porous bronze disk was used to stabilise a premixed H_2/air flame. Temperatures for various equivalence ratios, flow rates and heights above the burner disk were measured by Coherent Anti-Stokes Raman Spectroscopy (CARS). An uncertainty of approximately 2.5% is reported, the accuracy of the CARS measurements being the dominant error contribution. It is also reported that the same device has been used successfully to calibrate a Raman scattering apparatus [8-9] and laser induced fluorescence (LIF) apparatus [10]. Temperatures in the range 1000 to 1900 °C were accessible by this method, and the use of chemical equilibrium codes were shown to be in qualitative agreement with the measured CARS values. With measurements made at various heights along the burner axis, a stable temperature region of approximately 10mm was found to exist. The authors also found that careful selection of the flow rates and equivalence ratio was essential to avoid large heat losses to the water-cooled burner plate. Several other identical burners were also investigated, with the results being the same within the accuracy of the experiment. Other investigations of an identical burner [11], using CARS and LIF to characterise the flame, report a temperature uncertainty of approximately the 3%. A high-pressure burner has also been reported [12] in which the flame is used as a spectroscopic calibration standard. Thermometry performed on this flame is reported to have an accuracy of 1-8% depending on the fuel/flow conditions.

Several advantages of using these stabilised flames are apparent:

- The temperature field is reproducible from one burner to another.
- Operation is simple and safe.
- Optical access is unrestricted.
- The spatial uniformity of the post-flame region is good.
- A wide range of temperatures and gas compositions are possible by simple variation of the equivalence ratio and flow rate.

1.1.3 GAS FILLED TUNGSTEN FILAMENT LAMPS

Gas filled tungsten filament lamps can provide stable high temperature fields that can be modelled using laminar flow codes. A tungsten filament lamp of this type has been evaluated using CARS thermometry [13]. Measurements were made about a horizontal, linear incandescent tungsten filament in a N_2 filled optical cell. A high spatial resolution was achieved using a folded-boxcar phase matching configuration producing a 6 mm x 0.2 mm x 0.2 mm measurement volume. CARS temperatures were measured to an accuracy of 1.5% and agreed with a suitable fluid flow model for steady laminar flows to within the accuracy of the measurements. Temperatures were obtained in a vertical line above the centre of the filament, the maximum being approximately 2000 °C close to the filament itself, falling off in a well defined manner with increasing height above the coil. The coil temperature was also determined using a two colour pyrometric technique with good agreement. Although there is no explicit reference to using the lamp as a standard, the fact that pyrometric measurements and fluid flow modelling measurements are made allows a certain level of traceability to be given to the CARS measurements.

A second lamp, reported by the same authors [14] carries on this work and has been operated up to 3200 °C. More importantly, the lamp is presented as a temperature calibration device. The temperature field of the inner region of the tungsten coil was investigated using CARS and compared with fluid flow models and pyrometric measurements. Once the field is characterised, optical diagnostic systems, such as CARS, can be calibrated by this technique. Agreement between the fluid flow model and CARS was as good.

The gas filled tungsten filament lamps offer the advantages that they are moderately simple to implement, give good spatial resolution and can operate at very high temperatures - encompassing a large range of theoretical adiabatic flame temperatures of typical combustion processes. Disadvantages of this method include the lack of compatible gases for use with tungsten and the larger uncertainties in determination of the true temperature via radiometry at the lower temperatures. The tungsten lamps are not particularly representative of combustion environment, which can also be a disadvantage. Uncertainties of the order of 2% are reported.

1.2 ASSESSMENT OF CALIBRATION TECHNIQUES

Once a suitable gas/flame source has been developed, it will need to be characterised. By this we mean to determine the temperature field by a traceable thermodynamic method and possibly, as an integral part of the process, the species concentrations. A great wealth of work on gas temperature measurements have been performed over the past 50 years, with the advent of the laser producing many new diagnostic techniques over the last 30 years or so. An assessment of the main techniques in relation to providing accurate, traceable temperature measurements follows.

1.2.1 ABSORPTION AND EMISSION SPECTROSCOPY

Absorption spectroscopy relies upon measurements of the frequency dependence of the absorption of a suitably chosen light source, often a tuneable laser, due to one or more atomic or molecular transitions. Alternatively, the Fourier transform technique can be used. Generally, measurements are made with a source and detector fixed with respect to the sample under interrogation, with the result that the measured parameter is a weighted average of its distribution along the line of sight. This method is thus not suitable for samples with rapid spatial variations. The utilisation of the absorption and or emission technique for thermometry is possible but fraught with difficulties in realistic combustion processes as many emitting species are formed by chemiluminescent reactions highly dependent on the local details of the combustion process. A breakdown of the various techniques follows.

1.2.1.1 LINE REVERSAL METHOD

The determination of flame temperatures through the use of spectral reversal measurements is well established and widely exploited. By reversal we mean that the spectral radiance emitted by the luminous gas or flame equals the part from a reference source that is absorbed as it passes through the investigated volume. At reversal, the flame temperature can be determined from the temperature and emissivity of the reference source. The method is limited in that it requires a uniform temperature distribution along the selected pathway and the reversal temperature is the weighted average along this path.

Generally, the radiation L_λ^1 from the black body is imaged by a lens into the flame and passes through the investigated radiating flame zone where some of the incident radiation is absorbed. The transmitted portion, L_λ^2, together with the flame radiation, L_λ^3, is focused onto the detector. A filter is used to select an appropriate wavelength region $\Delta\lambda$ at which the reversal temperature is determined. To detect the reversal point, the temperature of the reference source is adjusted until the radiation of the flame matches the background spectrum, i.e. the flame emits as much radiation as it absorbs from the black body, and therefore, the black body cannot be distinguished when observed through the flame. At this point, the black body, as read by a suitable pyrometer, is at the same temperature as the flame zone under test.

If S_λ is the brightness temperature of the black body reference source, L_λ^1 the spectral radiance of this source, L_λ^2 the spectral radiance of the non absorbed portion of the radiation stemming from the reference source after it has passed through the flame, and L_λ^3 the spectral radiance emitted by the flame zone, then we have:

$$L_\lambda^1(T) = L_\lambda^b(S_\lambda) \tag{1.01}$$

$$L_\lambda^2(T) = (1 - a_\lambda(T))L_\lambda^b(S_\lambda) \tag{1.02}$$

$$L_\lambda^3(T) = a_\lambda(T)L_\lambda^b(T) \tag{1.03}$$

At the reversal point for a particular wavelength λ we have:

$$a_\lambda(T)L_\lambda^b(T) + (1 - a_\lambda(T))L_\lambda^b(S_\lambda) = L_\lambda^b(S_\lambda) \tag{1.04}$$

$$a_\lambda(T)L_\lambda^b(T) = a_\lambda(T)L_\lambda^b(S_\lambda) \tag{1.05}$$

$$L_\lambda^b(T) = L_\lambda^b(S_\lambda) \tag{1.06}$$

$$T = S_\lambda \tag{1.07}$$

Thus, the flame temperature is obtained by measuring the (adjusted) brightness temperature of the reference source at the reversal point with the pyrometer. This basic method has the disadvantage of being a line of sight technique, and that some form of tomography would be required to produce spatial temperature information. It also requires that the flame temperature remains stable during the measurement process, which again is rarely the case in realistic combustion situation, but need not be a problem in stabilised laboratory flames. A transient reversal technique can be utilised to allow for changing flame temperatures using a laser source of known frequency and a suitable photomultiplier. A brief description follows.

If the black body reference source is firstly viewed in the place of the flame with a suitable photomultiplier, we can obtain the spectral radiance of the calibrated source at a given brightness temperature, S_λ^*, and relate it to the measured intensities of the photomultiplier signals thus establishing a relationship between L_λ^1, L_λ^2, L_λ^3, and S_λ. After this initial 'calibration' of the photmultiplier, the system is arranged so as to view the flame firstly on its own and secondly with a light source (laser) behind it. This is achieved by the use of either an opto-acoustic coupler or a chopper. Frequencies of 10 MHz for the acoustic coupler and 100 KHz for a mechanical chopper are possible. For the case of line reversal with a line absorptance a_λ, effective spectral width of the line emission $\delta\lambda$, effective spectral response of the photomultiplier $\Delta\lambda$ and the brightness temperature of the calibrated black body S_λ^* and making use of Wien's and Kirchoff's equations we have:

$$L_\lambda^1 = \frac{c_1}{\lambda^5}\exp\left(\frac{-c_2}{\lambda S_\lambda^*}\right)\Delta\lambda \qquad (1.08)$$

$$L_\lambda^2 = \frac{c_1}{\lambda^5}\left[\exp\left(\frac{-c_2}{\lambda S_\lambda^*}\right)\Delta\lambda - a_\lambda(T)\exp\left(\frac{-c_2}{\lambda S_\lambda^*}\right)\delta\lambda\right] \qquad (1.09)$$

$$L_\lambda^3 = a_\lambda(T)\frac{C_1}{\lambda^5}\exp\left(\frac{-c_2}{\lambda T}\right)\delta\lambda \qquad (1.10)$$

The ratio of spectral radiances is independent of $\Delta\lambda$ and $\delta\lambda$:

$$\frac{L_\lambda^3}{L_\lambda^1 - L_\lambda^2} = \frac{L_\lambda^b(T)}{L_\lambda^b(S_\lambda^*)} = \exp\left[-\frac{c_2}{\lambda}\left(\frac{1}{T} - \frac{1}{S_\lambda^*}\right)\right] \qquad (1.11)$$

By taking the natural logarithm and rearranging, it follows that:

$$\frac{1}{T} = \frac{1}{S_\lambda^*} + \frac{\lambda}{c_2}\ln\left(\frac{L_\lambda^1 - L_\lambda^2}{L_\lambda^3}\right) \qquad (1.12)$$

Which allows the flame temperature to be calculated from the measured values L_λ^1, L_λ^2, L_λ^3, and S_λ^* of the calibrated black body.

The errors associated with this technique can be large especially if the flame temperature is not close enough to the brightness temperature of the backlight or calibrated source. It is also important to have sufficient emission from the flame at the measurement temperature. This is not always the case for low temperature or very thin flames.

A possible improvement to the emission signal can be utilised by seeding the flame with a metal, such as sodium and then using a laser tuned to one of its absorption/emission lines. A sufficient quantity of metal to give a good emission is required and it is not always possible to guarantee that the metal is in local thermodynamic equilibrium with the flame. If this is not the case, the best that can be hoped for is a measure of the effective electronic excitation temperature of the metal, which is no more than a measure of the ratio of the populations in the corresponding electronic states and not of true temperature. Other errors are introduced due to loses in the lens system and include errors due to the deformation of the transmitted beam. Stray light from the gas surrounding the investigated volume may also cause errors. It is also important to ensure that light from the reference source is present in every part of the investigated gas volume and in every solid angle contributing to the detected radiation. A sufficient condition for this is that the aperture of the first lens does not restrict the solid angle of the reference light. Scattering by flame particulates can also degrade the signal.

1.2.1.2 SINGLE AND TWO LINE TRANSITION METHODS

When a single spectral line or spectral band emission, corresponding to a known quantum transition, can be isolated from overlapping from other lines or bands, the gas temperature can be determined by measuring the radiance integrated over the frequency bandwidth of the line or band. The method is best suited for optically thin flames since there may be significant self-absorption at typical flame temperatures around 1700 °C.

The radiance of the spectral line is given by:

$$L_{nm} = \frac{h\nu_{nm}}{4\pi} A_{nm} N_0 \ell \frac{g_n}{Q} \exp\left(\frac{-E_n}{kT}\right) \tag{1.13}$$

where Q is the partition function and g_n the statistical weight.

This, in principal allows the determination of the gas temperature T from the measured intensity of the spectral line radiation, if optically thin conditions prevail. Providing that ν_{nm} and the transition n→m are known, A_{nm}, g_n and E_n can be found in published tables. However, values of A_{nm} are known accurately for only a limited number of lines but this may not be a problem since L_ν depends much more strongly on temperature T than A_{nm}, so that moderate accuracy in A_{nm} may be sufficient. The number density of neutral atoms N_0 is also a function of temperature. If the gas consists of mainly a single species, the ideal gas law may be used to estimate N_o by assuming an approximate temperature. If more than 1% absorption occurs, in the frequency region considered, then corrections need to be made for possible self-absorption. The line of band radiation used in the temperature measurement must also be free of superimposed radiation stemming from other line or band emissions. These requirements limit the use of the single line transition method.

Similarly, the two line ratio method can be used when the transition probability, statistical weight of the upper state, energy of the upper state, and frequency of the two atomic lines are known. The ratio of two spectral line emission of radiation intensities is given by:

$$\frac{L_{\nu_1}}{L_{\nu_2}} = \frac{\nu_1}{\nu_2}\frac{A_1}{A_2}\frac{g_1}{g_2}\exp\left(\frac{-(E_1-E_2)}{kT}\right) \tag{1.14}$$

where the subscripts refer to the two spectral lines. Taking logarithms gives:

$$\ln\left(\frac{L_{\nu_1}}{L_{\nu_2}}\right) = \ln\left(\frac{\nu_1}{\nu_2}\frac{A_1}{A_2}\frac{g_1}{g_2}\right) - \left(\frac{-(E_1-E_2)}{kT}\right) \tag{1.15}$$

Using this equation, it is not necessary to know the number density or path length as was the case for the single line method, and we can use relative rather than absolute transition probabilities. A disadvantage of this method is that the calculated temperature is critically dependent upon the accuracy of the ratio of line intensities if the difference in upper energy states is small (i.e. E_1-E_2 < 0.4eV), as it usually is for spectral lines of practical value to this method. The method is also critically sensitive to any errors in the ratio of the transition probabilities, which can be expected to be large, since few transition probabilities are known to better than 15%.

The two line method described above can be extended to many lines and is called the atomic Boltzmann plot. Rotational temperatures for diatomic molecules can also be found using the rigid rotor approximation and neglect higher order terms in energy, e.g. terms in $J^2(J+1)^2$, and ignore rotation-vibration interactions [15].

1.2.1.3 ABSORPTION METHOD

Temperatures can be obtained from absorption measurements. The quantity measured in this case is the spectral absorptance in a very narrow wavelength interval $\Delta\lambda$ which depends on temperature. The emission, however, varies much more with temperature than the absorption. This is due to the fact that the emission is associated with an excited state where the population changes rapidly, whereas the absorption is mostly associated with the ground state where the temperature change is less significant. It is for this reason that absorption methods are normally only utilised for low temperature gases where the emission is of low intensity i.e. below 1200 °C.

1.2.1.4 SPECTRAL LINE WIDTH METHOD

The two significant mechanisms responsible for the broadening of a spectral line (emission or absorption) are Doppler and pressure broadening. Doppler broadening, due to the thermal motion of atoms or molecules and the corresponding shifts in emitted radiation frequency is temperature dependent. Calculating the Doppler shifts for all velocities gives rise to a Gaussian distribution whose full width at half maximum is given by:

$$\Delta\nu_D = \frac{2\nu_0}{c}\sqrt{\frac{2\ln 2kT}{m}} \tag{1.16}$$

where ν_0 is the line centre frequency, m the mass of the particular species, k the Boltzmann constant and T is the temperature. Doppler broadening is dominant at low pressure.

Pressure broadening, due to the interaction of radiation with molecules occurs when a molecule interacting with radiation either in absorption or emission is periodically interrupted by collisions. This leads to a line broadening known as collision or pressure broadening. The statistically averaged effect of the distribution of collision times gives rise to the Lorentz lineshape function:

$$g_C(\nu) = \frac{\Delta\nu_C}{2\pi}\frac{1}{(\nu-\nu_0)^2 + (\Delta\nu_C/2)^2} \tag{1.17}$$

At 300 K and atmospheric pressure, pressure broadening dominates Doppler broadening by an order of magnitude, while at 2000 K pressure and Doppler broadening line widths are of the same magnitude. For a pressure broadened ionic line, the full width half maximum is proportional to the electron density and by use of the Saha equation, ionic temperatures may be determined. When neither Doppler or collision broadening dominate, the two effects combine to give the line shape described by the Voigt profile. Due to the fact that natural line widths are generally very small ($<10^{-5}$ nm) a high resolving power spectrometer with large dispersion is required. Otherwise the single line may overlap with neighbouring emission or the band lines will superimpose to form a continuum. For these reasons and the high cost of equipment, the spectral line width method is not frequently used as a temperature measurement technique [15].

A summary of temperature measurements made using emission and absorption methods is presented in [1] and together with other sources [16 – 37] the outcome is quite clear, with these methods providing generally poor accuracy. Typically it is not better than 2-5% of temperature (i.e. ± 40 to ± 100 °C at 2000 °C). The reasons for low accuracy being attributed to the need for prior knowledge of the appropriate molecular parameters such as oscillator strengths, transition probabilities, pressure-broadened line-widths, and the need to fit the measured spectrum to theoretical models.

1.2.2 TWO COLOUR PYROMETRY

Two colour pyrometry can be used to determine the line of sight averaged temperature in a hot gas or flame by ratio of two signals taken at different wavelengths. This method, as it stands is not capable of high spatial resolution and is therefore of little practical use. If however, a temperature perturbation is introduced along a line within the flame, we can then, in practice, determine local temperatures. This is the basis of a novel thermometry technique described in §1.2.2.1.

1.2.2.1 MODULATED EMISSION IN GASES (MEG) TECHNIQUE

A new technique for gas temperature measurement, developed at NPL [38], Modulated Emission in Gases (MEG) is shown in Figure 1.1. The basic method involves producing a small temperature modulation and measuring the modulated (A.C.) signal with two detectors at two wavelengths either side of the flame or hot gas.

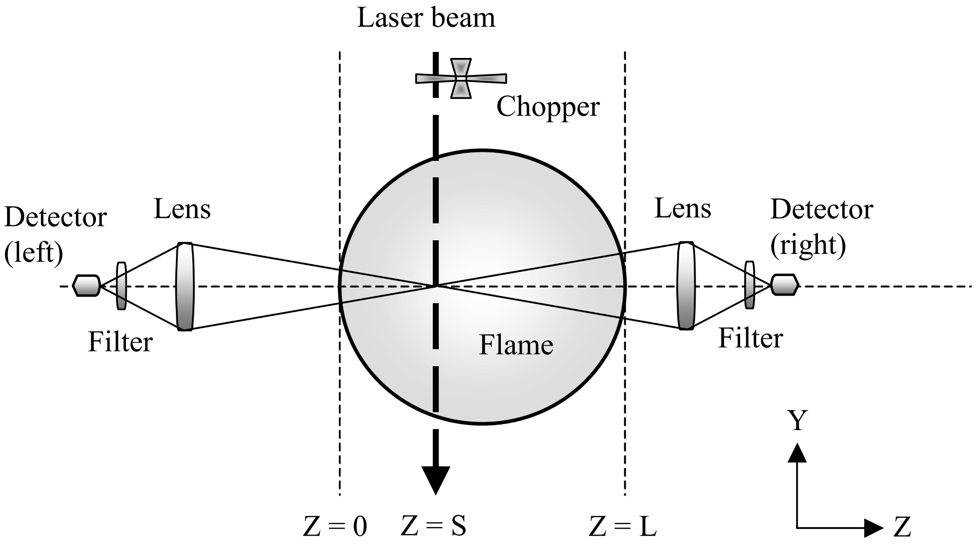

Figure 1.1 Modulated Emission in Gases (MEG) experimental arrangement.

The temperature modulation can be provided by a weakly absorbing laser beam tuned to a suitable spectral band of one of the combustion species, CO_2, CO or H_2O. In a homogeneous environment, the new technique has the potential to provide the thermodynamic temperature with an uncertainty of better than 1%. Since the evaluation and development of this technique is a sizable portion of this thesis, the reader is directed to chapter 3 for a full and rigorous description of the MEG technique.

1.2.3 GENERAL LASER BASED METHODS

These methods can be divided into several sub groups which depend on the scattering process, the signal coherence and excitation scheme used. A breakdown follows.

1.2.3.1 SPONTANEOUS RAYLEIGH SCATTERING

Rayleigh scattering is the elastic scattering (ignoring Doppler shifts) of light from molecules or very small particles. In an elastic scattering process there is no net energy exchange between the incident radiation and the target molecules or particles. Thus, the wavelength of the scattered light is unchanged and the scattered signal is proportional to the weighted sum of all species present. For this reason, Rayleigh scattering can't be used for individual species concentrations but only to measure total number density. Practically, Rayleigh scattering diagnostics suffer from Mie scattering interferences and spuriously scattered laser light. Since Mie scattering cross sections can be many orders of magnitude greater than Rayleigh, the measurement environment must be virtually free of particles. For this reason it is generally only possible to utilise Rayleigh scattering when the inlet gases are filtered for particulates and the products of combustion are non-sooting. New techniques are arising in which the effect due to Rayleigh and Mie scatters can be distinguished but it is not a trivial task. Rayleigh scattering is of interest since its cross sections are typically three orders of magnitude greater than those for vibrational Raman scattering. This is due to the fact that the Rayleigh scattering process arises from the induced polarizability, which is much stronger that the induced polarizability derivative which gives rise to vibrational Raman scattering. The differential cross section for Rayleigh scattering at 90° can be approximated as:

$$\left(\frac{\partial\sigma}{\partial\Omega}\right)_{Ray} = \frac{4\pi^2 (n_i - 1)^2}{N_0^2 \lambda^4} \tag{1.18}$$

where n_i and N_0 are the refractive index and the number density at standard temperature an pressure (STP) respectively. The strength of the scattering will scale as the orientation-averaged square of the induced polarizability. In a mixture of gases, the total Rayleigh scattering cross section is the mole fraction weighted average of the individual cross sections:

$$\left(\frac{\partial\sigma}{\partial\Omega}\right)_{mix} = \sum_i x_i \left(\frac{\partial\sigma}{\partial\Omega}\right)_i \tag{1.19}$$

where x_i is the mole fraction of constituent i. The Rayleigh scattered power from a mixture of gases may then be written as:

$$P_{Ray} = P_i N \left(\frac{\partial\sigma}{\partial\Omega}\right)_{mix} \Omega \ell \varepsilon \tag{1.20}$$

where ε is the optical collection efficiency, N the number density of scattering species which is proportional to the inverse of temperature, P_i the incident laser power and l the sampling extent. Complete knowledge of the gas composition and the Rayleigh cross section at the incident wavelength are required before the total density can be evaluated. Once the density is obtained, the temperature can be approximated from the ideal gas law:

$$p = NkT = const \tag{1.21}$$

The measurements can be degraded due to unwanted source radiation entering the Rayleigh collection optics and since the scattered radiation is at the same wavelength as the incident radiation care must be taken to discriminate between the two. For particulates of a diameter greater than $\xi > 0.3$, where ξ is the ratio of particle circumference to the incident light wavelength,

$$\zeta = \frac{2\pi r}{\lambda}, \tag{1.22}$$

the simple Rayleigh theory is not valid and a more complicated theory based on Mie scattering needs to be used. The problem with Mie scattering is that it is neither molecular-density or temperature dependent and cannot therefore be used as a temperature diagnostic tool.

At number densities characteristic of the higher temperature regions of atmospheric pressure flames, temperatures may also be obtained by measuring the temperature dependent Doppler width of the spectrally resolved Rayleigh line. This requires the use of high resolution spectral scanning and thus obviates the high frequency response capability of Rayleigh approaches. The line shape is related to temperature by the expression:

$$f(\nu) = \left(\frac{m}{2\pi kT}\right)^{\frac{1}{2}} \cdot \exp\left\{-\frac{m}{2kT}\left[\frac{(\nu-\nu_0)c}{2\nu_0 \sin\left(\theta/2\right)}\right]^2\right\} \tag{1.23}$$

where θ is the scattering angle, m the molecular mass, and ν_0 the line centre (or laser) frequency. At very high densities, the Rayleigh line will be predominately collision broadened and will surrender all explicit temperature sensitivity.

A summary of Rayleigh temperature measurements is given in [1]. The accuracy generally depends on prior knowledge of the species concentrations obtained by some other means. Theoretical models and laser-induced fluorescence have been used successfully [39]. Since the Rayleigh signal scales as the fourth power of frequency, UV laser can be used to improve signal strength. With regards to a standard flame, provided that the species can be mapped, the temperature sensitivity and accuracy can be good. Typical accuracies of 2-5% are quoted [1] but standard flames with good gas filtering and reasonably well known species concentrations can lead to much improved accuracies, with 1% of temperature being possible. Rayleigh systems also have the advantage of experimental simplicity and excellent spatial resolution. For these reasons, Rayleigh scattering has potential for standard flame systems.

1.2.3.2 RAMAN SCATTERING

Inelastic scattering of light from molecules may be rotational, vibrational, or electronic depending on the nature of the energy exchange that occurs. Such inelastic processes are known as Raman scattering.

Rotational Raman scattering is not widely employed in combustion diagnostics. This is due to the fact that the Raman shifts are small (<200 cm^{-1}) and that the spectra from the component gases in combustion usually interfere making interpretation difficult. It is also difficult to discriminate against the incident laser light due to the small spectral separation. For these reasons pure rotational Raman scattering is only used for simple mixtures or where one component is dominant. It is however, worth noting that for a single rotational Raman transition, the scattering cross section is an order of magnitude greater than for an entire vibrational branch. The most important selection rule for rotational Raman transitions is that the molecule must be anisotropically polarizable. By this we mean that in addition to any permanent dipole moment, the induced dipole moment $\mu = E\alpha$ acquired by the molecule in an electric field E must be different depending on the orientation of the molecule to the electric field. All linear molecules and diatomics (whether homonuclear or hetronuclear) have anisotropic polarisabilities and so are rotational Raman active. This is important when investigating molecules with no permanent dipole moment since they do not have a rotational microwave spectrum but do have a rotational Raman spectrum.

Vibrational-Rotational Raman scattering occurs when there is a change in the vibrational quantum number (V) as well as the rotational quantum number (J). The Q branch ($\Delta J = 0$) is the characteristic feature of the Stokes and anti-Stokes component of the vibrational rotational Raman spectrum and is usually two orders of magnitude more intense than the S ($\Delta J = +2$) and O ($\Delta J = -2$) branches. In the absence of vibrational-rotational interaction the Q branch transitions overlap completely but in reality there is interaction and the Q branches spread out in frequency for increasing J (i.e. as higher rotational levels become populated). Since the population of the higher J levels is strongly temperature dependent, i.e. Boltzmann distribution function, the utilisation of Raman scattering for thermometry is advantageous. The spectral line positions for the Q branch transitions can be written as:

Stokes, $\Delta V = +1$:
$$\bar{\nu}_{V+1,J:V,J} = \bar{\nu}_0 - \left[\omega_e - 2\omega_e x_e (V+1) - \alpha_e J(J+1)\right] \qquad (1.24)$$

Anti-Stokes, $\Delta V = -1$:
$$\bar{\nu}_{V-1,J:V,J} = \bar{\nu}_0 + \left[\omega_e - 2\omega_e x_e V - \alpha_e J(J+1)\right] \qquad (1.25)$$

where α_e is the rotational-vibrational interaction constant, $\omega_e = \nu/c$ and x_e the equilibrium diatomic bond length. From Equation 1.24/25 all the major characteristics of Q branch vibrational Raman scattering for linear molecules may be discerned.

In many practical situations the flame emission and laser induced fluorescence signals are larger than the Raman. It is therefore very important to understand these processes so that their contributions can be subtracted. If the Raman signal does not rise clearly above the fluorescence signal, measurements are difficult to accomplish without resorting to polarization and/or time sampling approaches. Pulsed laser systems can be used when the flame luminosity is high and provides a method to suppress background luminosity. Laser modulated particle incandescence signals can also be significant if the flame is not clean. Laser light incident on any particles, soot or other, can have the effect of heating them to temperatures in excess of the flame temperature. These particles then emit with the black body spectrum swamping the much smaller Raman signal. Mie scattering can also change the signals measured and may need to be taken into account. Since the Raman intensities are proportional to the fourth power of the pump laser frequency, it is advantageous to use high frequency lasers to maximise the scattered signal. For this reason ultraviolet sources, often in the form of excimer lasers, are used. It is also possible to improve the quality of the Raman signal by use of intra-cavity techniques which can effectively increase the pump beam power in the investigated volume. Polarization techniques can also be used to discriminate between Raman and background signals and the use of a Fabry-Perot interferometer with a spectral range that matches the Raman spectrum under investigation (i.e.N_2) can also improve the quality of the measured signal.

Temperatures are generally obtained by one of two methods. Firstly, a measurement of species concentration enables a calculation of temperature in the same way as for Rayleigh, by use of the ideal gas law. Secondly, a measurement of the Stokes scattering strength for two adjacent molecular lines, or for Stokes and anti-Stokes signals with the same line, allows a calculation of the temperature via the Boltzmann occupation factors for the lines in question. The second is generally only possible practically at high temperatures in common combustion processes due to the relative weakness of the anti-Stokes signal. Accuracies for Raman temperature measurements have been reported as 2-5% [1,40 - 45] with instrument calibrations primarily carried out at room temperature using STP air and correction made at elevated temperature with high temperature traceability being carried out by thermocouples in most cases.

It may be advantageous to use a combined Rayleigh / Raman system with the latter providing species information for input to the Rayleigh data reduction. Although Raman is limited to flames that are not highly luminous and not particle laden. This need not be a problem though for a carefully selected laboratory flame. The inherent signal weakness compared to Rayleigh, for example, can also hinder temperature determination.

1.2.3.3 COHERENT ANTI-STOKES RAMAN SCATTERING (CARS)

Since spontaneous Raman scattering is incapable of probing highly luminous, particle laden flames typical of practical combustion sources, there has been considerable impetus over the last 25 years to develop other diagnostic techniques that can deliver higher signal levels and possess alternative characteristics (i.e. coherence) to permit measurements in these environments. Coherent Anti-Stokes Raman Scattering (CARS) is such a method. The large increases in signal / background signal provided by CARS over spontaneous Raman scattering derive from both its high signal conversion efficiency and coherent, i.e. laser-like, signal characteristics. At atmospheric pressure, CARS signals are usually orders of magnitude stronger than spontaneous Raman scattering. Also, the CARS signal emerges in the form of a coherent beam allowing the entire signal to be captured. For example, in an isotropic scattering process, only about one percent of the scattered radiation is collected, even with relatively fast optics. In addition, because the CARS signal is captured within a very small solid angle, the collection of interference is greatly reduced. The interference signal still appear in CARS but much less of it is sampled. CARS detectivity is similar to spontaneous

Raman in that it is suited to major species concentrations and thermometry measurements at atmospheric pressure.

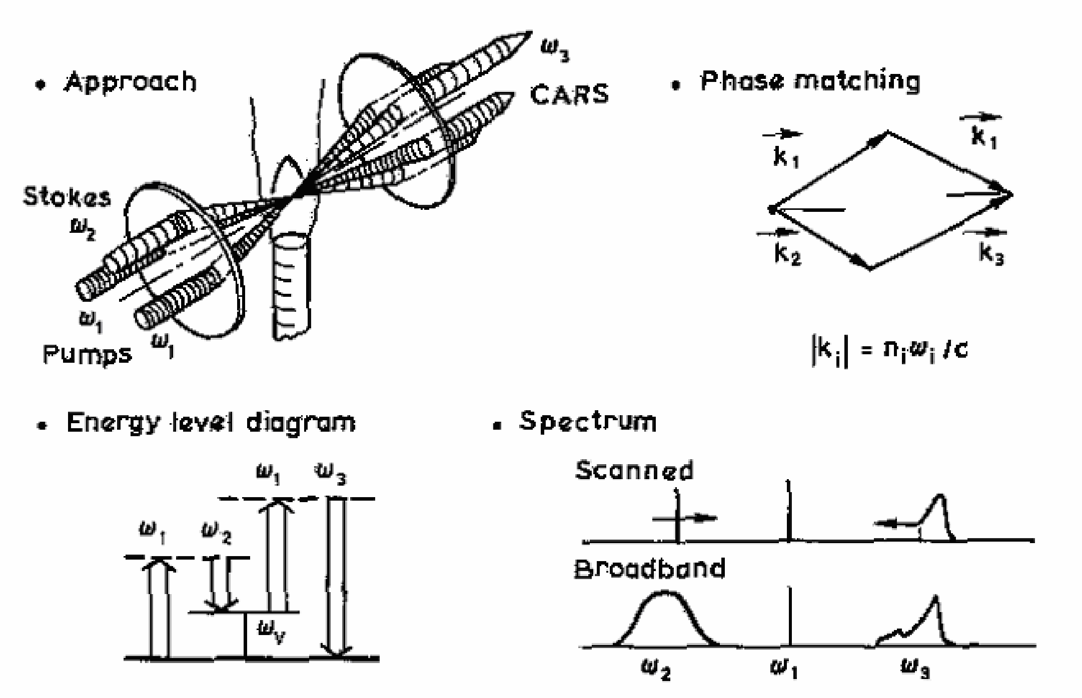

Figure 1.2 Coherent Anti-stokes Raman Scattering (CARS), from [15].

In this method, outlined in Figure 1.2, laser beams at frequencies ω_1 and ω_2 are mixed via a geometrical phase matching scheme to generate a coherent CARS signal at $\omega_3 = 2\omega_1 - \omega_2$. The laser interaction with the medium occurs through the third order non-linear susceptibility giving rise to an oscillating polarization at ω_3 and thus a new radiation beam that is also coherent. The phase matching ensures that the CARS signal produced at location z, for example, will be in phase with that generated at z + dz so that constructive signal growth will occur. ω_1 is called the pump beam, and ω_2 the Stokes beam, because it is downshifted by the vibrational-rotational Raman shift of the molecule being probed. If the frequency difference ($\omega_1 - \omega_2$) is adjusted to a particular Raman resonance, selective molecular components may be probed. The non-linear susceptibility is both density and temperature dependent providing the basis for diagnostics. Measurement of the medium's properties is obtained from the shape of the spectral signatures and / or the intensity of the CARS radiation. The temperature is almost always obtained from the spectral lineshapes and species concentrations from the strength of the signal in general. Another aspect of the CARS signal is that the spectral shapes are also concentration dependent in certain ranges. This is particularly useful for simultaneous temperature and species concentration diagnostics. In comparison to spontaneous Raman scattering, the CARS signal is propagated in the forward direction. This can be a great disadvantage since it requires double optical access to perform any kind of diagnostics, although a laboratory flame system would not necessarily have this problem. CARS species measurements are only really useful at elevated pressures due to poor sensitivity at lower pressures. CARS spectroscopic modelling is also considerably more complicated than the spontaneous Raman case. For spontaneous

Raman, the modelling may be achieved by the incoherent summation of all the transition magnitudes. These spectra are relatively insensitive to Raman transition linewidths or precise spectral location. CARS spectral synthesis on the other hand exhibit destructive and constructive interference effects and are quite sensitive to the Raman linewidths and the precise spectral locations of the transitions. Computationally intensive numerical programs are required to convolve over the laser profiles and non-linear susceptibilities in order to synthesise the spectra. Even with these difficulties, the potential capability of CARS for measurements in hostile environments justifies its study. Another advantage of CARS when utilised for measurements in 'clean' combustion environments is that the laser energies required can be of as much as an order of magnitude smaller than are required for a similar spontaneous Raman measurement. Due to the coherent nature of CARS, smaller optical apertures can also be used in comparison to the Raman technique. This can be a great advantage when investigating high pressure applications.

On a practical level, there are a number of other advantages offered by the CARS technique:

a) The short (~10ns) laser pulses can provide temporal information on the temperature field.
b) Due to the phase matching requirements, relatively small beam interaction volumes are possible enabling spatial temperature maps to be obtained.
c) The signal does not usually interfere with laser generated fluorescence.
d) Unlike laser induced fluorescence methods, increasing pressure does not generate excessive problems due to signal quenching.
e) CARS is not very perturbative, although is not wholly non-perturbative.

On the other hand, disadvantages of the CARS technique exist:

a) The signal level is very low due to the fact that CARS is a third order non-linear process with a pump laser beam not in resonance with a molecular transition. Resonant CARS would increase the signal strength but the problems with its practical implementation are immense.
b) Problems arise in the analysis of CARS data when the medium under investigation has large spatial temperature gradients, i.e. in turbulent combustion, due to the highly non-linear dependence of the signal on temperature.
c) Complications can arise due to non-resonant background signals from other gas species, relaxation effects, motional narrowing and laser induced breakdown. This particularly affects the usefulness of CARS for minority species detection.
d) The technique is expensive to set up

The main CARS technique utilises a broad-band dye laser for the study of nitrogen which is always present in air-fuel combustion. Other molecules can also be used. These include hydrogen, carbon dioxide and water. The vibrational Q branch spectrum is usually preferred for generating the CARS signal although it is also possible to utilise rotational or S branch spectra. Rotational CARS is claimed to have the advantage at low temperatures, due to large line separation in comparison to the vibrational method and the resulting simplification of effects due to line overlap.

CARS has excellent potential as a temperature measurement technique and has seen some utility in the standards community such as that of Greenhalgh, Devonshire et al [13-14] for measurements in high temperature tungsten filament lamps, as discussed earlier. Work investigating stabilised flames [8,11] has also utilised CARS, even at atmospheric pressure, with good accuracy in the range of 2.5-3%. Work has also been reported on the use of rotational CARS with good agreement (1%) with radiation corrected thermocouples up to 1950 K [46]. Poor accuracy utilising H_2 CARS at 2337 K has also been reported [5].

1.2.3.4 DEGENERATE FOUR WAVE MIXING (DFWM)

DFWM is generated by the non-linear interaction between four optical beams via the third order susceptibility tensor. This is the same mechanism that gives rise to CARS and there are great similarities between the two processes. The difference lies in the fact that in DFWM there are three input beams and an output beam that all have the same frequency. In the most common configuration, the phase-conjugate geometry, two of the input beams (the pump beams) are counter propagating while the third, the probe beam, is separated by a small angle. The signal (phase-conjugation) beam is then generated in a direction opposite to the probe beam. The signal beam's existence is due to the fact that there is scattering from a refractive index grating resulting from the spatial modulation in the molecular state populations generated by the high power input beams. A less frequently used geometry is one similar to CARS in which the signal beam is generated in a forward direction defined by the phase matching constraints of the interaction.

DFWM possess most of the advantages listed for CARS and some additional benefits:

a) The phase-matching conditions are always met in the phase-conjugation geometry.
b) The interaction is Doppler-free
c) The nature of the phase-conjugation process tends to lessen some problems due to beam aberrations and wander in a spatially inhomogeneous medium.
d) At molecular line centre the process is resonant, leading to much greater signal levels and excellent sensitivity for detection of minor species. In fact the sensitivity is comparable to that of Laser Induced Fluorescence (LIF) [1].

The DFWM technique can be used in either a scanning or time multiplex mode, with the latter allowing data acquisition from a single laser pulse. Because of the large signal level, DFWM can produce spatial temperature maps from a single laser shot, something which is not possible with the CARS technique. It is therefore suited to probing spatial inhomogeneous combustion processes. However, two-dimensional DFWM is experimentally challenging. Since most of the broadband laser energy is not resonant with a molecular transition, signal to noise levels are low. The choice of laser bandwidth is thus very important and for optimum sensitivity the laser wavelength is constrained to cover the molecular absorption lines of the molecule under investigation. For the OH radical, a commonly probed species in DFWM, these lie in the ultraviolet. High spectral dispersion is also required in order to resolve the rotational levels. DFWM is also quite sensitive to beam absorption and hence the precise location of the interacting volume may be difficult to define in an unquantified process. Collisional quenching although not as important a parameter as for LIF, can still lead to problems in data reduction as well as indirectly via the formation of thermal and acoustic gratings within the interaction volume. Typical temperature measurement uncertainties of 5 - 8% are reported [1]. Due to its complexity and relatively poor accuracy, DFWM is not considered suitable as a calibration technique.

1.2.3.5 LASER INDUCED FLUORESCENCE (LIF)

LIF is the process of emission of light from an atom or molecule after it has been promoted to an excited state by photon absorption. For this context, it is appropriate to regard fluorescence as an optical absorption processes followed by a spontaneous emission event. By definition, fluorescence requires that emission occurs between electronic states of the same multiplicity, i.e. the same electronic spin states. Fluorescent lifetimes vary from between 10^{-1} and 10^{-6} s. The emission of light may be at different frequencies than that of the incident photons; normal fluorescence, or at the same frequency; Resonant fluorescence. Generally it is the normal fluorescence that is of diagnostic use since interferences from Mie scattering and laser light scattering can be discriminated against the LIF signal. LIF is of great interest since it is species specific and has cross sections many orders of magnitude greater that those associated with Raman or near resonant Raman scattering. For this reason whereas Raman based approaches may have a species concentration detection limit of 0.1% (1000ppm), LIF is quite capable of detection limits in the 0.01% (100ppm) range or even better. Since LIF is due to electronic energy level changes (with rotational / vibrational fine structure), most electronic absorptions for combustion species occur in the 200 to 600 nm range. This range is readily accessible to tuneable dye lasers, generally ‘tuned’ by some frequency conversion scheme. It is the visible to ultraviolet spectral range that is of most practical use to combustion physics and not the fluorescence in the infrared range that is in more common use for fundamental chemistry studies.

To make use of the LIF of a species, the following criteria must be met:

a) The molecule must have a known emission spectrum.
b) The molecule must have an absorption wavelength that is accessible to a tuneable laser source.
c) The rates of radiative decay of the excited state must be known. This is because the fluorescence power is proportional to the rate of radiative decay.
d) The excited state loss rate may be increased considerably over the radiative rate due to collisions involving the excited state and other molecules. This is known as quenching. The quenching rate is very dependent on the types and densities of other molecule present and inter-system crossing processes.

In most cases the quenching rates are much larger than the spontaneous emission rates (Q>>A) and the steady state is determined by either the collisional quenching or the stimulated emission rate, depending on the laser intensity. The steady state assumption works well for typical flame quenching rates for laser pulses durations in the 10^{-8} to 10^{-6} sec range, but for laser pulses in the 10^{-9} to 10^{-8} sec range and modest laser spectral intensities, a steady state may not be achieved and temporal variations need to be modelled.

Until the advent of high power lasers, the linear regime was the only one accessible to LIF. But higher power lasers are very desirable and can make the data reduction much easier. This is because Q, the collisional quenching rate is difficult to know to a high degree of accuracy and since any error in Q will transfer to errors in the determination of the ground state population, N_1^0, it is advantageous to eliminate its dependency. High laser energies can provide this regime ($I\nu \gg I_{\mathrm{sat}}$). In the saturation regime, the fluorescence signal is independent of both laser intensity and the quenching so neither needs to be measured. In terms of physical processes, the saturation regime is when the rates of laser absorption and stimulated emission become so large that they dominate the state to state energy transfer in and out of the directly pumped levels. Saturation also gives the maximum fluorescence signal yield and hence the maximum species sensitivities. This is all well and good in theory but in practice several limitations to the method exist. Firstly, complete saturation is not easily achieved due to the wavelength region of the absorption or the required magnitude of the laser intensity. Secondly, saturation is not achieved in the ‘wings’ of the focused laser beam which can lead to significant errors. It is also worth noting that it is not possible to saturate for the whole duration of the laser pulse due to temporal variation of the laser beam intensity and in any case real molecular systems will exhibit rotational/vibrational structure, which also needs to be modelled.

Various schemes exist to either reduce the influence of or calculate the quenching rate. In the linear regime, it is possible, with very short laser pulses to remove the Q dependence but only for low pressure flames or for ultra short duration laser pulses.
LIF thermometry can be achieved by investigating the distribution of populations of two of more individual rotational / vibrational states. LIF however is not usually the first choice. This is due to the fact that many molecular radicals, OH being a good example, require high temperatures (>1500°C) to be abundant in sufficient numbers to give a suitable fluorescence signal. Many excitation schemes are available for LIF, two of the most common being excitation scans and the two line approache.

a) Excitation Scans

The excitation scan method is the most commonly used technique for LIF thermometry. High accuracy is possible for steady state flames when one has time to scan over the vibrational/rotational states of the ground electronic state. Scans are always performed at laser intensities in the linear fluorescence regime. The LIF signal is recorded for each transition, which is proportional to the lower absorbing state population. Thus the fluorescent distribution from the lower states J is proportional to the state populations and is given by:

$$F_J \propto n_J = f_J n = \frac{nhcB_V}{kT}(2J+1)\exp\left[-B_V J(J+1)\frac{hc}{kT}\right] \tag{1.26}$$

where f_J is the Boltzmann fraction in state J. The temperature is then found by a suitable graphical method.

b) Two Line Technique

The technique involves measuring the relative population of two states of a three level system and calculating temperature via the Boltzmann expression. Species are generally selected such that the energy level separation gives good sensitivity to temperature. The excitation is performed in a sequential manner. Level 3 is pumped from level 1 and fluorescence from the 3→2 transition monitored. Then level 3 is pumped from 2 and the fluorescence from the 3→1 transition monitored. Excitation is always to the same upper state when linear excitation is used. For each fluorescence transition, the effects of quenching and vibrational/rotational energy transfer are the same. Thus the fluorescence efficiency and the transition rates cancel out when the two signals are in ratio and so do not need to be known. The result is given below:

$$\frac{F_{31}}{F_{32}} = \frac{I_{23}\lambda_{32}^{3}}{I_{13}\lambda_{31}^{3}} \exp\left(\frac{-(E_2 - E_1)}{kT}\right) \tag{1.27}$$

where F_{ij} is the fluorescence signal for each transition and I_{23}, I_{13} the laser intensities for the i→j transitions. The accuracy of the two line method depends on how well the ratio I_{23}/I_{13} can be measured. It is usual to seed the flame with an atomic species, i.e. In, Th, Sn or Pb, that has a good sensitivity over the temperature range of use and also a strong Einstein A coefficient so that a good signal level can be achieved to minimise shot noise inaccuracies. To avoid the need to seed the flame source with an atomic species, one may make use of certain naturally occurring species, OH being the most common.

On a practical level, LIF has become a powerful and widely utilised technique for combustion diagnostics. The main reasons for this are:

i) Since it is an absorption method with high quantum efficiency, the sensitivity for trace species detection is very high.
ii) Multi-parameter measurements are possible, including temperature, pressure, density, species concentrations and velocity.
iii) Basic LIF measurements are possible using a relatively straightforward experimental setup. Although dual wavelength pumping systems are considerably more complex.
iv) Spatial and temporal resolutions are high, i.e. spatial: <1 mm^3 and temporal: ~10 nS.
v) Single shot two-dimensional mappings of temperature and species concentrations are feasible in the combustion zone.

There are several disadvantages of LIF, in particular when applied to quantitative thermometry. The main one is the quenching of the excited states due to various collisional processes, which in general, is dependent on composition, pressure and also the vibrational/rotational states involved in the process. Thus unless the exact quenching processes involved are identified, attempting to correct for them can be fruitless. Quenching problems aside, other perturbations can arise from Stark broadening, laser mode structure variations, polarisation effects, heating due to laser absorption and fluorescence trapping. It is also worth noting that LIF is a perturbative technique in that it involves real transitions to excited states, although the effect in flames is small. A summary of LIF excitation methods for temperature measurements is give in [47]. Typical temperature accuracies of 2 - 5% are possible [1, 48 – 50].

1.2.3.6 HOLOGRAPHIC AND SPECKLE METHODS

These methods of temperature measurement are both based on the distortion of an optical wavefront passing through a gaseous sample region and as such involve the same physical principles as methods such as photothermal deflection, optical interferometry and Schlieren photography. In all cases, it is the spatial variation of the refractive index that is measured. Provided that there is sufficient other information (pressure, composition) the temperature may be determined.

The holographic methods involve measurement of the phase shift due to the presence of the sample, while the speckle methods involve measurements of a shift in a speckle pattern. Typical temperature uncertainties of between 4 - 8% have been reported [1]. Both methods can in principal be used to determine 3 dimensional temperature fields but suffer from major practical disadvantages:

a) A measurement must be taken with and without the sample present - difficult for laboratory flames and generally not possible in practical combustion processes.
b) An Abel Inversion type data reduction is usually required which limits the types of combustion sources that can be probed to those with cylindrical symmetry fields. The inversion process is also very sensitive to errors.
c) Poor time resolution.
d) High sensitivity to noise.

For these reasons, holographic and speckle methods are not considered suitable as a calibration method.

1.2.3.7 PHOTO-ACOUSTIC AND PHOTO-THERMAL METHODS

Photo-acoustic and photo-thermal techniques both rely on the measurement of the deflection of a probe beam (a laser beam is most common) when passing through a region of varying refractive index (i.e. a flame). The passive variant of these techniques (i.e. no pump beam) is essentially a Schlieren one, in which the deflection of light passing through a spatially varying refractive index is measured with a suitable detector. If the light source is presented to the flame at various orientations, a two dimensional reconstruction of the refractive index field and hence, if the system is sufficiently understood, the temperature field can be obtained. With the advent of tuneable, high power lasers it is more common to pulse the beam to some absorption in the flame which in turn can produce a transient thermal and acoustic field which can then interact with the probe beam. Since quenching occurs on a very rapid timescale, the energy lost from the pumped excited electronic state results initially in a constant volume, localised heating of the gas and a corresponding sudden increase in pressure, which in turn launches a pressure pulse at the speed of sound in the medium. If a suitable microphone is place nearby, the line averaged speed of sound in the flame can be determined and hence the temperature.

Spatial resolution can be greatly enhanced by the utilisation of two closely placed parallel probe beams and suitable detectors. Once the acoustic pulse is initiated with a suitably focused laser beam, the deflection of the probe beams can be used to determine the velocity of the sound wave. Then the resolution is strictly limited by the accuracy in determining the probe beam separation and the time between detector signals. It is also important to measure the acoustic velocity sufficiently far away from the initiation point to avoid non-linear effects. This method has excellent potential for metrology, provided that the species contributing to the acoustic velocity measurement are known. Young *et al* [51] have shown that in typical combustion, lack of knowledge of the species results in a systematic error of less that 2% if N_2 is assumed to be the main flame component. Of course, if the species are known, this error is greatly reduced, Edwards *et al* [3] reporting a resolution of 1 in 10^5 for a well controlled laboratory gas cell. Various other measurements have been report with general accuracies of 2 - 4% in temperature. Zapka *et al* [52] reports an uncertainty of ± 30 °C at 2100 °C using this method and Grosjean *et al* [53] report good agreement with CARS measurements made on a laboratory flame.

Since this method offers the potential for high accuracy temperature measurement, a brief explanation of the technique follows.

Once the velocity of the acoustic wave has been measured, as described above, it may be related to temperature by the perfect gas law:

$$v = \left(k \frac{\partial p}{\partial \rho} \Big|_{s} \right) = \sqrt{\frac{\gamma R T}{\overline{m}}} \qquad (1.28)$$

where γ is the ratio of specific heats at constant pressure and constant volume, R the molar gas constant and $\overline{m}$ the average molecular weight of the gasses. Since:

$$\gamma = \frac{C_P}{C_V} = 1 + \frac{R}{C_V} \qquad (1.29)$$

we may write:

$$T = \frac{v^2 \overline{m}}{R\left(1 + \frac{R}{C_V(T)}\right)} \qquad (1.30)$$

where C_v is the temperature dependent average molar specific heat at constant volume. Providing that the species concentrations are known, and C_v from tabulated values, the temperature can be determined. The main advantages of photo-acoustic thermometry are listed below:

a) It is a non-intrusive / non-contact method.
b) High spatial and temporal resolution are possible.
c) The internal gas temperature is measured and hence, via the ideal gas law, gives rise to a thermodynamic determination of temperature.
d) No spectroscopic constants need to be known.
e) It is not sensitive to background luminescence or black body radiation from particles in the flame.

f) Detailed knowledge of the pump laser beams spatial and temporal profiles is not required.
g) Low sensitivity of the acoustic constant, γR, to temperature so that poor knowledge of species concentrations need not lead to large errors in the temperature determination.

Disadvantages of this method include:

a) Errors due to gas velocity/flow field.
b) Path bending problems due to density gradients.
c) High ambient noise levels although for ultra short laser pulses it is possible to filter out the low frequency noise due to the flame.
d) Problems due to non-linear wave propagation close to the initiation point.

Photothermal deflection techniques on the other hand allow for purely optical detection. Techniques can be divided into passive and active methods. The passive method involves measurements of the deflection of a probe beam due to gradients in the refractive index along the beam path. If species information is available, the temperature field may be reconstructed by a suitable tomographic technique. The signal is also more sensitive to the cold regions of the flame due to the associated higher gas densities. The active technique involves measurements of the deflection of a probe beam at the point of intersection with a pump beam, the latter producing localised heating along its path. The signal can be related to the diffusivity of the gas at the intersection point and no deconvolution is required. However, the diffusivity of the gas as a function of temperature needs to be known and this is species dependent. Providing a method to determine species concentrations is available, accuracies in the 2 - 5% range have been reported [1].

1.2.3.8 TOMOGRAPHIC IMAGING TECHNIQUES

Field imaging techniques can be conveniently divided into two areas. The onion peeling and the Abel inversion methods can only be utilised for radially symmetric flames where as the tomographic methods such as the Algebraic Reconstruction and Filtered Back Projection techniques can be applied to flames of arbitrary distribution. All the techniques listed above attempt to measure localised parameters within the flame. Once these parameters are known, the temperature may be determined. Generally speaking, the line averaged parameter is measured for many projections and by a suitable reconstruction scheme, Abel inversion being an example, the temperature field is reconstructed. Accuracy can vary depending on the nature of the temperature field, the number of projections and the inversion method utilised but are generally poor due to the propagation of errors from one projection to the next.

1.2.4 PHYSICAL PROBES

Contact probes are still widely used in high temperature applications particularly due to their relative simplicity of use and low cost. As mentioned earlier, a large proportion of traceability in the combustion industry is via corrected thermocouples. Fibre optic probes and chemical sampling have also seen some utility with the latter providing species information also. A breakdown of the various physical probes follows.

1.2.4.1 CHEMICAL SAMPLING

The utilisation of this method involves a gas sampling probe placed into the flame with the products drawn into an online gas analysis system. From a measurement of the major species concentrations in conjunction with the pre-combustion composition information, the temperature may be found. Many problems exist in attempting to sample flames, and careful control over the probe design is essential for accurate results. Problems can arise from turbulence, particle-laden gases and the difficulties of simultaneously preserving the molecular species of interest while promoting the quenching of unstable radicals. Various techniques can be used to determine the gas temperature including measurement of the air-fuel ratio, a minimisation of the Gibbs free energy and enthalpy balance. The first two depend somewhat on the assumption of chemical equilibrium, which is often not the case during combustion, while the third is less general. Chemical sampling has found extensive use in aero-engines with a fair degree of accuracy. Typical uncertainties of 3 - 5% of temperature have been reported provided the fuel mixtures are known to a high degree of accuracy [1] and heat losses have been corrected for.

1.2.4.2 UNSHIELDED THERMOCOUPLES

Unshielded thermocouples are not in frequent use for gas temperature measurement as they are subject to numerous errors. Improvements in reliability and stability can be achieved by suitable sheathing of the thermocouple and these probes are popular in combustion thermometry. For accurate measurements the complex interaction between the thermocouple and its environment needs careful modelling. Factors that need to be considered are given below:

i) Convective heat transfer across the boundary layer from flame to thermocouple, which depends on many factors including the velocity of the gas.
ii) Radiative heat exchange between the thermocouple, the gas, the particulate matter and the surrounding walls.
iii) The recovery factor from the transfer of gas kinetic energy to thermal energy within the boundary layer of the hot junction.
iv) Heat transfer along the thermocouple due to conduction.

It is usually only possible to characterise these factors in well understood measurement situations, which is not normally the case in combustion. Problems can also occur due to the possible catalytic nature of the thermocouple, in which the temperature may be higher due to catalytic enhancement of the reaction rates. Fine wire (10 - 25 μm dia.) thermocouples may be the useful for studying structure of unstable and turbulent flames where other optical methods are not effective. Practically, thermocouple thermometry is limited to below 1800 °C in combustion environments due to chemical degradation. High temperature Tungsten-Rhenium thermocouples are available for use up to 2300 °C but quickly degrade in air and are only really suitable for use in suitably protected high temperature furnace arrangements. With this in mind, they may be suitable for standard gas cell type standards work where the thermocouple is protected from the air, although drift and chemical incompatibility problems have been reported above 1800 °C in carbon vacuum furnaces [54]. Uncertainties of 2 - 5% for corrected thermocouples have been reported [1].

1.2.4.3 FIBRE OPTIC PROBES

Fibre optic probes are based on the detection of optical radiation but generally require insertion into the gas volume. The disadvantages stated for thermocouples apply to a certain extent to all physical probes, fibre optics being no exception. A selection of the most common types follows.

i) Fluorescence Doping of the Fibre Tip

This technique relies on the use of a short sensing element containing a fluorescent dopant placed at the high temperature end of an optical fibre (often Sapphire). When the element is pumped by a suitable light source so that it falls within an absorption band, it will fluoresce at a characteristic (longer) wavelength. The decay time of the fluorescence is highly temperature dependent and a measure of the decay time provides a good means of measuring the tip temperature. Pumping with a short duration square laser pulse results in an exponential decay response in the fluorescence lifetime. The problems associated with thermocouple sensors, i.e. convection, conduction and radiation losses also apply to this type of sensor. Rare-earth doped sensors may be capable of use up to 1400 °C. Short response times can also be achieved with careful selection of dopant/host materials. It is also important to note that at high temperatures, the fluorescent signal is poor. This is due to quenching effects and can seriously hinder temperature measurements. The fluorescence signal is also overwhelmed by the intense black body radiation present at high temperatures. Radiation losses along the fibre need not be a serious problem since it is the relative change in the fluorescence signal that is need for temperature determination and not the actual magnitude of the signal.

ii) Blackbody Tipped Fibre

Due to the limitations of fluorescence thermometry at the higher temperatures, a fibre coated with a suitable substance to form a black body may be used. The emitted black body radiation is then used to generate the temperature via Planck's radiation law:

$$L_{\lambda}^{b}(T) = \frac{c_1}{\pi\lambda^5} \cdot \frac{1}{\exp\left(\frac{c_2}{\lambda T}\right) - 1} \tag{1.31}$$

Combined fluorescence and black body sensors are also possible with the advantage that at low temperatures, when the black body radiance is small, the fluorescence signal is large. Two wavelength black body systems may also be utilised.

iii) Thin Film Etalon Sensors

A sapphire optical fibre can be coated with a suitable layer on its tip. The two surfaces of the thin coating (i.e. the fibre to coating interface and the coating to air/gas interface) act as a low finesse etalon. As the temperature increases, the refractive index of the coating also increases (and to a lesser extent, the length increases), so increasing the optical path length of the layer. A suitable monochromatic light source pumped into the fibre will interfere with the phase shifted reflected signal. From this, temperature information may be obtained.

iv) Radiation Pipe Sensor

This method involves measuring the radiation from the flame source by piping it away using a suitable optical fibre to a detector system. Problems can be caused by the losses in the fibre and the lack of local thermodynamic equilibrium at the fibre tip. On the positive side, this method can have a very fast response time since it is only limited by the detector response time and the requirement for adequate signal-to-noise. Generally, Fibre optic probes have several advantages over their thermocouple counterparts, namely immunity to electric noise and good corrosion resistance.

Due to the invasive nature of contact probes and the need to know many extra parameters in order to attempt to correct for errors, they are not regarded as suitable for the calibration of a standard flame but could be utilised if a standard gas cell were to be proposed.

1.3 SUMMARY

1.3.1 SUMMARY OF EXTANT WORK ON HIGH TEMPERATURE TRANSFER STANDARDS

Method	High purity gas cells	**References**	[3-5]
Cost	Moderate		
Equipment	High temperature furnace, optical pyrometer, high temperature thermocouples, fibre optic probes, sealed gas cells		
Scope of Measurements	CARS		
Maximum Temperature	1600 °C [3], 2100 °C [5]		
Traceability	Calibrated thermocouples [3], fibre optic probes and radiation pyrometers [3,5]		
Comments	Wide range of temperatures are accessible, limited to pure inert gas samples		

Method	Characterised stabilised flames	**References**	[6-11]
Cost	Low		
Equipment	Laminar premixed flame burner, gas metering and mixing apparatus, pure gas source, cooling system		
Scope of Measurements	CARS [6,11], LIF [10-11], Spontaneous Raman Scattering [8,9]		
Maximum Temperature	1900 °C [6,9]		
Traceability	CARS		
Comments	Hydrogen [6] and Methane [11] flames have been investigated. Potential for variety of gases and stoichiometries hence wide range of temperatures.		

Method	Gas filled tungsten filament lamps	**References**	[13-14]
Cost	Moderate		
Equipment	Tungsten lamp, optical pyrometer, regulated voltage supply		
Scope of Measurements	CARS, Spectroscopy		
Maximum Temperature	2000 °C [13], 3200 °C [14]		
Traceability	Radiation pyrometer, CARS		
Comments	Simple to implement, Very high temperature operation, limited to tungsten compatible gases.		

1.3.2 SUMMARY OF HIGH TEMPERATURE CALIBRATION TECHNIQUES

Technique	Cost	Maximum Temperature / °C	Accuracy / %	Comments
Line reversal method	Moderate	>2000	5%	Moderate accuracy, improved by seeding flame with metal i.e. sodium. Line of sight average temperature measured, scattering can degrade signal.
Single and two line transition methods	Moderate	>2000	5%	Moderate accuracy only. Prior knowledge of molecular parameters required. Requirement to fit observed data to theoretical model.
Modulated Emission in Gases	Moderate	>2000	<1%*	Potential for high spatial and temporal resolution. Thermodynamic temperature measured. Point by point method - no tomographic reconstruction required. S/N may be small. Careful selection of pump beam detector wavelengths required to maximise signal levels.
Spontaneous Rayleigh Scattering	Moderate	>2000	2-5%	Needs particle free environment. Large scattering cross-sections compared to Raman. Gives info on total species concentration and temperature via the ideal gas law. Need to discriminate scattered signal from incident beam. Simple to set up. Excellent spatial resolution.
Raman Scattering	High	>2000	2-5%	Species specific. Raman signal << Rayleigh. Vibr./Rot. Raman used for flames. Probe species that are not microwave active but are Raman active. Need to discriminate flame emission / LIF signals from Raman. Mie scattering can cause large errors. UV lasers can be used to improve Raman signal. Temperature obtained by Stokes/anti-Stokes lines and Boltzmann distribution or ratio of stokes scattering strength for 2 adjacent molecular lines.
Coherent anti-Stokes Raman Scattering (CARS)	High	>2000	2.5-3%	High spatial & temporal resolution. Signal does not generally interfere with LIF. Much larger signal / background signal than for Raman. Suited to simultaneous temperature and species concentration measurements. CARS spectral modelling is complex and data reduction is generally computationally intensive. Not effective if excessive temperature gradients exist.

---

* needs experimental verification

Technique	Cost	Maximum Temperature / °C	Accuracy / %	Comments
Degenerate Four Wave Mixing (DFWM)	High	>2000	5-8%	Can produce spatial temperature maps from single laser pulses. Resonant DFWM has excellent minor species detection capabilities. Experimentally challenging. S/N is low. Complex technique with generally poor accuracy.
Laser Induced Fluorescence	Moderate - High	>2000	2-5%	Very good species detection limits. Multi-parameter measurements possible. Straight forward set up for basic single pump beam system. High spatial and temporal resolution. Single shot 2D mapping of temperature field possible. Problems due to lack of knowledge of quenching mechanisms. LIF is perturbative technique.
Holographic & speckle methods	Moderate	>2000	4-8%	Measurements need to be made with and without the sample present. Field reconstruction, Abel or other, is generally limited to radially symmetric fields and the inversion process is very sensitive to errors. Poor time resolution and high sensitivity to noise are other disadvantages.
Photo-acoustic methods	Low-moderate	>2000	2-4%	Non-intrusive, high spatial and temporal resolution. Internal gas temperature measured - thermodynamic method. Not sensitive to background signals. Good temperature accuracy even for poorly determined species levels. Gas velocity errors. High ambient noise levels. Probe wander due to density gradients.
Photo-thermal methods	Low-moderate	>2000	2-5%	Purely optical detection. Good spatial and temporal sensitivities. Problems due to concentration gradients in probe region. Need to maintain probe and pump beams close together.
Physical probes	Low	<2000	2-5%	Chemical sampling, fibre-optic and thermocouple probes are all contact probes. Large errors due to radiation losses and catalytic effects. Errors due to perturbation of flame field. If corrected, thermocouples offer reasonable accuracy for well defined combustion environments. Maximum operating temperature can limit probes utility. Chemical sampling can allow for pre-cooling first.

1.4 RECOMMENDATIONS

A review has been undertaken of extant work on high temperature transfer standards. Although accurate knowledge of temperature is very important, little progress has been made into the provision of high accuracy, high temperature standard artefacts.

High purity gas cells have been developed as standards up to 2100 °C and through the use of traceable radiation pyrometers can be used as temperature standards. There are however several drawbacks that severely limit their utility. The first is the fact that there are very few suitable materials that can withstand frequent use at 2000 °C and above, and secondly, those that can generally require operation in an inert or vacuum environment. As a direct result of the latter, only high purity inert gases can be used in the test cells, which in turn means that typical combustion species are precluded from selection. For these reasons high purity gas cells will not be considered further. Tungsten filament lamps have good potential for use as very high temperature standards devices but again compatible problems arise with many gases reacting to a greater or lesser extent with tungsten at elevated temperatures, so limiting the gases that can be used. A characterised, stabilised flame with its low cost and simplicity of operation offers excellent potential as high temperature transfer standard. By variation of fuel and mixture ratios it is possible to produce laminar stabilised flames with different temperature and species profiles. Providing that the flame is sufficiently stable and reproducible, and can be calibrated by some non-perturbing method, an optical technique, for example, excellent potential exists. Other advantages include good optical access, no need to contain the flame, and good representation of the combustion environment. In light of these findings a McKenna burner system has been developed as the combustion standard.

A suitable thermometry technique needs to be implemented to characterise such a standard flame. Considering reproducibility and accuracy requirements, three suitable techniques have been identified:

- The Modulated Emission in Gases (MEG) technique.
- Spontaneous Rayleigh scattering thermometry.
- Photo-acoustic thermometry.

This thesis describes the full development and evaluation of the novel MEG technique. In light of experimental and theoretical limitations of MEG, I proceed to develop the well established Rayleigh scattering thermometry technique, taking a new direction by correcting for the temperature dependence of the scattering cross-sections of combustion species. This is the first time, to the author's knowledge, that such factors have been considered and allows for a marked improvement in Rayleigh scattering thermometry.

A photo-acoustic thermometry system utilising the beam deflection technique has also been developed to allow flame temperature measurement by an independent method and comparison with the Rayleigh temperatures is presented.

2. THE MCKENNA BURNER SYSTEM

2.1 GENERAL DESCRIPTION OF THE BURNER

The McKenna flat flame premixed burner [7] provided by *Holthuis & Associates* was chosen for this work. This burner has been evaluated by various authors [6,11,44] and has been shown to provide the required spatial and temporal uniformity in terms of temperature and species concentrations. The actual performance of the burner will be evaluated in later chapters.

Figure 2.1 shows the burner, which has a stainless steel outer housing, with a stainless steel porous burner plate of 60 mm diameter in its centre. Premixed propane and air flow through this plate and a thin flame is supported a few millimetres above it. Propane fuel was chosen since it is readily available in a high purity form and provides an adiabatic flame temperature above 2200 K. Other fuels can be used if higher or lower average flame temperatures are required but propane/air combustion was used extensively in this research.

The burner plate is water-cooled and has a coil sintered into it for this purpose. The burner can be operated with an inert shielding gas flowing through the outer ring but it was not found necessary for these experiments.

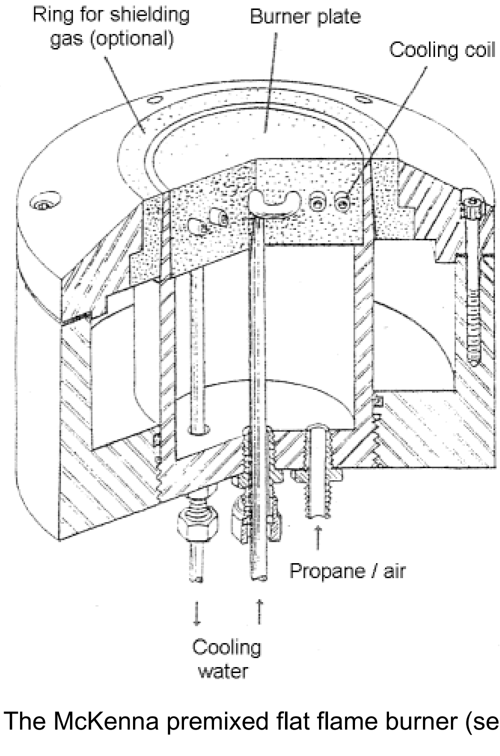

Figure 2.1 The McKenna premixed flat flame burner (sectional view).

Figure 2.2 shows a several photographs of the burner mounted on an XYZ translation stage. The burner has since been painted mat black to reduce spuriously scattered laser light.

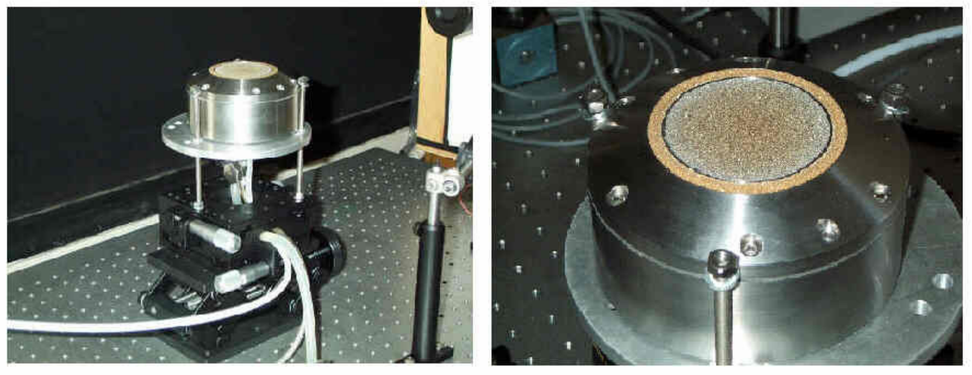

Figure 2.2 Photographs of the McKenna premixed flat flame burner.

Figure 2.3 shows the burner flame under interrogation by a 532 nm Nd-YAG laser beam. The thin premixed flame is seen anchored to the burner plate with the large diffusion flame seen above this due to operating the burner with excess fuel.

Figure 2.3 The fuel rich McKenna burner flame under laser interrogation.

2.2 GAS COOLING AND PREMIXING SYSTEM

Figure 2.4 shows the gas premixing and water cooling system for the McKenna burner. The burner cooling water and dry air firstly flow through a 100 litre water tank via individual copper coils in order to maintain all input substances to the burner at a common temperature. The propane and air then enter mass flow meters provided by Chell Instruments Ltd [55] which are calibrated with an uncertainty of better than 1%. The propane flow meter is connected to the air flow meter such that the ratio of the fuel to the air flow rate is constant. This constant ratio can then be adjusted via a potentiometer on one of the flow meters thus allowing for different fuel to air ratios. The air flow rate is then adjusted via a metering needle valve and the ratio of propane to air is automatically maintained throughout the measurements. Air flow rates of up to 100 Standard Litres Per Minute (SLPM) and fuel flow rates up to 10 SLPM were possible.

After metering, the two gases are thoroughly mixed in a specially designed turbulence generating chamber. The premixed gases then pass to the burner. The propane has a purity of 99.5% and the air is dry and of normal atmospheric composition. The burner cooling water flow rate was maintained at 0.7 standard litres per minute (SLPM), which resulted in a maximum temperature difference between the inlet and outlet cooling water of 6 °C.

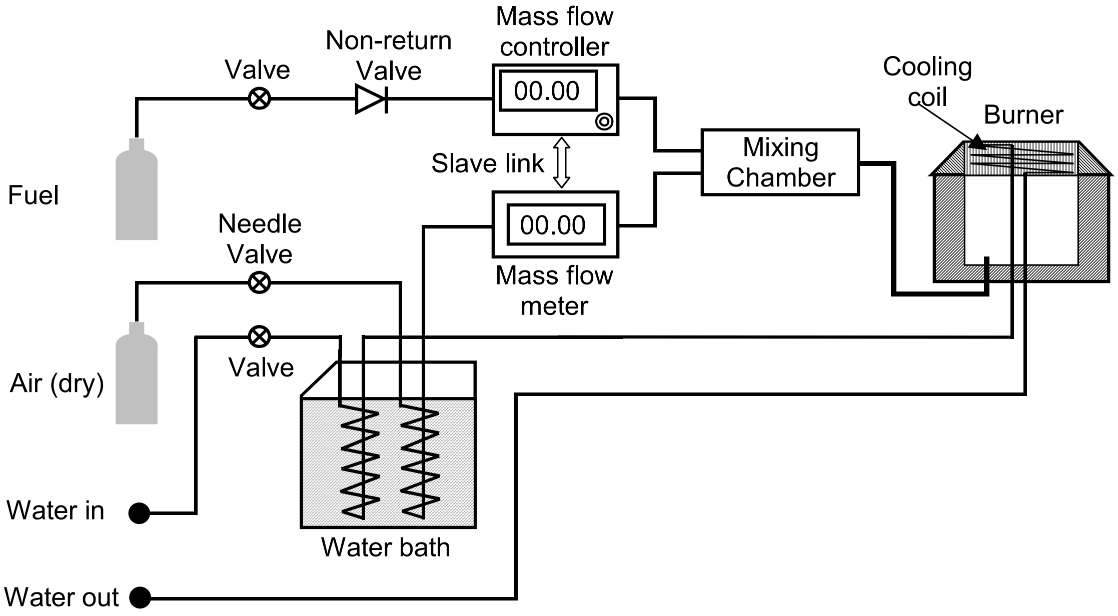

Figure 2.4 The gas premixing and water cooling system for the McKenna burner.

3. THE DEVELOPMENT AND EVALUATION OF THE MODULATED EMISSION IN GASES (MEG) THERMOMETRY TECHNIQUE

3.1 INTRODUCTION

The Modulated Emission in Gases (MEG) [56] thermometry technique is a new non-contact method of measuring gas temperatures. MEG utilises the local periodic heating provided by a weakly-absorbing laser beam tuned to a suitable spectral band of one of the combustion species, CO_2, CO or H_2O. Detection of the resulting thermal radiance with detectors placed either side of the measurement region gives the potential for high spatial resolution. In principle, the technique provides the thermodynamic temperature and does not rely on poorly known spectroscopic constants such as oscillator strengths or transition probabilities.

Unfortunately, detailed analysis has shown that MEG is not a usable thermometry technique. The principle difficulty arises from the spectral nature of the absorption coefficient of gases and the fact that the MEG theory assumes an *average* absorption coefficient over the optical detection bandwidth. This approximation leads to unacceptably large errors in the reconstructed temperature. A secondary difficulty arises from the lack of suitable high power laser that operates at a wavelength that coincides with a molecular absorption line in the hot gas. Since MEG requires absorption of the laser to generate localised heating of the gas, without such absorption, the technique cannot be used. However, before the limiting factors described above were fully realised and understood, a substantial amount of work had been undertaken to evaluate the MEG technique. This work provides valuable insights into the challenges of photo-thermal measurements in gases. The MEG theory is first described (§3.2), followed by a detailed sensitivity analysis (§3.3 to §3.4), including a computer simulation (§3.5). Attention is then moved to experimental implementation, with measurements made in the McKenna burner flame and a specially constructed 'Hot cell' (§3.6). Finally, the technique is reviewed and its limitations described in detail (§3.7 to §3.8).

3.2 MEG THEORY

The MEG measurement principle is illustrated in Figure 3.1. A small temperature modulation is produced in the y direction from absorption of a temporally modulated laser beam. Two detectors, one on each side of the measurement region, measure the resulting modulated radiance in two wavelength intervals. To scan the flame, the laser beam and detection optics are fixed and the burner is moved using an x-y translation stage.

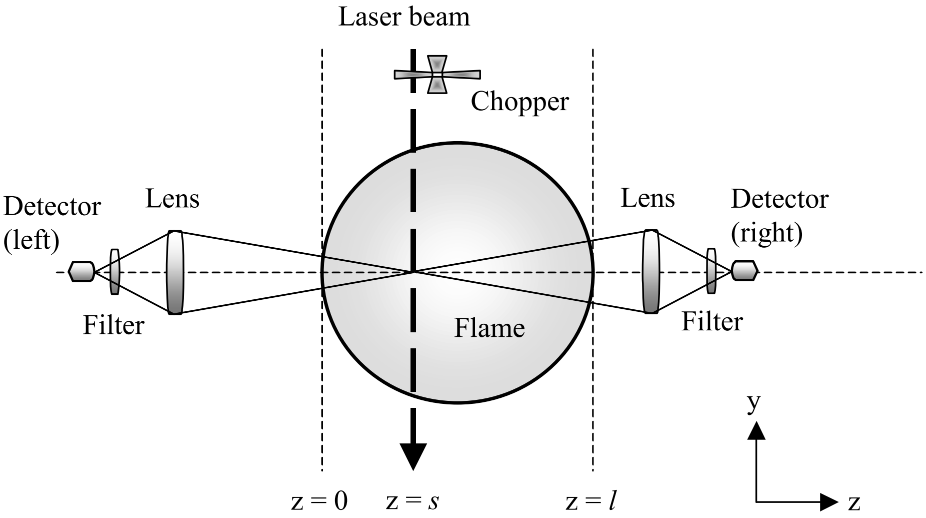

Figure 3.1 The MEG temperature measurement technique.

If we consider laser beam, modulated at frequency ω, which is weakly absorbed along the *y* direction, the equation of intensity of the radiation along the line between the two detectors, ignoring scattered radiation is:

$$\frac{dI(z,\lambda)}{dz}+\alpha(z,\lambda)I(z,\lambda)=\alpha(z,\lambda)I_b(z,\lambda) \tag{3.01}$$

The second term on the LHS represents absorption along *z* and the RHS represents emission along *z*. The *y*-dependence of the quantities has been omitted for clarity.

We now assume that the emission along *z* is due to two components: Firstly, the emission in the absence of the modulated beam, and secondly, the additional emission as a direct result of the small change in temperature due to absorption of the modulated beam. Based on this analysis we may then write:

$$I_b = L + L'\Delta T(z)e^{i\omega t} \tag{3.02}$$

Where L is the Planck function, $L' = {dL}/{dT}$ and $\Delta T(z)$ is the small temperature rise induced by the absorption of the laser beam. Strictly speaking $\Delta T(z)$ is not restricted to the pump beam region because of radiation interchange within the gas but this effect is very small.

Thus, *I(z)* will consist of a DC value and a component at ω due to the modulation, i.e.

$$I = I_0 + I_1 e^{i\omega t} \tag{3.03}$$

Considering the modulated signal, we may write:

$$\frac{dI_1}{dz}+\alpha(z)I_1=\alpha(z)L'(z)\Delta T(z) \tag{3.04}$$

Making use of an integrating factor, we can write the solution to Equation 3.04 as:

$$I_1 e^{\int_z^l \alpha(z')dz'} = \int \alpha(z) L'(z) \Delta T(z) e^{\int_z^l \alpha(z')dz'} dz \qquad (3.05)$$

If $\Delta T(z)$ has small enough extent, it can be treated as a delta function:

$$\Delta T(z) = Q(s)\delta(z-s) \qquad (3.06)$$

or

$$\int \Delta T(z) dz = Q(s) \qquad (3.07)$$

Therefore, it follows that:

$$I_1(z,s) = \alpha(s) L'(s) Q(s) e^{\int_s^l \alpha(z')dz'} e^{-\int_z^l \alpha(z')dz'} \qquad (3.08)$$

$$= \alpha(s) L'(s) Q(s) e^{-\int_z^s \alpha(z')dz'} \qquad (3.09)$$

Assuming measurements are made at two wavelengths for both detectors, we can generate four equations for the detector currents:

$$J_1^L(s) = A_1^L \alpha_1(s) L_1'(s) Q(s) e^{-\int_0^s \alpha_1(z')dz'} \qquad (3.10)$$

$$J_2^L(s) = A_2^L \alpha_2(s) L_2'(s) Q(s) e^{-\int_0^s \alpha_2(z')dz'} \qquad (3.11)$$

$$J_1^R(s) = A_1^R \alpha_1(s) L_1'(s) Q(s) e^{-\int_s^\ell \alpha_1(z')dz'} \qquad (3.12)$$

$$J_2^R(s) = A_2^R \alpha_2(s) L_2'(s) Q(s) e^{-\int_s^\ell \alpha_2(z')dz'} \qquad (3.13)$$

The subscripts define the wavelength of detection λ_1 or λ_2 and the superscripts define the left hand or right hand detectors. With A, the instrument constant given by:

$$A = R \Omega A_d \Delta\lambda \qquad (3.14)$$

with R the detector response (A/W), Ω the solid angle, A_d the detector area and $\Delta\lambda$ the optical bandwidth. α_1 and α_2 are the mean absorption coefficients at λ_1 and λ_2 over the optical bandwidth $\Delta\lambda$.

It is now possible to define the ratios of the LH and RH detector signals for the two wavelengths as:

$$R^L \equiv \frac{J_1^L(s)}{J_2^L(s)} = \frac{A_1^L}{A_2^L}\frac{\alpha_1(s)}{\alpha_2(s)}\frac{L_1'(s)}{L_2'(s)}e^{-\int_0^s \Delta\alpha_{12}(z')dz'} \tag{3.15}$$

$$R^R \equiv \frac{J_1^R(s)}{J_2^R(s)} = \frac{A_1^R}{A_2^R}\frac{\alpha_1(s)}{\alpha_2(s)}\frac{L_1'(s)}{L_2'(s)}e^{-\int_s^\ell \Delta\alpha_{12}(z')dz'} \tag{3.16}$$

With: $$\Delta\alpha_{12} = \alpha_1 - \alpha_2 \tag{3.17}$$

and the product of these two ratios as:

$$R^L R^R = B\left[\frac{\alpha_1(s)}{\alpha_2(s)}\right]^2\left[\frac{L_1'(s)}{L_2'(s)}\right]^2 e^{\int_0^\ell \Delta\alpha_{12}(z')dz'} \tag{3.18}$$

with : $$B \equiv \frac{A_1^L}{A_2^L}\frac{A_1^R}{A_2^R} \tag{3.19}$$

Since the exponential term in Equation 3.18 is the integral over the whole path $0 \rightarrow \ell$, it may be regarded as a constant for a given y position. Thus Equation 3.18 may be written as:

$$R^L R^R = C\left[\frac{\alpha_1(s)}{\alpha_2(s)}\right]^2\left[\frac{L_1'(s)}{L_2'(s)}\right]^2 \tag{3.20}$$

where C is a constant.

If we now ratio the detector signals at each wavelength we obtain:

$$R_1 = \frac{J_1^L}{J_1^R} = \frac{A_1^L}{A_1^R}e^{-\int_0^s \alpha_1(z')dz' + \int_s^\ell \alpha_1(z')dz'} \tag{3.21}$$

$$R_2 = \frac{J_2^L}{J_2^R} = \frac{A_2^L}{A_2^R}e^{-\int_0^s \alpha_2(z')dz' + \int_s^\ell \alpha_2(z')dz'} \tag{3.22}$$

Differentiating Equations 3.21 and 3.22 gives:

$$\frac{dR_1}{ds} = R_1\left(-2\alpha_1(s)\right) \tag{3.23}$$

$$\frac{dR_2}{ds} = R_2\left(-2\alpha_2(s)\right) \tag{3.24}$$

This means that if we measure $\frac{dR_1}{ds}$, the value of α_1 can be found and similarly, if we measure $\frac{dR_2}{ds}$, the value of α_2 can be found. Substituting these values into Equation 3.20 means that $\frac{L_1'(s)}{L_2'(s)}$ can be found and since this is only a function of *T*, the temperature can be found. The temperature is explicitly given by:

$$T(s) = \frac{C_2\left(\frac{1}{\lambda_2} - \frac{1}{\lambda_1} \right)}{Ln\left[\left(\frac{L_1'(s)}{L_2'(s)} \right) \left(\frac{\lambda_1}{\lambda_2} \right)^6 \right]} \tag{3.25}$$

3.3 MEG PRECISION ANALYSIS

Since the MEG technique requires discrimination of a small AC signal from that of a large DC background signal, it is important to determine the magnitude of temperature modulation required to provide an acceptable signal precision. A realistic value is a precision of 10^{-3} (i.e. 0.1%).

Considering a constant temperature and constant absorption coefficient over the investigated path length, the typical measured DC detector current, given by Equation 3.10, is:

$$I_0 = AL_1^0\left(1 - e^{-\alpha\ell}\right) \ , \qquad \text{and } A = R\omega A_d \Delta\lambda \tag{3.26}$$

Where R is the detector response (A/W)
ω the solid angle
A_d the imaged area
$\Delta\lambda$ the optical bandwidth
L^0_1 the spectral radiance
α the average absorption coefficient
l the path length

The AC detector current due to a temperature modulation at a point *s*, where 0 ≤ s ≤ *l*, is given by the MEG theory as:

$$I_1(s) = A\alpha L_1' \Delta T \Delta z e^{-\alpha s} \tag{3.27}$$

Where L_1' is the derivative of the spectral radiance with respect to the temperature *T*. ΔT and Δz are the temperature rise and the spatial extent of the temperature modulation respectively. The ratio of AC to DC signals can now be written as:

$$\frac{I_1(s)}{I_0} = T_0 \frac{L_1' \Delta z . e^{-\alpha s}}{L_1^0\left(1 - e^{-\alpha\ell}\right)} \left(\frac{\Delta T}{T_0} \right) \tag{3.28}$$

Assuming that the detector is ‘shot noise’ limited, the noise current is given by:

$$I_n^2 = 2qI_0B_0 \tag{3.29}$$

with q the electronic charge and B_0 the post-detection bandwidth.

We may now write the signal to noise ratio as:

$$\frac{I_1^2}{I_n^2} = \left(\frac{I_1}{I_0}\right)^2 \frac{I_0}{2qB_0} = \left(\frac{T_0 L_1' \Delta z e^{-\alpha s}}{L_1^0\left(1-e^{-\alpha\ell}\right)}\right)^2 \frac{I_0}{2qB_0}\left(\frac{\Delta T}{T_0}\right)^2 \tag{3.30}$$

Table 3.1 shows representative parameters for the 4.3μm band of CO_2 in the post flame region of the McKenna burner [7]. These values are used in the precision analysis since the MEG technique will ultimately measure the temperature of such a post flame region. The value for the average absorption coefficient, α, was chosen by considering the partial pressure of CO_2 in the exit gas from the burner for stoichiometric combustion of Propane and air.

Parameter	Typical value
I_0 [A]	0.00009
α [m^{-1}]	10
T_0 [K]	2000
Δz [m]	0.005
L_1'/L_1^0 [K^{-1}]	0.000835
l [m]	0.06
$S = l/2$ [m]	0.03
B_0 [Hz]	1

Table 3.1 Typical post flame parameters.

Simplifying Equation 3.30 leads to the original requirement that:

$$SNR = \frac{I_1}{I_n} = \left(\frac{T_0 L_1' \Delta z e^{-\alpha s}}{L_1^0\left(1-e^{-\alpha\ell}\right)}\right)\sqrt{\frac{I_0}{2qB_0}}\left(\frac{\Delta T}{T_0}\right) \geq 10^3 \tag{3.31}$$

Substituting the parameters from Table 3.1 into Equation 3.31 yields, to the nearest order of magnitude, the result:

$$\frac{\Delta T}{T_0} \geq 10^{-3} \tag{3.32}$$

Thus for T_0 = 2000 K, a temperature modulation of 2 K will satisfy the original precision requirement. We now need to estimate the temperature rise due to laser absorption; this is presented in the next section.

3.4 TEMPERATURE RISE DUE TO ABSORPTION OF A LASER BEAM

To determine the signal levels that a weakly absorbed laser beam would produce in the flame, two models have been constructed. The first allows the temperature increase and subsequent decay to be found for a delta function laser pulse (i.e. the impulse response function) and the second calculates the signal amplitude of a modulated laser beam for a range of angular frequencies (ω). Both models are to be viewed as order of magnitude approximations only.

3.4.1 TEMPERATURE RISE DUE TO A SINGLE LASER PULSE

Assuming cylindrical geometry with the laser beam propagating in the *z* direction, with a gaussian radial intensity distribution of total energy P_0, we may write the laser intensity as:

$$I(r,t) = \frac{2P_0}{\pi a^2} e^{\frac{-2r^2}{a^2}} \delta(t) \tag{3.33}$$

where $\delta(t)$ is the delta function, representing the instantaneous nature of the laser pulse, *a* is the 1/*e* beam radius and *r* the radial distance from the beam centre.

For a small average absorption coefficient β and an average specific heat capacity of C_v, the instantaneous temperature rise ΔT_0 is given by:

$$\Delta T_0 = \frac{2\beta P_0}{\pi a^2 C_v \rho} e^{\frac{-2r^2}{a^2}} \tag{3.34}$$

where ρ is the average gas density.

We now need to obtain the transfer function of this pulse in the medium, for which we assume that we have radial diffusion *D*, and that the heating due to the pulse uniform along the *z* axis; we can assume this as β is small.

The equation of heat transfer for the pulse heating the gas is given by the standard radial diffusion equation:

$$\frac{1}{r}\frac{\partial}{\partial r}\left(r\frac{\partial T}{\partial r}\right) - \frac{1}{D}\frac{\partial T}{\partial t} = 0 \tag{3.35}$$

with the boundary condition:

$$T(r,0) = \Delta T_0 = \frac{2\beta P_0}{\pi a^2 C_v \rho} e^{\frac{-2r^2}{a^2}} \tag{3.36}$$

By applying the Hankel Transform to Equation 3.35, the general solution can be written as:

$$T_{H0}(\lambda) = F_{H0}(\lambda) e^{-D\lambda^2 t} \tag{3.37}$$

Applying the inverse Hankel transform we obtain:

$$T(r,t) = \int_0^\infty e^{-D\lambda^2 t} F_{H0}(\lambda)\lambda J_0(\lambda r)d\lambda \tag{3.38}$$

with the boundary condition:

$$F_{H0}(r) = B\int_0^\infty r J_0(\lambda r) e^{\frac{-2}{a^2}r^2} dr = \frac{Ba^2}{4} e^{\frac{-\lambda^2 a^2}{8}} \tag{3.39}$$

by standard integrals and $B = \dfrac{2\beta P_0}{\pi a^2 C_v \rho}$

Substitution of Equation 3.39 into Equation 3.38 yields:

$$T(r,t) = \int_0^\infty e^{-D\lambda^2 t} \frac{Ba^2}{4} e^{\frac{-\lambda^2 a^2}{8}} \lambda J_0(\lambda r)d\lambda \tag{3.40}$$

So,

$$T(r,t) = \frac{\beta P_0}{2\pi C_v \rho} \int_0^\infty \lambda J_0(\lambda r) e^{\frac{-(a^2+8D\lambda^2 t)}{8}\lambda^2} d\lambda \tag{3.41}$$

Making use of the same standard integral used in Equation 3.39, we may finally write

$$T(r,t) = \frac{2\beta P_0}{\pi C_v \rho} \frac{e^{\frac{-2r^2}{b^2}}}{b^2} \tag{3.42}$$

with $b^2 = a^2 + 8Dt$

So Equation 3.42 is the transfer function for our laser system for a $\delta(t)$ input signal. i.e. the temperature rise due to an incident laser pulse.

We are now in a position to determine the temperature rise one might expect for a given set of input parameters. Typical values for the flat-flame burner with propane/air at stoichiometric are given in Table 3.2. The pulse laser power is typical of a pulse TEM CO_2 laser used in initial studies.

Parameter	Estimate of magnitude	Comments
P_0	15 mJ	Energy per laser pulse
C_v	1043 kg.K^{-1}	Heat capacity – assumed 100% N_2
ρ	0.14 kg.m^{-3}	Gas density – assumed 100% N_2
K	0.1314 W.m^{-1}.K^{-1}	Thermal conductivity - assumed 100% N_2
D	9 x 10^{-4} m^2.s^{-1}	Thermal diffusivity ($D=K/\rho C_v$)
β	1.75 m^{-1}/ 0.855 m^{-1}	10% / 5% absorption over 6cm length
T	2300 K	All parameters calculated @ 2300 K*
a	1 x 10^{-3} m / 2 x 10^{-3} m	Laser beam radius (1/e)

Table 3.2 Typical post flame parameters.

Figure 3.2 shows the temperature rise and decay for the above parameters; the gaussian beam profile is seen to decay as time progresses.

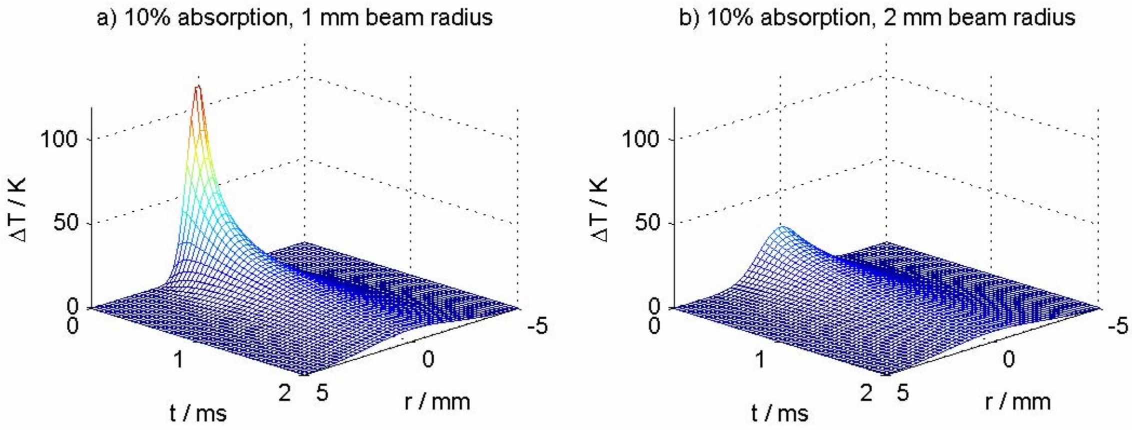

a) 10% absorption, 1 mm beam radius

b) 10% absorption, 2 mm beam radius

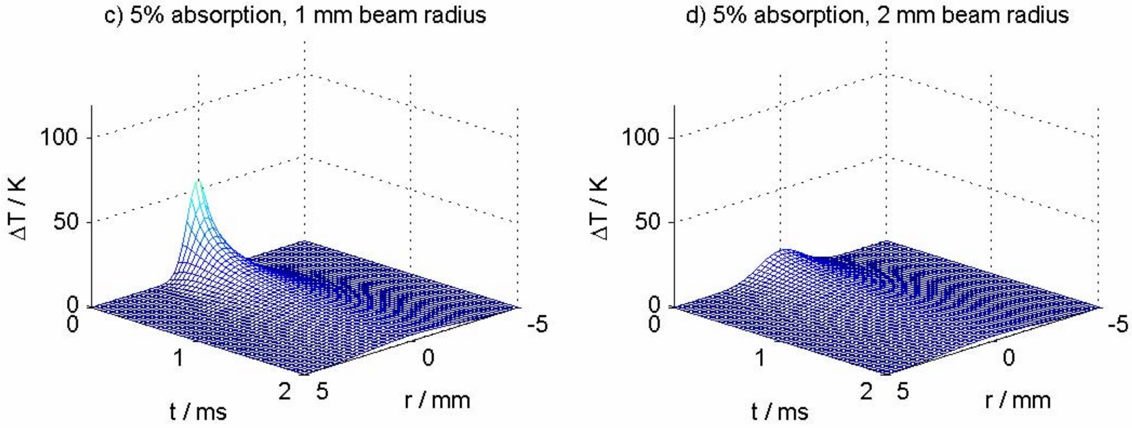

c) 5% absorption, 1 mm beam radius

d) 5% absorption, 2 mm beam radius

Figure 3.2 Temperature rise due to absorption of pulse laser radiation.

For a typical 1 mm beam radius, 5 % and 10 % absorption over the flame region (60 mm) give rise to temperature increases of 55 K and 120 K respectively. For a 2 mm beam radius, 5 % and 10 % absorption over the flame region give rise to temperature increases of 15 K and 28 K respectively.

This model assumes broadband absorption but in reality, in a high temperature gas, line absorption would be the dominant energy exchange process so temperature rises of several orders of magnitude less may be expected. The model does however give the indication that the temperature rise is significant if a suitable molecular absorption can be utilised.

3.4.2 TEMPERATURE RISE DUE TO A MODULATED CONTINUOUS WAVE LASER

The second model was developed to determine the magnitude of the temperature rise that a modulated laser beam would produce in the flame. The parameters from Table 3.2 were used except that a CW laser of 25 W was assumed as the laser source.

Since Equation 3.42 gives the transfer function for a $\delta(t)$ pulse, it is a relatively simple task to develop the response due to a modulated beam. We simply need to integrate the product of the pulse transfer function and cosine modulation term for all times previously, i.e. from t = - ∞ to the current elapsed time. This is achieved by the following integral:

$$T(r,t) = \alpha \int_{-\infty}^{t} \frac{1}{b^2} e^{\frac{-2r^2}{b^2}} Cos\left[w(t-t')\right] dt' \qquad (3.43)$$

with: $$\alpha = \frac{2\beta P_0}{\pi C_V \rho}, \text{ and } b^2 = a^2 + 8Dt'.$$

Figure 3.3 shows the amplitude of temperature modulation due to a cosine laser beam for angular frequencies from 50 to 1000 rad.s^{-1}. The signal levels are significant, reducing as the modulation frequency is increased. A typical value being 3 K for 900 rad.s^{-1} (approximately 140 Hz).

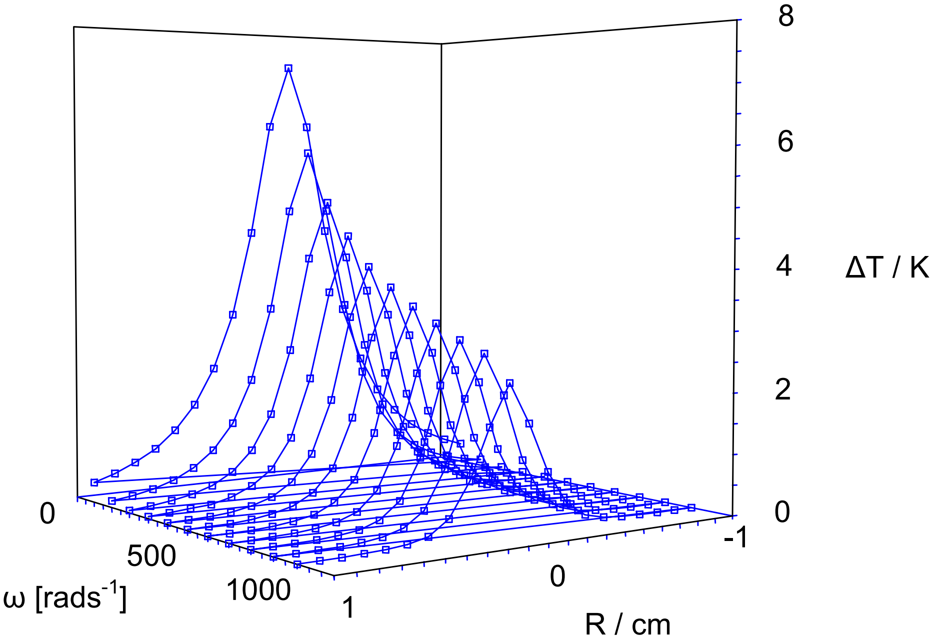

Figure 3.3 Temperature modulation amplitude due to cosine laser beam. β=10%, a=2 mm.

The MEG precision analysis presented in §3.3 indicated that a temperature rise of at least 2 K would provide the technique with a sensitivity of 0.1%. Based on the models presented above, we should be able to satisfy this requirement provided we can obtain sufficient absorption (5-10%) in the flame and confine the beam to a 1/e radius of less than 2 mm.

3.5 MEG COMPUTER SIMULATION

3.5.1 MODEL DEFINITION

A MEG computer simulation has been written in MATLAB [57]. The aim of the simulation was to model the uncertainty in the recovered temperature as a result of the addition of random noise in the measured signals. The random noise is assumed to result from the shot-noise associated with the large D.C. radiance signals that are incident on the detectors; although the A.C. MEG signals are small, the D.C. radiance of the gas in the path between the detectors contributes a significantly larger noise signal.

Figure 3.4 shows the user interface to the MEG evaluation program with the default parameters shown. All parameters are adjustable including the functional form of the temperature profile and the two absorption coefficients. The default value for the flame width is 0.06m (the physical width of the McKenna burner flame region) and the magnitude of the temperature modulation is set to 2K (the approximate temperature rise predicted for 10% absorption of the pump laser beam). The modulation extent is set to 0.005m, which corresponds to the 1/*e* diameter of the gaussian pump beam. All the detector parameters can also be adjusted, including the detection wavelengths, the optical bandwidths and the post detection bandwidth (PDB).

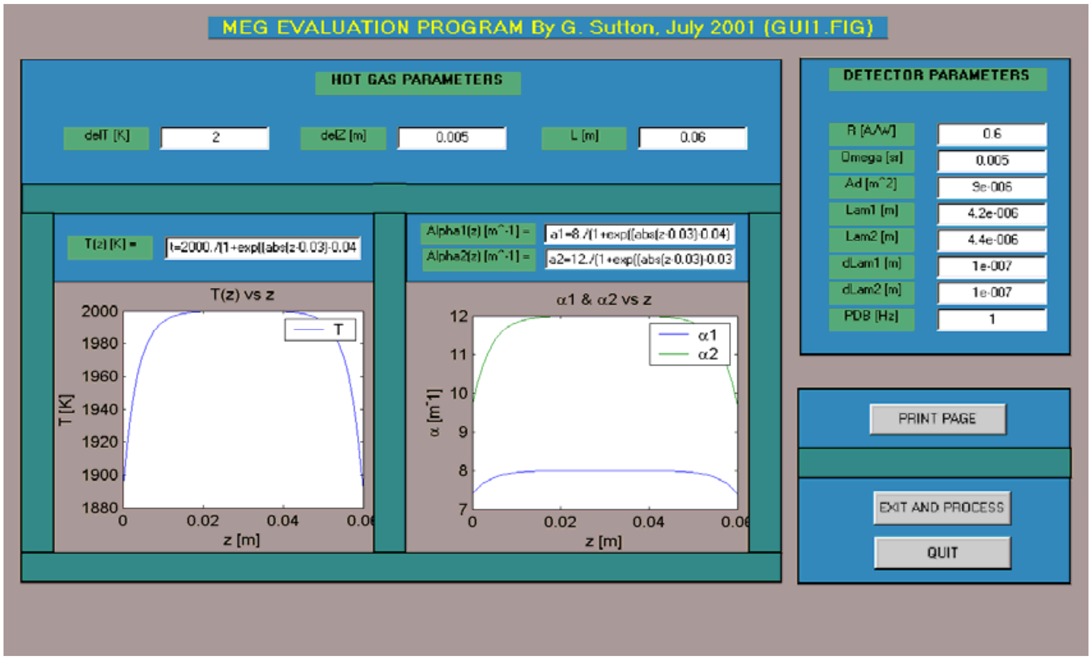

delT [K] 2
delZ [m] 0.005
L [m] 0.06
T(z) [K] = t=2000./(1+exp((abs(z-0.03)-0.04
Alpha1(z) [m^-1] = a1=8./(1+exp((abs(z-0.03)-0.04)
Alpha2(z) [m^-1] = a2=12./(1+exp((abs(z-0.03)-0.03

R [A/W] 0.6
Omega [sr] 0.005
Ad [m^2] 9e-006
Lam1 [m] 4.2e-006
Lam2 [m] 4.4e-006
dLam1 [m] 1e-007
dLam2 [m] 1e-007
PDB [Hz] 1

Figure 3.4 The MEG Simulation user interface.

The two wavelength regions selected are at either end of the 4.3 µm band of CO_2, the strongest absorption band of CO_2 by an order of magnitude. The optical bandwidth by default was set to 0.1 µm. The values for the average absorption coefficients of these two regions can be approximated by considering a stoichiometric Propane/air atmospheric pressure flame at approximately 2000 K. The partial pressure of CO_2 in the post flame region can be approximated by the mole fraction of CO_2 present. The classical single reaction model provides the method to obtain this pressure:

$$C_3H_8+5O_2+(79/21*5)N_2 \rightarrow 3CO_2+4H_2O+(79/21*5)N_2$$

This gives a CO_2 partial pressure of:

$$P_{CO2} = 3/(3+4+79/21*5)*P_{atm} = 0.116 \text{ atm}$$

This partial pressure is then used as the input parameter to a suitable spectral synthesis program to calculate the spectral absorption coefficient. The program TRANS [58] has been used for this purpose with the spectral data taken from the HITEMP [59] spectral database. Figures 3.5 and 3.6 show the absorption coefficients for the 4.2 µm and 4.4 µm region for a CO_2 partial pressure of 0.116 atm, at 2000 K. From these figures, the average absorption coefficients are: α_1 = 8 m^{-1} and α_2 =12 m^{-1} in the 4.2 µm and 4.4 µm regions respectively.

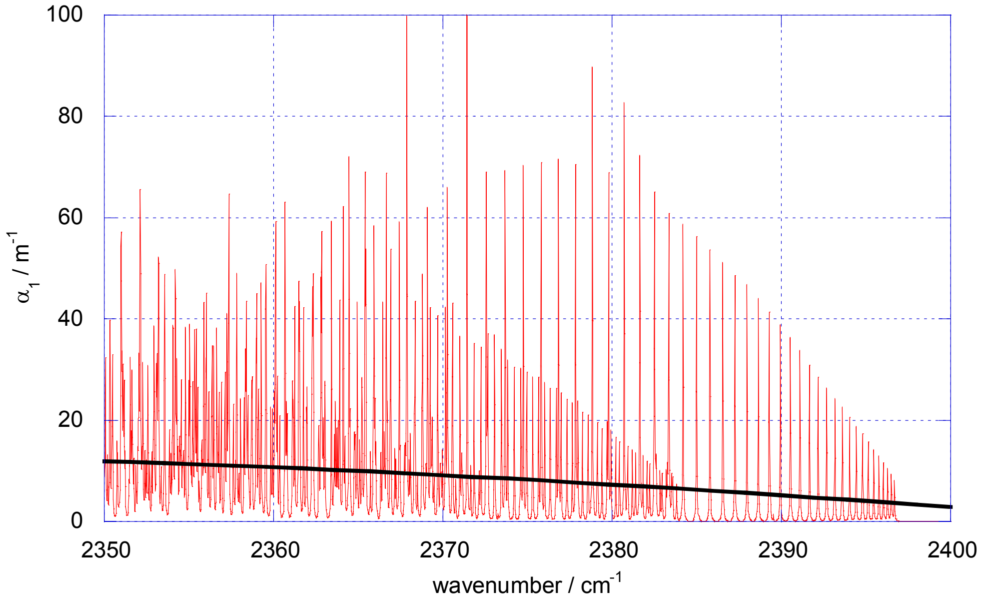

Figure 3.5 Absorption coefficient for 0.116 atm CO_2 at 2000 K for the 4.2 µm region (mean value shown in black).

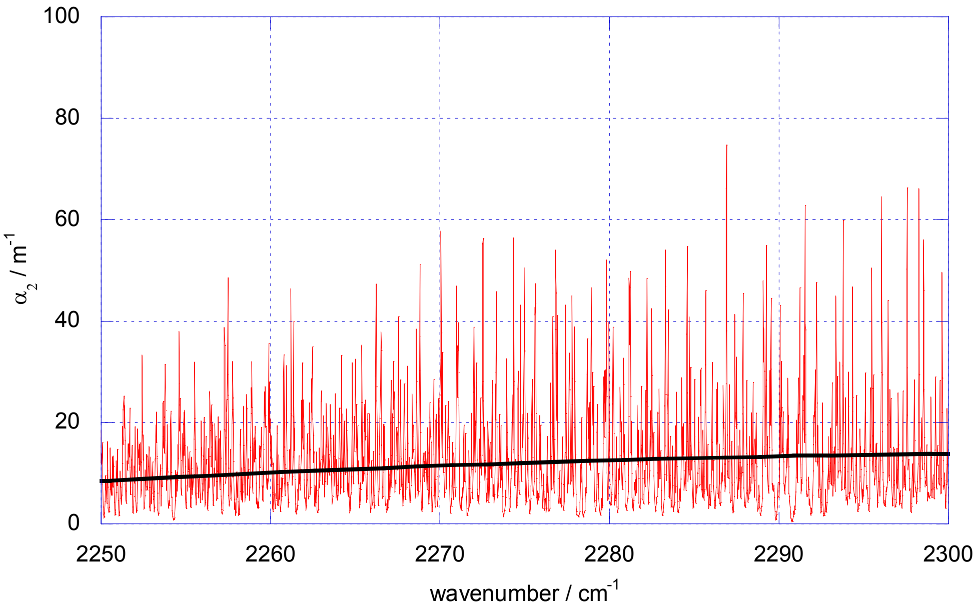

Figure 3.6 Absorption coefficient for 0.116 atm CO_2 at 2000 K for the 4.4 μm region (mean value shown in black).

The procedure used to calculate the 'MEG temperature' is as follows:

i) Calculate the DC radiance from the whole path through the flame.
ii) Convert this value to a detector current.
iii) Assuming that the detectors are shot noise limited, determine the mean amplitude of the noise by using the standard shot noise formula: $I_n^2 = 2qI_0B_0$ with q, the electronic charge, B_o the post detection bandwidth and I_0 the DC signal current.
iv) Determine the four AC detector currents for all points along the flame path using Equations 3.10-13.
v) Add normally distributed random noise of variance I_n^2 to the four AC detector signals.
vi) Calculate the various signal ratios; R^L, R^R (Equations 3.15/16), R_1, R_2 (Equations 3.21/22) and R^LR^R (Equation 3.18) and smooth.
vii) Reconstruct the absorption coefficients α_1 and α_2 by using Equations 3.23/24, i.e.

$$\frac{dR_1}{ds} = R_1(-2\alpha_1(s)) \qquad \text{and} \qquad \frac{dR_2}{ds} = R_2(-2\alpha_2(s))$$

It was very important to smooth the R_i data since calculating the derivative of a noisy signal can introduce large errors.

viii) Determine the ratio of the derivatives of the Planck function by using Equation 3.20, i.e.

$$\left[\frac{L_1'(s)}{L_2'(s)}\right]^2 = \frac{R^LR^R}{C\left[\frac{\alpha_1(s)}{\alpha_2(s)}\right]^2} \qquad \text{where C is a known constant.}$$

ix) The derivative, w.r.t T, of the Planck function is given by:

$$L' = \frac{2C_1C_2}{\lambda^6 T^2} e^{-\frac{C_2}{\lambda T}} \tag{3.44}$$

x) Making use of Equation 3.44 we recover the temperature in Equation 3.25, i.e:

$$T(s) = \frac{C_2\left(\frac{1}{\lambda_2} - \frac{1}{\lambda_1} \right)}{Ln\left[\left(\frac{L_1'(s)}{L_2'(s)} \right) \left(\frac{\lambda_1}{\lambda_2} \right)^6 \right]} \tag{3.25}$$

For simplicity, it is assumed that both detectors have the same characteristics, view the same solid angle, and that the optical bandwidth is the same for both wavelengths. It is for this reason that no detector calibration factors appear in Equation 3.25.

xi) The reconstructed temperature profile given by Equation 3.25 can now be compared with the original profile and the differences can be investigated.

3.5.2 APPLICATION OF THE MODEL AND RESULTS

With the default parameters described above, the MEG model can now be tested. Figure 3.7 shows a typical example of the detector signals and ratios with shot noise present (post detection bandwidth of unity).

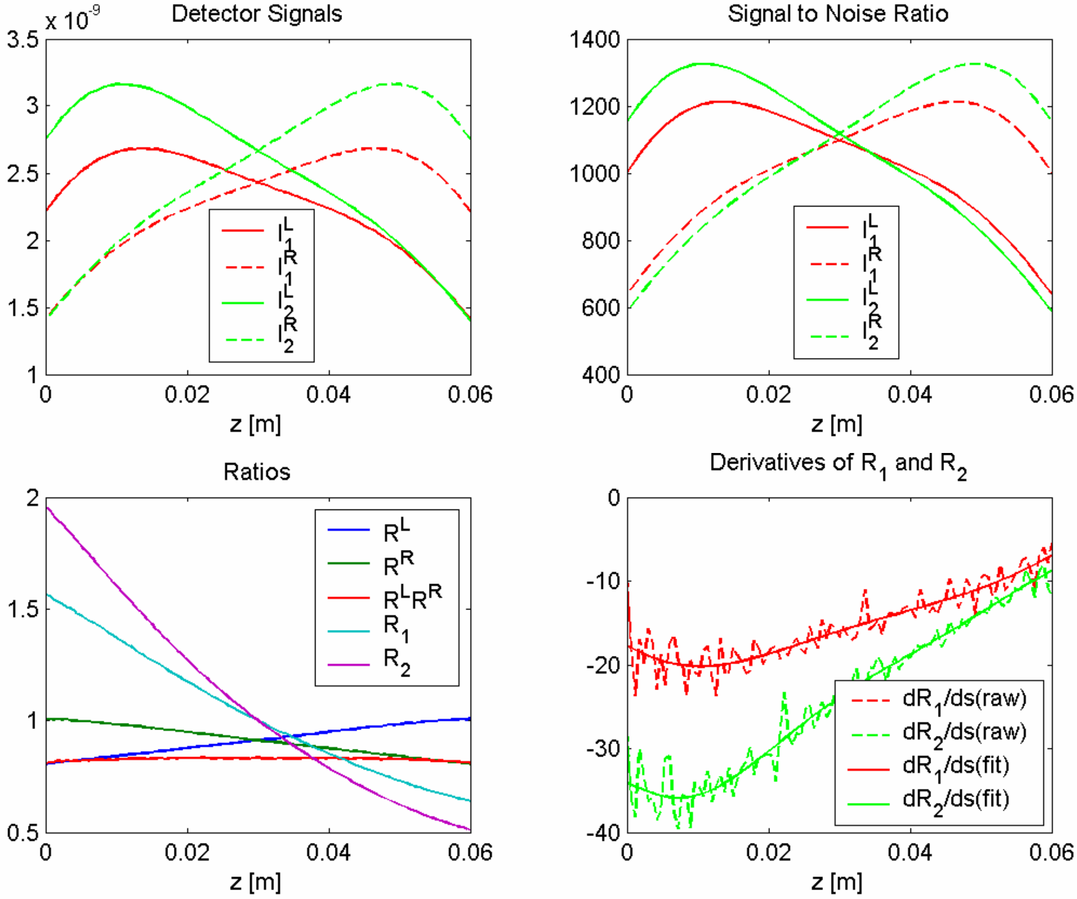

Figure 3.7 Typical detector signals, ratios and derivatives.

To verify that the software was capable of reconstructing the original temperature profile, the snot noise signal contribution was initially switched off. Figure 3.8 shows the original/reconstructed temperature fields and the error in the reconstruction. The temperature/absorption coefficient profiles were modelled on a 'Top-hat' function, which was thought to be representative of the McKenna burner flame. We see that the original temperature profile has been reproduced with negligible error (E < 0.007 %).

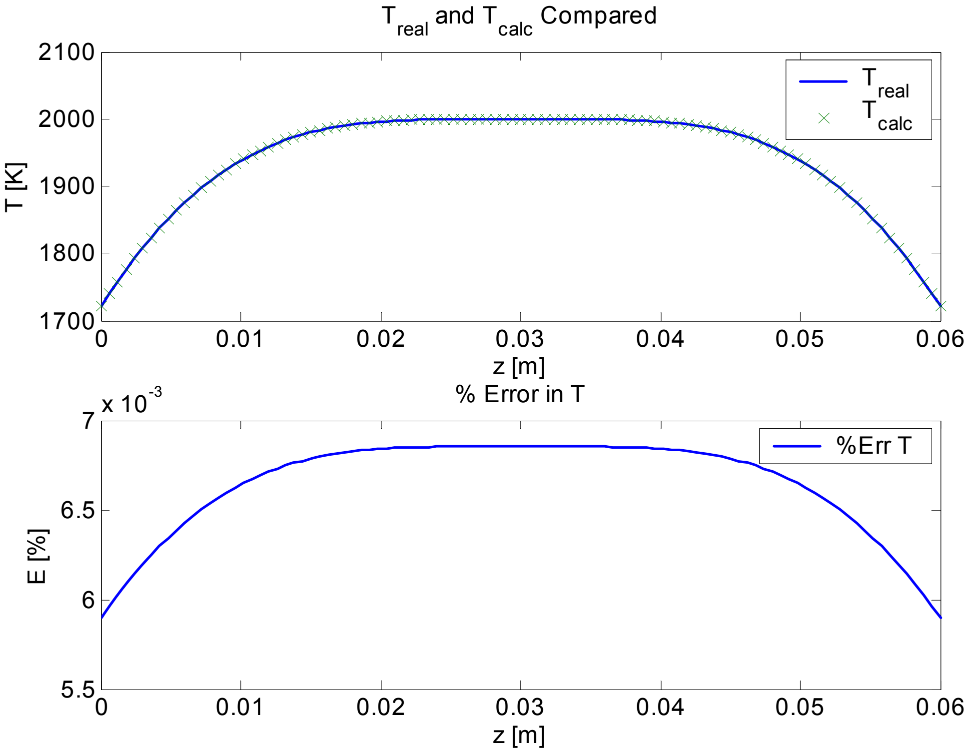

Figure 3.8 Assumed (T_{real}) and reconstructed temperature (T_{calc}) field with no shot noise.

Once it had been confirmed that the model reproduced the original temperature field satisfactorily, the shot noise term was re-introduced and investigation into the S/N and temperature accuracy continued. For a temperature modulation of 2 K it was earlier found (§3.3) that a S/N ratio of order 10^3 would be achievable for a post detection bandwidth of 1 Hz. The MEG model verifies this estimation, as shown in Figure 3.9**,** which shows the S/N for the four AC detector signals. Note that in the middle of the flame (z = 0.03 m) the S/N is very close to 10^3.

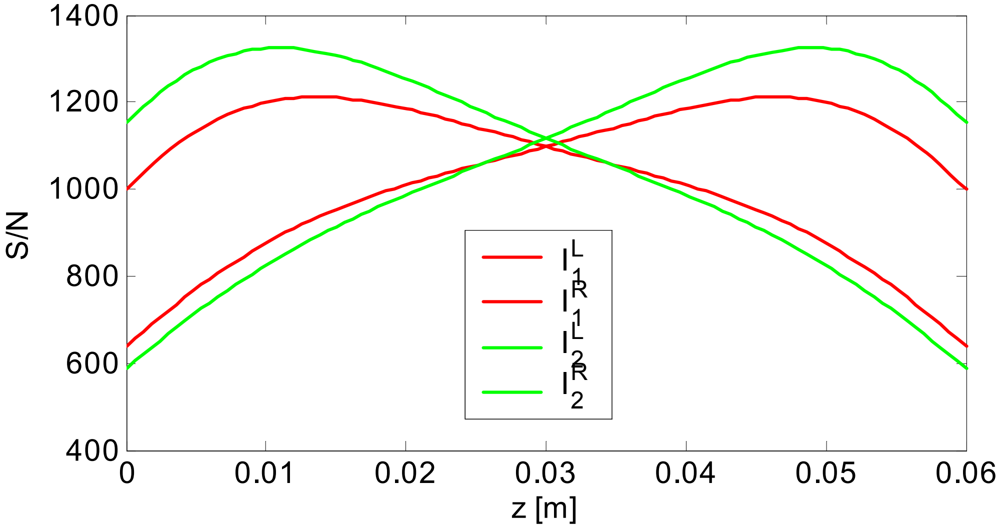

Figure 3.9 Signal to noise ratio for a 2 K temperature modulation.

To utilise the MEG technique as a calibration method, the temperature field must be reproduced with an uncertainty of less than 1%. The simulation was run for various post detection bandwidths, corresponding to averaging the detector signals for longer periods of time. Figures 3.10-3.14 show the temperature fields for various PDBs.

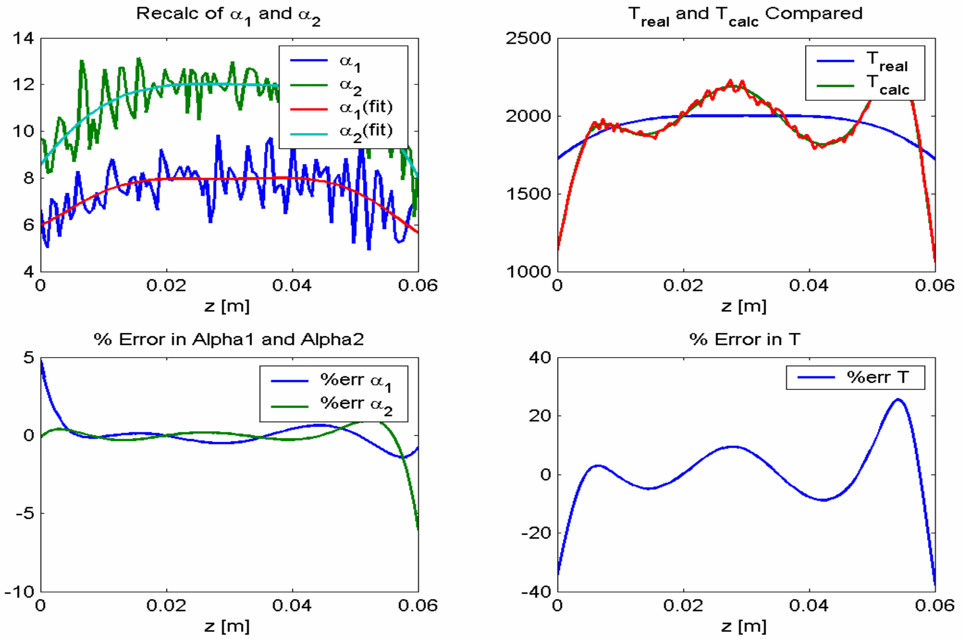

Figure 3.10 Reconstructed absorption coefficients and temperature for P.D.B of 1 Hz.

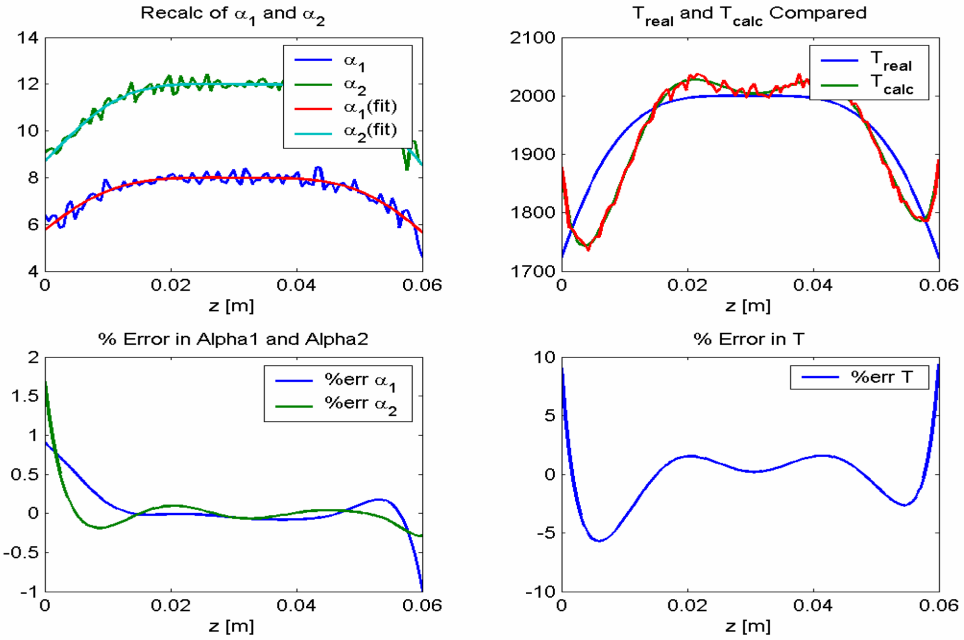

Figure 3.11 Reconstructed absorption coefficients and temperature for P.D.B of 0.1 Hz.

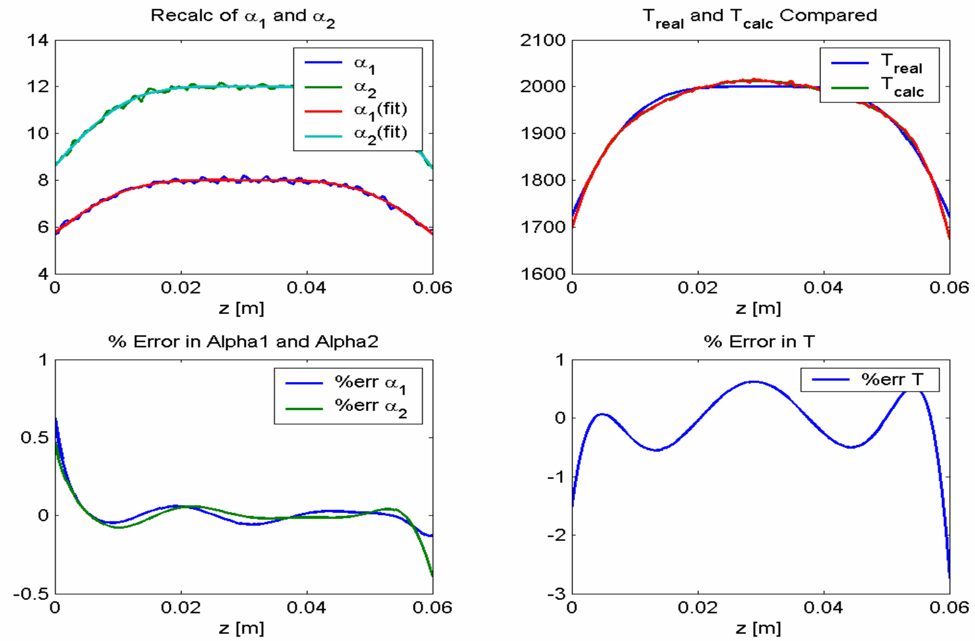

Figure 3.12 Reconstructed absorption coefficients and temperature for P.D.B of 0.01 Hz.

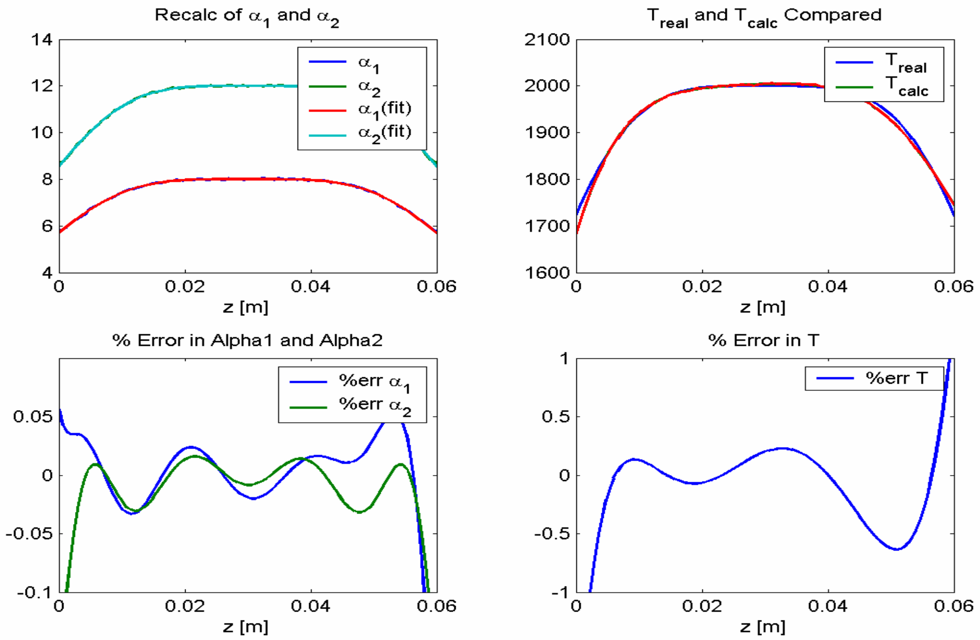

Figure 3.13 Reconstructed absorption coefficients and temperature for P.D.B of 0.001 Hz.

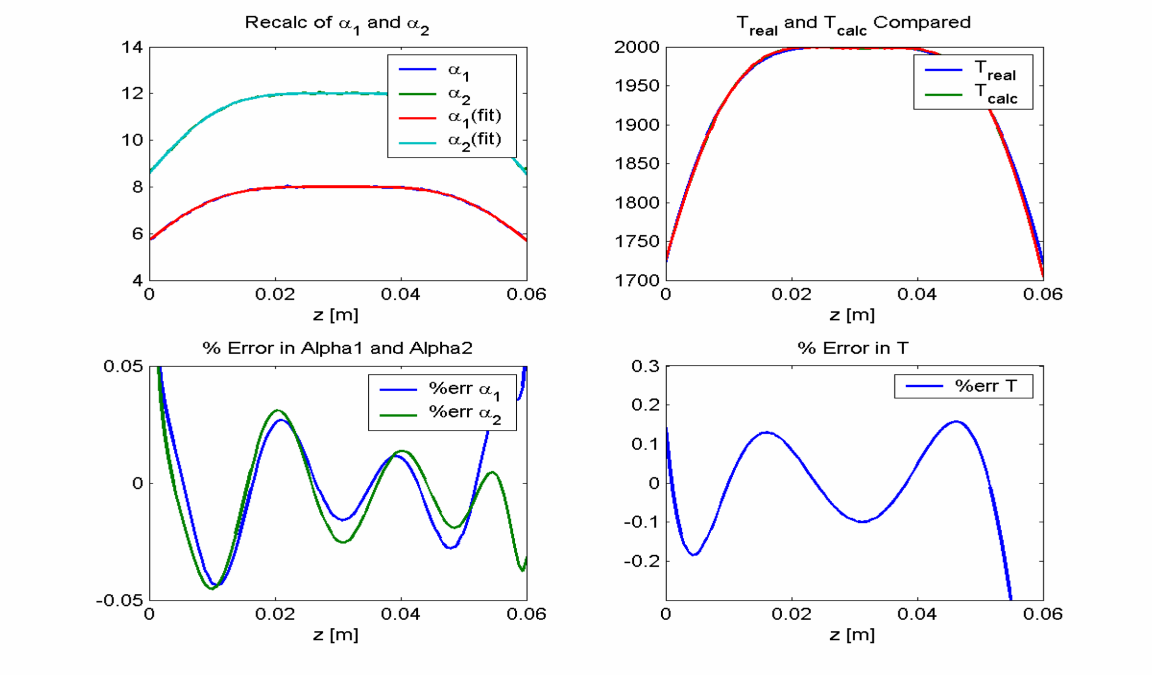

Figure 3.14 Reconstructed absorption coefficients and temperature for P.D.B of 0.0005 Hz.

The fitting algorithms used to smooth the derivative data (dR_1/ds and dR_2/ds) perform a polynomial fit and as such introduce a certain amount of oscillation in the reconstructed temperature. In realistic experimental conditions, the fitting functions will be optimised to reduce this oscillation.

In summary, the approximate error (± E [%]) in the reconstructed MEG temperature is proportional to the square root of the post detection bandwidth. Figure 3.15 shows this result.

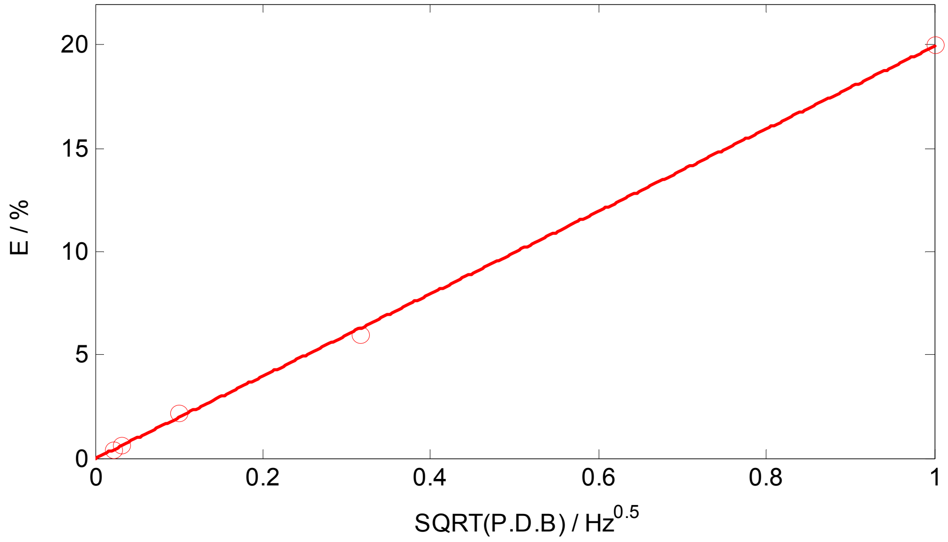

Figure 3.15 % error in reconstructed temperature vs SQRT(Post Detection Bandwidth).

Optimising the MEG detection wavelength can improve the signal/noise ratio. We see from Figure 3.16 that at 1 μm the S/N ratio increases with temperature where as at 4 μm the S/N ratio decreases with increasing temperature. This simply arises from the form of the Planck function in that the wavelength of its peak changes with temperature. The results presented above assumed measurements around 4 μm – in a strong band of CO_2, but it is clear that moving to shorter wavelengths increases the S/N up until the peak of the curve is reached (i.e. $\lambda_{max} = 2$ μm for T = 1000 K and $\lambda_{max} = 1$ μm for T = 2000 K).

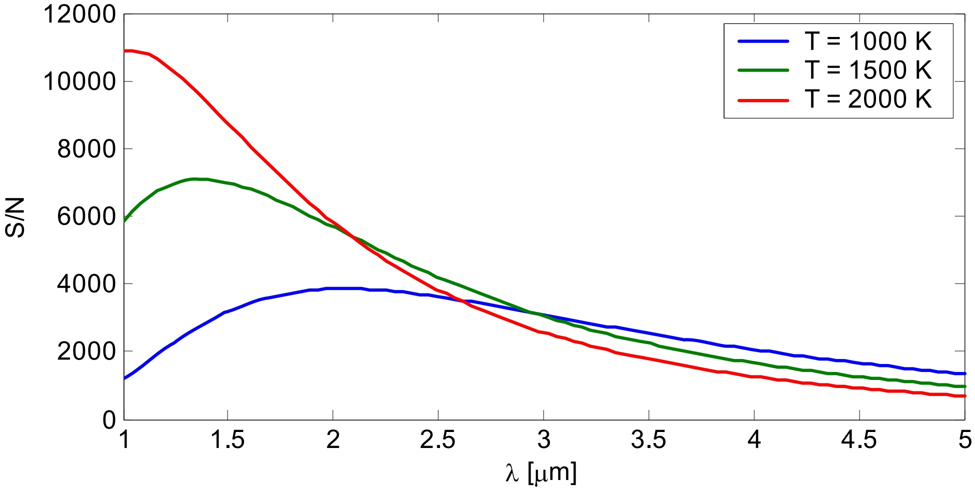

Figure 3.16 Signal/noise ratio versus detector wavelength and temperature (P.D.B. = 1 Hz).

Figure 3.17 shows the effect of small and large absorption coefficients in the flame. If the flame approaches the optically thick regime as seen in 3.17(b) the signals are very strong close to the flame edge but are almost completely attenuated by the time they have passed through the flame and reached the other side. For example: the signals measured by the LHS and RHS detectors as a result of temperature modulation at z = 0 are large for $I_1^L(z=0)$ but very small for $I_1^R(z=0)$.

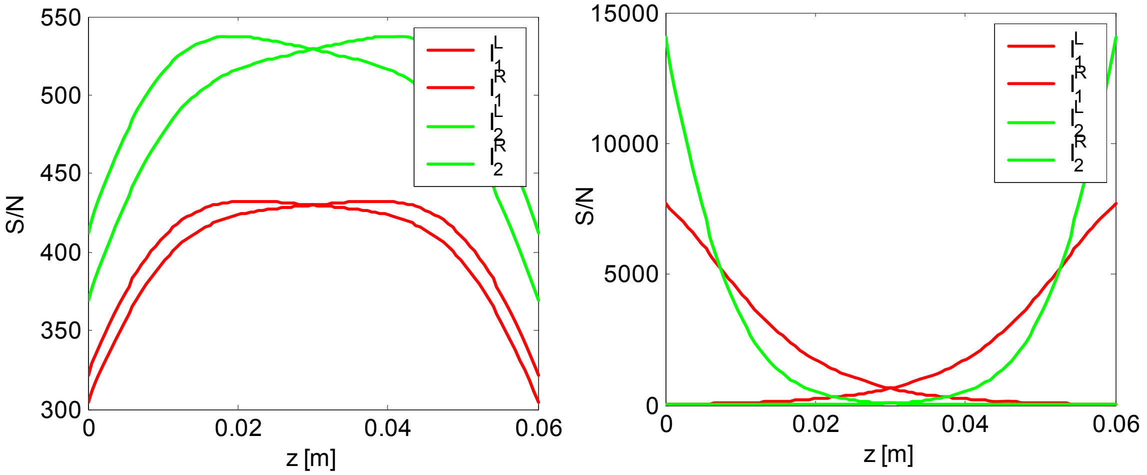

Figure 3.17 Signal/noise ratio for (a) $\alpha_1 = 1$, $\alpha_2 = 2$ and (b) $\alpha_1 = 100$, $\alpha_2 = 200$. (P.D.B. = 1 Hz). (Shown as a function of position across the burner).

In conclusion, the model clearly demonstrates that provided the post detection bandwidth (P.D.B.) is less that 0.001 (integrating time of approximately 15 minutes) we can reconstruct the temperature to an accuracy of better that 1%. This was an encouraging result implying that in theory it should be possible to utilise MEG for accurate temperature determination. In practice, it should be possible to optimise the smoothing algorithms to suit the observed signal profiles resulting in a reduction in spurious oscillations in the output temperature field.

3.6 EXPERIMENTAL EVALUATION OF THE MEG TECHNIQUE

3.6.1 FTIR MEASUREMENTS ON THE MCKENNA BURNER FLAME

In order to understand the emitting, and to a certain extent, the absorbing species present in the burner flame, a Fourier transform spectrometer was set up. Containing a liquid nitrogen cooled MCT detector, and with a spectral resolution of 0.1 cm^{-1}, the passive emission spectrum was measured over the wavelength range from 1.5 to 16 μm. Figure 3.18 shows one such spectrum obtained from a propane/air flame by imaging 2 cm above the flame zone along the axis of the burner. The mixture was close to stoichiometric but may have been slightly on the lean side. The dominant band is due to CO_2 at around 2300 cm^{-1} (4.3 μm).

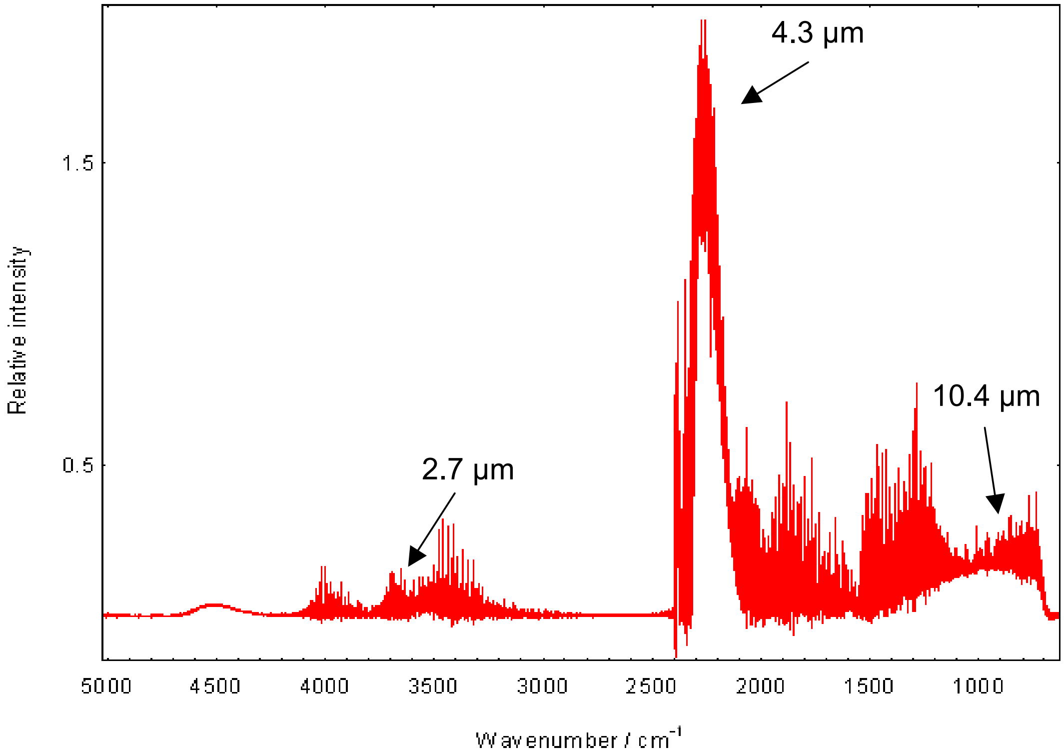

Figure 3.18 FTIR emission spectra of propane/air flame. Dominant CO_2 bands are labeled.

Figures 3.19 and 3.20 show the presence of H_2O at 3450 cm^{-1} (2.9 μm) and CO at 2060 cm^{-1} (4.8 μm) respectively, the band structure being clearly visible.

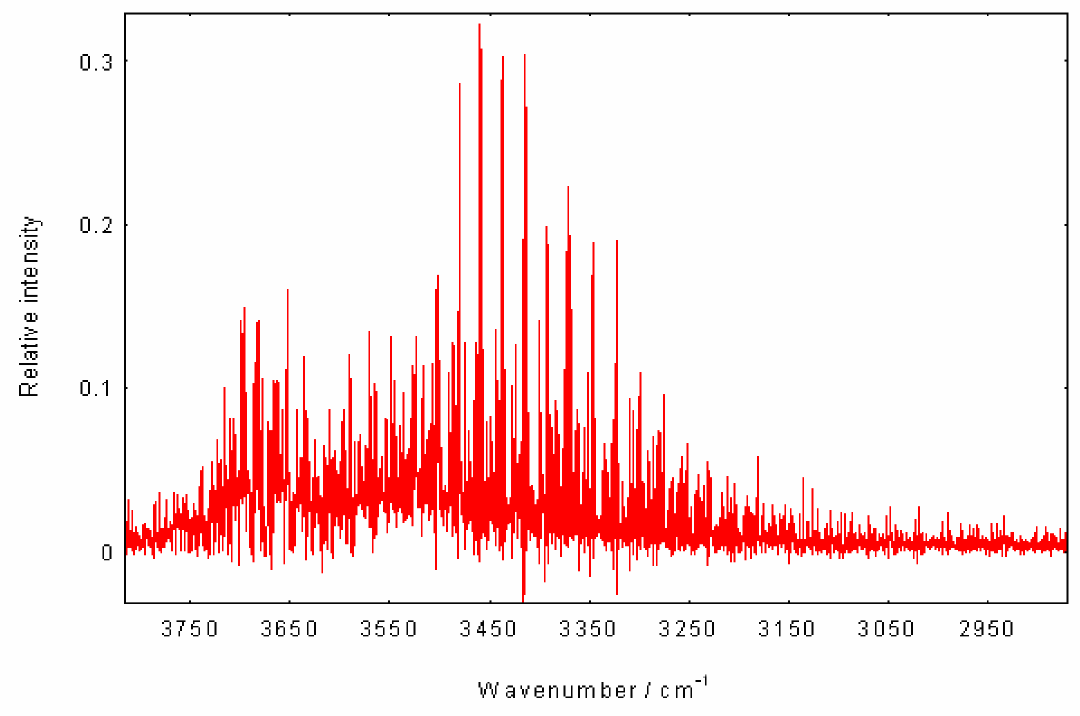

Figure 3.19 FTIR emission spectra of propane/air flame. H_2O Band (2.9 μm).

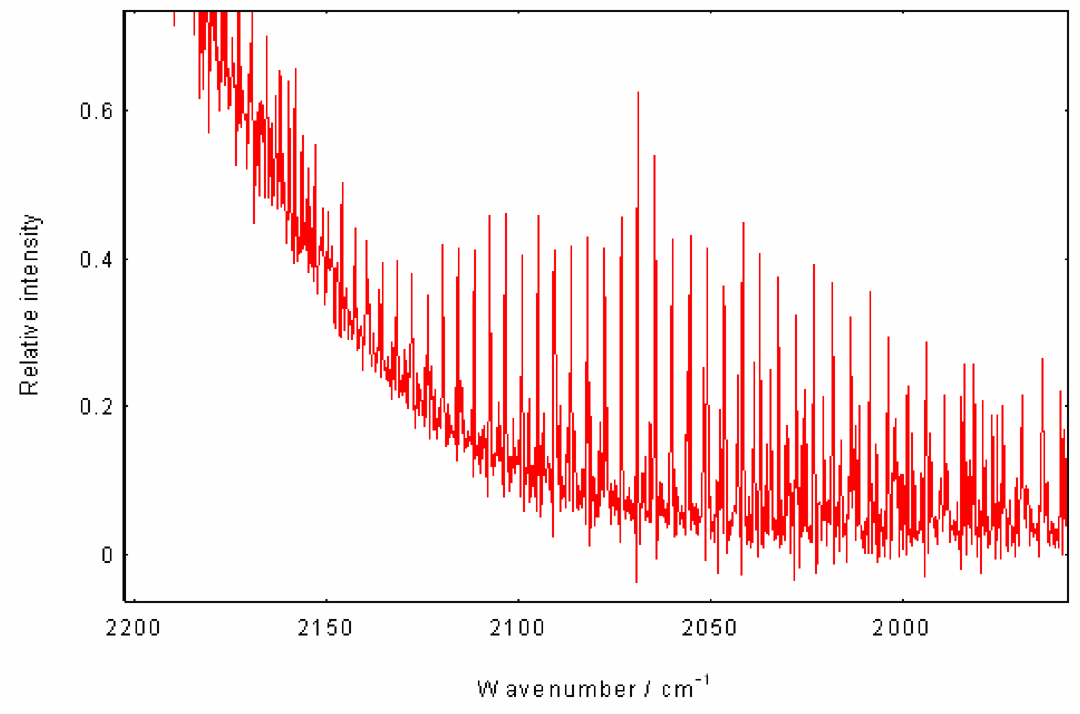

Figure 3.20 FTIR emission spectra of propane/air flame. CO band (4.8 μm).

Other spectra were taken for rich propane / air mixtures exhibiting similar spectra. No bands due to propane were observed. They would be expected at around 3000 wavenumber (3.3 μm) due to the C-H symmetric stretch mode of vibration. The absence of a propane signal is best explained by the fact that in the primary flame reaction zone (approximately 2 mm above the burner disk) temperatures are in excess of 2000 K and any excess fuel would be rapidly decomposed into smaller fragments.

In light of the dominance of the CO_2 emission it was decided that detection for the MEG technique should to be around this region. To this end, a PbSe detector is well suited. Since the MEG thermometry technique requires a reasonably powerful laser source to provide the temperature modulation, a readily available 25 W CW CO_2 laser operating around 10.4 μm was used. With evidence of emission (and hence absorption) at this wavelength in Figure 3.18, it was believed to be a good candidate excitation source.

3.6.2 MEG MEASUREMENTS ON THE MCKENNA BURNER FLAME

By making use of the 25W CW CO_2 laser, work was undertaken to experimentally validate the MEG technique. Figure 3.21 shows the basic experimental set up.

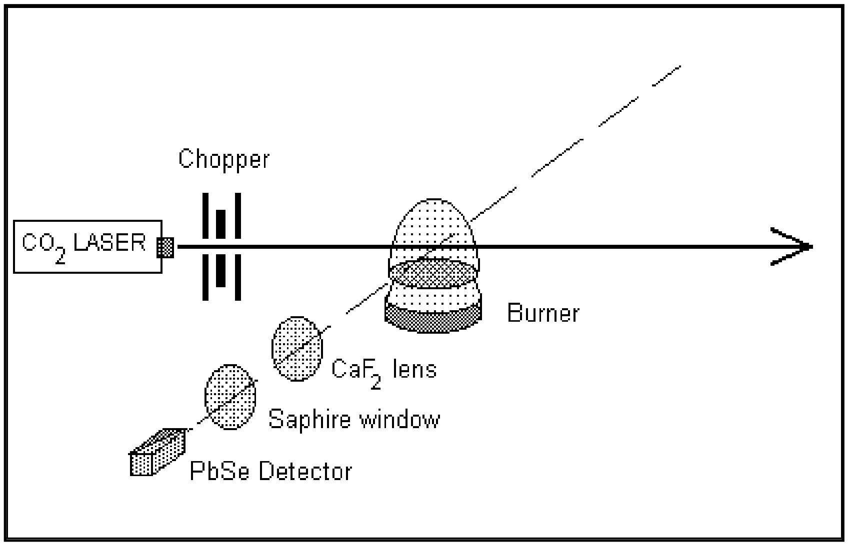

Figure 3.21 Initial MEG experimental set up.

The burner was operated with propane and air at a stoichiometric mixture ratio. A calcium fluoride (CaF_2) lens (f = 7 cm) was positioned to give 1:1 imaging and a sapphire window was placed directly in front of the detector to remove any signal pick-up from the laser itself. A mechanical chopper was installed as shown and the output from a PbSe detector and the chopper were input to a lock-in amplifier.

With the stoichiometric soot free flame condition, no emission was measured. This was attributed to the fact that there was negligible absorption of the laser beam within the flame zone.

Further tests were performed with a sooty ethene/air flame. A substantial flow of inert nitrogen gas from the burner shroud ring was needed to stabilise the flame and contrary to normal operating conditions the flame resembled a large yellow hemisphere with its base on the burner disk. In this configuration it was possible to measure a modulated emission from flame. Absorption of the laser beam of approximately 10% was measured over the length of the flame, indicating that energy was being absorbed. Figure 3.22 shows the signal measured by the PbSe detector after input to the lock-in amplifier, with the absorption coefficient shown on the right hand graph.

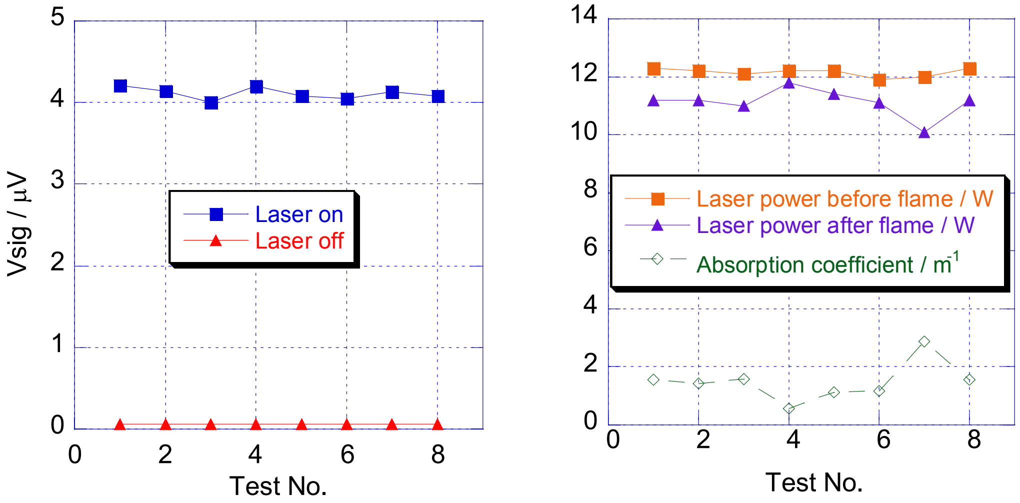

Figure 3.22 MEG signal for sooty ethene/air McKenna burner flame (the absorption coefficient is also shown).

Although a signal was measured, the rich, sooty flame conditions were not ideal and the flame was very difficult to stabilise on the burner surface. For the burner to produce a stable, uniform and reproducible post flame region requires operation with the flame zone anchored to the burner disk. The sooty flame regime did not satisfy these requirements and was not pursued further.

3.6.3 MEG MEASUREMENTS MADE ON THE HOT CELL APPARATUS

Since it was not possible to generate a MEG modulated signal in a clean stabilised McKenna burner flame due to the lack of absorption of the CO_2 laser, a hot gas cell system was developed. The hot cell apparatus allowed for the heating of a small volume of gas and the introduction of a small percentage of ethene gas that is a known absorber of 10 µm CO_2 laser radiation. This provided a mechanism for laser absorption and hence emission from the gas as a whole.

3.6.3.1 HOT CELL CONSTRUCTION

Figure 3.23 shows a schematic diagram of the hot cell apparatus including the gas mixing and pumping system and figure 3.24 shows the cell's internal structure.

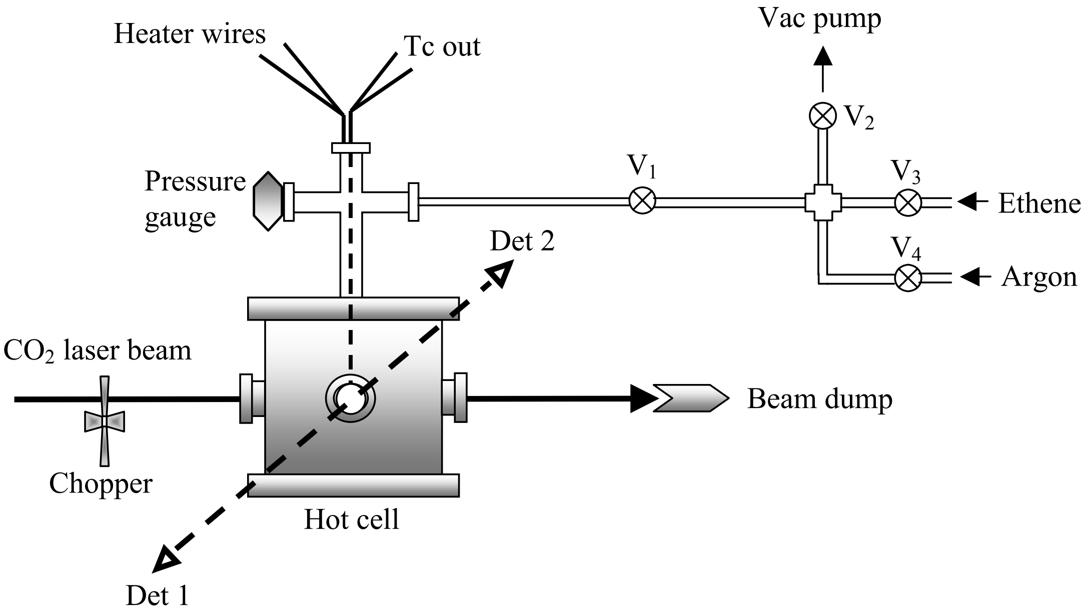

Figure 3.23 The hot cell apparatus and pumping/filling system (Modulation laser beam and detection axes shown also).

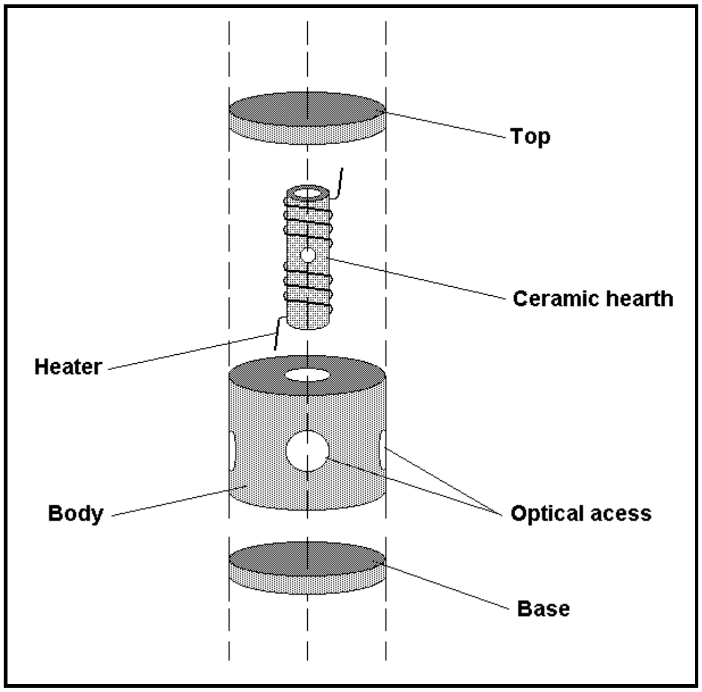

Figure 3.24 The hot cell internal structure.

The hot cell was designed to operate up to approximately 700°C. A central ceramic hearth with four 1 cm holes cut equally spaced on its circumference was wound with resistance wire and care was taken to avoid the holes. A ceramic cement was then applied over the wires to hold them in position.

The heater wires were fed from a vacuum tight connection at the top of the cell. A ceramic brick with optical access and a top and base section were then placed around the hearth. The whole assembly was then placed inside a metal container. The container had optical access to line up with the holes on the hearth tube, with two zinc selenide windows for entry and exit of the pump beam and two barium fluoride windows to allow optical access for the detection system. A type K thermocouple was fed into the cell along the axis of the hearth with its tip positioned approximately centrally such that it could not be seen through the optical access ports.

A pumping system was installed on the top of the cell to allow for evacuation of the cell and subsequent filling with ethene, a CO_2 mixture and /or argon. Two pressure gauges were also attached to the cell, one with a full scale deflection (FSD) of 1000 mBar and the second with a FSD of 10 mBar. This allowed for accurate metering of the ethene pressure during initial filling and coarse metering for maintaining the total gas pressure at 1 Atm during operation. The cell dimension from window to opposite window was 0.2 m and the cell height was approximately 0.3 m. The hot cell temperature was controlled by adjusting the voltage of a DC power supply connected to the heater coils and the set-point temperature controlled by adjusting the voltage with a potentiometer.

3.6.3.2 HOT CELL RADIATION TRANSFER SPECTROSCOPIC MODEL

To better understand potential MEG signals generated in the hot cell apparatus, a spectroscopic model for the radiation transfer was developed. This model assumed a 5 cm hot zone (1000 K) followed by a 10 cm cool zone (300 K) with a 1 cm zone central to the hot zone containing the temperature modulation (the MEG signal).

Various magnitudes of modulation were chosen, namely ΔT = 2 K, 5 K, 10 K, 20 K, 50 K and 100 K. Table 3.3 and Figure 3.25 illustrate the model.

Region	**T / K** [temperature]	**S / m** [pathlength]
s_1	1000	0.02
s_2	1000+ΔT	0.01
s_3	300	0.10
s_4	1000	0.05

Table 3.3 MEG model parameters for the hot cell apparatus.

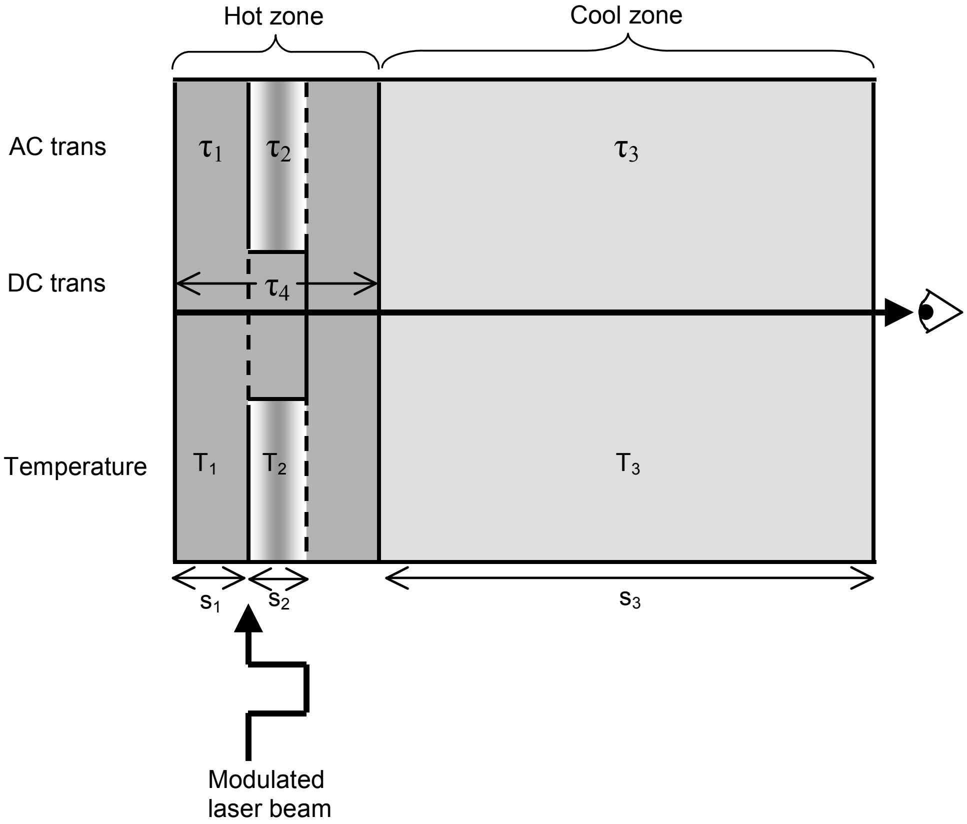

Figure 3.25 MEG spectroscopic model for the hot cell apparatus.

Neglecting the emission from the cool gas (region s_3 above) and dropping the wavenumber subscript, the emission from the cell may be described by Equation 3.45 and Equation 3.46 for the DC and DC+AC components respectively. Where T_i represents the temperature and τ_i the fractional transmission.

DC (no modulation): $$I_{DC} = L_b(T_1)\cdot(1-\tau_4)\cdot\tau_3 \tag{3.45}$$

DC+AC:

$$I_{DC+AC} = \underbrace{L_b(T_1)\cdot(1-\tau_1)\cdot\tau_2\cdot\tau_1\cdot\tau_3}_{radiance\cdot from\cdot s_1\cdot(LHS)} + \underbrace{\left(L_b(T_1)+L_b'\cdot\Delta T\right)\cdot(1-\tau_2)\cdot\tau_1\cdot\tau_3}_{radiance\cdot from\cdot s_2\cdot(CENTRE)} + \underbrace{L_b(T_1)\cdot(1-\tau_1)\cdot\tau_3}_{radiance\cdot from\cdot s_1\cdot(RHS)} \tag{3.46}$$

where $L_b(T_2)$ has been approximated to $L_b(T_1)+L_b'(T_1).\Delta T$.

Subtracting Equation 3.45 from Equation 3.46 and letting $\tau_4 = \tau_1^2\tau_2$ (this assumes that the transmission for the modulated layer of gas is the same as for a layer without modulation) we get:

$$I_{AC} = L_b'(T_1).\Delta T.(1-\tau_2).\tau_1.\tau_3 \tag{3.47}$$

By evaluating Equation 3.47 for the 4.3 μm band of CO_2 (0.15 atm) for various modulated temperature rises, it was possible to predict the AC radiance that exits the hot cell apparatus. The TRANS [58] computer code was utilised to generate the spectral transmission values used above and a summation performed to obtain the total radiance exiting the cell for each modulated temperature rise.

Figure 3.26 shows the AC spectral radiance exiting the cell for different temperature modulations. Attention should be drawn to the two separate regions in which appreciable energy is emitted. When the summation of all spectral components in Equation 3.47 has been performed, the total AC radiance due to the temperature modulation can be determined. This is shown in Figure 3.27 and Table 3.4.

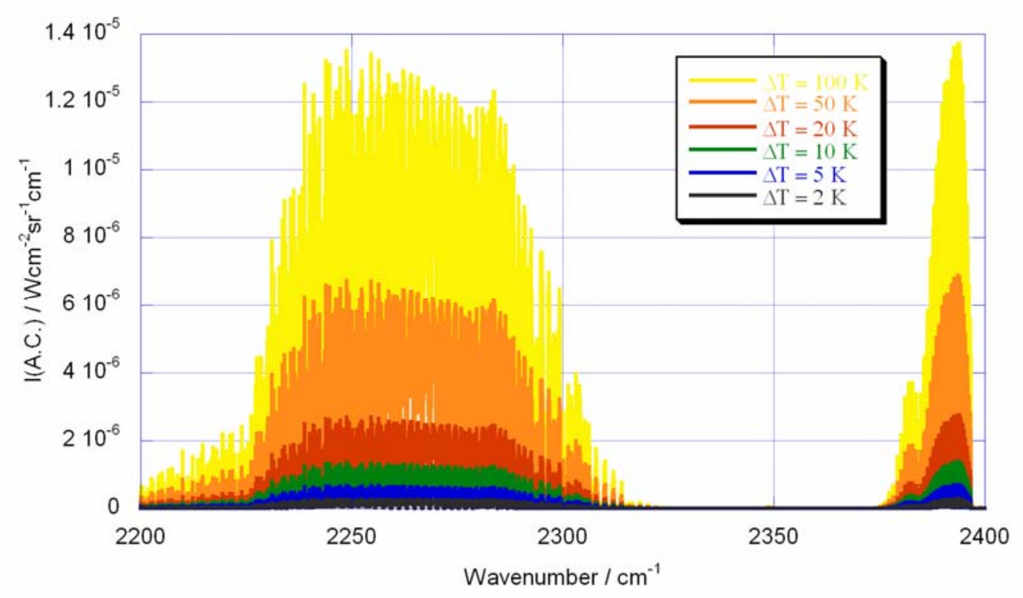

Figure 3.26 A.C spectral radiance from the hot cell. 4.3 μm band, 0.15 atm CO2. Various temperature modulations.

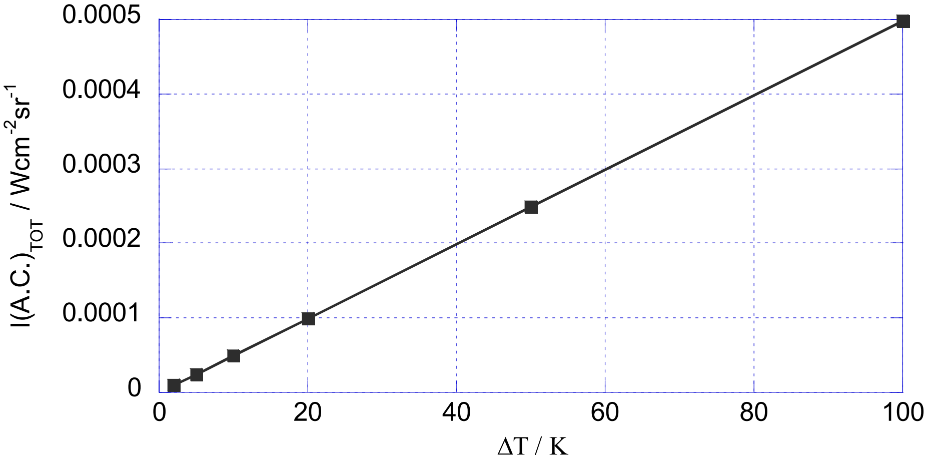

Figure 3.27 Total A.C. radiance from the hot cell. 4.3 μm band, 0.15 atm CO2. Various temperature modulations.

ΔT [K]	2	5	10	20	50	100
Iac [w/cm^2/sr]	0.00001	0.000025	0.00005	0.00010	0.00025	0.0005

Table 3.4 Total A.C. radiance from the hot cell. 4.3 μm band, 0.15 atm CO_2. Various temperature modulations.

It is clear from figure 3.27 that the AC signals are proportional to the magnitude of temperature modulation and this, to first order, is to be expected since the MEG theory makes the assumption that:

$$\Delta L \approx L^{'}.\Delta T + O(T^2 + T^3 + ...) \tag{3.48}$$

3.6.3.3 MEASUREMENTS ON THE HOT CELL APPARATUS

Initial tests indicated that a partial pressure of 2 mBar of ethene was found to absorb approximately 10 % of the incident CO_2 laser energy. This concentration was maintained throughout the tests.

With the PbSe detector characterised and in good working order, tests were carried out to measure the modulated emission from the hot cell apparatus at one of the two viewing ports. The experimental set up is as shown in Figure 3.23. All tests were carried out with the CO_2 laser at full power (~ 25 W) and the modulation frequency was varied from 20 Hz to 200 Hz. The detector output was coupled to a lock-in amplifier together with the output signal of the mechanical chopper. The cell was first evacuated and preliminary tests carried out to ensure that no laser light was measured on the detector. It this configuration no signal was measured.

The cell was subsequently filled to 2 mBar pressure with ethene, and Laser mix gas (15% CO_2, 15% N_2 and 70% He) was then admitted to the cell to give a total pressure of 1 Atm. Measurements were made for various cell temperatures, with the pressure maintained at 1 atm. throughout by 'bleeding off' any excess as the temperature increased. The set point was maintained by manual adjustment of the potentiometer on the DC power supply feeding the hot cell resistance heater. Tests were carried out at room temperature and in temperature increments of 100 °C up to the maximum operating temperature of the hot cell – approximately 700 °C (1000 K).

Although absorption of the pump beam was measured at each temperature (~ 15 % average including window contributions), no modulated emission was measured for temperatures less than 600°C.

For tests at 610 °C and 685 °C, modulated emission was measured. To ensure that this was not due to stray laser radiation entering the detection optics or electrical coupling of the mechanical chopper signal to the detector signal, the window between the cell and detector system was periodically covered. In the covered position, the signal fell to approximately zero.

During tests, the temperature modulation due to laser absorption was picked up by the control thermocouple and was of order of several degrees. Figure 3.25 shows the relationship between the measured MEG signal and the modulation frequencies for two different cell temperatures. A 1/*frequency* dependence is seen. This is consistent with theoretical calculations.

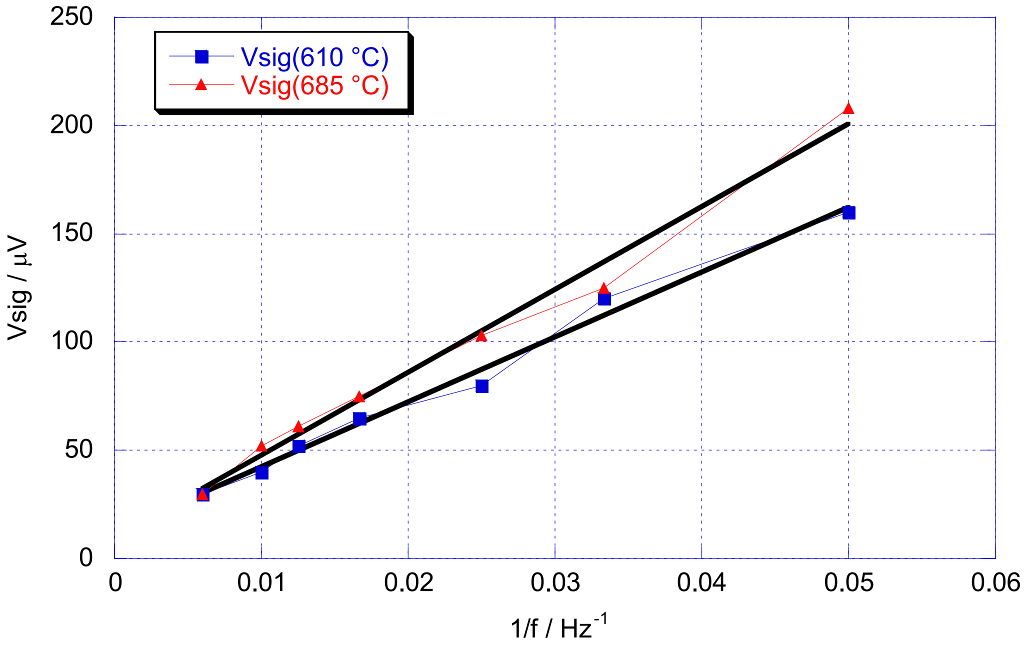

Figure 3.25 MEG signal vs 1/(modulation frequency) for the hot cell at 610 °C and 685 °C respectively.

The predicted total AC radiance for the 4.3 µm band of CO_2 for a temperature modulation of 2 K and a hot cell temperature of approximately 1000 K was 0.00001 W/cm^2/sr (from Table 3.4). Using this value and assuming that experimentally we do indeed produce the modulation of 2 K, we can compare theory with experiment.

The A.C. signal measured on the PbSe detector is given by:

$$V_{\det} = \underbrace{R_{\det}}_{\det sensitivity} \cdot \underbrace{A_{\det}}_{\det area} \cdot \underbrace{\Omega}_{solid \cdot angle} \cdot \underbrace{I_{AC}(\Delta T = 2K)}_{total.AC.signal} \tag{3.49}$$

The experimental values of the parameters shown above are:

$R_{det} = 30000$ V/W
$A_{det} = 0.09$ cm^2
$\Omega = 0.005$ sr
$I_{AC} = 0.00001$ W/cm^2/sr

Leading to a predicted AC signal voltage of $V_{det} = 130$ µV. Experimentally a value of V_{det} between 30 µV and 200 µV depending on modulation frequency was measured. The two values are of the same order of magnitude and this fact adds confidence to the validity of the MEG spectroscopic model. There are several possible reasons why the two values are not in better agreement. Firstly, the model does not take the hot cell window transmission factors in to consideration, secondly the AC radiances are strongly dependent on the temperature modulation level (i.e. if the modulation is slightly less that 2 K, the AC radiance will be considerably lower) and thirdly, there may be a small amount of atmospheric absorption once the energy exits the cell itself (this has not been modelled). It is for these reasons that an order of magnitude agreement is seen as a positive result.

3.7 TECHNICAL CHALLENGES IN REALISATION OF THE MEG TECHNIQUE IN REAL FLAMES

Since MEG signals were observed from the hot cell apparatus it was decided to further scrutinise the validity of the MEG method for real flames.

A major assumption made in defining the MEG technique was that the local absorption coefficient could be approximated by a mean value over the optical bandwidth of the detector (one mean value for each of the two detection wavelengths). Investigation into the validity of this assumption follows.

To recap, considering one wavelength band, the MEG theory gives the signals for the left and right detectors (as a function of pump laser beam position, *s*) as:

$$J_1^L(s) = A\overline{\alpha}_1(s)L_1'(s)Q(s)e^{-\int_0^s \overline{\alpha}_1(z')dz'} \tag{3.50}$$

$$J_1^R(s) = A\overline{\alpha}_1(s)L_1'(s)Q(s)e^{-\int_s^\ell \overline{\alpha}_1(z')dz'} \tag{3.51}$$

Explicitly identifying $\overline{\alpha}_1$ as the *mean* absorption coefficient at λ_1 over the optical bandwidth $\Delta\lambda$ and with $Q(s)$ the modulated heating term. The subscripts define the wavelength of detection, λ_1 in this case and the superscripts define the left hand or right hand detectors. With *A* and, the instrument constant, given by:

$$A = R\Omega A_d \Delta\lambda \tag{3.52}$$

with *R* the detector response (A/W), Ω the solid angle, A_d the detector area and Δλ the optical bandwidth.

Forming the ratio of Equations 3.50 and 3.51 gives:

$$R_1 = \frac{J_1^L}{J_1^R} = \frac{A_1^L}{A_1^R} e^{-\int_0^s \overline{\alpha}_1(z')dz' + \int_s^\ell \overline{\alpha}_1(z')dz'} \tag{3.53}$$

Differentiating Equation 3.53 gives:

$$\frac{dR_1}{ds} = R_1\left(-2\overline{\alpha}_1(s)\right) \tag{3.54}$$

This means that if we measure $\frac{dR_1}{ds}$, the value of $\overline{\alpha}_1$ can be found.

If we no longer assume that the absorption coefficient is constant over the optical bandwidth of the detector, Equations 3.50 and 3.51 can be written as:

$$J_1^L(s) = \int_{\Delta\lambda_1} F_1(\lambda) C_1^L \alpha_1(s,\lambda) L_1^{'}(s,\lambda) Q(s) e^{-\int_0^s \alpha_1(z^{'},\lambda)dz^{'}} d\lambda \tag{3.55}$$

$$J_1^R(s) = \int_{\Delta\lambda_1} F_1(\lambda) C_1^R \alpha_1(s,\lambda) L_1^{'}(s,\lambda) Q(s) e^{-\int_s^l \alpha_1(z^{'},\lambda)dz^{'}} d\lambda \tag{3.56}$$

with: $\alpha_1(s,\lambda)$ the spectral absorption coefficient at λ for position s.
$F_1(\lambda)$ the detector/filter spectral response function.
C_1^L and C_1^R the calibration factors depending on the solid angle and detector area only.

If we assume that $F_1(\lambda) = F$, $C_1^L = C_1^R$ and that $L_1^{'}(s,\lambda) = L_1^{'}(s)$ we may write the ratio R_1 as:

$$R_1(s) = \frac{J_1^L}{J_1^R} = \frac{\int_{\Delta\lambda} \alpha_1(s,\lambda) e^{-\int_0^s \alpha_1(z',\lambda)dz'} d\lambda}{\int_{\Delta\lambda} \alpha_1(s,\lambda) e^{-\int_s^l \alpha_1(z',\lambda)dz'} d\lambda} \tag{3.57}$$

Note that since the absorption coefficient now appears inside the integrals, we cannot cancel them (compare this to Equation 3.53). In an effort to investigate this further, we assume that the temperature is constant across the flame and that the absorption coefficient is also constant but still varies with wavelength: $\alpha(z,\lambda) = \alpha(\lambda)$. Equation 3.57 now becomes:

$$R_1(s)_{TRUE} = \frac{J_1^L}{J_1^R} = \frac{\int_{\Delta\lambda} \alpha_1(\lambda) e^{-\alpha_1(\lambda)s} d\lambda}{\int_{\Delta\lambda} \alpha_1(\lambda) e^{-\alpha_1(\lambda)(l-s)} d\lambda} \tag{3.58}$$

This compares to the MEG theory which, for this model gives:

$$R_1(s)_{MEG} = \frac{J_1^L}{J_1^R} = \frac{\overline{\alpha}_1 e^{-\overline{\alpha}_1 s} \Delta\lambda}{\overline{\alpha}_1 e^{-\overline{\alpha}_1 (l-s)} \Delta\lambda} \tag{3.59}$$

To determine the errors introduced by using the MEG approximation we need to evaluate the numerators and denominators of Equations 3.58 and 3.59. A flame width of 0.1 m is assumed and a gas composed of 0.116 atm. CO_2 (the partial pressure for propane/air flame at an equivalence ratio of 1) is used. The Trans [58] spectral synthesis software utilising the HITEMP [59] spectral database is used to generate the spectral absorption coefficient of CO_2 for the 4.3 μm band for temperatures ranging from 1400 K to 2400 K. A spectral resolution of 0.02 cm^{-1} was used in synthesising the spectra. Figure 3.26 shows the spectral absorption coefficient and the mean values over the band for various temperatures.

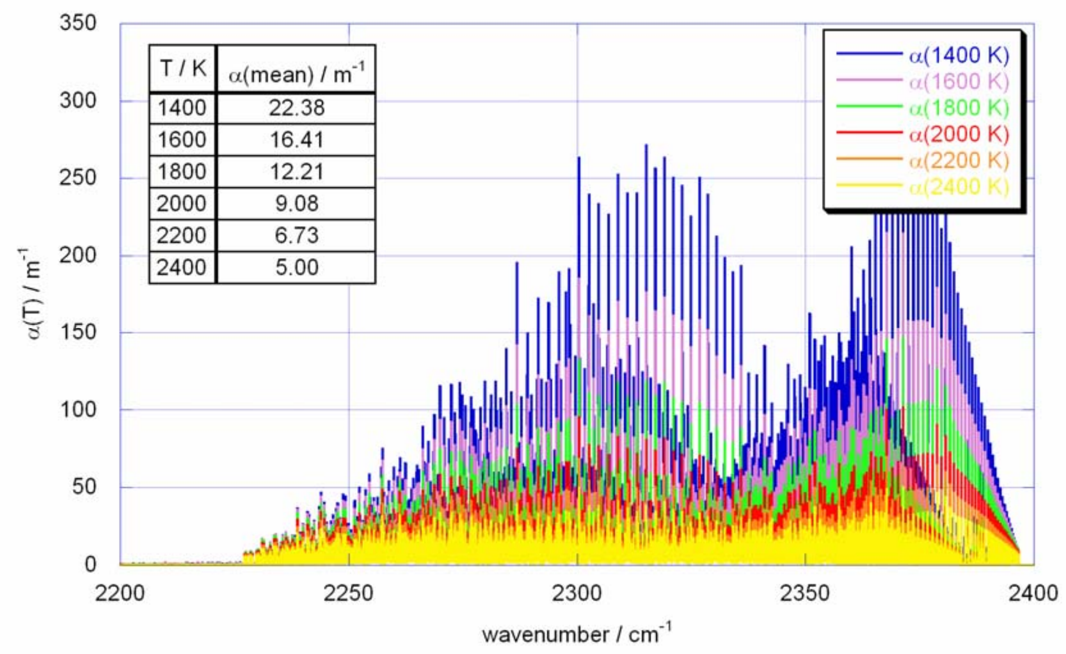

Figure 3.26 spectral absorption coefficient for 0.116 atm co_2, 4.3 μm band, for various temperatures (mean absorption coefficient over the band also shown).

Figure 3.27 shows the evaluation of the numerators and denominators of Equations 3.58 and 3.59. In Figure 3.27(a) full integrals are used (Equation 3.58) where as in Figure 3.27(b) the MEG approximation is used (Equation 3.59). Both figures display the same trend as one moves from one side of the flame (s = 0.0 m) to the other (s = 0.1 m). Two main differences are:

- The MEG approximation model exhibits a more gradual fall off with distance than the exact model.
- The MEG approximation model shows a larger variability with temperature in the central flame region than the exact model.

It is hoped that presenting the components of Equations 3.58 and 3.58 in this way gives a clear indication of the difficulty in approximating rapidly varying functions (the spectral absorption coefficient) especially when summation is over two variables (s,λ)

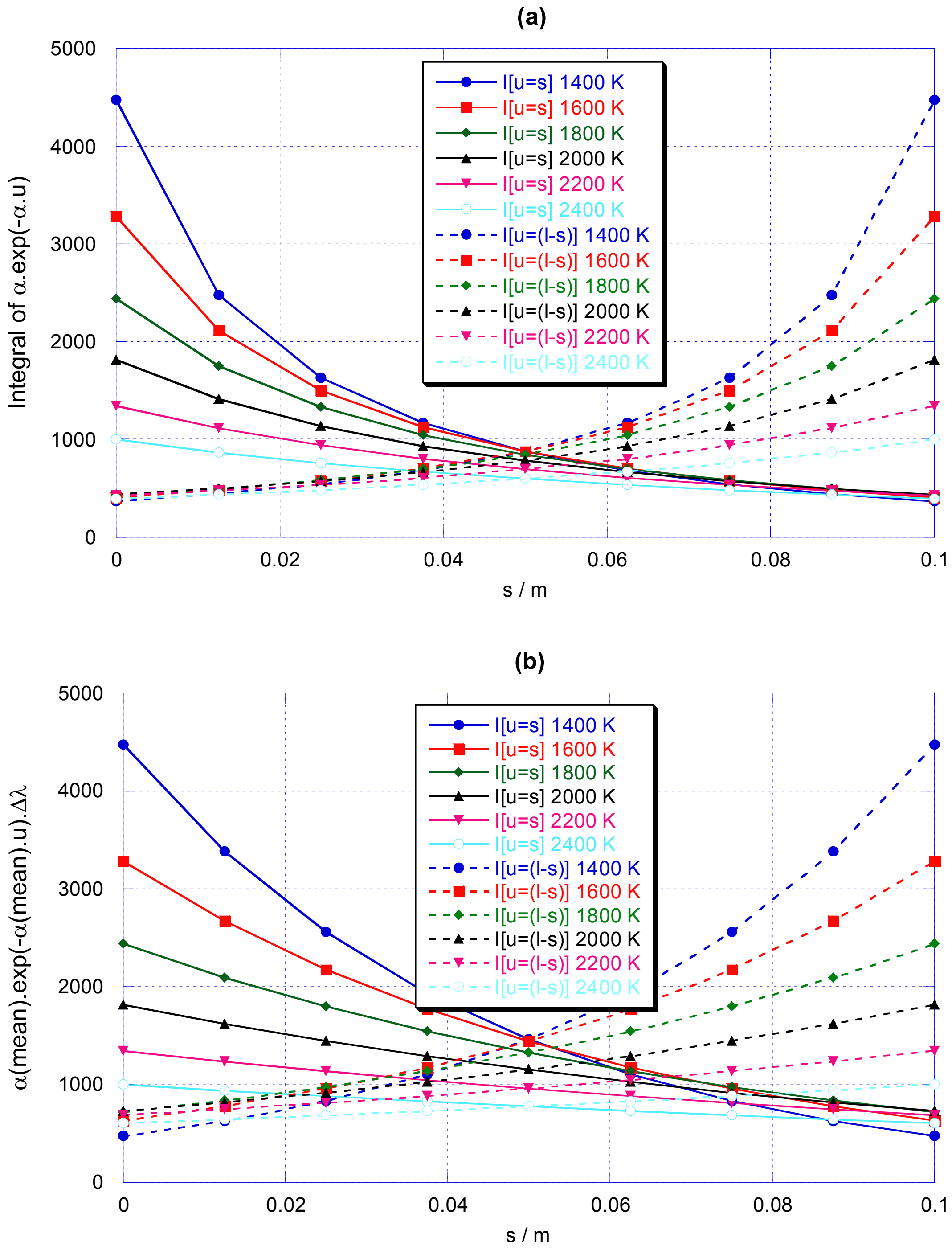

Figure 3.27 Evaluation of the numerators and denominators of Equations 3.58 and 3.59:

(a) Integrals for exact model:

$$I(u=s)=\int_{\Delta\lambda}\alpha_1(\lambda)e^{-\alpha_1(\lambda)s}d\lambda \quad \text{and} \quad I(u=l-s)=\int_{\Delta\lambda}\alpha_1(\lambda)e^{-\alpha_1(\lambda)(l-s)}d\lambda$$

(b) MEG approximation:

$$I(u=s)=\overline{\alpha}_1e^{-\overline{\alpha}_1 s}\Delta\lambda \quad \text{and} \quad I(u=s)=\overline{\alpha}_1e^{-\overline{\alpha}_1(l-s)}\Delta\lambda$$

Figure 3.28 shows the evaluation of $R_1(s)_{TRUE}$ (Equation 3.58) and $R_1(s)_{MEG}$ (Equation 3.59). Differences are seen most clearly at s = 0.0 m and s = 0.1 m where the MEG approximation underestimates and overestimates the ratios respectively.

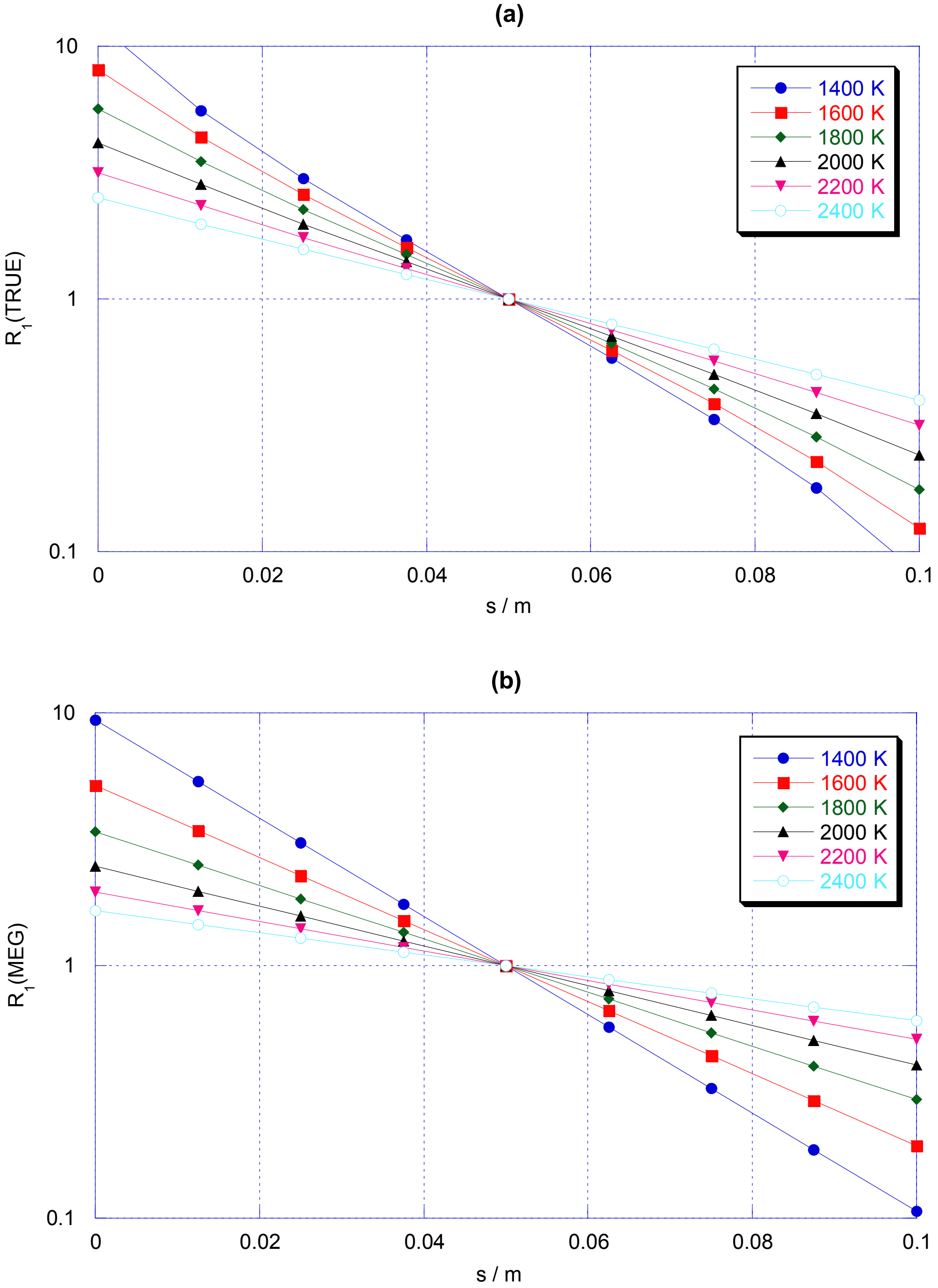

Figure 3.28 Evaluation of **(a)** $R_1(s)_{TRUE}$ (Equation 3.58) and **(b)** $R_1(s)_{MEG}$ (Equation 3.59).

To quantify the differences between $R_1(s)_{TRUE}$ and $R_1(s)_{MEG}$ more clearly, the percentage error can be defined as:

$$\%\,\text{error in } R_1(s) = \frac{R_1(s)_{MEG} - R_1(s)_{TRUE}}{R_1(s)_{TRUE}} * 100 \qquad (3.60)$$

Figure 3.29 shows this % error for various constant temperatures.

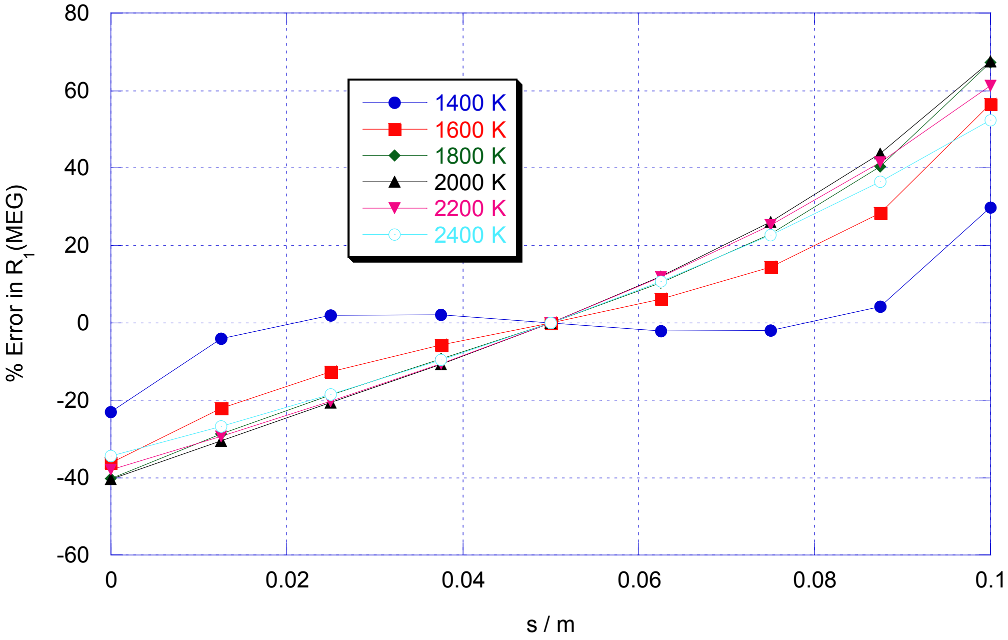

Figure 3.29 % error in $R_1(s)_{MEG}$ for various temperatures. 0.116 atm. CO_2, 4.3 μm band.

Large errors in $R_1(s)_{MEG}$ are seen, increasing substantially with temperature. In extreme cases, errors as large as 70% are found. Since errors in $R_1(s)_{MEG}$ (and $R_2(s)_{MEG}$ for the second detection wavelength) directly relate to the errors in the reconstructed MEG temperature, the outlook for the method is poor. The trend of the 'S' shaped error curve at low temperatures (1400 K) becomes linear as we approach high temperatures (T = 2400 K). This can be attributed to the non-linear way in which the spectral absorption coefficient increases with temperature (ultimately depending on the Boltzmann state populations).

The errors in the MEG method could be reduced by decreasing the optical detection bandwidth ($\Delta\lambda$). The model above assumes a $\Delta\lambda$ of 0.38 μm (2200 – 2400 cm^{-1}) but there will always be a trade off between reducing $\Delta\lambda$ and the associated reduction in signal/noise levels.

The main reason for the poor performance of the MEG technique in real flames made evident in Figure 3.29 is the fact that real gases have absorption coefficients that are strongly varying functions of wavelength and in such cases, the approximation:

$$\int_{\Delta\lambda} \alpha_1(\lambda) e^{-\alpha_1(\lambda)s} d\lambda \approx \overline{\alpha}_1 e^{-\overline{\alpha}_1 s} \Delta\lambda \tag{3.61}$$

does not hold.

However, the technique may have utility in sooting flames. The optical detection bandwidth ($\Delta\lambda$) could be selected such that the emissivity of the soot particles remains constant. Equation 3.61 would then hold. Provided a) the soot density is not too high so that the some of the modulation laser beam can pass through the flame and b) the MEG signals can also exit the flame, the technique should perform well.

Another solution for clean flames would be to measure the MEG signals using a high-resolution spectrometer. In this way there would be no need to approximate the absorption coefficient over the optical detection bandwidth since the spectrometer could collect the whole spectrum. Unfortunately a spectral resolution of the order of 0.01 cm^{-1} would be needed to resolve typical molecular lines with HWHM of 0.05 cm^{-1}. The cost of such instruments is prohibitive and it is uncertain whether such devices could perform sufficiently fast to detect the A.C. MEG signals.

In light of these technical challenges, investigation into other gas thermometry techniques was undertaken and the MEG technique was not taken any further.

3.8 SUMMARY AND RECOMMENDATIONS

3.8.1 SUMMARY

The Modulated Emission in Gases (MEG) thermometry technique has been fully evaluated. Theoretical models and computer simulations have been developed and experiments have been carried out to validate the technique. A summary follows:

- The theoretical basis of the MEG thermometry technique has been described fully.
- The MEG precision analysis has demonstrated that a temperature modulation of 2 K will provide a signal to noise ratio of 10^3 for typical flame parameters.
- The temperature rise due to 5 – 10 % absorption of an incident laser beam has been modeled for both a pulse and a modulated continuous wave (CW) laser source. For typical flame parameters, temperature rises of 28 K and >2 K were predicted for pulse and CW laser sources respectively.
- A detailed MEG computer simulation has been written in MATLAB [57] allowing for determination of the uncertainty in the reconstructed MEG temperature for various flame/laser parameters. A propane/air flame operating at an equivalence ratio of 1 was considered in detail. The model introduced shot noise to the detector signals, which was due to the large DC radiance incident on the detectors as a consequence of viewing the flame. In summary:

  - The expected signal to noise ratios for a 2 K temperature modulation agreed with the MEG precision analysis performed earlier ($S/N > 10^3$).
  - The uncertainty in the MEG temperature scales as the square root of the post detection bandwidth with an integration time of 15 minutes shown to provide an uncertainty in the temperature of less than 1 %.
  - Determination of the optimum detection wavelength(s) was found to depend on the flame temperature. For temperatures of 1000 K the best signal to noise ratio was obtained for a detection wavelength of 2 μm compared to 1 μm for temperatures of 2000 K. In choosing the optimum wavelength consideration to absorbing/emitting flame species lead to a superior signal around 4.3 μm due to the strong absorption band of CO_2 at this wavelength.
  - Constraints on the absorption coefficient were needed to successfully recover good signals. If the absorption coefficient was too large, the flame became optically thick with little or no modulated radiation exiting the flame. A value of 1.7 m^{-1} corresponding to 10 % absorption across a width of 0.06 m (the width of the McKenna burner flame) were found from spectroscopic synthesis software for CO_2 which was suitable for successful extraction of the MEG signals and hence temperature.
  - Practically, optimisation of the smoothing algorithms used in the processing of the raw signals would be needed to reduce oscillation in the reconstructed MEG temperature.
  - The model demonstrates that in principle it should be possible to recover the true flame temperature with an uncertainty of less than 1%.

- FTIR measurements made on the McKenna burner flame indicated the presence of strong absorption bands of CO_2 at 4.3 μm, 2.7 μm and 10.4 μm with weaker bands of H_2O at 2.9 μm and CO at 4.8 μm. In light of this, a readily available high power C.W. CO_2 laser operating at 10.4 μm was used as the temperature modulation source. A signal detection wavelength around 4.3 μm was chosen to coincide with the strong CO_2 band.
- MEG measurements on a soot-free stoichiometric propane/air McKenna burner flame did not yield any signals. This has been directly attributed to the lack of absorption of the pump laser beam, perhaps due to the weakness of the CO_2 absorption lines at 10.4 μm, the operating wavelength of the laser.
- With the burner operated with an ethane/air flame in the rich limit, it was possible to generate a sooty flame region. By operating the flame in this way, it was found that approximately 10% of the laser energy was absorbed over the length of the flame. A modulated thermal radiance signal (MEG signal) was measured for this type of flame. The sooty flame was very unstable and not well anchored to the burner disk.
- A hot cell apparatus was constructed, providing a clean particle free environment up to 700 °C. With small amounts of ethene added to CO_2 gas it was found that the absorption of the 10.4 μm laser radiation was encouraged thus guaranteeing the thermal modulation required for the MEG technique. For gas temperatures above 600 °C it was found that MEG signals could be measured, following the predicted 1/(modulation frequency). A theoretical spectroscopic model of the hot cell apparatus was also developed to determine the magnitude of the expected signals. Reasonable agreement was obtained between the model and experiment.

- Further analysis of the MEG theory as applied to real flames has since shown that extraction of the temperature information from the MEG signals is technically challenging. The primary reason for this is the spectral nature of the absorption coefficient of gases. Although the theory can predict *average* absorption coefficients to the correct order of magnitude, the sensitivity required to reconstruct accurate temperatures cannot be achieved.
- The use of a high-resolution infrared spectrometer would allow determination of the spectral absorption coefficient and the MEG temperature could then be obtained. A suitable spectrometer would need to resolve the spectral lines of the high temperature gases. Since these lines have a HWHM of 0.05 cm^{-1}, such an instrument would be very expensive and its utilisation is not regarded as the best approach to meeting the requirements of the project.

3.8.2 RECOMMENDATIONS

In light of technical difficulties experienced with the MEG technique other calibration techniques were considered. The initial survey identified two other techniques that offer potential for high accuracy temperature determination. The first is the Rayleigh scattering method and the second the photo-acoustic method.

Work has been undertaken to determine the flame temperature of the premixed flat flame burner by utilisation of the Rayleigh scattering technique and compared with photo-acoustic technique. This work is presented in Chapters 4 and 5.

4. THE DEVELOPMENT AND EVALUATION OF HIGH ACCURACY RAYLEIGH THERMOMETRY

In light of technical difficulties with the Modulated Emission in Gases (MEG) technique (described in chapter 3), the Rayleigh scattering thermometry technique has been developed to measure the temperature of the standard flame (McKenna burner). A summary follows:

- A detailed survey and technical evaluation of the Rayleigh scattering phenomena has been undertaken.
- The total and differential Rayleigh scattering cross-sections have been derived.
- The theoretical evaluation of Rayleigh scattering as an accurate thermometry technique has been undertaken:
  - The differential Rayleigh scattering cross-section for air and major combustion species has been found.
  - The species concentrations in the post flame region of a propane/air flame have been calculated from equilibrium software for various equivalence ratios.
  - The temperature dependence of the differential scattering cross-section has been investigated by considering the contributions of the mean molecular polarisability and the molecular anisotropy.
  - A correction has been developed to provide high accuracy Rayleigh thermometry provided the equivalence ratio is measured precisely.
- The experimental evaluation of the Rayleigh scattering as an accurate thermometry technique has been undertaken:
  - The optimised Rayleigh scattering thermometry system is presented.
  - Technical challenges in obtaining the highest accuracy have been described including the reduction of electromagnetic interference and background scattered light, improvement of the detector linearity, optimisation of the Rayleigh signal collection optics and evaluation of the long-term stability of the system.
  - The effect of the inlet gas temperature and water content on the flame temperature has been investigated.
  - The effect of the ambient pressure on the flame temperature has been explored.
  - The effect of the fuel purity on the flame temperature has been investigated.
  - Detailed measurements on the McKenna burner flame operated with propane and air have been undertaken indicating a long-term reproducibility of better than 0.5% and an absolute temperature accuracy of better than 1%.

4.1 RAYLEIGH SCATTERING THEORY

4.1.1 INTRODUCTION

Laser Rayleigh scattering is an effective diagnostic tool for the determination of the temperature of gas mixtures providing the composition is known [39-42, 60-62]. Rayleigh scattering has a simple origin: the electrons in atoms, molecules or small particles radiate like dipole antennas when an oscillatory electromagnetic field is applied. In a gas, the motion of the molecules leads to microscopic density fluctuations that randomise the phases of the secondary waves and causes the scattering to be incoherent in all but the forward direction. Away from the forward direction, rapidly changing interferences occur which average to remove any coherent effects resulting in a scattering intensity that, in the far field, is only proportional to the number of scatterers. Providing the pressure and species concentrations remain constant or are known, the temperature may be determined from this signal via the ideal gas law.

The simple dipole model gives very good results for monotonic gases such as helium and argon where no internal degrees of freedom are present. The case for molecules is not so simple, with vibrational and rotation degrees of freedom adding complexity to the scattering spectrum. Inelastic vibrational and rotational Raman scattering frequencies arise associated with changes of vibrational and rotational energy states during the scattering process, and thus the ‘elastic’ Rayleigh scattering spectrum is partly depolarised and de-phased, even in the forward scattering direction. Since it is intended to use Rayleigh scattering in the post combustion zone of a stabilized flame, where molecular species are present, these effects must be taken into account for a proper analysis.

As an example, the various components of light scattering for molecular nitrogen are shown in Figure 4.1. Furthest away from the laser wavelength are the vibrational Raman bands. These are generally of the order of a few hundred to a few thousand wavenumbers (cm^{-1}) away. Closer to the laser line is the rotational Raman band. This consists of a series of lines with $\Delta J = \pm 2$ generally separated by a few tens of wavenumbers. The central feature is associated with elastic scattering and does not change the internal energy of the molecule. It lies closest to the laser line and has features that reflect the translational motion. If the motion is collision dominated (hydrodynamic limit), acoustic sidebands are present at frequency shifts associated with the speed of sound in the medium and the line shapes are Lorentzian. At low pressure or high temperature, the molecular motion is thermally dominated and the scattering lineshape takes the form of a thermally broadened Gaussian profile. For 1 atmosphere of nitrogen at room temperature, observed with a frequency-doubled Nd:YAG laser (532 nm), the scattering is intermediate between these two regimes and the line profile shape reflects both acoustic and thermal processes.

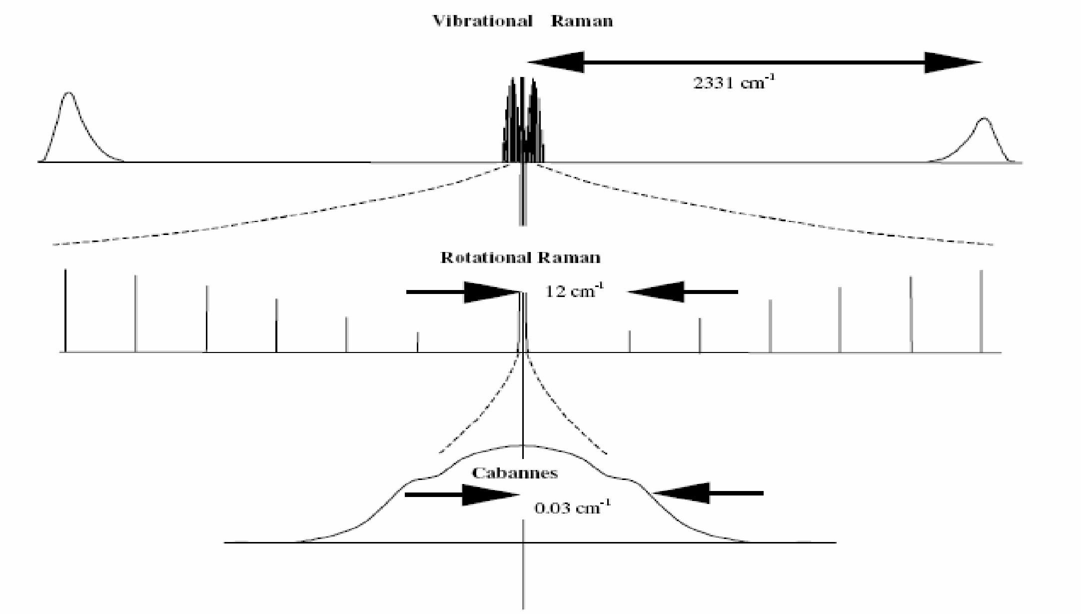

Figure 4.1 Scattering components from laser illuminated diatomic molecules at sequentially higher resolutions (figures for N_2 shown).

For anisotropic molecules, the scattering is partially depolarised by molecular orientational averaging, and the central feature of the band has added to it a component of the rotational Raman scattering which corresponds to a re-orientation of the molecular spin, but no change in energy (rotational Q-branch) [60]. This component is small - less than 1% of the total scattering. Literature suggests [60] that the features associated with elastic scattering from translational motion (plus the rotational Q-branch) be called the ‘Cabannes’ line in honour of Lord Rayleigh’s student, Jean Cabannes.

With narrow bandwidth filters centred on the lasing wavelength it is the so-called elastic scattering signal or ‘Cabannes’ line that we regard as the measured Rayleigh signal - the total inelastic vibrational Raman signal is generally 3 orders of magnitude smaller than the elastic component and has negligible contribution. Since the ‘Cabannes’ (Coherent) scattering is the dominant contributor to the Rayleigh signal, the light will be strongly polarised and it is important to have the detection optics in the correct orientation in relation to the polarisation of the incident laser beam to obtain the maximum signals.

‘Rayleigh scattering’ is used to describe scattering from molecules as well as scattering from small particles and clusters whose circumference is substantially less than the wavelength of the incident light [61]. For both molecules and small particles, the induced dipole moment of the particle is established in a time short compared to the oscillation period of the electromagnetic wave, so Rayleigh scattering is ‘instantaneous’ in nature. When the illumination source is turned off, Rayleigh scattering immediately ceases, in contrast to fluorescent processes where emission can continue for some time.

4.1.2 THE SCATTERING CROSS-SECTION

The Rayleigh scattering cross-section is an intrinsic property of a given molecule. The total Rayleigh scattering cross-section of a molecule can be defined as the ratio of the total power scattered out of an incident beam to the power of that beam. The differential Rayleigh scattering cross-section can be defined in a similar way as the ratio of the power scatted into unit solid angle to the power of the incident beam. The scattering cross section for spherically symmetric molecules such as argon and helium will be derived first using the classical expression for radiation emitted from an infinitesimally small oscillating dipole. This can then be extended to the case for non-symmetric molecules by the addition of two parameters invariant with respect to rotation, the mean polarizability, *a*, and the anisotropy, *γ*.

4.1.3 THE SPHERICALLY SYMMETRIC MODEL

The amplitude and intensity of the electric field propagating from a single dipole oscillating in an applied electric field are given by [63]:

$$\left|\vec{E}_s(r,\phi)\right| = \frac{\omega^2 p \sin\phi}{4\pi r \varepsilon_0 c^2} \tag{4.1}$$

$$I_s(r,\phi) = \frac{\varepsilon_0 c \left|\vec{E}_s(r,\phi)\right|^2}{2} \tag{4.2}$$

where ω is the oscillation frequency, p is the magnitude of the oscillating dipole moment (charge multiplied by displacement) induced by the external field, ε_0 is the permittivity of free space, c is the speed of light in a vacuum and ϕ is the angle of observation with respect to the dipole vector.

Figure 4.2 shows the amplitude and intensity of the electric field propagating from a single dipole. It is worth noting that for a spherically symmetric molecule there is no radiated field component along the axis of oscillation of the dipole. Non-radiating field components die out much faster than *1/r* and are neglected since it is assumed that the field is being measured in the far field (i.e. many wavelength from the dipole).

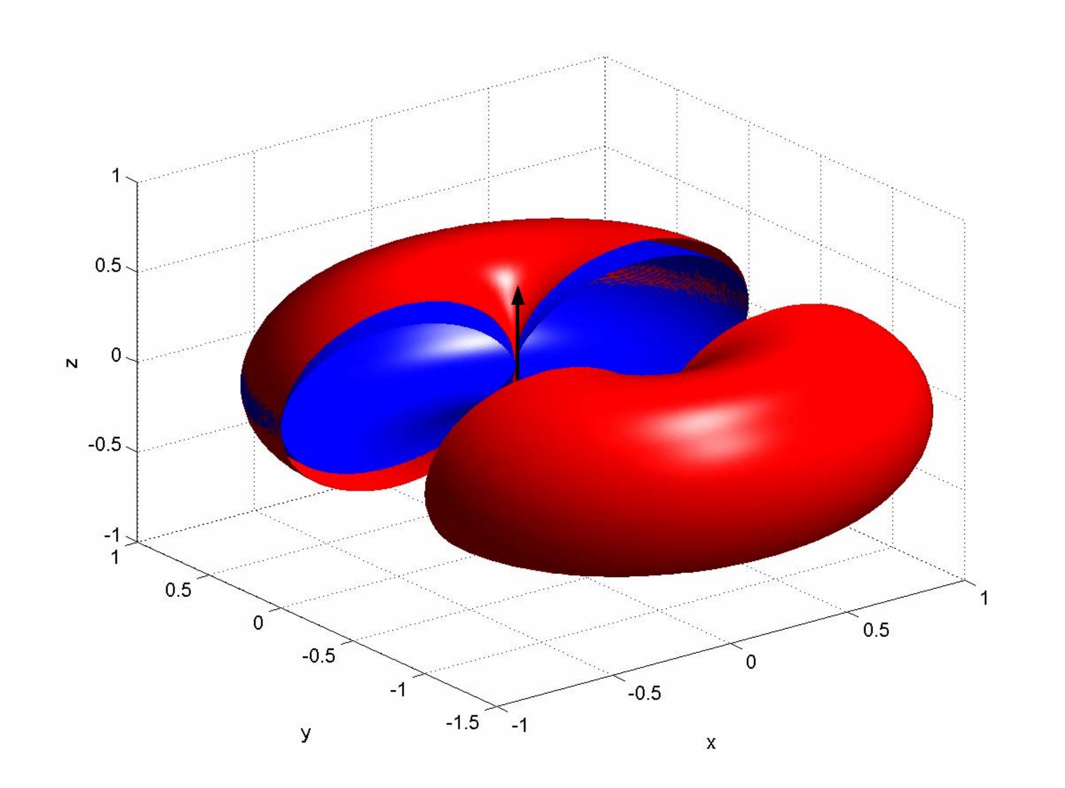

Fig. 4.2 Polar diagram of electric field (red) and intensity (blue) around a single dipole. The dipole (arrow) is aligned along the z axis. At any point on the surface, the radial distance from the origin is proportional to the electric field / intensity at that location.

The intensity of the light scattered from a single oscillating dipole is:

$$I_s(\phi) = \frac{\pi^2 c p^2 \sin^2 \phi}{2\varepsilon_o \lambda^4 r^2} \tag{4.3}$$

Light scattering occurs when the dipole oscillation is driven by incident electromagnetic radiation. In the case of a spherically symmetric molecule, the dipole moment, $\vec{p}$, is induced in the same direction as the incident field polarization, and is linearly proportional to the incident electric field, $\vec{E}_I$. The scalar constant of proportionality is termed the molecular polarizability α:

$$\vec{p} = \alpha \vec{E}_I \tag{4.4}$$

By substituting $p^2 = \alpha^2 |E_I|^2$ and $I_I = (\varepsilon_0 c/2)|E_I|^2$, the scattering intensity from one molecule can be found:

$$I_S(\phi) = \frac{\pi^2 \alpha^2}{\varepsilon_0^2 \lambda^4 r^2} I_I \sin^2 \phi \tag{4.5}$$

Defining the differential scattering cross section such that:

$$I_S(\phi)=\frac{\partial\sigma_{SS}}{\partial\Omega}\frac{1}{r^2}I_I \tag{4.6}$$

where the subscript ‘ss’ refers to scattering from a spherically symmetric scatterer and:

$$\frac{\partial\sigma_{SS}}{\partial\Omega}=\frac{\pi^2\alpha^2}{\varepsilon_0^2\lambda^4}\sin^2\phi \tag{4.7}$$

Integrating this intensity over the surface enclosing the dipole leads to the total scattered power from one molecule:

$$P=\frac{8\pi^3\alpha^2}{3\varepsilon_0^2\lambda^4}I_I \tag{4.8}$$

Writing the total scattered power in terms of the total scattering cross section leads to:

$$\sigma_{SS}=\frac{P}{I_I} \tag{4.9}$$

or

$$\sigma_{SS}=\frac{8\pi^3\alpha^2}{3\varepsilon_0^2\lambda^4} \tag{4.10}$$

The polarizability can be related to the index of refraction, *n*, by the Lorentz-Lorenz equation [62]:

$$\alpha=\frac{3\varepsilon_0}{N}\frac{n^2-1}{n^2+2} \tag{4.11}$$

where *N* is the number density of the gas (molecules m^{-3}), so the scattering cross section of a spherically symmetric scatterer is given by:

$$\sigma_{SS}=\frac{24\pi^3}{\lambda^4N^2}\left(\frac{n^2-1}{n^2+2}\right)^2 \tag{4.12}$$

It is worthy of note that $(1/N)(n^2-1)(n^2+2)$ is independent of density, as required for α to be a property of the individual atom or molecule. The differential scattering cross section can be written as:

$$\frac{\partial\sigma_{SS}}{\partial\Omega}=\frac{9\pi^2}{\lambda^4N^2}\left(\frac{n^2-1}{n^2+2}\right)^2\sin^2\phi \tag{4.13}$$

When Rayleigh scattering is used for diagnostic purposes, the scattered light is usually collected over some finite solid angle defined by the lens size and focal length. The power collected is thus derived from the differential scattering cross section:

$$\Delta P=I_I\int_{\Delta\Omega}\frac{\partial\sigma_{SS}}{\partial\Omega}\partial\Omega \tag{4.14}$$

The motion of the molecules randomizes the interference of the electric fields scattered from each individual molecule so that, when seen from afar, these coherent effects cancel and the total scattering becomes the sum of the individual intensities scattered from each molecule. The total power that is collected is the integral of the differential cross section over the solid angle subtended by the collection optics, $\Delta\Omega$, multiplied by the number of scatterers in the observation volume, *NV*, and further multiplied by whatever efficiencies, η, are appropriate for the optical elements and the detector:

$$P_{DET} = \eta I_I NV \int_{\Delta\Omega} \frac{\partial \sigma_{SS}}{\partial \Omega} \partial\Omega \tag{4.15}$$

Thus it is possible to determine the number density for a single component monotonic gas at a constant pressure and temperature. If the temperature were to change it would be possible to determine the new temperature provided all other parameters are invariant. This is the basis of Rayleigh scattering thermometry.

4.1.4 SCATTERING FROM DIATOMIC MOLECULES

Scattering from molecules is more complicated than scattering from atoms because, in general, molecules are not spherical. Rotational Raman lines appear, and the Rayleigh scattering is slightly depolarised since the induced dipole moment is not necessarily in the direction of the applied field. The random orientation of the molecule with respect to the incident field, and with respect to the observation direction and observed polarization, leads to the requirement that the scattering model include averaging over the molecular orientations.

If it is assumed that the incident laser field is propagating in the *x*-direction, then it can have only two polarization components, E_y and E_z. The induced electric dipole moment, $\vec{p}$, is described by a dipole polarizability tensor whose components are, therefore:

$$\begin{aligned} p_x &= \alpha_{xy} E_y + \alpha_{xz} E_z \\ p_y &= \alpha_{yy} E_y + \alpha_{yz} E_z \\ p_z &= \alpha_{zy} E_y + \alpha_{zz} E_z \end{aligned} \tag{4.16}$$

Since the molecules in the sample volume are randomly oriented, the scattering needs to be averaged over all molecular angles. This averaging can be expressed in terms of two parameters which are invariant with respect to rotation: the mean molecular polarizability *a*, and the molecular anisotropy *γ*. Summing over all orientations and integrating over an area enclosing the dipole [60] yields the total scattering cross section:

$$\sigma = \left(\frac{8\pi^3}{3\varepsilon_0^2 \lambda^4} \right) \left(\frac{45a^2 + 10\gamma^2}{45} \right) \tag{4.17}$$

This result is identical to the scattering cross section for the spherically symmetric molecule (Equation 4.10) except for the addition of the anisotropy factor.

This expression is often written in terms of ρ_0, the depolarisation ratio, which is defined as the ratio of the intensity of horizontally-polarised to-vertically polarized light scattered perpendicular to the beam propagation direction for unpolarised (natural) incident light:

$$\rho_0 = \frac{6\gamma^2}{45a^2 + 7\gamma^2} \tag{4.18}$$

Making use of the Lorentz-Lorenz relation (Equation 4.11), the total scattering cross section for a single molecule can be written as:

$$\sigma = \sigma_{SS}\left(\frac{6+3\rho_0}{6-7\rho_0}\right) = \sigma_{SS}\left(1+\frac{10}{45}\frac{\gamma^2}{a^2}\right) \tag{4.19}$$

The ratio $\left(\frac{6+3\rho_0}{6-7\rho_0}\right)$ is called the 'King correction factor' and accounts for the departure from the spherically symmetric case.

Noting the expression for the total cross section for a spherically symmetric scatterer (Equation 4.12), the total scattering cross section for a single molecule can be written as:

$$\sigma = \frac{24\pi^3}{\lambda^4 N^2}\left(\frac{n^2-1}{n^2+2}\right)^2\left(\frac{6+3\rho_0}{6-7\rho_0}\right) \tag{4.20}$$

For most experiments utilizing a polarized incident laser beam, the laser propagates along the *x*-axis, is polarized to a very high degree along the *z*-axis and light is collected along the *y*-axis. Under these conditions the differential scattering cross sections for the two orthogonal polarization components are given by:

$$\frac{\partial\sigma_z}{\partial\Omega} = \frac{3\sigma}{8\pi}\left(\frac{2-\rho_0}{2+\rho_0}\right) \tag{4.21}$$

$$\frac{\partial\sigma_y}{\partial\Omega} = \frac{3\sigma}{8\pi}\left(\frac{\rho_0}{2+\rho_0}\right) \tag{4.22}$$

Noting that generally, polarization insensitive detectors are utilized for Rayleigh scattering measurements, the above two equations can be added together and combined with the expression for the total cross section above to yield an expression for the differential scattering:

$$\frac{\partial\sigma}{\partial\Omega} = \frac{9\pi^2}{\lambda^4 N^2}\left(\frac{n^2-1}{n^2+2}\right)^2\left(\frac{6+3\rho_0}{6-7\rho_0}\right)\left(\frac{2}{2+\rho_0}\right) \tag{4.23}$$

It is important to note that both n and ρ_0 are wavelength dependent and specific to a single molecular species.

4.2 RAYLEIGH SCATTERING THERMOMETRY

4.2.1 INTRODUCTION

The total Rayleigh scattering signal collected over a solid angle $\Delta\Omega$ for a laser beam of intensity I_I incident on a gas mixture can be written as:

$$P_{DET} = \eta I_I NV \int_{\Delta\Omega} \left(\frac{\partial\sigma}{\partial\Omega} \right)_{mix} \partial\Omega \tag{4.24}$$

Where N is the number density of scatterers, V is the observation volume, η is the optical collection efficiency and $\left(\frac{\partial\sigma}{\partial\Omega} \right)_{mix}$ is the differential scattering cross-section of the gas mixture given by the mole fraction weighted sum of all species present in the observation volume:

$$\left(\frac{\partial\sigma}{\partial\Omega} \right)_{mix} = \sum_i \left(\frac{\partial\sigma}{\partial\Omega} \right)_i X_i \tag{4.25}$$

with X_i the mole fraction of the i^{th} species.

In this work, two Rayleigh scattering signals are measured. Firstly, a calibration point is obtained by flowing dry air of known temperature T_1 through the burner giving a signal $S(T_1)$. Secondly the signal for the post-flame species at an unknown flame temperature T_2 giving $S(T_2)$. Assuming the solid angle of collection is small and the entire width of the incident laser beam is included in the observation area, the signals so measured are given by:

$$S(T_1) = \eta I N_1 V \left(\frac{\partial\sigma}{\partial\Omega} \right)_{air} \Delta\Omega \tag{4.26}$$

$$S(T_2) = \eta I N_2 V \left(\frac{\partial\sigma}{\partial\Omega} \right)_{\substack{post\\flame}} \Delta\Omega \tag{4.27}$$

where N_1 and N_2 are the number densities of dry air and the post-flame species respectively. For atmospheric pressure flames it can be shown that the ideal gas law may be applied with negligible error [60], leading to:

$$N_1 k T_1 = N_2 k T_2 \Rightarrow T_2 = \frac{N_1}{N_2} T_1 \tag{4.28}$$

where k is the Boltzmann constant. By taking the ratio of Equations 4.26 and 4.27 and making use of Equation 4.28 it is possible to write:

$$T_2 = \delta \frac{S(T_1)}{S(T_2)} T_1 \tag{4.29}$$

with
$$\delta = \frac{\left(\dfrac{\partial \sigma}{\partial \Omega}\right)_{\substack{post\\ flame}}}{\left(\dfrac{\partial \sigma}{\partial \Omega}\right)_{air}} \tag{4.30}$$

where δ represents the ratio between the differential scattering cross-section for the two different temperatures and species regimes. So provided T_1 (room temperature) is well known, the optical system is invariant and δ can be determined by some other means, it is possible to determine T_2, the flame temperature.

4.2.2 DETERMINATION OF THE DIFFERENTIAL RAYLEIGH SCATTERING CROSS-SECTION

It can be seen from Equations 3.29 and 4.30 that in order to determine the post flame temperature, T_2, the ratio δ must be evaluated. Determining the differential scattering cross section for air at ambient temperature, at the measurement wavelength is trivial and can be found [60] to a high accuracy. This leaves the task of determining the differential scattering cross-section of the high-temperature post-flame gas. The three factors that need to be considered here are (1) the composition of the post-flame gas, (2) the differential scattering cross-section of each species present and (3) the variation in these scattering cross-sections with temperature, for which corrections are rarely made [63].

4.2.2.1 DETERMINATION OF THE POST FLAME SPECIES CONCENTRATIONS

The thin pre-mixed flame of the McKenna burner is supported 2 mm above the burner plug and we choose to make measurements in the centre of the burner 20 mm above this zone where the temperature is uniform and it is reasonable to assume that the species concentrations have reached chemical equilibrium [6,8-9]. By making this assumption it is possible to employ the method of the minimization of the Gibbs free energy to obtain the equilibrium species concentrations and the adiabatic flame temperature. This method [64] is outlined below.

Consider the simple gas phase chemical reaction:

$$aA + bB \Rightarrow eE + fF \tag{4.31}$$

By definition, when the products and reactants have reached equilibrium, the ratio of the partial pressures will be:

$$K = \frac{P_E^e P_F^f}{P_A^a P_B^b} \tag{4.32}$$

where K by definition is known as the equilibrium constant.

It may be shown that the reaction rate for a given reaction is related to the change in the Gibbs free energy thermodynamic state function under standard state conditions. ΔG for a given reaction is very important as it can be shown that in order for a reaction to proceed spontaneously at a constant pressure and temperature, ΔG must be negative. This is explicitly stated as:

$$\Delta G^0 = -RT \ln K \qquad (4.33)$$

with R the molar gas constant, T the temperature and K the equilibrium constant defined above. A fuller derivation of Equation 4.33 is given in [65].

Assuming there are L chemical elements present in specific proportions in an equilibrium mixture, i.e., the mass fraction of the eth element is given by β_e, such that:

$$\sum_{e=1}^{L} \beta_e = 1 \qquad (4.34)$$

Assume also that s chemical species (atoms, molecule or radicals) are present in the mixture with the mole fraction of the i^{th} species given by χ_i. In practice the choice of species and hence the size of s would be limited to those present in significant proportions and once the choice of species has been made, it is possible to write L independent relations of the form:

$$\frac{A_e \sum_{i=1}^{s} v_{ie} \chi_i}{\sum_{i=1}^{s} \chi_i M_i} = \beta_e \qquad (e = 1,2,\ldots,L) \qquad (4.35)$$

where v_{ie} is the number of atoms of the eth element in a molecule of the ith species, A_e is the atomic weight of the eth element and M_i is the molecular weight of the ith species. From the L species chosen as independent components, one can then write s-L chemical reactions which form the other s-L species. Each of these will have an equilibrium constant K of the form of Equation 4.32. Performing the minimisation of the Gibbs free energy by using Equation 4.33 will allow a solution giving the concentrations of each species at the equilibrium condition (generally taken as constant pressure and a given final temperature).

The equilibrium composition calculation requires the initial temperature and species information and will calculate the species concentrations for a given final temperature. The only way to accurately perform this function is to assume that the flame reaction proceeds in an adiabatic manner (no net heat flow into or out of the system) and at a constant pressure. Under these conditions it is possible to write the specific enthalpy of the unburnt mixture as:

$$H_u = \frac{\sum_i (\chi_i)_u (H_i^0)_{T_u}}{\sum_i (\chi_i)_u M_i} \qquad (4.36)$$

The absolute molar enthalpies at the inlet temperature $\left(H_i^0\right)_{T_u}$ are obtained from reference tables. Since the flame is assumed to be an adiabatic constant pressure process, the final enthalpy of the burned gas must be the same as that of the unburned gas:

$$H_u = H_b \tag{4.37}$$

The procedure is then to estimate the final flame temperature T_b', calculate the equilibrium composition of the gas mixture at this temperature and specific pressure by the method outlined above, and then compute the specific enthalpy corresponding to this estimated temperature:

$$H_b' = \frac{\sum_i (\chi_i)_b' \left(H_i^0\right)_{T_b'}}{\sum_i (\chi_i)_b' M_i} \tag{4.38}$$

The value of H_b' obtained is then compared to H_u and iteration with T_b' is carried out until: $H_u = H_b'$. This procedure is usually carried out by computer.

Three different software packages that perform the minimization process have been evaluated, the primary difference being that the first two packages, *STANJAN* [66] and *GASEQ* [67] utilize reference data from the *JANAF* thermochemical tables [68] where as the third package, *MTData* [69] utilizes data from the SGTE substance database developed at the *National Physical Laboratory (NPL)*. It was found that there was negligible difference between the results generated by the three packages. Since all experiments were carried out using a propane/air flame, the equilibrium species concentrations and adiabatic flame temperatures were determined for the flammability limits of this system: $0.5 < \phi < 2.8$, where the equivalence ratio ϕ is:

$$\phi = \frac{(V_F / V_O)}{(V_F / V_O)_{ST}} \tag{4.39}$$

Where V_F / V_O is the ratio of the volume of fuel to the volume of oxidizer (air) and $(V_F / V_O)_{ST}$ is the same ratio for stoichiometric conditions.

Figure 4.3 shows the calculated equilibrium composition of products from the combustion of propane and air and the adiabatic flame temperature for various equivalence ratios for the major species. Minor species are not shown but are included in the calculations. The model clearly shows:

- Excess O_2 for $\phi < 1$ (lean mixture).
- A gradual increase in H_2 and CO as ϕ becomes greater than 1 (rich mixture).
- The main gas component is unburnt N_2.
- A maximum adiabatic flame temperature of approximately 2700 K for ϕ slightly greater than 1.

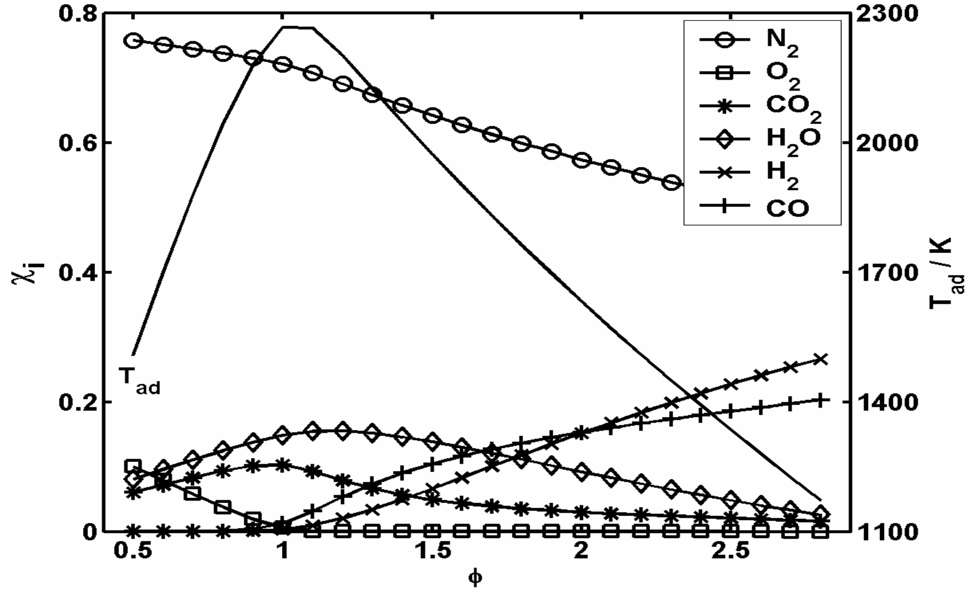

Figure 4.3 Major species concentrations (L.H. axis) and adiabatic flame temperature (R. H. axis) for propane/air combustion.

4.2.2.2 DETERMINATION OF THE DIFFERENTIAL RAYLEIGH SCATTERING CROSS-SECTION OF EACH SPECIES

We begin by evaluating the cross-section (Equation 4.23) at Standard Temperature and Pressure (STP) and then proceed to develop a temperature-dependent correction.

For most experiments utilizing a polarized incident laser beam, the laser propagates along the x-axis, is polarized to a very high degree (better than 99.9% in this case) along the z-axis and light is collected along the y-axis. As derived earlier (Equation 4.23), under these conditions the differential scattering cross-section of a single molecular species, at a single wavelength, is given by:

$$\frac{\partial\sigma}{\partial\Omega} = \frac{9\pi^2}{\lambda^4 N^2}\left(\frac{n^2-1}{n^2+2}\right)^2\left(\frac{6+3\rho_0}{6-7\rho_0}\right)\left(\frac{2}{2+\rho_0}\right) \tag{4.40}$$

Simplifying Equation 4.40 and introducing the molar refractivity [71]:

$$R_L = \left(\frac{n^2-1}{n^2+2}\right)\frac{N_A}{N} \tag{4.41}$$

where N_A is the Avogadro constant.

We can finally write:

$$\frac{\partial\sigma}{\partial\Omega}=\frac{9\pi^2 R_L^2}{\lambda^4 N_A^2}\left(\frac{6}{6-7\rho_0}\right) \tag{4.42}$$

The values of R_L and ρ_0 at the laser wavelength (532 nm) are accurately tabulated [71-72] for all major combustion species allowing for precise determination of the differential scattering cross-section at STP. Table 4.1 provides a summary of the two parameters and the calculated differential scattering cross-section for the major products of combustion and for dry air.

Species	R_L **/ cm^3.mol^{-1}**	ρ_0	$\frac{\partial\sigma}{\partial\Omega}$ **/ cm^2 (x10^{-28})**
N_2	4.4840	0.020194	6.2965
O_2	4.0650	0.054475	5.3958
CO_2	6.6900	0.075257	1.5003
H_2O	3.7820	0.000600	4.3769
H_2	2.0860	0.017839	1.3589
CO	5.0340	0.010702	7.8469
Ar	4.2290	0	5.4688
Air	4.3930	0.028430	6.1036

Table 4.1 Molar refractivity R_L, depolarisation ratio ρ_0 and differential scattering cross-section $\partial\sigma/\partial\Omega$ for the major combustion species and air at 532 nm and STP.

4.2.2.3 DETERMINATION OF THE TEMPERATURE DEPENDENCE OF THE RAYLEIGH SCATTERING CROSS-SECTION

It is common practice when applying Rayleigh scattering thermometry, to determine the combustion species concentrations and assume that the scattering cross-section for a given species remains unchanged with respect to temperature. However, this assumption can be shown to lead to errors of up to 2% in the cross-section for typical combustion gases [63] and needs further investigation. In determining the temperature-dependence of the scattering cross-section it is convenient to recast the differential scattering cross-section in terms of the mean polarizability, $a(T)$, and anisotropy $\gamma(T)$ [60]. This can be achieved by noting that the mean polarizability is related to the molar refractivity by:

$$a(T)=\frac{3\varepsilon_0}{N_A}R_L(T) \tag{4.43}$$

Equation 4.42 may now be written as:

$$\frac{\partial\sigma(T)}{\partial\Omega}=\frac{\pi^2}{\varepsilon_0^2\lambda^4}\left(a^2(T)+\frac{7}{45}\gamma^2(T)\right) \tag{4.44}$$

We now proceed to quantify the temperature dependence of $a(T)$ and $\gamma(T)$.

4.2.2.3.1 THE TEMPERATURE DEPENDENCE OF THE MEAN POLARISABILITY

In the limiting case of small electric field strengths $\vec{F}$, the dipole moment of the molecular interaction can be written as:

$$\vec{\mu} = \vec{\mu}^{(0)} + \vec{\alpha}\vec{F} \tag{4.45}$$

where $\vec{\mu}^{(0)}$ is the permanent dipole moment of the molecule and $\vec{\alpha}$ is the dipole polarisability tensor of rank two. In the following, we consider only the mean dipole polarizability a, as this is the quantity that gives rise to the scattering cross-section in these experiments. This is given by the summation of the diagonal elements of the polarizability tensor:

$$a = \frac{Tr(\vec{\alpha})}{3} = \frac{(\alpha_{11} + \alpha_{22} + \alpha_{33})}{3} \tag{4.46}$$

The mean dipole polarizability is a scalar, which depends on the frequency ω of the applied electric field $\vec{F}$. For the electronic ground state outside any absorption bands, this frequency dependence can be written as [72]:

$$a_{nvJ}(\omega) = -2\sum_{n'v'J'} \frac{\langle \psi | \vec{\mu}_i | \psi' \rangle^2 (E - E')}{\left[(E - E')^2 - (\hbar\omega)^2\right]} \tag{4.47}$$

where $\vec{\mu}_i$ is the dipole moment operator. The eigenvalues E_{nvJ} of the state ψ_{nvJ} and $E_{n'v'J'}$ of the state $\psi_{n'v'J'}$, are characterized by the electronic quantum numbers (n, n'), the vibrational quantum numbers (v, v') and the rotational quantum numbers (J, J'). The prime on the summation indicated that the term with $n = n'$, $v = v'$ and $J = J'$ is excluded. As a result of Equation 4.47 it is seen that each state defined by the three quantum numbers has its own dynamic polarizability $a_{nvJ}(\omega)$. By summing some of the quantities in Equation 4.47 and using the definition of the oscillator strength:

$$f = \frac{2\langle \psi | \vec{\mu}_i | \psi' \rangle^2 (E - E')m}{(\hbar e)^2} \tag{4.48}$$

and the transition frequency:

$$\omega' = \frac{(E - E')}{\hbar} \tag{4.49}$$

the following expression for the polarizability is obtained:

$$a_{nvJ}(\omega) = \frac{e^2}{m} \sum_{n'v'J'}{}' \frac{f}{\omega'^2 - \omega^2} \tag{4.50}$$

where e is the elementary charge and m the electron rest mass. This equation indicates that as the upper states become populated the polarizability will change.

The first temperature related contribution to $a_{nvJ}(\omega)$ can be determined by considering the case of atoms. Here, the measured mean polarizability will be the Boltzmann average over all polarizablities $a_n(\omega)$ of the electronic levels *n* in Equation 4.50 (neglecting *v* and *J*):

$$a(\omega,T)=\frac{\sum g_n a_n(\omega)e^{-\frac{E_n}{kT}}}{\sum g_n e^{-\frac{E_n}{kT}}} \tag{4.51}$$

where E_n is the energy of the transition between the ground state, *n* = 0, and state *n* and g_n is the degeneracy of level *n*. For temperatures below 5000 K this contribution is negligible [72].

The second temperature related contribution to $a_{nvJ}(\omega)$ results from the interaction of the ambient radiation field with the particle under consideration – an effective 'Stark shift' in the energy levels due to the fact that the atoms are immersed in a blackbody field [73-74]. The polarizability is then the ensemble average at this temperature and is given by:

$$a(T)=\frac{\int_0^\infty \frac{\omega^3 a(\omega)}{e^{\hbar\omega/kT}-1}d\omega}{\int_0^\infty \frac{\omega^3}{e^{\hbar\omega/kT}-1}d\omega} \tag{4.52}$$

This interaction is of the order of 0.18% for argon at 2000 K and 0.08% for helium at the same temperature [72]. In all cases the theory predicts an *increase* in polarizability with temperature. The effect is small and it will be seen later that changes in the polarizability due to molecular properties are more significant than either of these 'atomic' effects.

In contrast to atoms, molecules can additionally occupy rotational (*J*) and vibrational (*v*) levels. According to Equations 4.47 and 4.50 each state of the molecule has its own polarizability a_{nvJ}. Substituting *n* with *v* and *J* in turn in Equation 4.51 leads to two additional contributions to the polarizability of molecules, which are not present for atoms. *Ab initio* calculations of $a_{vJ}(\omega)$ are predominantly restricted to atomic species [75-77]. In all cases that have been investigated an increase in the polarizability with increases of quantum number *v* and *J* is reported. Since higher excited state populations occur for higher temperatures it directly follows that the polarizability increases with increasing temperature.

A semi-empirical approach to quantify the dependency of $a_{nvJ}(\omega)$ on temperature for diatomic molecules is given by Hohm [72]. He assumes that $a_{nvJ}(\omega)$ is directly related to changes in the mean internuclear distance *r*, which may be caused by temperature variations. In diatomic molecules, *r* increases with *v* due to the asymmetrical nature of the potential energy curve. $a_{nvJ}(\omega)$ also increases with *J* due to centrifugal stretching.

Using the theory of Buckingham [78] and utilizing Placzeks theory of Raman scattering [79] far from electronic resonances, $a(\omega)$ may be expanded in powers of the dimensionless distance $\xi = \frac{(r - r_e)}{r_e}$, where r_e is the equilibrium internuclear distance in the ground state:

$$a(\omega) = a_0(\omega) + a_e'(\omega)\xi + a_e''(\omega)\xi^2/2 + ... \tag{4.53}$$

where the coefficients $a_e'(\omega)$ and $a_e''(\omega)$ are given by:

$$a_e'(\omega) = [\partial a(\omega)/\partial r]_e r_e \quad \text{and} \quad a_e''(\omega) = \left[\partial^2 a(\omega)/\partial r^2\right]_e r_e^2 \tag{4.54}$$

The subscript *e* represents equilibrium conditions. The potential energy of the rotating vibrator can then be written as:

$$V(\xi) = \left(\frac{hc\sigma_e^2}{4B_e}\right)\left(\xi^2 + a_a\xi^3\right) - hcB_eJ(J+1)(2\xi - 3\xi^2) \tag{4.55}$$

where B_e is the rotational constant, σ_e the vibration wavenumber in the lowest state and a_a is the anharmonicity constant. The temperature dependence of the polarizability (including Boltzmann averaging) is then given by:

$$a(\omega, T) = a_0(\omega) + (B_e/\sigma_e)\frac{\left[a_e''(\omega) - 3a_a a_e'(\omega)\right]}{\left[e^{hc\sigma_e/kT} - 1\right]} + R(T) \tag{4.56}$$

with:

$$R(T) = 4(B_e/\sigma_e)^2 \frac{\sum J(J+1)(2J+1)e^{-hcB_eJ(J+1)/kT}}{\sum (2J+1)e^{hcB_eJ(J+1)/kT}} a_e'(\omega) \tag{4.57}$$

The summation in *R(T)* must be carried out over all $J \geq 0$ and can be replaced in almost all cases by an integration, leading to the simple result:

$$R(T) = 4kTB_e a_e'(\omega)/hc\sigma_e^2 \tag{4.58}$$

The temperature dependence of $a(\omega)$ is seen from Equations 4.56 and 4.57. Hohm [72] has applied these relationships to some common diatomic molecules and with some simplifying assumptions to methane. The results are clear and agreement with experiment is good. Table 4.2 shows changes of between 0.2 % and 1.4 % in mean molecular polarizability of typical combustion species for a rise in temperature of 1000 K at λ = 532 nm.

Species	$\frac{\Delta a}{a}$ ***100** **% / 1000K**
N_2	0.2 %
O_2	0.7 %
CO_2	1.1 %
H_2O	0.5 %
H_2	1.4 %
CO	0.4 %
Ar	0.0 %

Table 4.2 The change in mean molecular polarizability $a(T)$ of typical combustion species for a rise in temperature of 1000 K (from 273 K) for λ = 532 nm (corrected from [72] where measurements where made at λ = 632.99 nm).

4.2.2.3.2 THE TEMPERATURE DEPENDENCE OF THE MOLECULAR ANISOTROPY

The temperature-dependence of the molecular anisotropy has not been established experimentally. However, it is possible to use theoretical arguments to assess the appropriate trend. *Ab initio* calculations of the polarizability of H_2 reveal a larger relative increase in the anisotropy than in the polarizability with increasing inter-nuclear distance [71,77]. For typical combustion species the increase is estimated to be of the order of 2 % per 1000 K rise in temperature [71]. This seems reasonable since we see from Equation 4.44 that the contribution to the differential scattering cross-section of the anisotropy term is weighted by a factor 7/45 and since for all relevant combustion species, the sensitivity to the anisotropy is small compared to that of the polarizability term. An increase in the anisotropy of 2 % / 1000 K is thus assumed for this work. The uncertainty in the flame temperature due to this approximation is less than ± 0.15 %.

4.2.2.3.3 COMBINING THE TEMPERATURE DEPENDENCE OF THE MEAN MOLECULAR POLARISABILITY AND ANISOTROPY

We now proceed to determine the cumulative effect of the temperature-dependence of the mean molecular polarizability and the molecular anisotropy. Considering Equation 4.44, the fractional change in the differential scattering cross-section of a single molecular species, *i*, due to a temperature rise of 1000 K can be written as:

$$\Delta_i = \frac{\Delta \left.\frac{\partial \sigma_i}{\partial \Omega}\right|_{\Delta T = 1000K}}{\frac{\partial \sigma_i}{\partial \Omega}} = 2\left[\frac{a_i^4\left(\frac{\Delta a_i}{a_i}\right)^2 + \frac{7}{45}\gamma_i^4\left(\frac{\Delta \gamma_i}{\gamma_i}\right)^2}{\left(a_i^2 + \frac{7}{45}\gamma_i^2\right)^2}\right]^{\frac{1}{2}} \tag{4.59}$$

where $\left(\frac{\Delta a_i}{a_i}\right)$ and $\left(\frac{\Delta \gamma_i}{\gamma_i}\right)$ are the fractional changes in the mean molecular polarizability and anisotropy of the i^{th} species respectively, for a temperature rise of 1000 K.

with $\Delta \left.\frac{\partial \sigma_i}{\partial \Omega}\right|_{\Delta T=1000K}$ the absolute change in the scattering cross-section of the i^{th} species for the same temperature rise.

4.2.3 DETERMINATION OF δ

The main Rayleigh scattering measurement equations described earlier (Equations 4.29 and 30) are:

$$T_2 = \delta \frac{S(T_1)}{S(T_2)} T_1 , \qquad \delta = \frac{\left(\frac{\partial \sigma}{\partial \Omega}\right)_{\substack{post\\flame}}}{\left(\frac{\partial \sigma}{\partial \Omega}\right)_{air}} \tag{4.60/61}$$

where $S(T_1)$ is the Rayleigh signal measured for air at temperature T_1 and $S(T_2)$ is the Rayleigh signal measured in the post flame region at a temperature T_2. To obtain the true post-flame temperature, T_2, we require accurate knowledge of δ. By combining the determination of the species concentrations of the post flame region and the temperature-dependence of the scattering cross-section of these species we can write:

$$\delta = \underbrace{\left[\frac{\sum_i X_i \frac{\partial \sigma_i(T_0)}{\partial \Omega}}{\frac{\partial \sigma_{air}(T_0)}{\partial \Omega}}\right]}_{\substack{Species\\correction}} \underbrace{\left[1 + \left[\frac{\sum_i X_i \frac{\partial \sigma_i(T_0)}{\partial \Omega}\Delta_i}{\sum_i X_i \frac{\partial \sigma_i(T_0)}{\partial \Omega}}\right]\left[\frac{T_{ad}-T_0}{1000}\right]\right]}_{\substack{Temperature\\correction}} \tag{4.62}$$

where T_0 is 298.15 K, T_{ad} and X_i are the adiabatic flame temperature and the mole fraction of the i^{th} species in the post flame region obtained from the equilibrium calculations and Δ_i is defined in Equation 4.59. Applying Equation 4.62 to the propane/air flame used in this work allows the accurate determination of the post flame temperature. Table 4.3 and Figure 4.4 show the species correction, temperature correction and the total correction, δ, to the differential scattering cross-section for this system for various equivalence ratios. Clearly the main contribution to δ is due to the difference between the chemical composition of the post flame region compared to that of air, peaking at around 13% for a ϕ of 1.0. The temperature-dependent contribution reaches 2 % for a similar equivalence ratio, falling off either side for weak and rich mixtures. The total uncertainty in δ is $\pm 0.3\%$. Applying this correction allows the accurate determination of the post flame temperature.

φ	$\left(\frac{\partial\sigma}{\partial\Omega}\right)_{\mathrm{MIX},T_0}$ **/ cm^2 x 10^{-28}**	**T_{ad} / K**	**Species correction (compared to air at STP)**	**Temperature correction (at T_{ad})**	**Total correction, δ**
0.5	6.57201	1507.3	1.07674	1.00979	1.08728
0.6	6.65507	1699.2	1.09035	1.01174	1.10316
0.7	6.73290	1877.9	1.10310	1.01367	1.11818
0.8	6.80261	2040.6	1.11452	1.01551	1.13181
0.9	6.85489	2177.9	1.12309	1.01707	1.14226
1	6.86436	2265.2	1.12464	1.01791	1.14478
1.1	6.78756	2263.7	1.11206	1.01742	1.13144
1.2	6.65402	2199.4	1.09018	1.01620	1.10784
1.3	6.52102	2123.1	1.06839	1.01503	1.08445
1.4	6.40030	2046.8	1.04861	1.01405	1.06335
1.5	6.29168	1972.6	1.03081	1.01323	1.04446
1.6	6.19313	1900.7	1.01467	1.01254	1.02739
1.7	6.10276	1831.1	0.99986	1.01192	1.01178
1.8	6.01910	1763.5	0.98616	1.01137	0.99737
1.9	5.94093	1697.7	0.97335	1.01086	0.98392
2	5.86738	1633.7	0.96130	1.01039	0.97128
2.1	5.79808	1571.7	0.94994	1.00993	0.95938
2.2	5.73217	1511.1	0.93915	1.00950	0.94807
2.3	5.66918	1451.8	0.92883	1.00907	0.93725
2.4	5.60893	1394.1	0.91895	1.00865	0.92691
2.5	5.55096	1337.6	0.90946	1.00824	0.91695
2.6	5.49488	1282.4	0.90027	1.00783	0.90732
2.7	5.44058	1228.5	0.89137	1.00743	0.89799
2.8	5.38911	1177.3	0.88294	1.00703	0.88915

Table 4.3 The species correction, temperature correction and total correction to the differential scattering cross-section for propane/air combustion at a given equivalence ratio, ϕ.

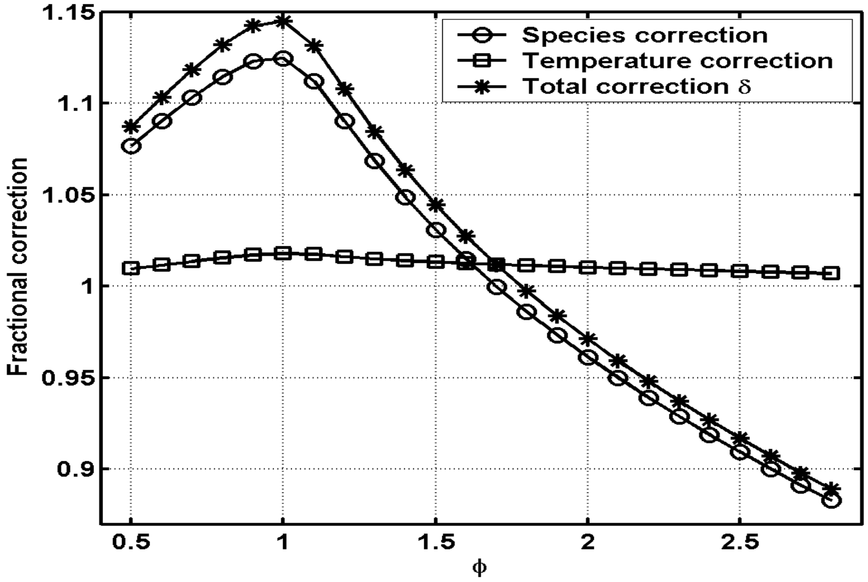

Figure 4.4 The species correction, temperature correction and total correction, δ, to the differential scattering cross-section for propane/air combustion at a given equivalence ratio, ϕ.

4.3 EXPERIMENTAL EVALUATION OF THE RAYLEIGH THERMOMETRY TECHNIQUE

4.3.1 DESCRIPTION OF THE RAYLEIGH THERMOMETRY APPARATUS

The Rayleigh thermometry system including the McKenna burner is shown schematically in Figure 4.5. The laser, provided by *GSI Lumonics* [80], is a Nd-YAG frequency doubled (532 nm) Q-switched pulse system with a repetition rate of 30 Hz and average pulse energy of 100 mJ.

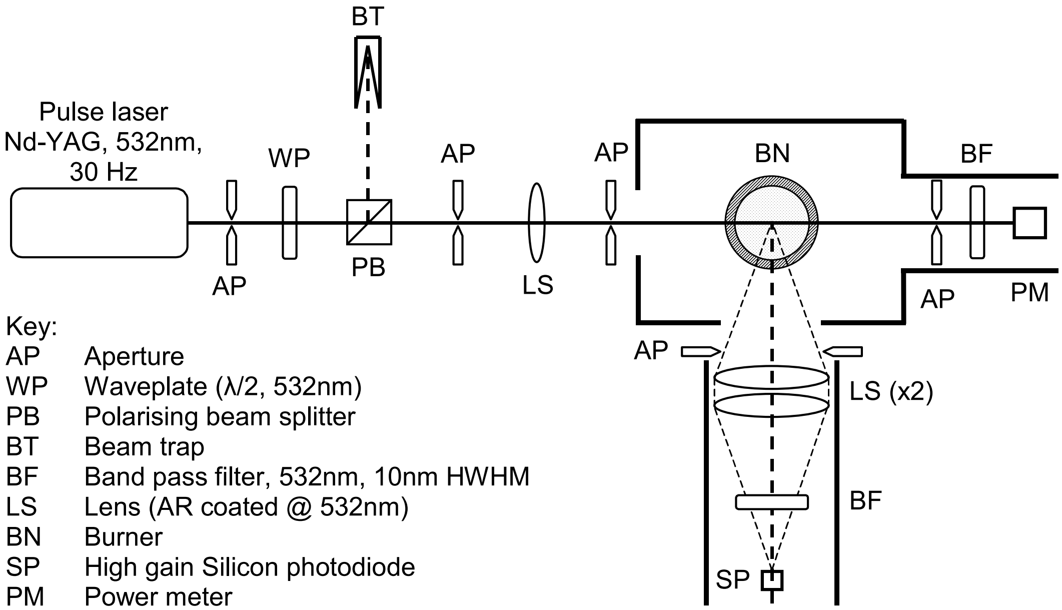

Figure 4.5 Plan view of the Rayleigh thermometry system including the McKenna burner.

The beam first passes through an aperture (AP) followed by a half waveplate (WP) and a polarizing beam splitter (PB). These components condition the beam such that only vertically polarized light will pass and in addition to this, rotation of the half waveplate allows the laser power to be adjusted with the horizontally polarized component being dumped in a blackened beam trap (BT). The beam is then focussed by an anti-reflection coated lens (LS) of focal length 75 cm such that the beam waist (0.4 mm diameter) is positioned 2 cm directly above the centre of the burner (BN). The Rayleigh scattered light is collected perpendicular to the beam propagation and polarization directions by an anti-reflection coated lens pair (LS) of diameter 7.5 cm over a solid angle of 0.1 sr. After passing through a 532 nm bandpass filter (BF) with a HWHM of 10 nm, the scattered light is collected by a 3.6 mm x 3.6 mm amplified silicon photodiode (SP).

The majority (99.99%) of the laser beam passes straight through the region above the burner and is collected, after passing through a second 532 nm bandpass filter (BF) by a high linearity pulse energy meter (PM) provided by *Litron Lasers* [81]. The Rayleigh signal and the laser power signal are then passed, via coaxial cables, to a high-speed transient digitiser model PXI-5122, provided by *National Instruments* [82]. The digitiser has a resolution of 14 bits and a digitising rate of 100 Million samples/second per channel. Software developed in *Labview* [82] averages a number of pulses and determines the ratio of the Rayleigh scattered signal to the laser energy signal. Active baseline subtraction is also used to zero the detectors by pre-triggering the signal collection system and measuring the detector signals when the laser is not firing. The reason for measuring the ratio of the Rayleigh signal to that of the laser signal is to remove drift in the laser energy, which was found to be significant. The McKenna burner system and associated gas premixing and water-cooling system is described in Chapter 2.

4.3.2 TECHNICAL CHALLENGES IN ACHIEVING THE HIGHEST ACCURACY

In order to achieve the highest accuracy in the Rayleigh thermometry measurements, several obstacles need to be overcome:

- Reduction of laser generated electromagnetic interference.
- Reduction of background laser light scattering.
- Improvement of the linearity of the detectors and the digitiser.
- Optimisation of the Rayleigh scattering signal collection system.
- Evaluation of the long term stability of the Rayleigh scattering system.

A description follows.

4.3.2.1 REDUCTION OF LASER GENERATED ELECTROMAGNETIC INTERFERENCE

It is widely reported that Q-switched pulse lasers, such as that used in this work, produce a large amount of electromagnetic interference when the Q-switch process occurs. This interference should not strictly be called ‘noise’ since it is quasi-random in its nature - the usual $1/\sqrt{N}$ improvement in the signal to noise by averaging N measurements is not achieved for this type of interference. In effect, the noise has a distinct envelope that changes slowly over time and thus long term averaging does not reduce such errors. Figure 4.6 shows the remarkable effect of covering standard BNC leads, used to connect the detectors to the measuring equipment, with copper braid.

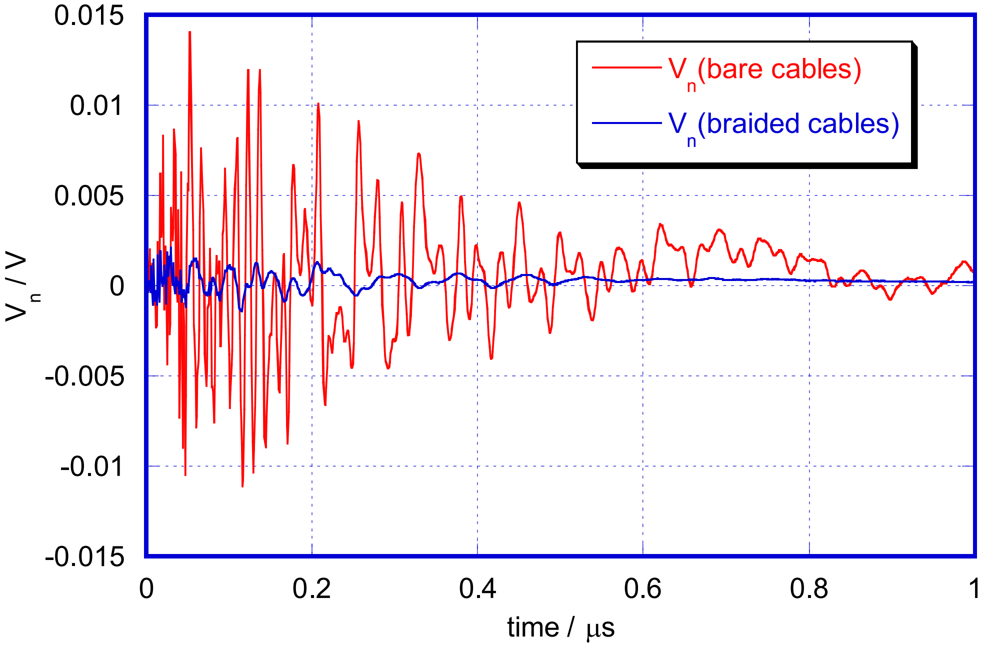

Figure 4.6 Noise reduction with instrument leads covered in copper braiding (Laser fires but shutter is closed).

The Rayleigh scattering detector, a 3.6 mm square silicon photodiode with integral high gain amplifier (G ~ 10^4), was also found to 'pick-up' interference from the laser. Ultimately 6 steps were carried out to reduce the noise level by a factor of 35. These were:

1. Reduction of the length of the leads from the detector head to the digitiser instrumentation; the leads were shortened from 2 m to 0.5 m.
2. Replacement of the detector's mains power supply with a battery and enclosure of the whole detector/battery assembly inside an aluminium shielded box.
3. Installation of large parasitic capacitors across the detectors power supply to earth.
4. Placing of the braided signal cables inside copper tubing earthed to the optical table of the experiment.
5. Installation of ferrites around the signal cables.
6. Removal of the laser to an adjacent room.

Figure 4.7 shows the reduction in the peak-to-peak (P-P) noise levels for each step described above.

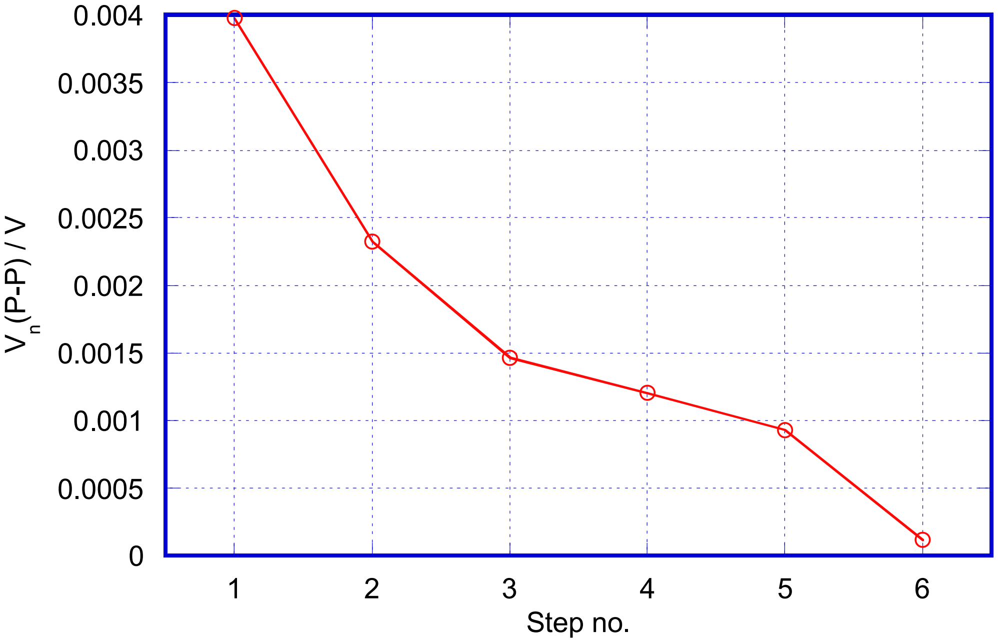

Figure 4.7 Signal noise level (P-P) vs steps 1-6 given above.

4.3.2.2 REDUCTION OF BACKGROUND LASER LIGHT SCATTERING

It was necessary to reduce the spuriously scattered laser light collected by the Rayleigh detector. This scattered light was found to be due to reflections from the burner itself and from other optical components in the beam path. A simple way to gauge the level of this unwanted signal contribution was to measure the signals collected by the Rayleigh detector while flowing first pure nitrogen and then pure helium through the burner. For signals with no spurious scatter and an optically invariant detection system, we expect the ratio of the two signals to be identical to the ratio of the differential scattering cross-sections of the two gases at the detection wavelength (532 nm). Hence we require that:

$$\frac{S(nitrogen)}{S(helium)} = \frac{\left(\frac{\partial\sigma}{\partial\Omega}\right)_{nitrogen}}{\left(\frac{\partial\sigma}{\partial\Omega}\right)_{helium}} = 75.57 \tag{4.63}$$

By painting the McKenna burner with matt black paint, careful shielding of the collection optics and accurate positioning of the various apertures in the system it was possible to obtain a signal ratio of 75.52 ± 0.08 which is within the experimental uncertainty of the literature value. Figure 4.8 shows the unpainted McKenna burner with sources of background scatter clearly visible and Figure 4.9 shows the blackened burner and shields.

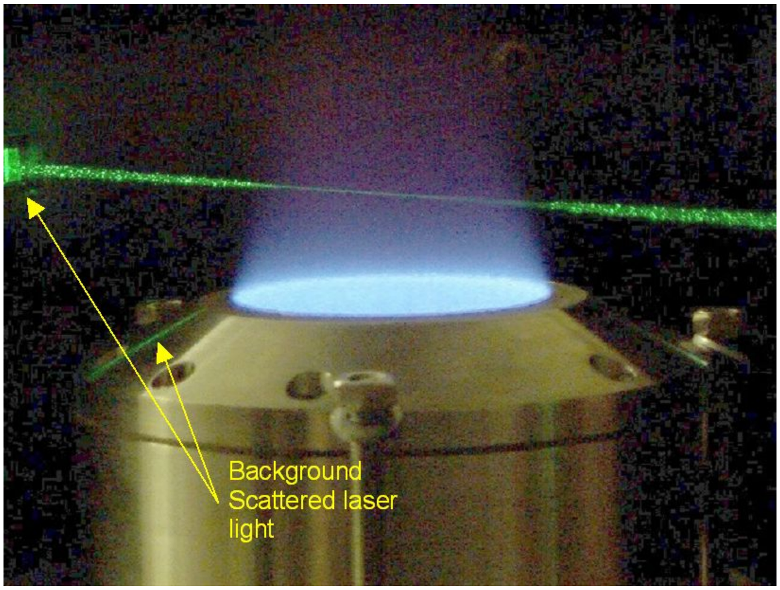

Figure 4.8 The unpainted McKenna burner under interrogation by the Nd-YAG laser at 532 nm, showing spuriously scattered laser light.

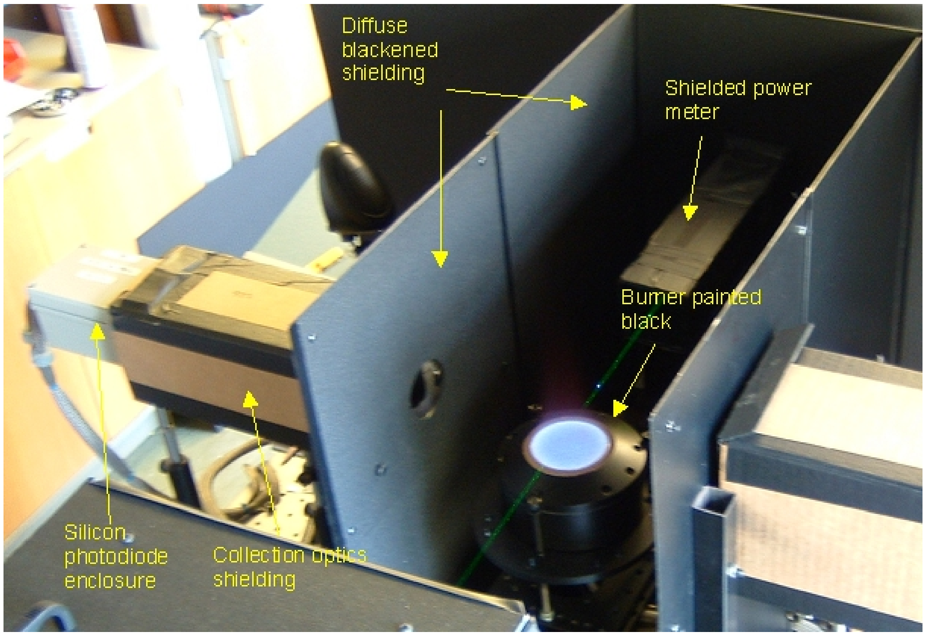

Figure 4.9 The Rayleigh system showing the burner painted black and various blackened shields.

4.3.2.3 LINEARITY OF THE DETECTORS AND THE DIGITISER

For the highest accuracy Rayleigh thermometry, the linearity of the detection system is critical. For an arbitrary gas at a constant temperature and pressure, the ratio of the Rayleigh scattering signal to that of the laser power meter signal should be constant regardless of the incident laser power. This is equivalent to saying the whole system is linear, i.e. if the laser power increases by 5%, the detected increase in both the power meter signal and the Rayleigh scattering signal will be 5% also.

Before purchase of the transient digitiser system, a boxcar integrator from *Stanford Research Systems* [83] was evaluated. The system comprised two *SRS250 boxcar integrators* with preamplifiers and maths processing modules. After extensive tests and communication with the suppliers, it was concluded that the system could not meet the linearity requirements needed for this Rayleigh scattering system. Figure 4.10 shows typical performance figures for the boxcar integrator, with the percentage deviation from the linear response for each voltage range shown. The boxcar integrator was configured to sample a DC voltage from a stabilised voltage source over a gate width of 1 μs. The voltage was simultaneously measured with a high precision voltmeter. Three voltage ranges were examined: 2 mV to 20 mV, 20 mV to 200 mV and 200 mV to 2 V with the gain of the boxcar system adjusted accordingly. If the boxcar signal is divided by the gate width, the DC voltage is recovered. This value is directly compared with the voltmeter output. We see that the response of the boxcar for large signals (low instrument gain) is linear to approximately 2% (V_0 = 0.2 V and V_0 = 2 V) but for small signals (high instrument gain) the departure from linearity approaches 13 % (V_0 = 0.02 V).

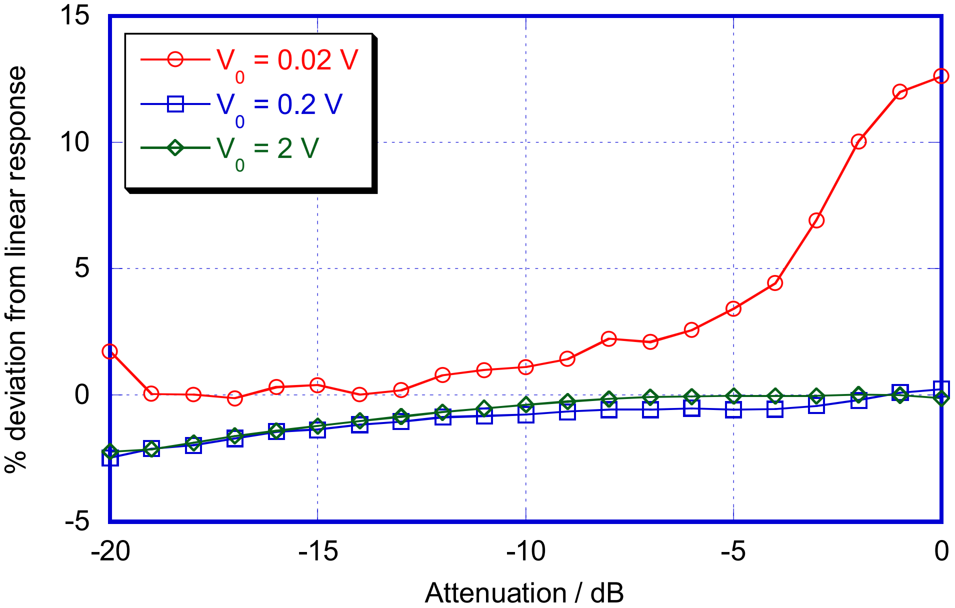

Figure 4.10 Linearity performance of the *SRS250 boxcar integrator*. Three voltage ranges shown: 2 mV to 20 mV (V_0 = 0.02 V), 20 mV to 200 mV (V_0 = 0.2 V) and 0.2 to 2 V (V_0 = 2 V).

PERFORMANCE OF THE TRANSIENT DIGITISER

In light of the poor performance of the boxcar integrator system a second approach was investigated. The two fast detectors, Rayleigh and power meter were adjusted to give substantially higher gain. Since the gain bandwidth product remains relatively constant, the effect was to 'slow' the captured signals down (effectively smearing them over a much longer period of time). This then paved the way for a purchase of a 'fast' transient digitiser. A two-channel transient digitiser system from *National Instruments* [82], the *PXI5122*, was purchased. With a speed of 100 Million samples per second per channel at 14 bit voltage resolution, it is one of the fastest available devices for the resolution. Computer code written in Labview controls the device and performs all the functions of the older gated integrator – summing, averaging and signal 'ratioing'.

The linearity tests performed on this device are shown in Figure 4.11. Typical signal amplitudes for the Rayleigh system are of the order of 100 mV. In this signal regime the non-linearity is less than 0.05 % as seen in the figure.

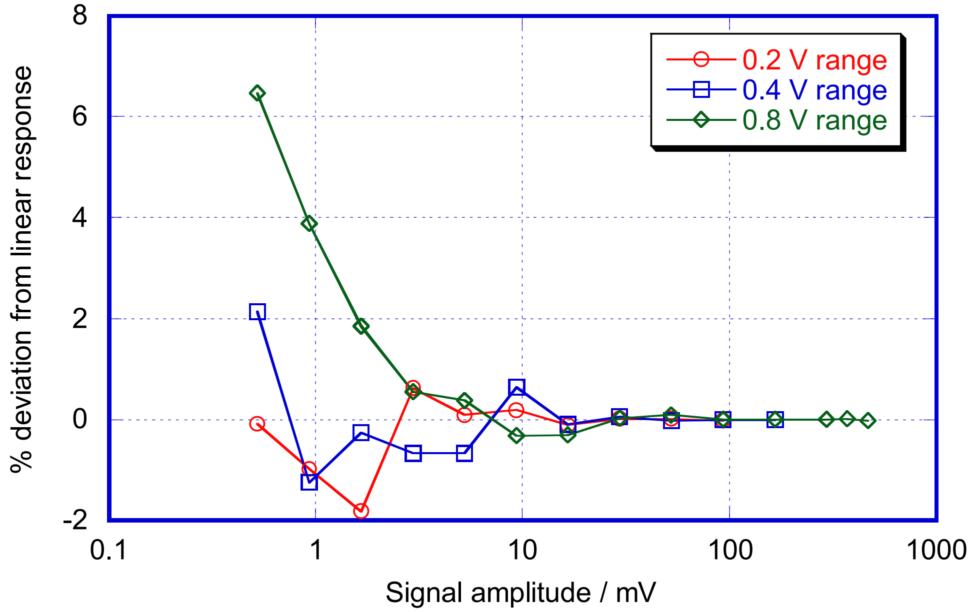

Figure 4.11 Linearity performance of the *PXI-5122 transient digitiser*. Three voltage ranges shown: 0.2 V, 0.4 V and 0.8 V.

PERFORMANCE OF THE DETECTOR SYSTEMS

With the post detector instrumentation (PXI-5122) providing sufficient linearity, the performance of the detector systems (laser power meter, Rayleigh scattering photodiode and associated filters and attenuators) was evaluated.

Before installation of the current *Litron* [81] laser power meter, the laser power was measured by sampling a small proportion of the incident beam with a beam sampler (which reflects 4% of the beam) and various neutral density filters. The laser power level was also only adjustable from the laser control unit which retarded the Q-switch trigger to release the laser cavity energy at different times after the flash lamps had fired. In this configuration, serious sources of error where identified.

Flowing air through the burner at a constant temperature and varying the laser power via the laser controller resulted in changes of up to 7% in the ratio of the Rayleigh signal to the power meter signal – a ratio that should remain constant for a given temperature and gas composition. Figure 4.12 shows this, with the normalised Rayleigh signal, I(Ray), and power meter signal, *I(Power)*, shown on the left axis and the ratio of these two signals shown on the right axis. Changes in the ratio are seen when the laser power is adjusted and there is also evidence of a general drift when the laser power is not changed.

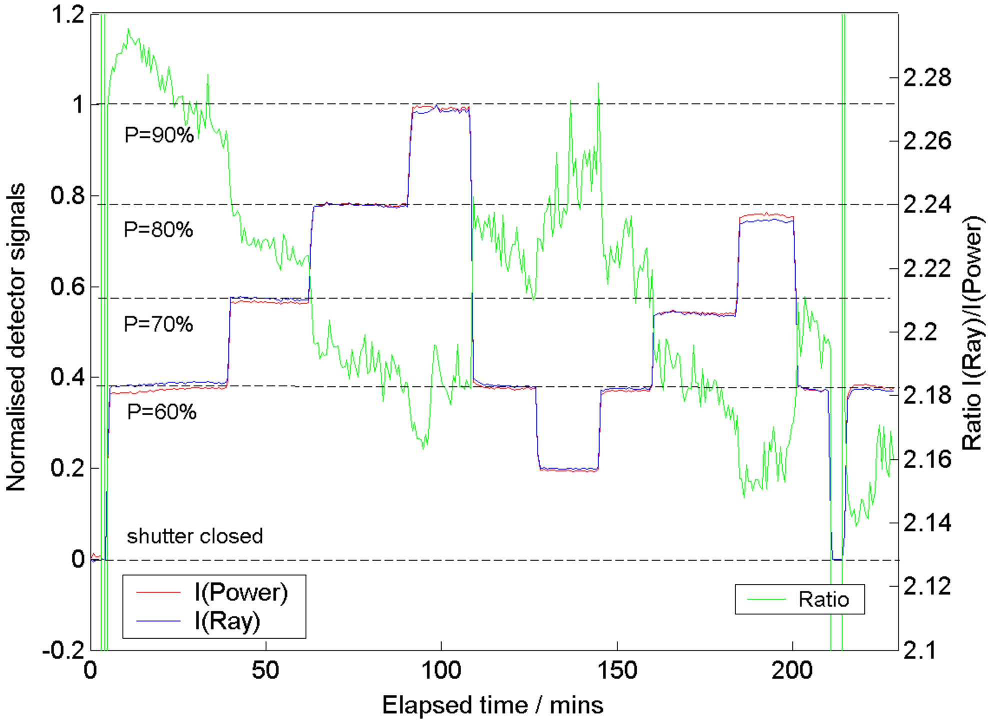

Figure 4.12 Normalised signals for the Rayleigh and power meter detectors (Left axis) and the ratio of these two signals (right axis) vs time for various laser power levels.

Detailed investigation revealed that several sources of errors were operating:

- Poor linearity and temperature sensitivity of the original power meter.
- Variability in the transmission with temperature and position of neutral density filters used in the original power meter system.
- Changes in the beam position, quality and polarisation with laser power level.
- General change in the beam position as the laser ‘warms up’.

To resolve these issues we took several steps:

- The laser power was adjusted by the addition of a half-wave plate and a polarizing beam splitter with the laser left operating at full power continuously and the power level adjusted by rotation of the half-wave plate.
- The *Litron* [81] power meter was positioned after the beam had passed over the burner such that the total laser power was measured. The linearity of this device was better than 0.1% for all power levels.
- The laser was allowed to warm up for approximately 4 hrs prior to measurements. After this time the ratio *I(Ray)/I(power)* was reasonably stable.

- Beam wander issues are dealt with in Section 4.3.2.4.

With this new configuration, the drift in the ratio of the Rayleigh signal to the power meter signal was reduced and the variation of the ratio with laser power was completely removed. Figure 4.13 shows the improvements with 4.13(a) showing the normalised Rayleigh and power meter signals and 4.13(b) showing the ratio, which apart from the random noise evident for low signal levels, remains constant for all laser powers with no sign of drift over time.

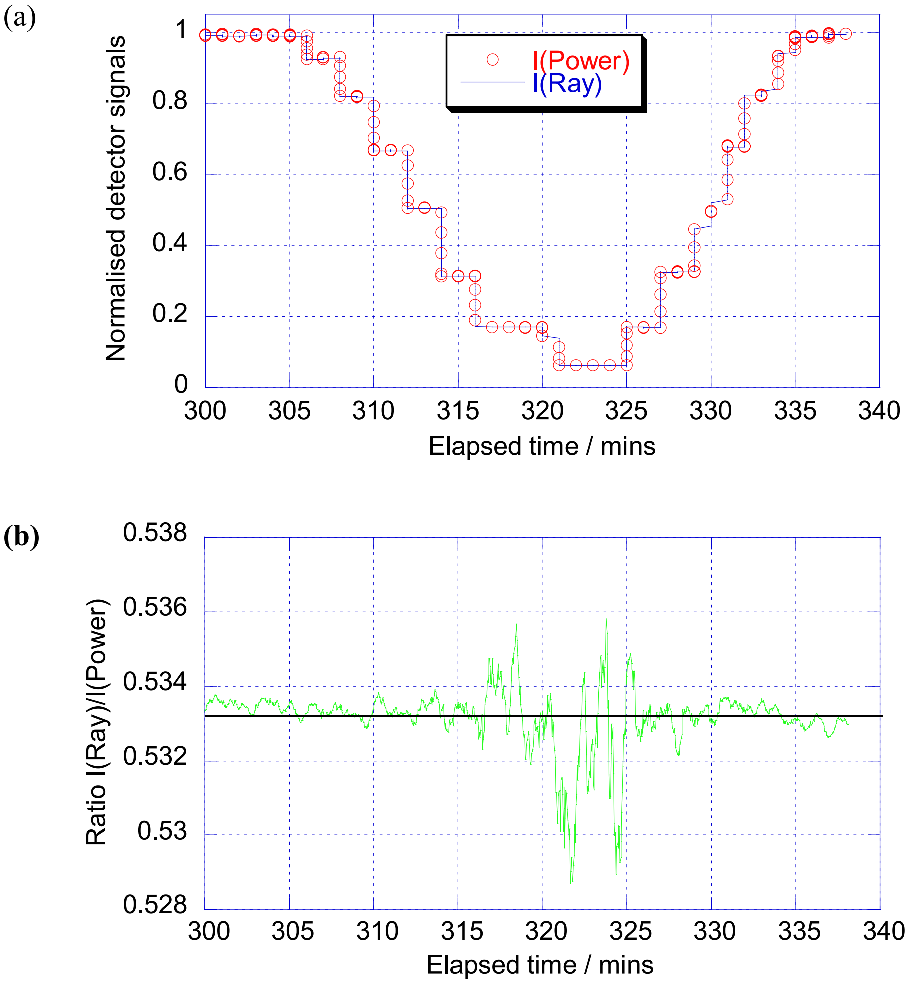

Figure 4.13 (a) Normalised Rayleigh and power meter signals vs time and laser power. (b) The ratio of the Rayleigh to the power meter signal vs time and laser power.

4.3.2.4 OPTIMISATION OF THE RAYLEIGH SCATTERING SIGNAL COLLECTION SYSTEM

Due to the low intensity of the imaged 532 nm Rayleigh signal, it was difficult to find the focus of the beam onto the silicon detector by eye. A test was carried out to make sure that the beam was indeed focused sufficiently well to ensure that any small beam wander would not cause the imaged beam to move off the detector. This was achieved by firstly moving the detector vertically so that the whole imaged beam was scanned for the original position – the position of best beam focus (by eye). The whole Rayleigh detector assembly was then moved horizontally from its original position to a new 'best focus' position – called *pos1* in Fig. 4.14, the detector was again moved vertically to scan the imaged beam. This was repeated for two other positions, one 5mm closer to the imaging lenses and one 5 mm farther away. Fig. 4.14 shows the results.

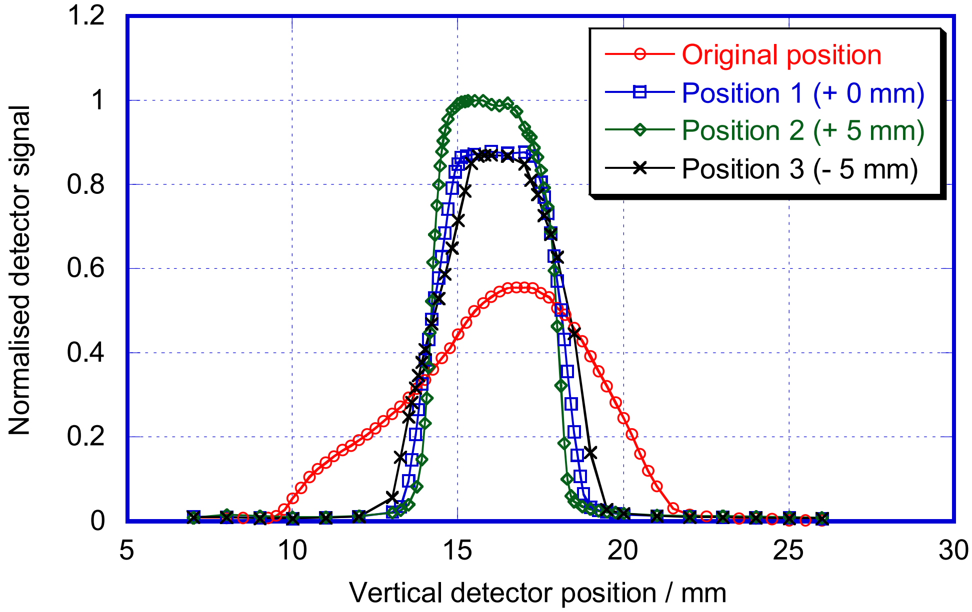

Figure 4.14 Normalised Rayleigh signal (for air at 20 °C) versus detector vertical position for various distances from the imaging lens.

The detector is 3.6mm high and the focussed imaged beam should be around 0.2 mm high. We therefore expect a 'top hat' type curve as the small beam image is swept past the large detector. Figure 4.14 shows that the original detector position was incorrect, with the imaged beam out of focus and the signal profile spread out. The best position was found for pos2 (5 mm further away from the imaging lenses).

With the detector in this position it was decided to investigate changes in detector sensitivity across its surface. Literature suggests that typical silicon photodiode detectors such as the one used here can have a variation in sensitivity to incident light at one wavelength of up to two percent across their total surface. Any beam movement, even on a small scale may cause the drift observed earlier.

Three sweeps of the detector were performed one immediately after the other (Figure 4.15). The centre of the detector corresponds to $y = 16$ mm and it was found that with the beam imaged at $y = 15.5$ mm (a region with the smallest change in sensitivity), there was negligible change in the measured signal with beam wander. All subsequent Rayleigh thermometry measurements were carried out with the Rayleigh detector in this optimum position.

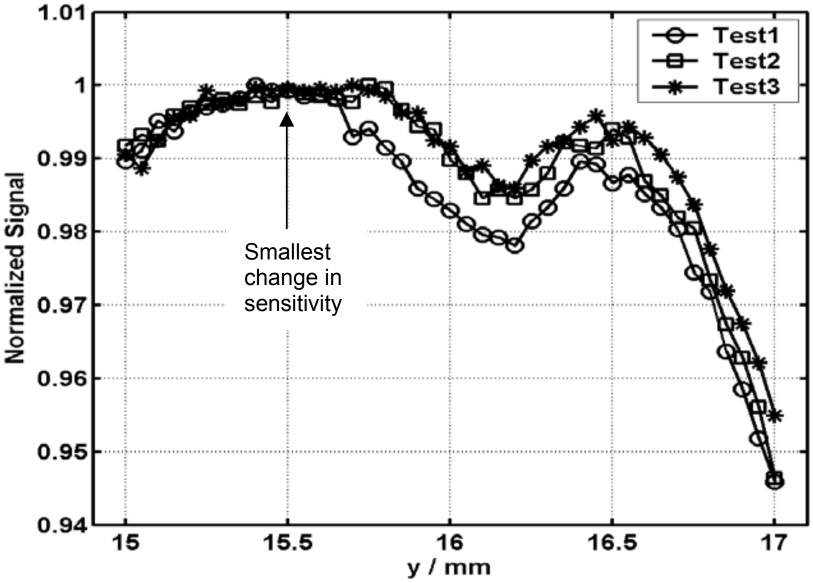

Figure 4.15 Normalized Rayleigh detector signal versus imaged beam position. y = 16 mm corresponds to the beam imaged on the middle of the detector. Note: smallest change in sensitivity around y = 15.5 mm.

4.3.2.5 LONG TERM STABILITY OF THE RAYLEIGH SCATTERING SYSTEM

With all the refinements described above, it was possible to reproduce the same ratio (R) of the Rayleigh signal to the power meter signal indefinitely. Figure 4.16 shows an example of the ratio over 28 measurement days spanning 3 months. The ratio is measured for air and corrected to 20 °C and 1000 hPa pressure. For each measurement, the laser was allowed to warm up first. A downward drift in R was always seen for the first 2 to 4 hrs after the laser was switched on but remained stable thereafter. After the first 10 measurements, the ratio has a standard deviation of less than ± 0.2 %.

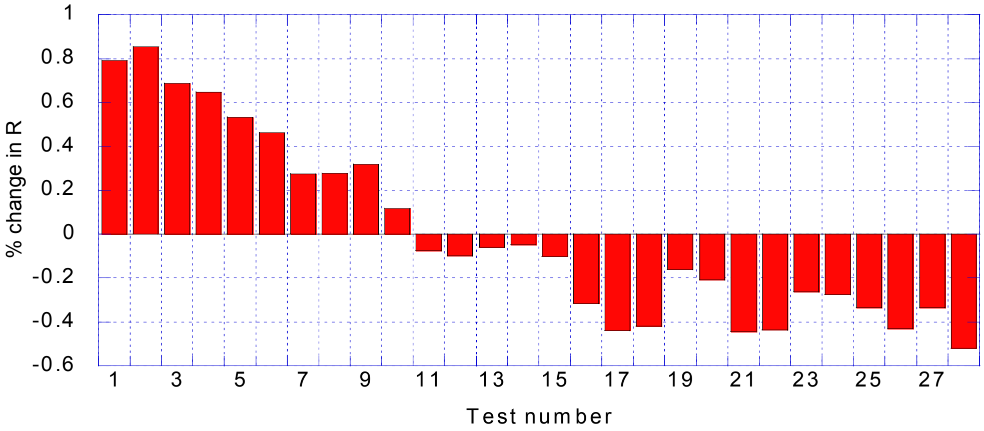

Figure 4.16 Rayleigh system stability: Percent change in R_{air}(20 °C, 1000 hPa) over a 3 month period.

4.3.3 EFFECT OF INPUT PARAMETERS ON THE FLAME TEMPERATURE

Since the objective of this work is to develop a stable reproducible combustion standard, it is important to evaluate all factors that could potentially change the flame temperature. The combustion standard was designed so that different temperatures and species are deliberately produced by changing the air-flow rate and equivalence ratio for the propane/air flame. However, other environmental parameters outside our control can affect the flame temperature, even though the flow rate and equivalence ratio remain unchanged. The factors that have been considered in great detail are:

- The uncertainty in the equivalence ratio
- The uncertainty in the post-flame composition due to non-LTE
- The inlet gas temperature.
- The inlet gas water content.
- The purity of the propane fuel.
- The ambient pressure.

Let us consider the effect of each of these in turn.

4.3.3.1 EFFECT OF UNCERTAINTY IN THE EQUIVALENCE RATIO

The accuracy of the measured Rayleigh flame temperature depends critically on accurate knowledge of the equivalence ratio ϕ, which in tern depends on the accuracy of the flow meters used. Recapping, the Rayleigh scattering temperature measurement equation is given by:

$$T_2 = \delta(\phi)\frac{S(T_1)}{S(T_2)}T_1 \tag{4.29}$$

where S_1 and S_2 are the Rayleigh scattering signals for air at T_1 = 293 K (20°C) and the post flame region at T_2 respectively and $\delta(\phi)$ is given by:

$$\delta(\phi) = \frac{\left(\frac{\partial\sigma}{\partial\Omega}(\phi)\right)_{\substack{post\\flame}}}{\left(\frac{\partial\sigma}{\partial\Omega}\right)_{air}} \tag{4.30}$$

where $\left(\frac{\partial\sigma}{\partial\Omega}(\phi)\right)_{\substack{post\\flame}}$ is the differential Rayleigh scattering cross-section of the post flame species and $\left(\frac{\partial\sigma}{\partial\Omega}\right)_{air}$ differential scattering cross-section for air at 20°C (assumed exact).

In this analysis, we wish to find the uncertainty in the post flame temperature T_2 resulting from uncertainty in the equivalence ratio ϕ and associated error in $\delta(\phi)$.

Using Equation 4.29 and assuming that $\frac{T_2}{T_1} \approx 7$, we can write:

$$T_2 \approx 2100\delta(\phi) \tag{4.64}$$

Differentiating w.r.t. ϕ gives:

$$\frac{\partial T_2(\phi)}{\partial \phi} \approx 2100 \frac{\partial \delta(\phi)}{\partial \phi} \tag{4.65}$$

For small increments, we can write:

$$\Delta T_2(\phi) = 2100 \frac{\partial \delta(\phi)}{\partial \phi} \Delta \phi \tag{4.66}$$

with $\delta(\phi)$ found from Table 4.3.

Figure 4.17 shows the percentage uncertainty in the post flame temperature, T_2 versus ϕ for various uncertainties in ϕ (0.5%, 1% and 2%).

Since the flow meters are calibrated to 1% accuracy, we may reasonably expect a maximum uncertainty in ϕ (note: $\phi \propto \frac{\text{fuel flowrate}}{\text{air flowrate}}$) of the quadrature sum of two 1% uncertainties, i.e. approximately 1.4% in total. This leads to a maximum uncertainty in the post-flame temperature of approximately 0.3% as seen in the figure.

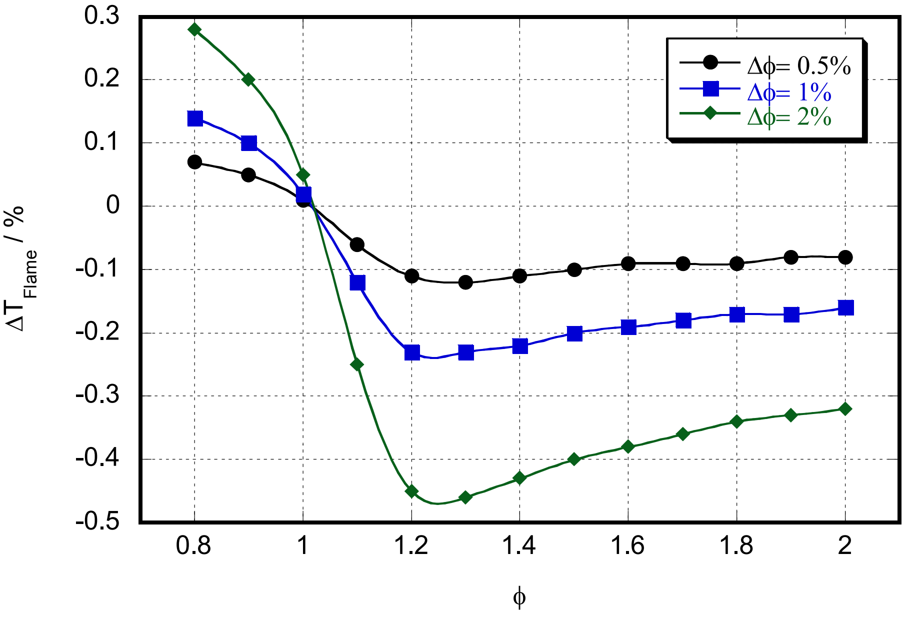

Figure 4.17 Uncertainty in the Rayleigh post-flame temperature versus ϕ for various uncertainties in ϕ.

It is worth noting that for ϕ slightly greater than 1, small uncertainties in ϕ have negligible effect on the calculated post-flame temperature.

4.3.3.2 EFFECT OF UNCERTAINTY IN THE POST-FLAME COMPOSITION DUE TO NON-LTE CONDITIONS

In this analysis, we wish to find the uncertainty in the post flame temperature T_2 resulting from uncertainty in $\delta(\phi)$ due to the post-flame gases CO_2, CO and Un-burnt Hydrocarbons (UHc) <u>not</u> being in Local Thermodynamic Equilibrium (LTE) as is assumed in the modelling software Gaseq [67] used to generate $\delta(\phi)$.

Since we are measuring in the post flame region well above the flame front and since it is a premixed flame it is reasonable to assume that there will be negligible Uhc. This is borne out by FTIR emission spectra shown in Thesis figure 3.18 (p.55) with no evidence of typical symmetric stretch emissions typical of hydrocarbon fuels usually present around 3.3 μm. Uhc will <u>not</u> be considered further.

However, CO_2 and CO are present in the post-flame region and we proceed to determine $\delta(\phi)$ when these gases are not at LTE. This can be achieved in Gaseq by constraining the product species to be in lower or higher concentrations than LTE and evaluating $\left(\frac{\partial\sigma}{\partial\Omega}(\phi)\right)_{\substack{post\\flame}}$.

Using the same assumptions given in §4.3.3.1, we start with the simplified measurement equation:

$$T_2 \approx 2100\delta(\phi) \tag{4.64}$$

Assuming that the scattering cross-section of the air at 20°C is constant and known with negligible uncertainty, the percentage error in T_2 can be written as:

$$\%\,\text{Error in } T_{Ray} = \left(\frac{\left.\frac{\partial\sigma}{\partial\Omega}\right|_{\substack{\text{POST FLAME}\\\text{NON-LTE}}}}{\left.\frac{\partial\sigma}{\partial\Omega}\right|_{\substack{\text{POST FLAME}\\\text{LTE}}}} - 1 \right) * 100 \tag{4.67}$$

Figure 4.18 shows the percentage errors in T_{Ray} when LTE is assumed but in fact the CO_2 mole fraction is lower by 1,2 and 5%. We see that T_{Ray} is under-estimated with a maximum error near ϕ=1 of approximately –0.1%, -0.2% and –0.5% for CO_2 concentrations 1%, 2% and 5% below LTE respectively, reducing as ϕ increases.

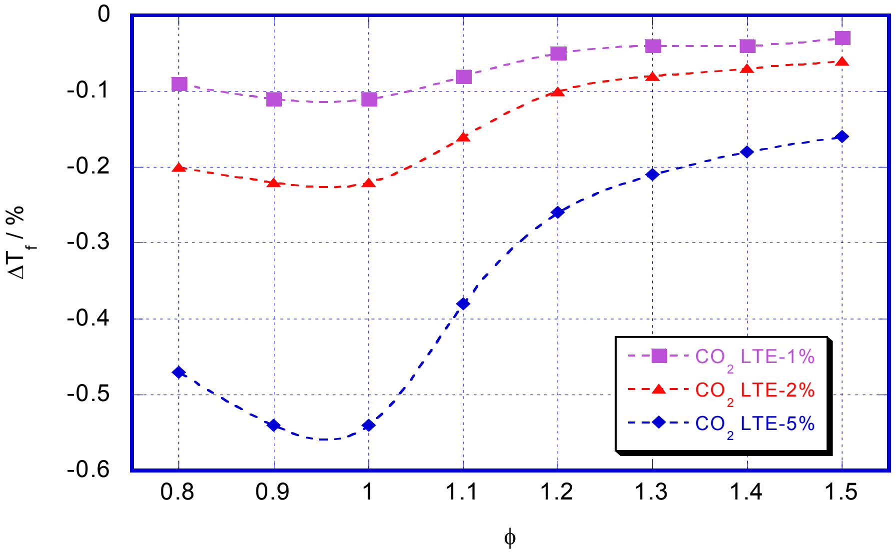

Figure 4.18 Percentage error in T_{Ray} due to non-LTE for CO_2.

Figure 4.19 shows the percentage errors in T_{Ray} when LTE is assumed but in fact the CO mole fraction is lower by 1,2 and 5%. We see that T_{Ray} is now over-estimated with a maximum error of approximately 0.07%, 0.14% and 0.35% for CO concentrations 1%, 2% and 5% below LTE respectively.

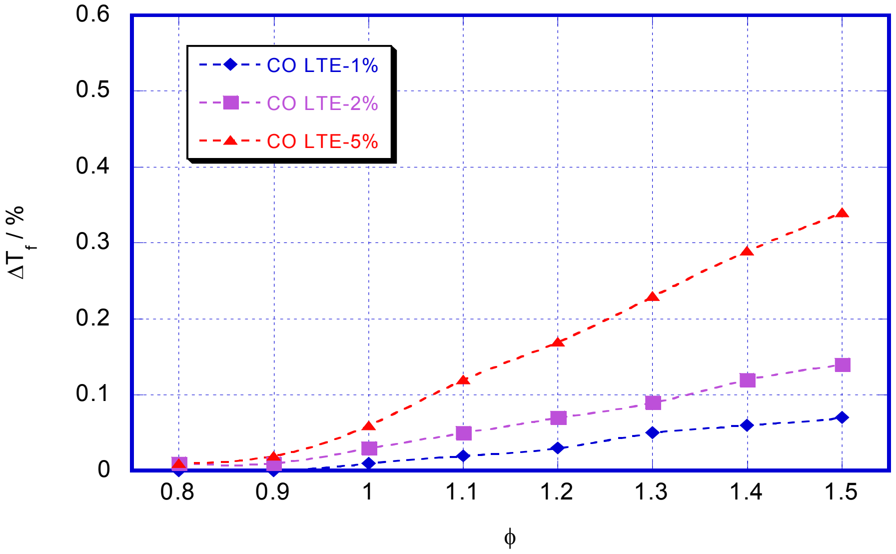

Figure 4.19 Percentage error in T_{Ray} due to non-LTE for CO.

In conclusion, if we assume that LTE for CO and CO_2 are in error by 2%, then:

- T_{Ray} may be in error by -0.2% for non-LTE for CO_2.
- T_{Ray} may be in error by +0.15% for non-LTE for CO.
- Since the two errors have a different sign, we expect the combined error of non-LTE for CO_2 and CO will be small.

4.3.3.3 EFFECT OF THE INLET GAS TEMPERATURE ON THE FLAME TEMPERATURE

The sensitivity of the flame temperature to changes in the inlet gas (fuel/air) temperature (T_0) has been investigated. *Gaseq* [67] software has been used to determine the adiabatic flame temperature of propane/air combustion for various inlet gas temperatures for a wide range of equivalence ratios. Figure 4.20 shows the increase in the adiabatic flame temperature for increases in the inlet gas temperature. T = 273 K is the baseline inlet temperature i.e. ΔT = 0 K. The maximum increase for a given ΔT is seen for weak ($\phi < 1$) mixtures and the minimum is for $\phi = 1$ which coincides with the maximum heat capacity of the combustion products.

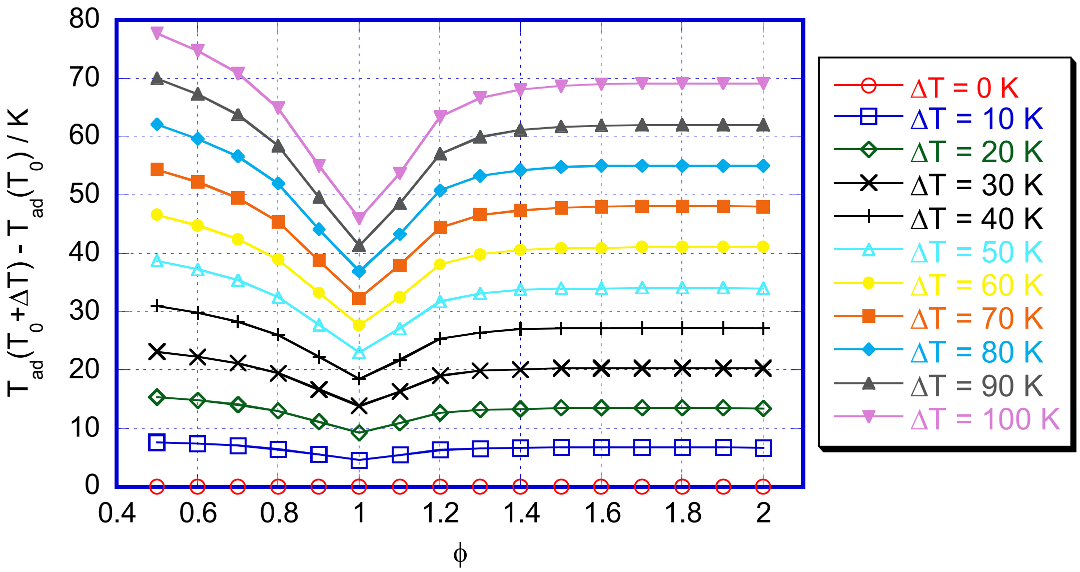

Figure 4.20 Increase in adiabatic flame temperature versus equivalence ratio (ϕ) for propane/air combustion for various inlet gas temperatures above T = 273K. i.e. ΔT = 20 K corresponds to an inlet temperature of 293 K and so on.

Measurements of the flame temperature for propane/air combustion for an equivalence ratio of $\phi = 1$ and an airflow rate of 60 SLPM are shown in figure 4.21. With details of the temperature determination process given later, this figure is presented to demonstrate the real correlation between the inlet gas and cooling water temperature and the flame temperature only. Two sets of measurements are shown, taken three months part, one during late summer and one during winter. The key difference between the two sets of measurements was the burner inlet gas and cooling water temperatures. The set taken in late summer corresponded to inlet temperatures of approximately 293 K (19.9 °C) and the set taken in winter corresponded to 287.5 K (14.4 °C). This demonstrates a correlation of the order of:

$$\frac{\mathrm{d}T_{FLAME}}{\mathrm{d}T_{AIR/WATER}} = \frac{2\mathrm{K}}{1\mathrm{K}\ \text{(inlet air)}} \tag{4.68}$$

This correlation is larger than that predicted from the adiabatic model shown in Figure 4.18, the difference can be understood since the model only assumes a different inlet gas temperature where as the experiments contain a contribution from the difference in the cooled burner disk temperature.

Ideally, a closed-circuit chilled water system would improve flame temperature reproducibility. This was not available for this work, however, a large water reservoir containing 100 *l* of water placed inside the laboratory was used to precondition the mains water and site compressed air. This is described in more detail in chapter 2.

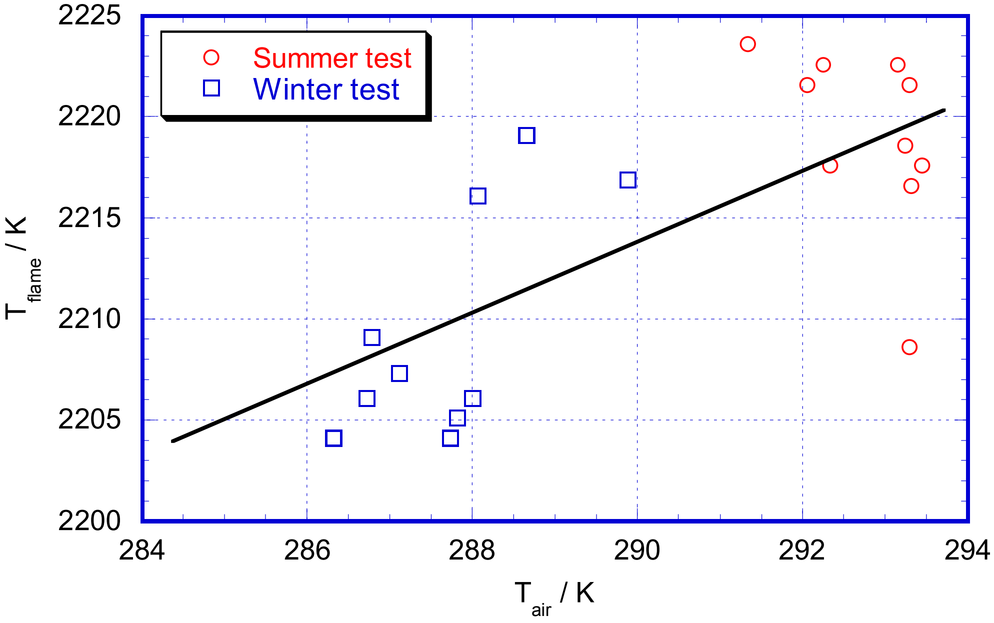

Figure 4.21 Flame temperature (propane/air, $\phi = 1$, 60 SLPM airflow) versus inlet gas/cooling water temperature.

4.3.3.4 PRESSURE DEPENDENCE OF THE FLAME TEMPERATURE

The Rayleigh thermometry technique used in this work utilises the ratio of signals measured first in air and secondly in the flame and assumes that the pressure remains the same. Even if this condition is always met, the flame temperature will have an intrinsic sensitivity to the ambient pressure. Using *Gaseq* [67] equilibrium software, it was possible to model the change in the adiabatic flame temperature for propane/air combustion as a result of changes in the ambient pressure (Figure 4.22).

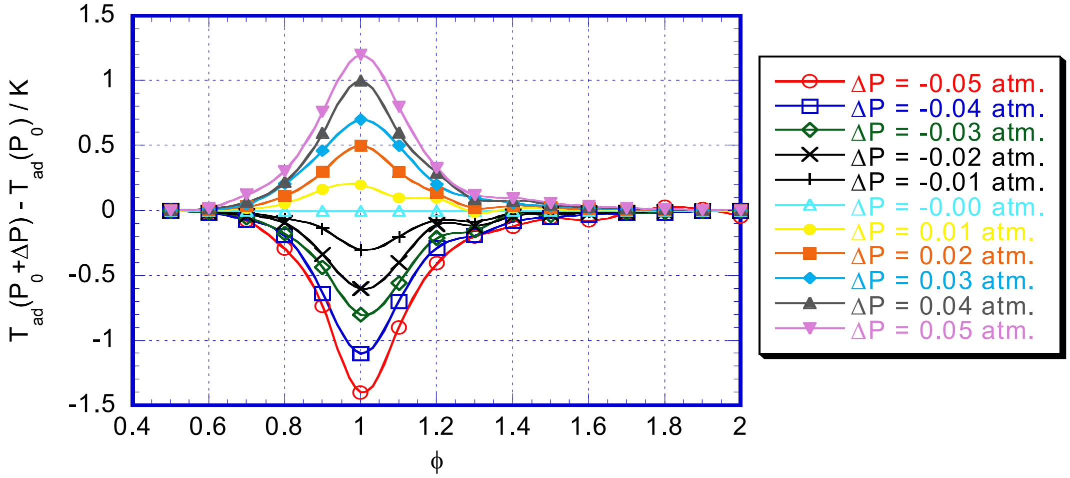

Figure 4.22 Change in adiabatic flame temperature versus equivalence ratio (ϕ) for propane/air combustion for various ambient pressures. $\varDelta P = 0$ corresponds to P = 1 atm.

Using this ideal model, we see that the ambient pressure has little effect on the adiabatic flame temperature. However, experiments reveal slight pressure dependence. Figure 4.23 shows the measured flame temperatures for propane/air combustion for an equivalence ratio of $\phi = 1$, for an airflow rate of 60 SLPM.

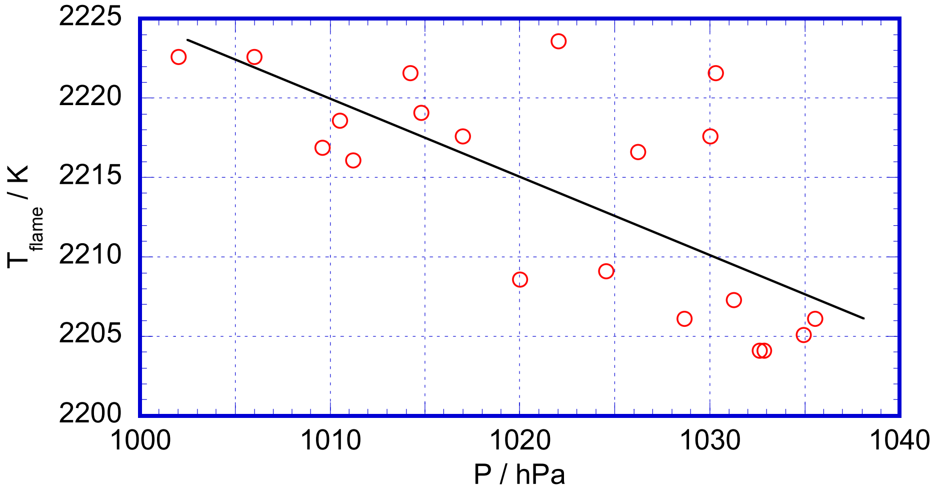

Figure 4.23 Flame temperature (propane/air, $\phi = 1$, 60 SLPM airflow) versus measured pressure.

This amounts to a correlation of the order of:

$$\frac{dT_{FLAME}}{dP} = -0.5\,\mathrm{K/hPa} \tag{4.69}$$

This can be understood by an increase in the flame speed with pressure [84], resulting in the flame being stabilised slightly closer to the cooled burner surface, with an increase in the heat loss from the flame and subsequent reduction in the flame temperature. This effect is small and for the typical variability in ambient pressure, amounts to changes of less than 0.5% in temperature.

4.3.3.5 EFFECT OF INLET GAS WATER CONTENT ON THE FLAME TEMPERATURE

Gaseq [67] software has been used to determine the adiabatic flame temperature of propane/air combustion for various water concentrations for a wide range of equivalence ratios. Air at ambient temperature can hold up to 3% water by volume. Figure 4.24 shows the percentage difference in the adiabatic flame temperature for various water concentrations up to 3% with the largest changes in T_{ad} (up to 5%) seen for rich mixtures, with $\phi>1$.

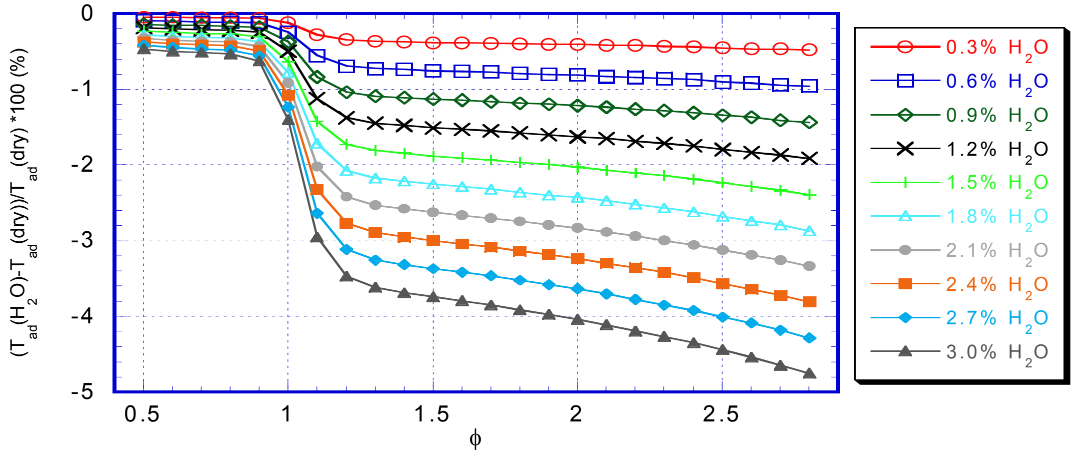

Figure 4.24 Percentage change in the adiabatic flame temperature versus equivalence ratio (ϕ) for propane/air combustion for inlet gases containing various amounts of water.

It is clear from this figure that any water content or variability in the water content of the inlet gases will *drastically* affect the flame temperature. In terms of the actual Rayleigh scattering measurements, the scattering cross-section of the combustion species will also change, resulting in errors if the inlet gases were assumed dry. Figure 4.25 shows the change in the Rayleigh scattering cross-section of the combustion species for various inlet gas water concentrations. Errors of up to 1.5% are possible.

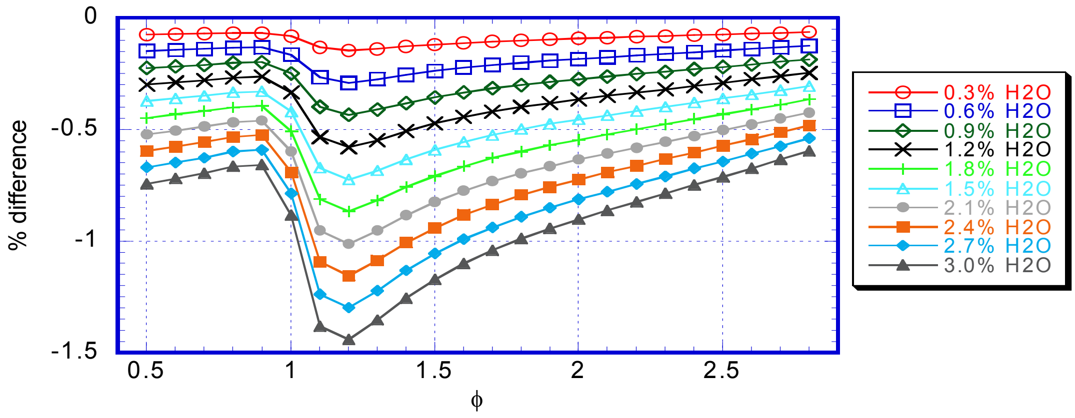

Figure 4.25 Percentage difference in the Rayleigh scattering cross section for propane/air combustion species vs ϕ for various % H_2O in air.

In light of this drastic variability of both the flame temperature and scattering cross-section with inlet gas water content, steps were taken to dry the air and high purity propane was used. NPL site services later revealed that the water content of the site compressed air system was less than 0.1%. With this figure, there is negligible change in the adiabatic flame temperature and the scattering cross-section.

4.3.3.6 EFFECT OF FUEL PURITY ON THE FLAME TEMPERATURE

In order to determine if impurities in propane change the flame temperature, tests were carried out with industrial grade propane (95% propane, 5% other similar weight hydrocarbons) and research grade propane (99.5% propane). Figure 4.26 shows the results. No changes were observed indicating that the flame is not sensitive to small amounts of fuel impurities.

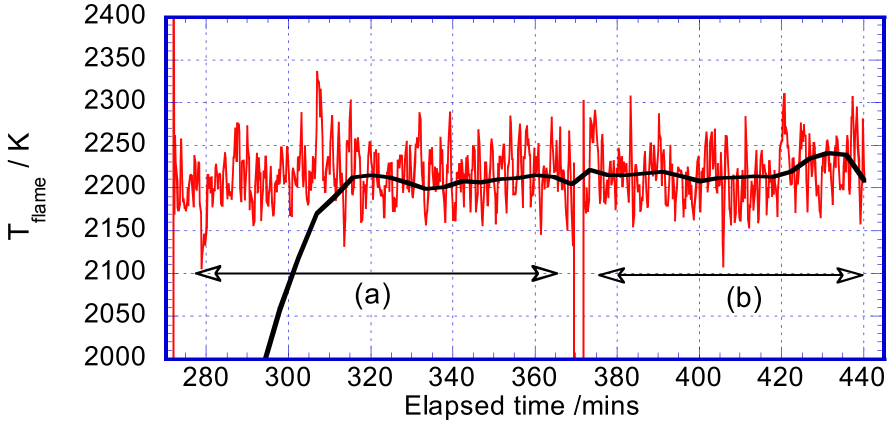

Figure 4.26 Comparison of the flame temperature for propane/air, $\phi = 1$, 60 SLPM. Two propane sources. (a) Technical grade (99.5% propane) and (b) Industrial grade (95% propane). The black line is the *running average* of the *raw* data.

4.3.4 RAYLEIGH THERMOMETRY ON THE MCKENNA BURNER FLAME

Two courses of measurements A an B were made, separated by a period of 3 months to determine the performance of the burner, its long-term stability and reproducibility. Each course comprised of a complete measurement cycle made on 10 different days. For each day:

- The Rayleigh signals were first obtained for dry air of known temperature flowing through the burner
- The burner flame was then ignited, the air flow rate set to 30 SLPM and the equivalence ratio for the propane/air mixture adjusted to $\phi = 0.8$ using the flow meters.
- The Rayleigh scattering signal for the post flame region was then measured.
- The procedure was repeated for air-flow rates of 40, 50 and 60 SLPM and for all values of ϕ up to 1.5 in increments of 0.1.

Figure 4.27 shows the measured flame temperature for propane/air combustion as a function of equivalence ratio for various airflow rates for course A. The calculated adiabatic flame temperature is also shown. An iterative process has been employed in which the measured flame temperature is first determined by finding the differential Rayleigh scattering cross-section for equilibrium species concentrations at T_{ad} using *Gaseq* [67]. This initial value $T_F(0)$ is then fed back into *Gaseq* to determine the species concentrations at this temperature and constant pressure. With the new species concentrations, the cross-section and flame temperature are re-calculated to obtain $T_F(1)$. The method is repeated until the flame temperature converges. This procedure is performed for all ϕ and flow rates. Convergence is fast and only 3 iterations were required to bring the values to within 2 K of the previous iteration.

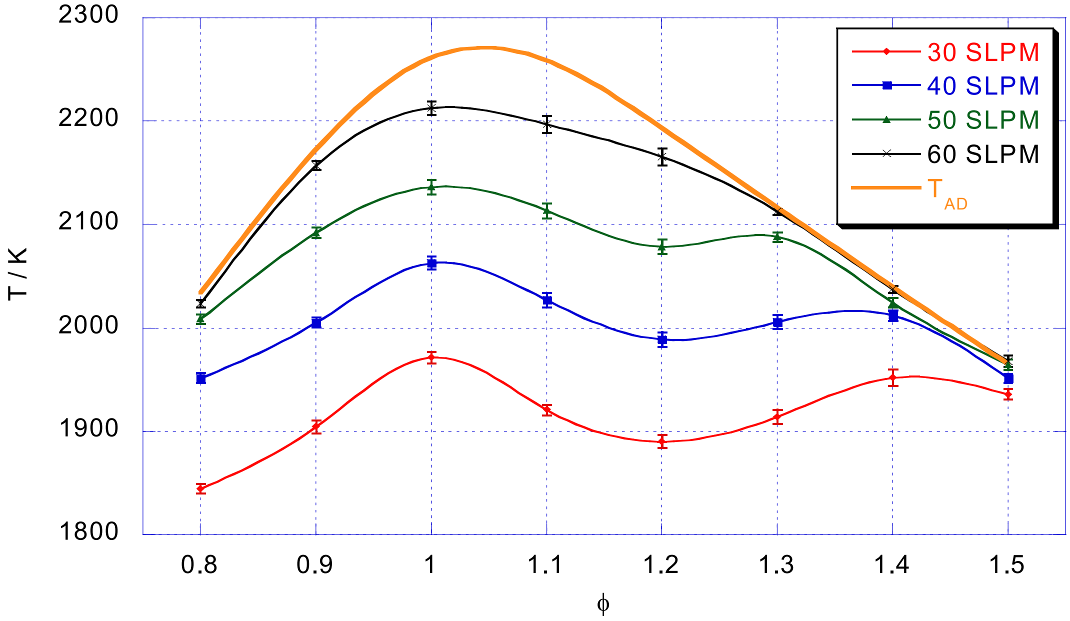

Figure 4.27 The measured flame temperature for propane/air combustion vs equivalence ratio for various airflow rates. The Adiabatic flame temperature is also shown (T_{AD}).

Interpreting this data shows:

- The maximum flame temperature is obtained for an equivalence ratio (ϕ) close to unity. The enthalpy of the reactant mixture is greatest at this equivalence ratio so we expect the resultant temperature to have its maximum here also.
- The calculated adiabatic flame temperature (T_{ad}) forms an envelope above the measured temperatures. This is expected since the adiabatic temperature is the maximum that can be obtained if there are no heat losses to the burner plate and clearly heat losses decrease as the airflow rate is increased and the flame stabilises slightly higher above the cooled burner plate.
- The non-linear change in flame temperature with equivalence ratio can be explained by the complex interaction between the flame speed, the subsequent flame height above the cooled burner disk and the heat capacity of the combustion products.
- The flame temperature is close to the adiabatic value for high airflow rates and equivalence ratios in the weak and rich mixture regions. This can be explained by the fact that the flame speed is lower for these parameters and subsequently the flame stabilises higher above the burned disk with an associated reduction in heat loss from the flame.
- The error bars indicate the standard deviation of identical measurements made on ten different days.

Figure 4.28 shows the result of applying the iterative procedure described above. The largest corrections in the flame temperature are for low airflow rates where the flame temperatures are farthest from the adiabatic case.

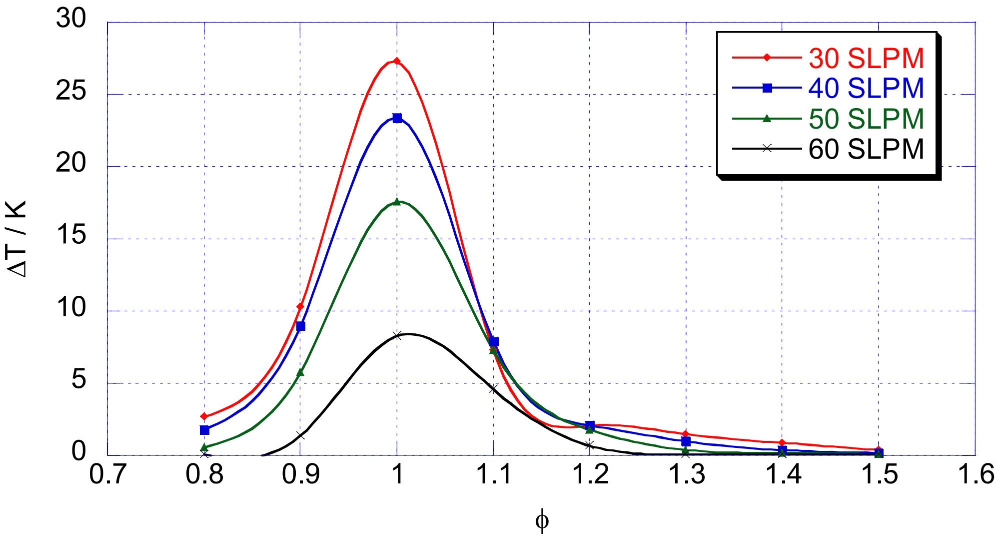

Figure 4.28 Absolute change in the flame temperature after iterative process.

Figure 4.29 shows the standard deviation of the flame temperature for the 10 measurement sets of course A. The flame temperature is reproducible to better than 9 K for all ϕ corresponding to 0.4% of temperature. The systematic difference between the means of course A an B taken 3 months apart was less than 0.4% of temperature. This difference is attributed to the fact that the inlet air and cooling water were lower by 5 K for the second set of measurements due to seasonal variations (see §4.3.3.3).

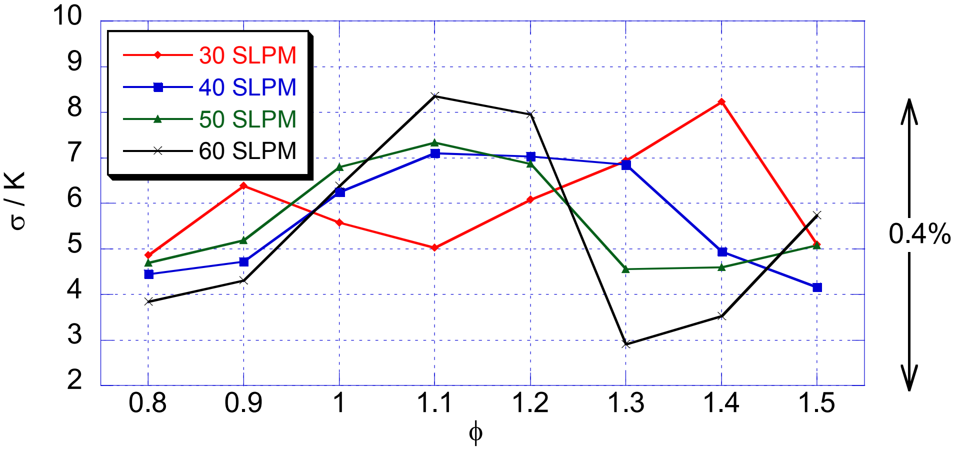

Figure 4.29 The standard deviation of the post flame temperature versus equivalence ratio, for measurement course A, for various airflow rates (SLPM) (propane/air combustion).

A third course of 10 days measurements was made for $\phi = 1$ and 60 SLPM airflow (Figure 4.30) with the mean post flame temperature being 2214 ± 4.5 K. This amounts to a standard deviation of 0.2% of temperature with no evidence of drift at all. This result demonstrates the suitability of the McKenna burner as a combustion temperature standard.

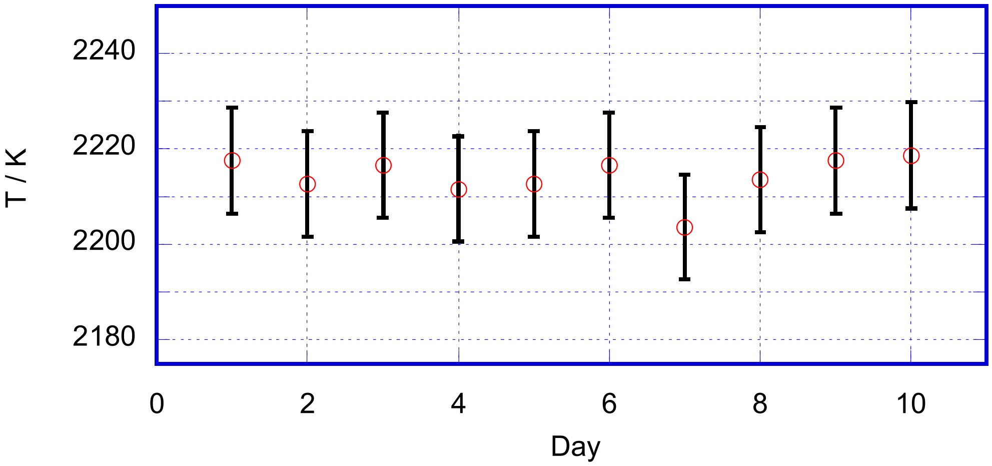

Figure 4.30 Mean post flame temperature measured over a 10 day period for $\phi = 1$ and an air flow rate of 60 SLPM for propane/air combustion. Error bars indicate ± 0.5 % of temperature.

A typical temperature measurement is shown in Figure 4.31. The temperature stabilises one hour after ignition with a standard deviation of 0.25%.

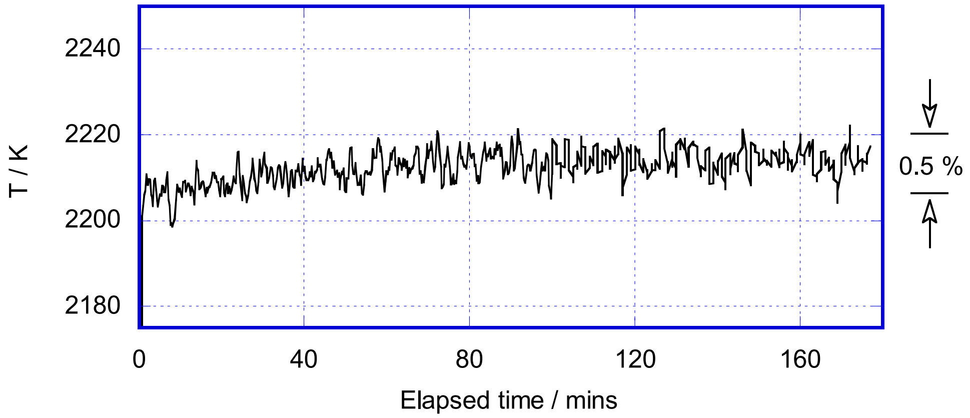

Figure 4.31 Typical flame temperature measurement for $\phi = 1$, 60 SLPM, propane/air combustion. The temperature stabilises after 1 hour.

Measurements of the radial and vertical flame temperature profiles (Figure 4.32) were obtained by moving the burner relative to the laser beam. For a region 2 cm above the burner, the variation is less than 0.4% over the central 15 mm, increasing to 1% over the central 30 mm. The temperature variation vertically is 2% over the region from Δy = -10 mm (10 mm above burner) to Δy = +20 mm (40 mm above burner), although the variation over the central 10 mm is still less than 0.6%.

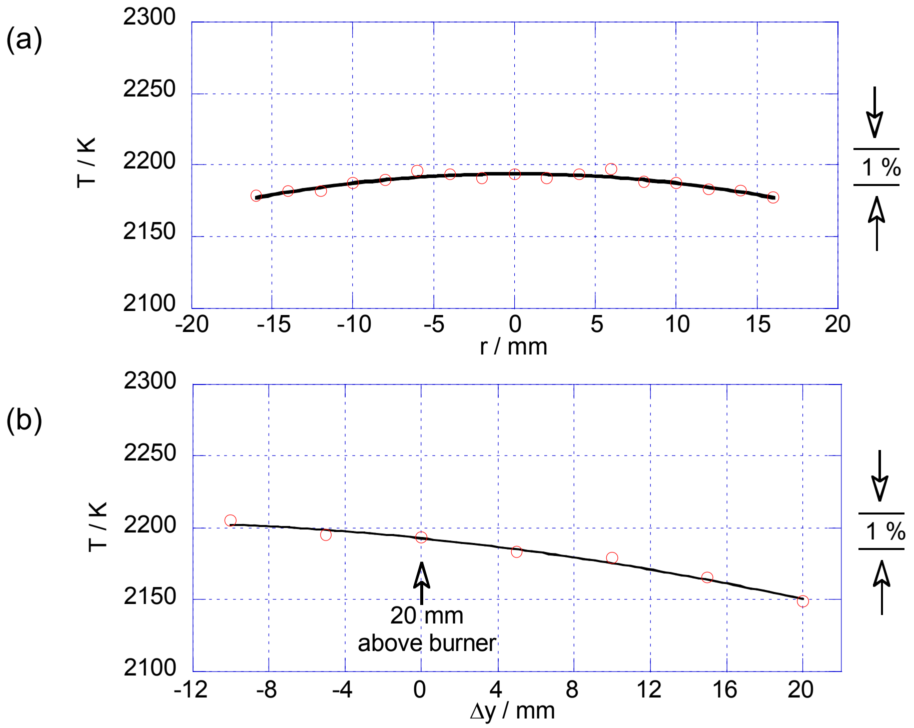

Figure 4.32 (a) Radial temperature profile 2 cm above the burner and (b) Vertical temperature profile above burner centre, for $\phi = 1$ and airflow rate of 60 SLPM for propane/air combustion.

Provided the measurement volume is within 5 mm in any direction of the zone 2 cm above the centre of the burner, we can conclude that the temperature remains constant to within 0.5%. This is encouraging since it shows that observing precisely the same region above the flame is not critical in measuring the same temperature. This could be of great benefit when calibrating other optical diagnostic techniques that may not necessarily have the same observation volume as the Rayleigh thermometry system.

The temperature above the propane/air flame has been fully evaluated, and a summary follows:

- A constant temperature is attained within one hour of igniting the burner and is shown to remain constant subsequently.
- Measurements made over a 10 day period show a standard deviation of 0.2 % of temperature for the same flow and equivalence ratio with no drift evident.
- The temperature profile above the burner shows a radial variation of 0.4% over the central 15 mm of the burner at a height of 20 mm above the burner plate and a vertical variation of 0.6% over a 5 mm region above and below the central 20 mm position.
- The temperature 20 mm above the centre of the burner plate is effectively constant in a volume given by a cylinder of diameter 30 mm and height 10 mm. The deviation by measuring at random in this volume is less than 0.5%. This makes the burner amenable to the calibration of a variety of different optical diagnostic techniques with different measurement volumes.

By accurate adjustment of both the air flow rate and the equivalence ratio it is possible to produce a variety of stable reproducible temperatures and species concentrations. For propane combustion in air, fixed temperatures ranging from 1850 K to 2210 K were possible.

4.4 SUMMARY

The utility of the McKenna premixed flat flame burner as a flame temperature standard has been demonstrated. Using high accuracy Rayleigh scattering thermometry, and applying corrections for the temperature dependence of the scattering cross-section, it has been possible to determine the temperature in the post flame region above a pre-mixed propane/air flame to better than 1%.

An uncertainty budget for the Rayleigh scattering measurements is presented in Table 4.4 showing that the estimated total uncertainty in the temperature measurements is approximately 0.5% at one standard deviation.

In an effort to further validate the Rayleigh thermometry technique and to improve confidence in its absolute accuracy, a second unrelated high accuracy thermometry technique has be developed. The photo-acoustic thermometry technique, identified earlier in the survey was chosen for this purpose. Chapter 5 describes this work and compares the two techniques.

Source	**Size (1σ)**	**Type**
Molar refractivity data	0.1%	B
Flow-meter uncertainty	0.3%	B
Chemical equilibrium assumption	0.2%	B
Electromagnetic interference	0.2%	A/B
Background scattered signal	0.1%	A
Linearity of the detectors and digitiser	0.1%	A
Inlet air/water temperature	0.2%	A/B
Atmospheric pressure	0.1%	A/B
Gas purity	0.0%	B
Combined uncertainty (in quadrature)	**0.5%**	**(A/B)**
Flame temperature reproducibility (measured)	**0.4%**	**Type**

Table 4.4 Uncertainty budget for the Rayleigh scattering thermometry measurements.

THE DEVELOPMENT AND EVALUATION OF HIGH ACCURACY PHOTO-ACOUSTIC THERMOMETRY

5.1 INTRODUCTION

Photo-acoustic thermometry, in which measurements of the speed of sound in a gas are related to its temperature, was originally identified as a candidate high accuracy thermometry technique suitable for calibration of the *McKenna burner* flame standard (see §1.4).

Such a system has been developed and temperature measurements have been directly compared with those measured with the Rayleigh scattering thermometry system described in Chapter 4. In this Chapter:

- In §5.2 the relationship between gas temperature and the speed of sound is defined.
- In §5.3 the photo-acoustic beam deflection technique is presented as a method for measuring the speed of sound and hence the temperature of the McKenna burner flame.
- In §5.3.1 the variation in the separation of the two probe beams is modelled for typical radially symmetric flame temperature fields and found to be negligible for measurements in the centre of the flame.
- In §5.4 the cylindrical blast wave model for laser induced sparks is presented and found to fit the experimental data well. This allowed for extrapolation to the small amplitude speed of sound, which was the quantity sensitive to the flame temperature.
- In §5.5 the beam deflection system including data processing software is developed and found to be stable and reproducible. The temperature of the propane/air McKenna burner flame is successfully measured for various equivalence ratios and airflow rates using the photo-acoustic beam deflection technique.
- In §5.6 comparison of the flame temperatures measured by the photo-acoustic and Rayleigh scattering thermometry system has shown good agreement. For low airflow rates, photo-acoustic temperatures are approximately 3.6% higher than the Rayleigh temperatures, however, at high airflow rates the agreement is better than 1% of temperature.
- Further work is needed to determine the source of the discrepancy between the two thermometry techniques at low airflow rates.

5.2 PHOTO-ACOUSTIC THERMOMETRY THEORY

Photo-acoustic gas thermometry involves the measurement of the speed of sound in a gas. By assuming ideal gas behaviour and that the sound wave propagates adiabatically, the temperature can be found [85]:

- The small amplitude speed of sound in a gas, c_0, is determined by its bulk modulus, B, and its density, ρ:

$$c_0 = \sqrt{\frac{B}{\rho}} \tag{5.1}$$

- When sound travels through an ideal gas, the rapid compressions and expansions associated with the longitudinal wave can reasonably be expected to be adiabatic [86] and therefore the pressure and volume obey the relationship:

$$P = \frac{C}{V^{\gamma}} \tag{5.2}$$

  where P is the pressure, γ is the ratio of specific heats (C_P/C_V), V is the volume and C is a constant.
- The bulk modulus B is given by:

$$B = -V\frac{\mathrm{d}P}{\mathrm{d}V} \tag{5.3}$$

  and the density, ρ, is given by:

$$\rho = \frac{n\overline{m}}{V} \tag{5.4}$$

  where n is the number of particles and $\overline{m}$ is the mean molecular mass of the particles.
- By substituting the differential with respect to volume of Equation 5.2 into Equation 5.3 and substituting Equations 5.3 and 5.4 into Equation 5.1 we can write:

$$c_0 = \sqrt{\frac{\gamma PV}{n\overline{m}}} \tag{5.5}$$

- Making use of the ideal gas law:

$$PV = nRT \tag{5.6}$$

  we can write:

$$c_0 = \sqrt{\frac{\gamma RT}{\overline{m}}} \tag{5.7}$$

  where T is the thermodynamic temperature of the gas and R is the universal gas constant.

Equation 5.7 shows the temperature-dependence of the speed of sound and it is this result that we use in photo-acoustic thermometry.

It is convenient to define the acoustic constant, C_a as:

$$C_a = \frac{\gamma R}{\overline{m}} \tag{5.8}$$

We may then write the temperature as:

$$T = \frac{c_0^2}{C_a} \tag{5.9}$$

We see from Equation 5.9 that in order to determine the flame temperature, the acoustic constant, C_a needs to be known to sufficient accuracy. Considering the propane/air flame used exclusively in this work we can calculate C_a for a given equivalence ratio (ϕ) by using the chemical equilibrium software *Gaseq* [67]. Figure 5.1 shows the acoustic constant versus temperature for various equivalence ratios for propane/air combustion at atmospheric pressure.

Points to note are:

- C_a at a given ϕ only changes by approximately 1% over the temperature range 1700 K - 2200 K.
- For rich mixtures ($\phi > 1$), C_a changes by 10% as ϕ increases from 1 to 1.5.
- For excess O_2 ($\phi < 1$), C_a does not change significantly with ϕ.

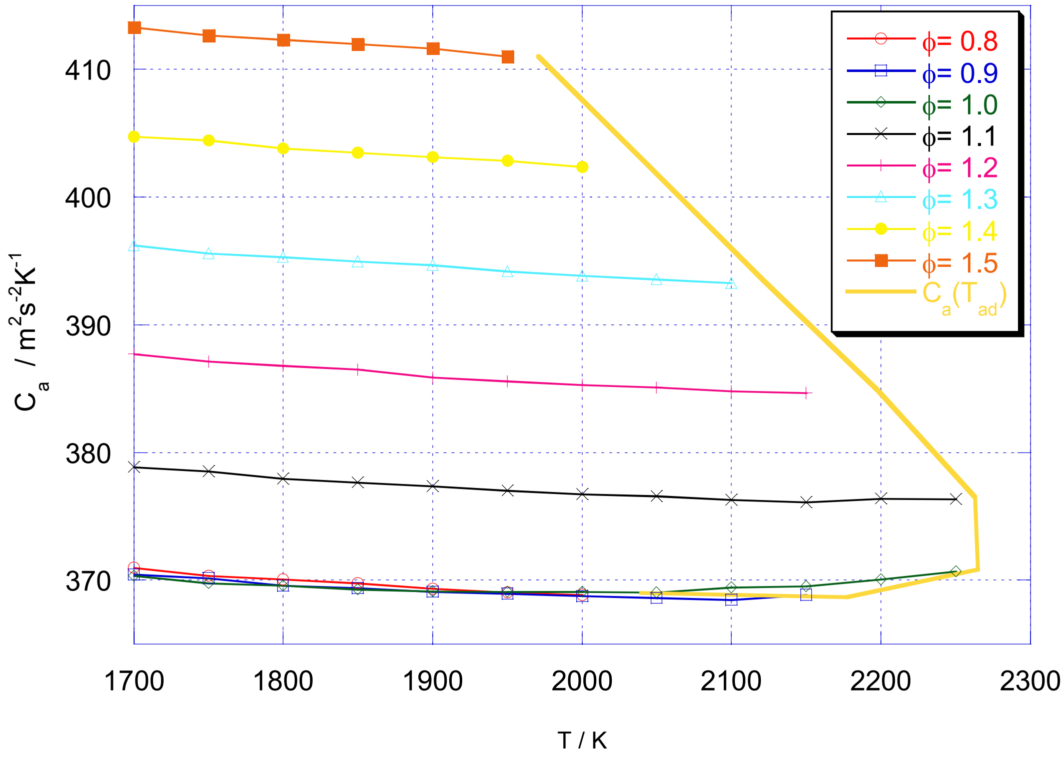

Figure 5.1 Calculation of the acoustic constant, C_a versus temperature for propane/air combustion, various equivalence ratios (ϕ).

Re-arranging Equation 5.9, we see that:

$$c_0 = \sqrt{C_a T} \tag{5.10}$$

Figure 5.2 shows the speed of sound, c_0, versus the flame temperature for propane/air combustion. Over the limited temperature range shown, the curve looks linear, and it is not clear that the speed of sound follows the square root of the temperature although it does.

Points to note are:

- The speed of sound, c_0 is a monotonic increasing function of temperature for a given equivalence ratio (ϕ).
- Considering Equation 5.10, the strong variation in the acoustic constant for $\phi > 1$ produces a similar variation in the inferred flame temperature.
- For $\phi < 1$, the speed of sound is constant for a given flame temperature.

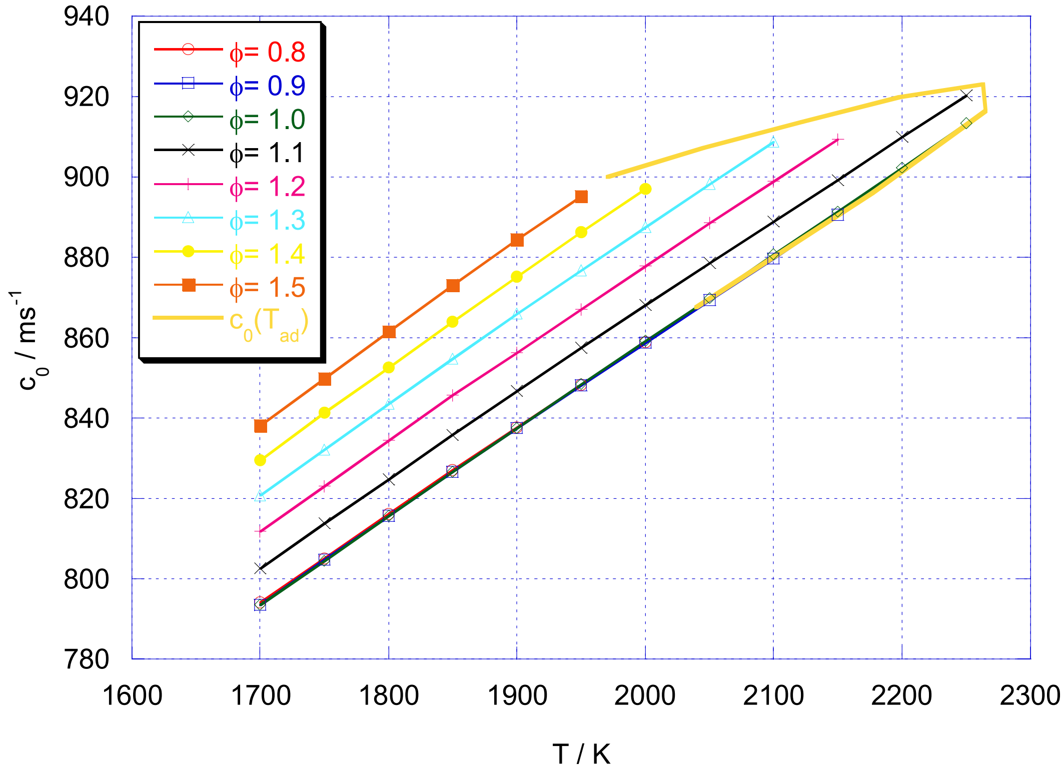

Figure 5.2 The speed of sound (c_0) versus temperature for propane/air combustion, various equivalence ratios (ϕ).

To summarise, provided the equivalence ratio (ϕ) is accurately measured, it is possible to determine the flame temperature un-ambiguously from a measurement of the speed of sound (c_0) by using the chemical equilibrium software *Gaseq* [67].

5.3 PHOTO-ACOUSTIC BEAM DEFLECTION TECHNIQUE

5.3.1 INTRODUCTION

The photo-acoustic beam deflection technique [87-90], first demonstrated in 1982 [87], is a non-contact method for measuring the local speed of sound in a transparent or semi-transparent gas. A description of the technique (shown in Figure 5.3) follows:

- Two parallel low-power (HeNe) ‘probe’ laser beams a fixed distance apart pass through the flame region of interest.
- After passing through the flame, half of each probe beam is obscured by a knife edge with the remaining part incident on one of two high-speed silicon detectors.
- A high-power pulse laser produces a plasma spark at a fixed distance from the probe beams generating a sound wave.
- As the sound wave passes each of the probe beams, the change in refractive index associated with the passage of the sound wave causes the two probe beams to deflect by a small amount.
- The deflected probe beams are then either obscured more or less by the knife edges and the detector signals change.
- If the probe beam separation (Δx) is known to a high accuracy, the speed of sound (c_0) can be calculated by the simple formula:

$$c_0 = \frac{\Delta x}{\tau} \tag{5.11}$$

where τ is the time taken for the sound wave to pass the two probe beams.

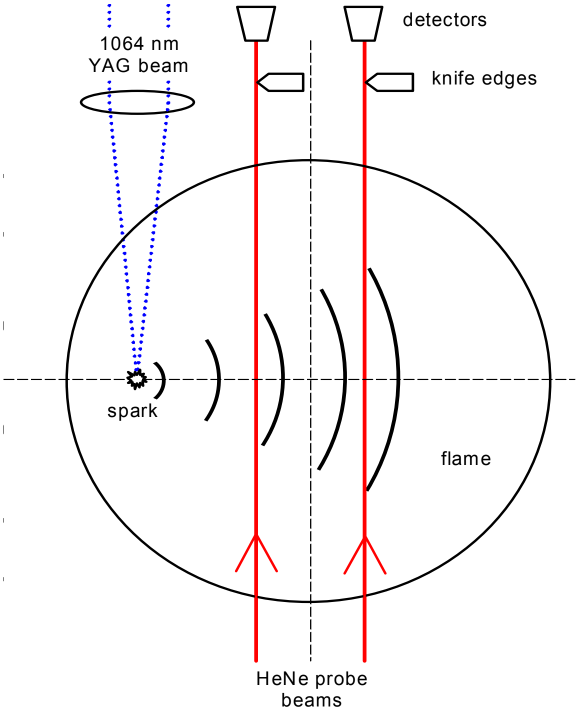

Figure 5.3 Schematic diagram of the photo-acoustic beam deflection technique.

Typical photo-acoustic beam deflection signals (for air at 20 °C) are shown in Figure 5.4. The speed of sound measured by this method is the average over the region bounded by the two probe beams and the sound wavefront extent (typically 4 mm by 10 mm). The full experimental details are described in Section 5.4.2.

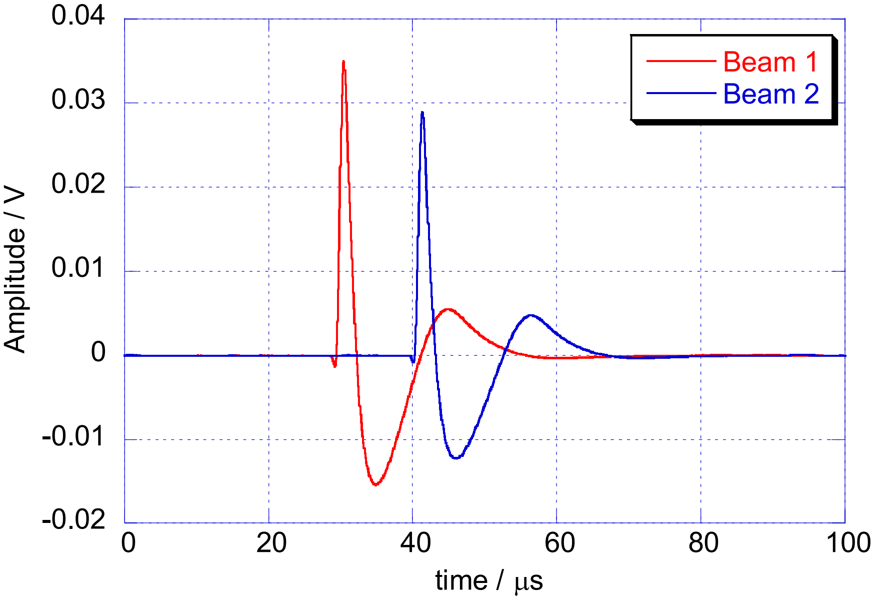

Figure 5.4 Typical photo-acoustic beam deflection signals for air at 20 °C.

5.3.2 VARIATION OF THE PROBE BEAM SEPARATION IN THE FLAME

As the probe beams pass though the flame, they experience small deflections due to changes in the refractive index of the gas (the refractive index is a function of the gas temperature and composition [70]). Since the photo-acoustic beam deflection technique depends critically on the separation of the two parallel probe beams, it is important to investigate the changes in this separation. A computer model written in *Visual Basic* [91] has been developed to investigate this further. The geometry used in this model is shown in figure 5.5.

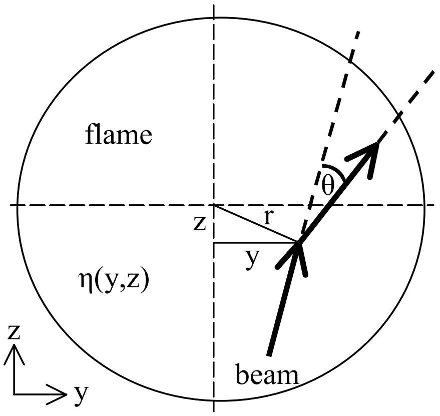

Figure 5.5 Beam deflection model geometry.

For small angles, the change in the beam deflection angle, θ, due to a refractive index gradient perpendicular to the beam direction is given by [92]:

$$\left.\frac{\partial\theta}{\partial z}\right|_{y} = \frac{1}{\eta}\left.\frac{\partial\eta}{\partial y}\right|_{z} \tag{5.12}$$

By making use of this equation it is possible to predict the beam path inside the flame and hence the distance between the two probe beams along the measurement axis.

The flame temperature at a radial position r is modelled by the function:

$$T(r) = T_0 - (T_0 - T_1)\left(\frac{r}{r_1}\right)^{\alpha} \tag{5.13}$$

where T_0 is the temperature at the centre of the flame and T_1 the temperature at r_1, the outer edge of the flame. α is an adjustable parameter equal to two, four or six that allows us to change the decay of the temperature field with distance r.

The refractive index, modelled on a single component ideal gas, is given by:

$$\eta(T) = 1 + \frac{300}{T}(\eta_0 - 1) \tag{5.14}$$

where η_0 is the refractive index at 300 K. From Equation 5.12, we need to find $\left.\frac{\partial \eta}{\partial y}\right|_z$. Noting that η is only a function of r, this can be done using the 'chain-rule':

$$\left.\frac{\partial \eta}{\partial y}\right|_z = \frac{\mathrm{d}\eta}{\mathrm{d}r}\left.\frac{\partial r}{\partial y}\right|_z = \frac{\mathrm{d}\eta}{\mathrm{d}r}\frac{y}{r} \tag{5.15}$$

and $\frac{\mathrm{d}\eta}{\mathrm{d}r}$ is given by making use of Equations 5.13 and 5.14 and applying the 'chain-rule' again:

$$\frac{\mathrm{d}\eta}{\mathrm{d}r} = \frac{\mathrm{d}\eta}{\mathrm{d}T}\frac{\mathrm{d}T}{\mathrm{d}r} = \frac{-300(\eta_0 - 1)}{T^2}(T_0 - T_1)\frac{\alpha}{r}\left(\frac{r}{r_1}\right)^{\alpha} \tag{5.16}$$

Combining Equations 5.12 and 5.16 gives us the final result:

$$\left.\frac{\mathrm{d}\theta}{\mathrm{d}z}\right|_y = \frac{1}{\eta}\left[\frac{300(\eta_0 - 1)}{T^2}(T_0 - T_1)\frac{\alpha}{r}\left(\frac{r}{r_1}\right)^{\alpha}\right]\frac{y}{r} \tag{5.17}$$

The computer model performs the integration of Equation 5.17 for probe beams entering the flame along the z axis (at $z = -r_1$) for all positions along the y axis and provides two graphs of the output parameters:

- The total displacement of a single probe beam when it crosses the y axis at $z = 0$ (the measurement region).
- The fractional change in the separation of two probe beams at the same location.

Adjustable parameters in the model include:

- T_0, T_1 and r_1.
- The refractive index of the gas at 300 K.
- The parameter α, which determines the shape of the temperature profile (see Equation 5.13).
- The number of discrete integration steps.

Table 5.1 shows the value of the parameters that were kept fixed in the model and Table 5.2 shows the parameters that were varied including a reference to the corresponding figure.

Parameter	Description	Value
T_1	Temperature outside the flame	300 K
r_1	Distance to flame edge	40 mm
η_0	Refractive index at 300 K	1.0003
Δx	Probe beam separation	4 mm
z_num	The number of integration steps	2000

Table 5.1 Fixed parameters used in the probe beam separation computer program.

Graph number	T_0 / K [maximum flame temperature]	α [temperature decay parameter]
5.6 (a)	1700	2
5.6 (b)	1700	6
5.6 (c)	2200	2
5.6 (d)	2200	6

Table 5.2 Variable parameters used in the probe beam separation program.

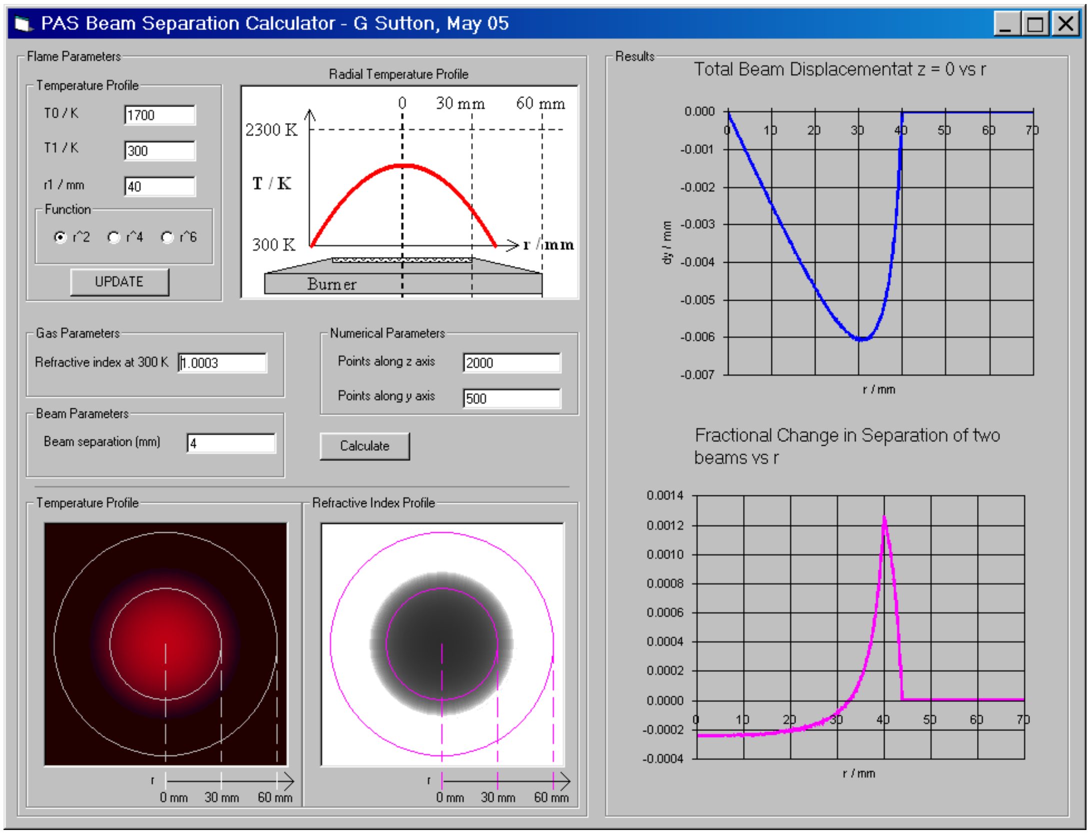

T0 / K 1700

T1 / K 300

r1 / mm 40

● r^2 ○ r^4 ○ r^6

Refractive index at 300 K 1.0003

Points along z axis 2000

Points along y axis 500

Beam separation (mm) 4

Figure 5.6(a) Beam displacement program: results for the parameters in Table 5.1 and 5.2 (a).

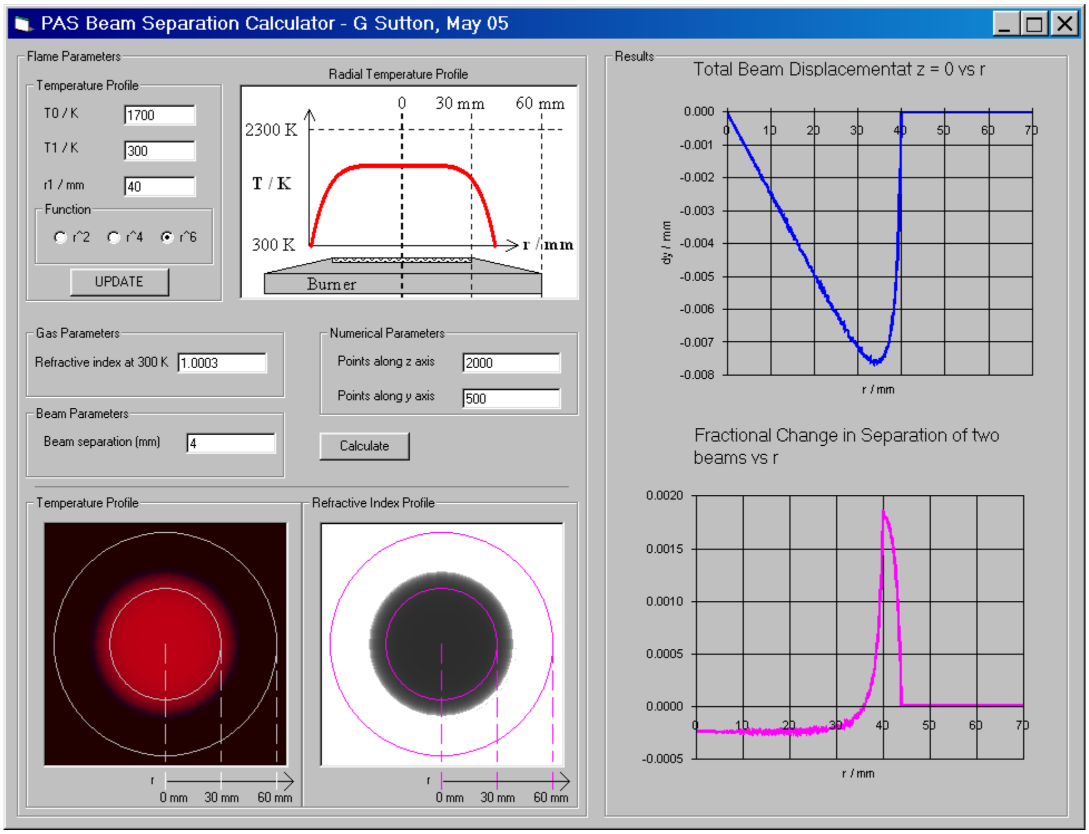
PAS Beam Separation Calculator - G Sutton, May 05

T0 / K 1700

T1 / K 300

r1 / mm 40

Function ○ r^2 ○ r^4 ● r^6

Refractive index at 300 K 1.0003

Points along z axis 2000

Points along y axis 500

Beam separation (mm) 4

Figure 5.6(b) Beam displacement program: results for the parameters in Table 5.1 and 5.2 (b).

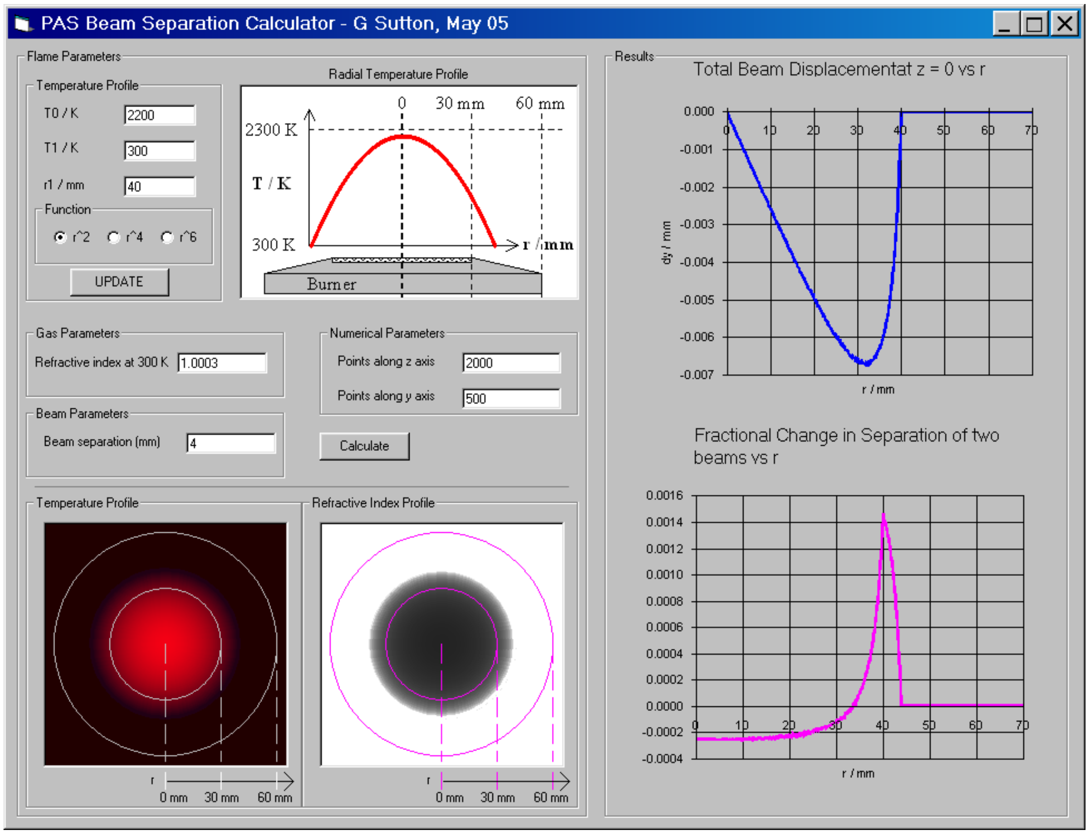
PAS Beam Separation Calculator - G Sutton, May 05

T0 / K 2200

T1 / K 300

r1 / mm 40

Function ● r^2 ○ r^4 ○ r^6

Refractive index at 300 K 1.0003

Points along z axis 2000

Points along y axis 500

Beam separation (mm) 4

Figure 5.6(c) Beam displacement program: results for the parameters in Table 5.1 and 5.2 (c).

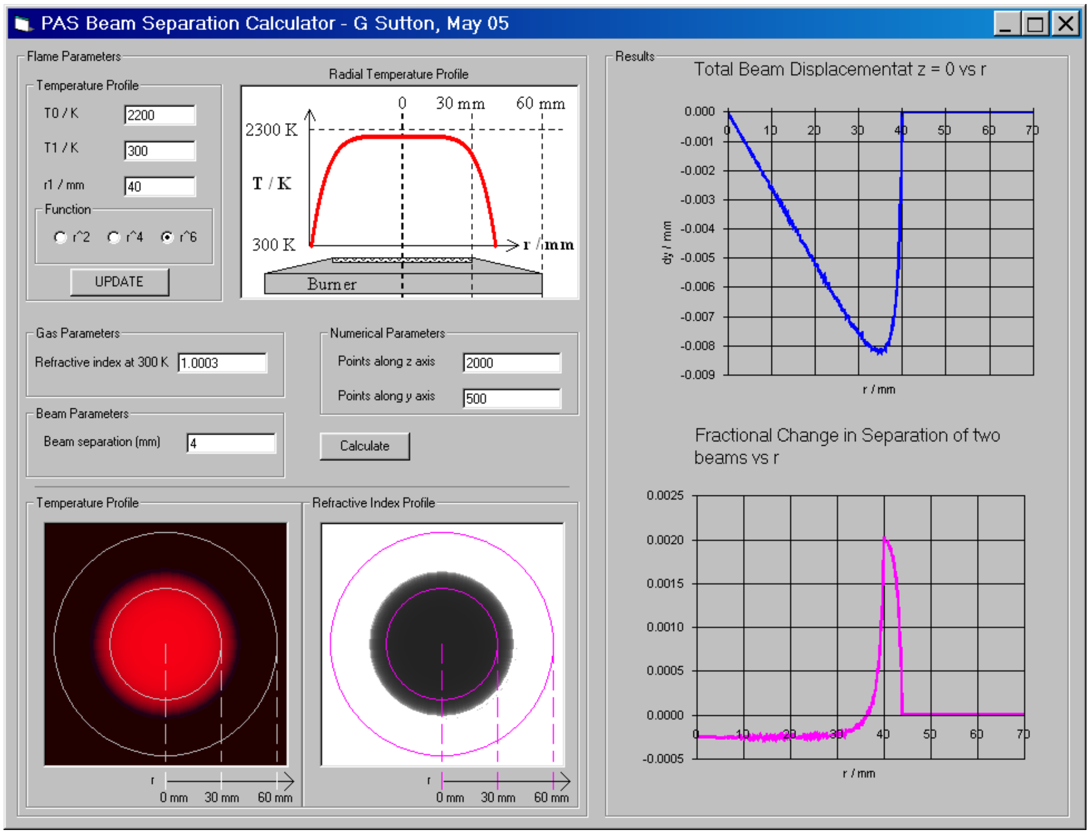

PAS Beam Separation Calculator - G Sutton, May 05

Flame Parameters

Temperature Profile

T0 / K 2200

T1 / K 300

r1 / mm 40

Function ○ r^2 ○ r^4 ● r^6

Gas Parameters

Refractive index at 300 K 1.0003

Numerical Parameters

Points along z axis 2000

Points along y axis 500

Beam Parameters

Beam separation (mm) 4

Figure 5.6(d) Beam displacement program: results for the parameters in Table 5.1 and 5.2 (d).

In summarising these results:

- The maximum change in the position of a single beam and in the separation of the two beams occurs at the edge of the flame. This is to be expected as the temperature gradient and hence the refractive index gradient (perpendicular to the beam direction) is greatest at this point. At this point, the beam separation can be in error by up to 0.2%.
- The minimum change in the separation of the two probe beams is seen in the centre of the flame, with errors of up to 0.03%.
- Since measurements are made in the centre of the flame, these results indicate that the error due to changes in the separation of two probe beams is negligible.

5.4 CYLINDRICAL BLAST WAVE MODEL

Preliminary beam deflection measurements in air at 20 °C showed a speed of sound, c, that depended on both the laser pulse energy (generating the spark) and the distance between the spark and the two probe beams. This was unexpected. Figure 5.7 shows an example of the measured speed of sound versus the distance between the spark and the probe beams, x, for three laser pulse energy levels.

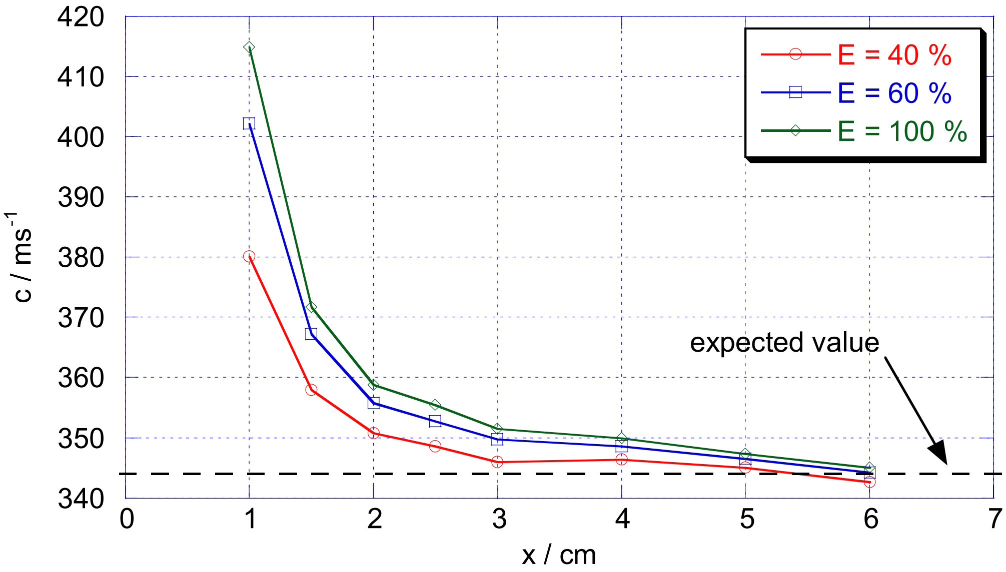

Figure 5.7 The measured speed of sound, c, versus the distance, x, between the spark and probe beams for three laser energy levels, E. (measurements made in dry air at 20 °C).

The small amplitude speed of sound, c_0 in dry air at 20 °C is 343.35 ms^{-1} [93 - 98]. From Figure 5.7, we see that the speed of sound is greater than this value but approaches it as the separation between the spark and the probe beams increases. As the laser energy (and hence the energy in the spark) decreases, the speed of sound also reduces slightly. For a speed of sound greater that the small amplitude value, we conclude that the spark has induced a blast wave that propagates non-linearly away from the source, decaying back to a normal small amplitude sound wave at long distances. Blast waves in gaseous media have been extensively studied [87 – 88, 98 - 100] and allow us to accurately model the speed of sound at a given distance from a spark of given energy and geometry. The small amplitude speed of sound can then be extracted and the gas temperature recovered. The theory is outlined below.

Since the spark source used in our experiments is approximately cylindrical (5 mm long by 1 mm wide) we make use of cylindrical blast wave theory [98]. Our starting point is the dimensionless equation that describes the shock front location, *R*, at a given time, *t*, after the initiation of the spark:

$$\tau = \frac{1}{2}\left[\left(1+4X^2\right)^{0.5} - 1\right] \tag{5.18}$$

where τ is the dimensionless time given by:

$$\tau = \frac{c_0 t}{R_0} \tag{5.19}$$

and X is the dimensionless shock front location given by:

$$X = \frac{R}{R_0} \tag{5.20}$$

R_0 is the characteristic length that depends on E_0, the energy per unit length released by the spark at $t = 0$, the ambient pressure P_0 and the dimensionless parameter B which is equal to 3.94 for cylindrical blast waves:

$$R_0 = \left(\frac{4E_0}{B\gamma P_0} \right)^{\frac{1}{2}} \tag{5.21}$$

where γ is the ratio of specific heats (C_p/C_v). Substituting Equations 5.19 – 5.21 into Equation 5.18 and rearranging leads to our working equation for R in terms of t:

$$R(t) = c_0 t \left(1 + \frac{R_0}{c_0 t} \right)^{\frac{1}{2}} \tag{5.22}$$

The time it takes the shock front to reach a distance R from the spark event can be found by solving for t in Equation 5.22, leading to:

$$t = \frac{R_0}{2c_0} \left[-1 + \sqrt{1 + \frac{4R^2}{R_0^2}} \right] \tag{5.23}$$

The shock front velocity is then given by:

$$c_1 = \frac{\mathrm{d}R}{\mathrm{d}t} = \frac{R_0 c_0}{2R} \sqrt{1 + \frac{4R^2}{R_0^2}} \tag{5.24}$$

Leading to:

$$c_1 = c_0 \sqrt{1 + \frac{R_0^2}{4R^2}} \tag{5.25}$$

The ratio of the shock front velocity to the small amplitude speed of sound is given by:

$$\frac{c_1^2}{c_0^2} = 1 + \frac{R_0^2}{4R^2} \tag{5.26}$$

But c_1 can be written as:

$$c_1 = \frac{\Delta x}{\Delta t} \tag{5.27}$$

with Δx, the separation of the two probe beams and Δt the time it takes the shock to pass them. Substituting Equation 5.27 into equation 5.26 and rearranging gives us our main linearised fitting equation:

$$\underbrace{\frac{1}{(\Delta t)^2}}_{\text{y =}} = \underbrace{\frac{c_0^2 R_0^2}{4(\Delta x)^2} \frac{1}{R^2}}_{\text{mx+}} + \underbrace{\frac{c_0^2}{(\Delta x)^2}}_{\text{d}} \tag{5.28}$$

Plotting $\frac{1}{(\Delta t)^2}$ versus $\frac{1}{R^2}$ will give us a straight line with:

$$\text{gradient} = \frac{c_0^2 R_0^2}{4(\Delta x)^2} \quad \text{and } y \text{ intercept} = \frac{c_0^2}{(\Delta x)^2} \tag{5.29}$$

So provided we determine the time it takes the shock to pass the two probe beams, Δt, for various 'spark to probe beam' distances, *R*, and we can fit Equation 5.29 to the data satisfactorily, we can determine the small amplitude speed of sound, c_0, from the y intercept. This is equivalent to extrapolating the shock/sound wave velocity to an infinite distance from the spark source, where the *sound* propagates at a velocity of c_0.

Figure 5.8 shows measurements of the blast wave probe beam transit time, Δt and the spark to probe beam distance, *R*, made in air for 100% and 60% laser power. We see that the model described by Equation 5.28 fits the measurements well. Both fits have the same *y* intercept indicating that although the spark energy is different in each case, the extrapolation to infinite *R* yields the same small amplitude speed of sound. From Equation 5.28, we see that R_0 has the effect of changing the gradient of the fit only.

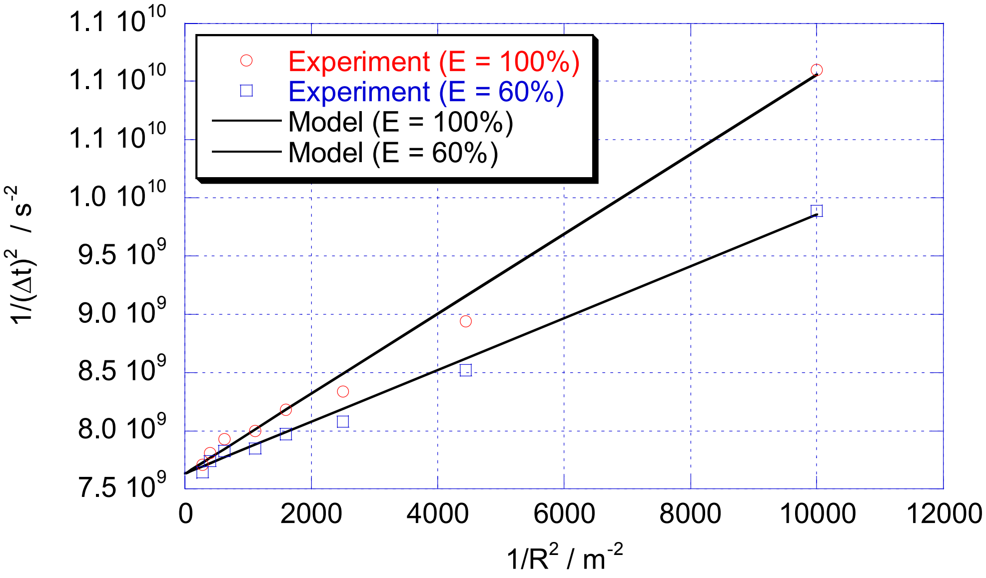

Figure 5.8 Example of fitting Equation 5.28 to measurements of the blast wave probe beam transit time, Δt and the spark to probe beam distance, *R*. Measurements made for 60% and 100% laser power in dry air at 20 °C.

With the blast wave model agreeing with experiment to better than 0.2%, the full photo-acoustic experimental system was developed. Details follow in Section 5.4.

5.5 EXPERIMENTAL EVALUATION OF THE PHOTO-ACOUSTIC THERMOMETRY TECHNIQUE

5.5.1 EFFECT OF UNCERTAINTY IN THE EQUIVALENCE RATIO ON THE PHOTO-ACOUSTIC TEMPERATURE

The accuracy of the measured photo-acoustic flame temperature depends critically on accurate knowledge of the equivalence ratio ϕ, which in tern depends on the accuracy of the flow meters used.

Recapping, the photo-acoustic temperature measurement equation is given by:

$$T = \frac{c_0^2}{C_a} \tag{5.9}$$

where c_0 is the speed of sound and C_a is the acoustic constant given by:

$$C_a = \frac{\gamma R}{\overline{m}} \tag{5.8}$$

where R is the molar gas constant, and γ and $\overline{m}$ are the ratio of specific heats and the mean molecular mass of the gas mixture respectively.

In this analysis, we wish to find the uncertainty in the post flame temperature T resulting from uncertainty in the equivalence ratio ϕ and associated error in $C_a(\phi)$. We assume that c_0 is approximately constant at 900 ms^{-1} (corresponding to a flame temperature of approximately 2100 K). The approximate maximum flame temperature is then given by:

$$T = \frac{8.1\text{x}10^5}{C_a(\phi)_{T_{ad}}} \tag{5.30}$$

Differentiating w.r.t. ϕ gives:

$$\frac{\partial T(\phi)}{\partial \phi} \approx 8.1\text{x}10^5 \frac{\partial}{\partial \phi}\left(\frac{1}{C_a(\phi)_{T_{ad}}}\right) \tag{5.31}$$

For small increments, we can write:

$$\Delta T(\phi) = 8.1\text{x}10^5 \frac{\partial}{\partial \phi}\left(\frac{1}{C_a(\phi)_{T_{ad}}}\right)\Delta\phi \tag{5.32}$$

The exact form of $C_a(\phi)$ can be found using the chemical equilibrium software Gaseq [67] or taken from figure 5.1.

Figure 5.9 shows the percentage uncertainty in the post flame temperature, T versus ϕ for various uncertainties in ϕ (0.5%, 1% and 2%).

Since the flow meters are calibrated to 1% accuracy, we may reasonably expect a maximum uncertainty in ϕ of the quadrature sum of two 1% uncertainties, i.e. approximately 1.4% in total. This leads to a maximum uncertainty in the post-flame temperature of approximately 0.3% as seen in the figure.

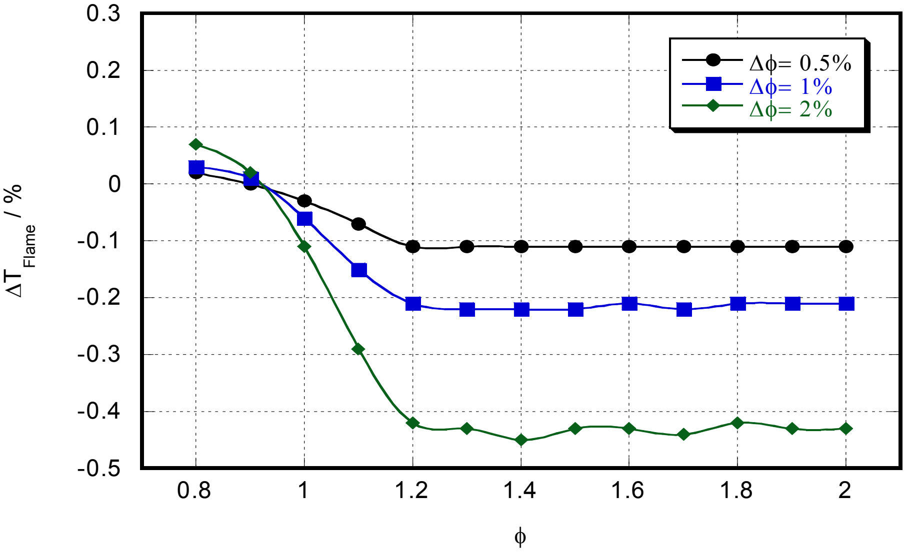

Figure 5.9 Uncertainty in the photo-acoustic post-flame temperature versus ϕ for various uncertainties in ϕ.

It is worth noting that the minimum uncertainty occurs for ϕ < 0.9 and not at ϕ=1 which was the case for the Rayleigh technique. In the case of the photo-acoustic technique, this can be explained by the fact that the acoustic constant does not change significantly for ϕ <1

5.5.2 EFFECT OF UNCERTAINTY IN THE POST-FLAME COMPOSITION DUE TO NON-LTE CONDITIONS

In a similar treatment to §5.5.1, we start with Equation 5.30 for the approximate photo-acoustic temperature:

$$T = \frac{8.1\text{x}10^5}{C_a(\phi)_{T_{ad}}} \tag{5.30}$$

The percentage error in T can be written as:

$$\%\ \text{Error in } T_{PAS} = \left(\frac{\left.\frac{\partial \sigma}{\partial \Omega}\right|_{\substack{\text{POST FLAME}\\ \text{LTE}}}}{\left.\frac{\partial \sigma}{\partial \Omega}\right|_{\substack{\text{POST FLAME}\\ \text{NON-LTE}}}} - 1 \right) * 100 \tag{5.33}$$

Figure 5.10 shows the percentage errors in T_{PAS} when LTE is assumed but in fact the CO_2 mole fraction is lower by 1,2 and 5%. We see that T_{PAS} is under-estimated with a maximum error near ϕ=0.9 of approximately –0.11%, -0.16% and –0.4% for CO_2 concentrations 1%, 2% and 5% below LTE respectively, reducing as ϕ increases.

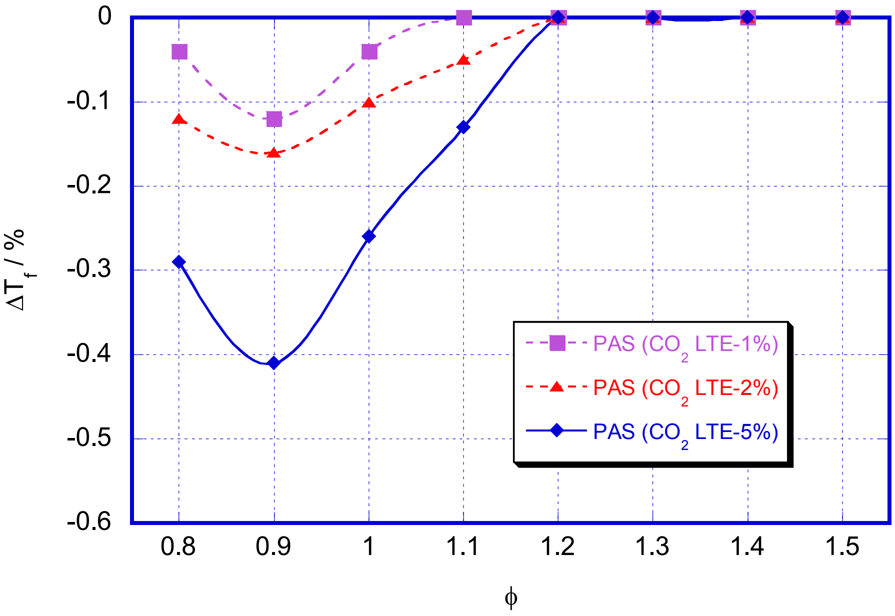

Figure 5.10 Percentage error in T_{PAS} due to non-LTE for CO_2.

A similar analysis for CO away from LTE by up to 5% did not show significant errors at all.

5.5.3 BEAM DEFLECTION NOISE SPECTRA IN THE McKENNA BURNER FLAME

Before development of the full photo-acoustic thermometry system, a preliminary experiment was carried out to determine the photo-acoustic noise spectra of the McKenna burner flame. Fluctuations in the temperature/density field in the flame produce variability in the probe beam position, which translate into noise in the detected signal. A schematic of the experiment is shown in Figure 5.11.

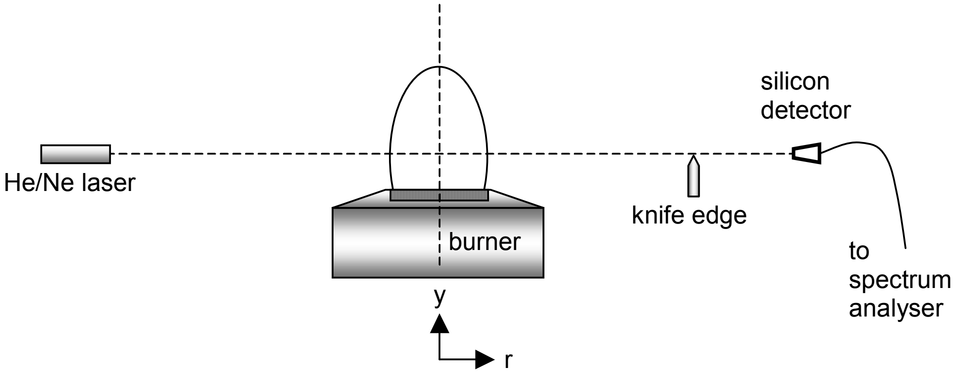

Figure 5.11 Schematic of the beam deflection noise spectra experiment.

The McKenna burner flame was fed with propane/air at an equivalence ratio (ϕ) of 1.0 for a flow rate of 60 SLPM of air. A 5 mW He/Ne probe laser beam was passed though the flame with half the beam incident on a knife edge and the remaining beam incident on a high speed silicon photo-diode. The signal from the detector was sent to a *Brüel and Kjuer Model 3550* spectrum analyser.

With the He/Ne probe laser beam, knife edge and detector geometry fixed, the burner was moved such that the noise spectra were obtained for vertical positions of y = 0.5, 2, 3 and 4 cm above the burner plate and for radial positions of r = 0, 1, 2 and 2.5 cm from the burner centre. Figure 5.12 and 5.13 show the noise spectra for r = 0 cm and r = 2.5 cm respectively. Note: a magnitude of 1 equals a detector noise voltage of 0.1 V.

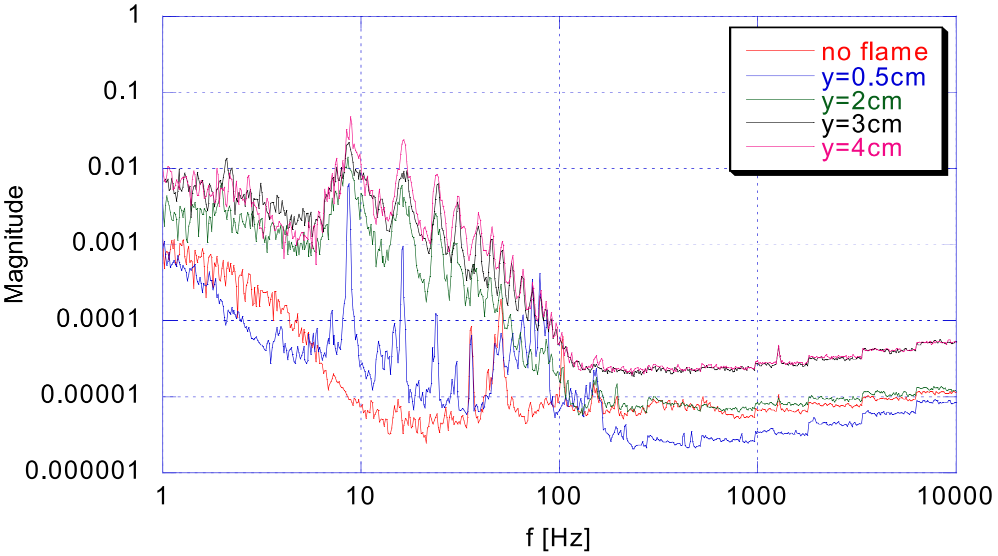

Figure 5.12 Photo-acoustic noise spectra for r = 0 cm for various heights above the burner.

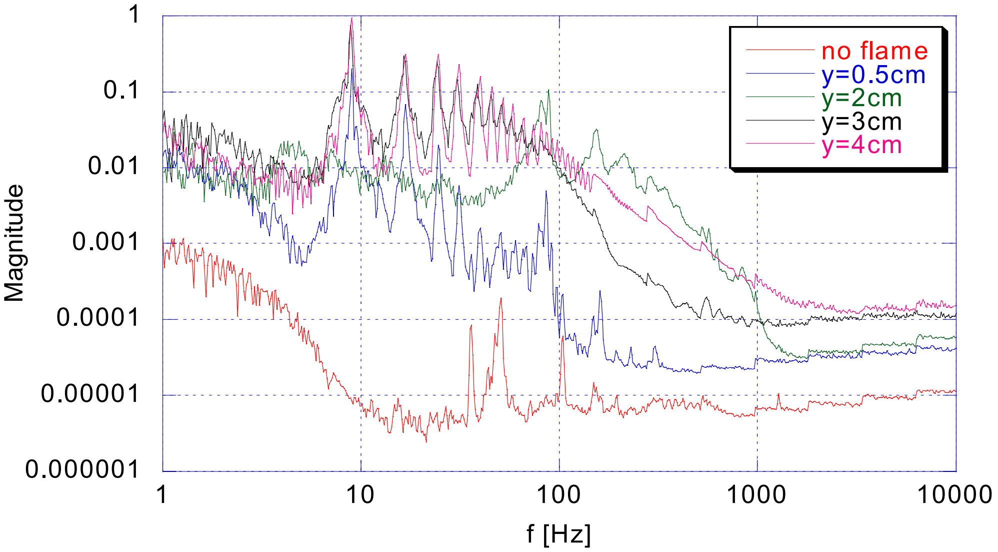

Figure 5.13 Photo-acoustic noise spectra for r = 2.5 cm for various heights above the burner.

We see from these spectra that:

- The noise dominates at low frequencies (<1000 Hz).
- The noise increases significantly as we move to the outer region of the flame ($r = 2.5$ cm).
- Major oscillations are evident at 8 Hz and harmonics of this frequency.
- The oscillations are clearly visible close to the burner ($y = 0.5$ cm) and are partially obscured by flame noise for larger heights above the burner.

We conclude that the majority of the low frequency oscillation and random noise can be removed by high pass filtering the detector signals.

5.5.4 DESCRIPTION OF THE PHOTO-ACOUSTIC BEAM DEFLECTION APPARATUS

The experiment, comprising the McKenna burner system (described in Chapter 2) and the beam deflection apparatus is shown schematically in Figure 5.14.

- The sound source to be measured is produced by a spark plasma generated by focussing the 1064 nm output of a NdYAG [80] pulse laser using a $f = 5$ cm focal lens a few centimetres from the probe beams.
- A 5 mW He/Ne laser operating at 633 nm is used to generate an initial single unpolarised probe beam.
- After passing though a single focussing lens ($f = 45$ cm), the beam enters a *beam displacing prism* provided by *Melles Griot* [101]. This birefringent crystal splits the single beam into two parallel probe beams of different polarisations. The prism is maintained at a temperature of 30 °C via a heater controlled by a PID controller and a 100 Ω platinum resistance thermometer.
- The two parallel probe beams are brought to a focus 2 cm above the centre of the burner before impinging on knife edges.
- The position of the knife edges are fully adjustable via miniature translation stages and are adjusted so that half of each probe beam is incident on an knife edge.
- In order to separate the two beams so that they can impinge on independent detectors, a polarising beam splitter is used. Since the two probe beams are highly polarised, the beam splitter allows one probe beam to pass straight through and totally reflects the other at 90 ° from its original direction.
- The beams are then incident onto band pass filters with a centre wavelength that matches the probe laser beam with a half width at half maximum (HWHM) of 10 nm. This blocks ambient light in the room, light from the sound generating spark and flame radiation from reaching the detectors.
- The filtered probe beams are then incident onto two biased high-speed silicon photodiodes provided by *Thorlabs* [102].
- The detector signals are then measured by a high-speed transient digitiser (model 5152 provided by National Instruments [82]) at a sample rate of up to 100 million samples per channel per second.
- Labview [82] software then averages the two signals and performs a cross-correlation to obtain the transit time of the sound wave as it passes the two probe beams.

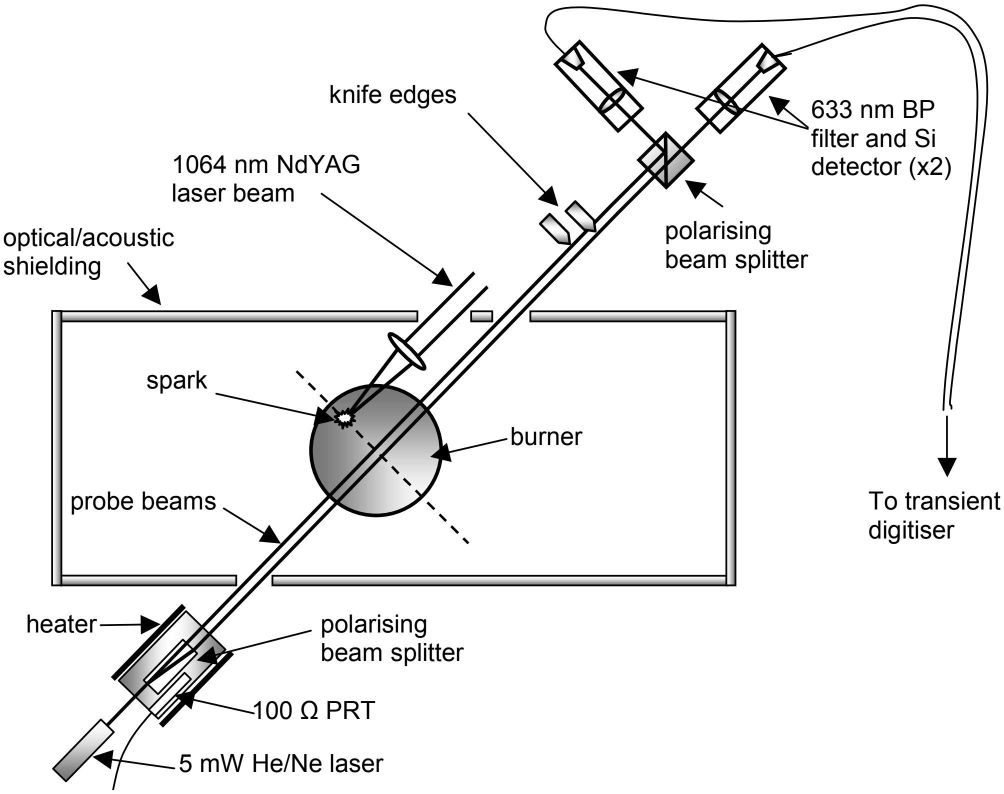

Figure 5.14 Schematic diagram of the photo-acoustic beam deflection apparatus.

Figure 5.15 shows the He/Ne laser, the temperature controlled beam displacing prism and the probe beam focussing lens. The vertical arrangement is to allow for the probe beams to pass above the elevated burner system (not seen in this photogragh).

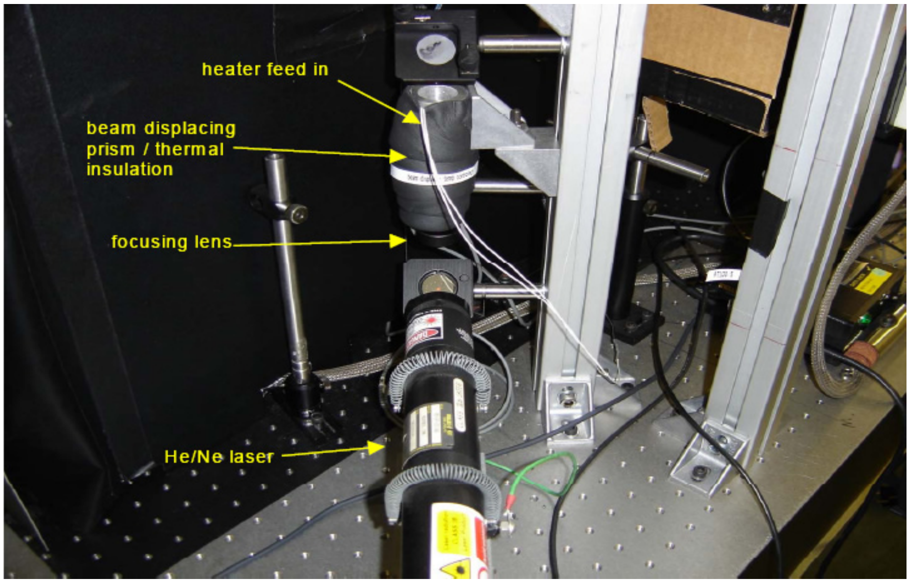

Figure 5.15 Photograph showing the He/Ne probe laser beam and the beam displacing prism.

Figure 5.16 shows the two probe beams and the laser induced spark (focussed by the lens) above the McKenna burner. Air flows through the burner in this photograph.

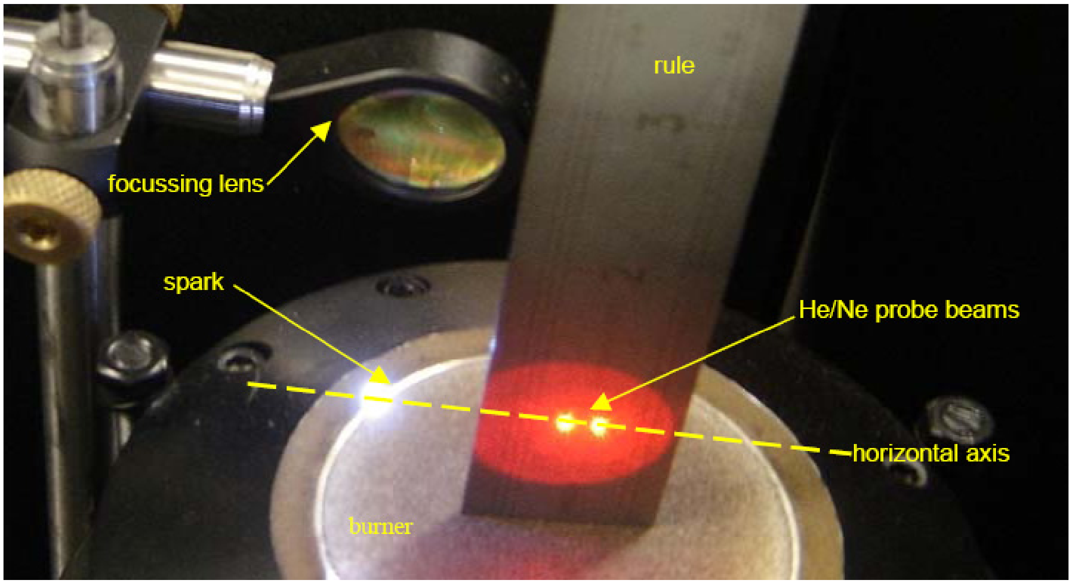

Figure 5.16 Photograph showing the two probe beams and the laser induced spark above the McKenna burner. The rule has been placed in front of the probe beams to aid visualisation.

Figure 5.17 shows the McKenna burner flame and the Nd-YAG laser induced spark in the flame. The temperature of the focussing lens, approximately 2 cm from the flame, reached 70 °C, however, no damage or change in the spark focus position was observed.

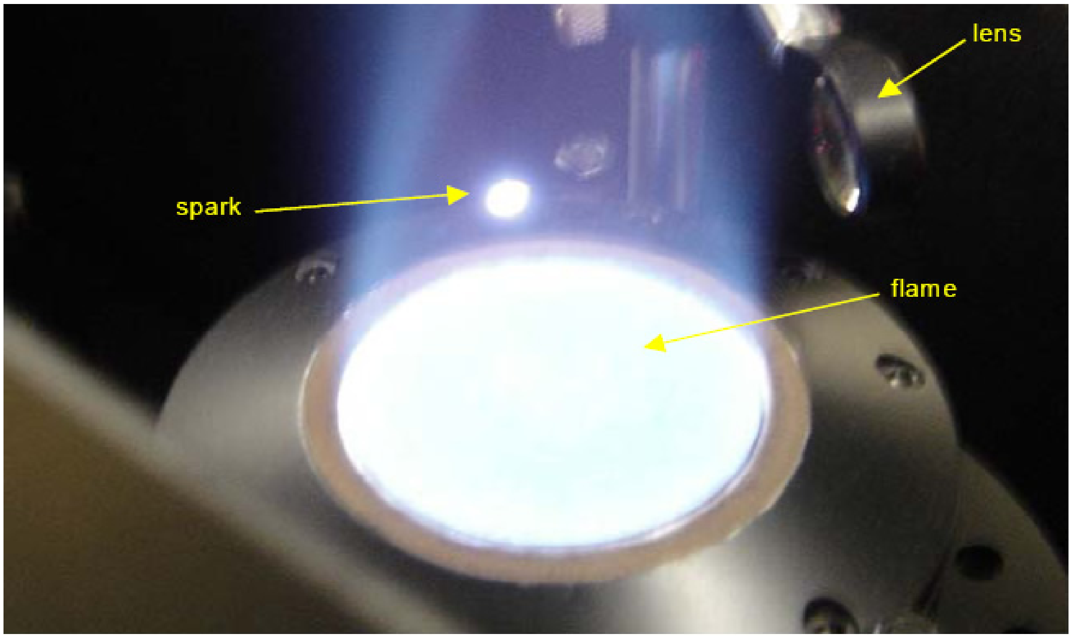

Figure 5.17 Photograph showing the McKenna burner flame and the spark induced by the Nd-YAG laser in the flame.

Figure 5.18 shows the twin silicon photodiode detector system including the knife edges and the beam splitter that separates the two closely spaced probe beams, directing them onto the individual detectors

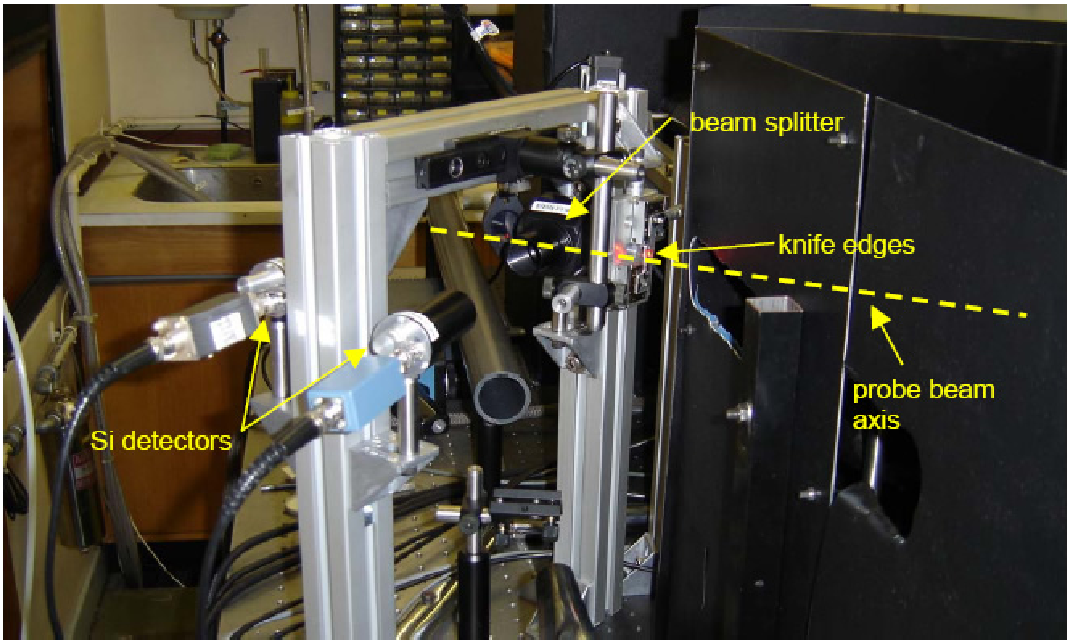

Figure 5.18 Photograph showing the twin silicon photodiode detector system.

The front panel of the photo-acoustic data processing software written in *Labview* [82] is shown in Figure 5.19. It shows:

- Raw data: the single shot *raw* photo-acoustic beam deflection signals for both probe beams.
- Averaged data: the running average of the last 1000 photo-acoustic beam deflection signals for both probe beams.
- Gas/air temperatures: the temperatures (measured by high accuracy platinum resistance thermometers) of the inlet/outlet burner cooling water, the room temperature, the beam displacing prism temperature and the air temperature above the burner (used for calibration purposes when the flame is no present).
- Ambient pressure: the ambient pressure in the room. If the pressure changes appreciably during the measurements, this indicator will show this.
- Cross correlation: the cross correlation of the two averaged beam deflection signals. This gives the time taken for the sound generated by the spark to pass the two probe beams.

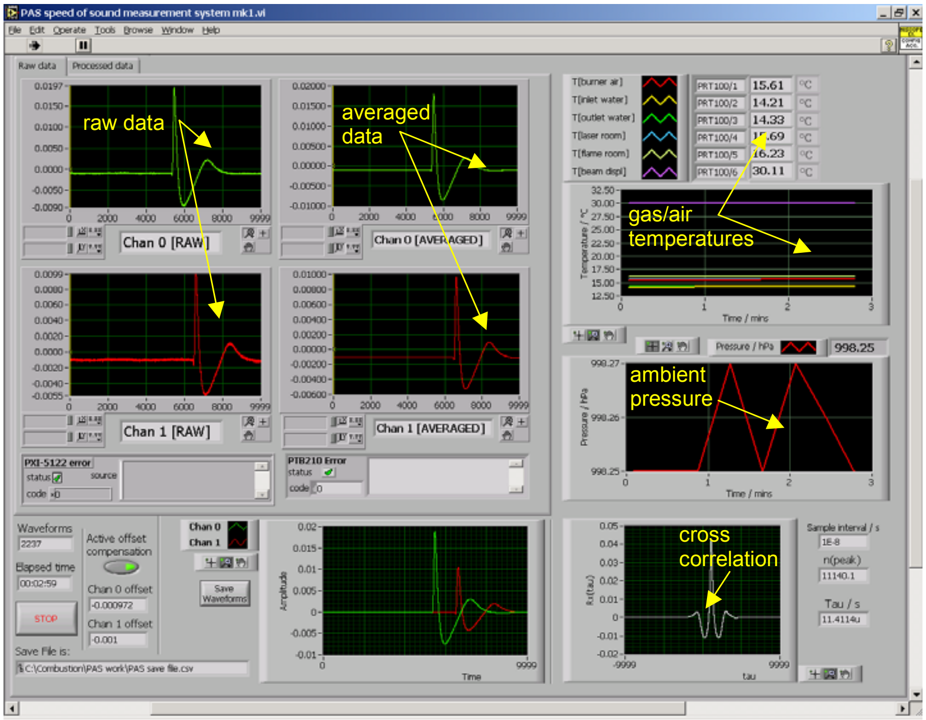

PRT100/1 15.61 °C
PRT100/2 14.21 °C
PRT100/3 14.33 °C
PRT100/4 15.69 °C
PRT100/5 16.23 °C
PRT100/6 30.11 °C
Pressure / hPa 998.25
Waveforms 2237
Elapsed time 00:02:59
Active offset compensation
Chan 0 offset -0.000972
Chan 1 offset -0.001
Save File is: C:\Combustion\PAS work\PAS save file.csv
Sample interval / s 1E-8
n(peak) 11140.1
Tau / s 11.4114u

Figure 5.19 The font panel of the data processing software.

The secondary panel of the photo-acoustic data processing software is shown in Figure 5.20. In addition to several of the items shown on the front panel, this panel provides the probe beam transit time history and a *web-cam* image (updated every second), which allows remote viewing of the whole photo-acoustic system.

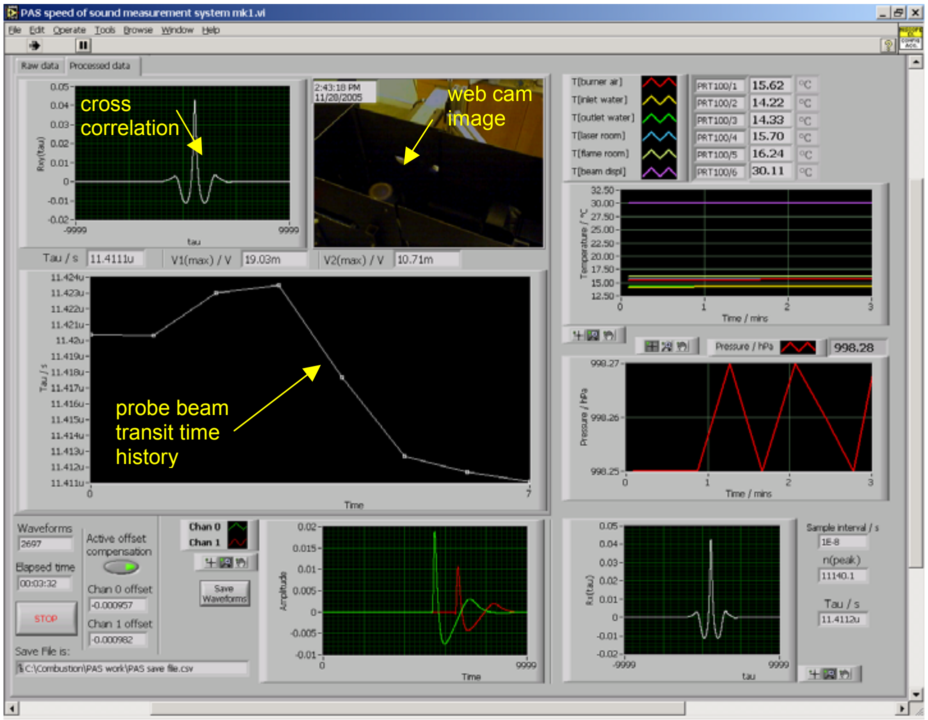

Tau / s 11.4111u
V1(max) / V 19.03m
V2(max) / V 10.71m
PRT100/1 15.62 °C
PRT100/2 14.22 °C
PRT100/3 14.33 °C
PRT100/4 15.70 °C
PRT100/5 16.24 °C
PRT100/6 30.11 °C
Pressure / hPa 998.28
Waveforms 2697
Elapsed time 00:03:32
Active offset compensation
Chan 0 offset -0.000957
Chan 1 offset -0.000982
Save File is: C:\Combustion\PAS work\PAS save file.csv
Sample interval / s 1E-8
n(peak) 11140.1
Tau / s 11.4112u

Figure 5.20 The secondary panel of the data processing software.

5.5.5 PHOTO-ACOUSTIC THERMOMETRY ON THE MCKENNA BURNER FLAME

A course of measurements was made over a four-day period using the photo-acoustic beam deflection apparatus described in §5.5.4. The non-linear blast wave behaviour of the sound wave (§5.4) close to the spark source meant that measurements needed to be made for different spark to probe beam distances and an extrapolation to *infinite* distances made to recover the small amplitude speed of sound, c_0. A description follows:

- The probe beams were set to pass 2 cm above the centre of the McKenna burner and remain fixed for the whole course of measurements.
- The distance between the spark and the midpoint between the probe beams, *R*, was varied from 1 cm to 2.5 cm, in increments of 0.5 cm each day (ie. day 1 = 1 cm, day 2 = 1.5 cm, day 3 = 2 cm day 4 = 2.5 cm).
- With dry air at room temperature passing though the McKenna Burner, the Nd-YAG pulse laser system was switched on at 100% power, producing a spark in the air. The temperature of the air was monitored with a PT100 PRT.
- The laser system was left to stabilise over a period of two to three hours. Stability was indicated when the photo-acoustic probe beam transit time stabilised to better than 0.1%. Once stability was achieved, the probe beam transit time in air was recorded.
- With the PT100 sensor removed from above the burner, the flame was ignited with a premix of propane/air.
- The equivalence ratio was varied from $\phi = 0.8$ to $\phi = 1.5$ in increments of 0.1 using the mass flow meters. For each ϕ the airflow rate was varied from 30 SLPM to 60 SLPM in 10 SLPM increments. This gave a set of 24 unique conditions for which the photo-acoustic beam defection transit times were measured.

With the data collection complete, the first task was to determine the probe beam separation, Δx. This was achieved by making use of the data collected for air flowing through the burner at a known temperature.

To recap, the blast wave model (Equation 5.28) is presented again:

$$\underbrace{\frac{1}{(\Delta t)^2}}_{\mathrm{y}\,=} = \underbrace{\frac{c_0^2 R_0^2}{4(\Delta x)^2}\frac{1}{R^2}}_{\mathrm{mx+}} + \underbrace{\frac{c_0^2}{(\Delta x)^2}}_{\mathrm{d}} \tag{5.28}$$

The linear fit of this equation for the photo-acoustic measurements made in air is shown in Figure 5.21:

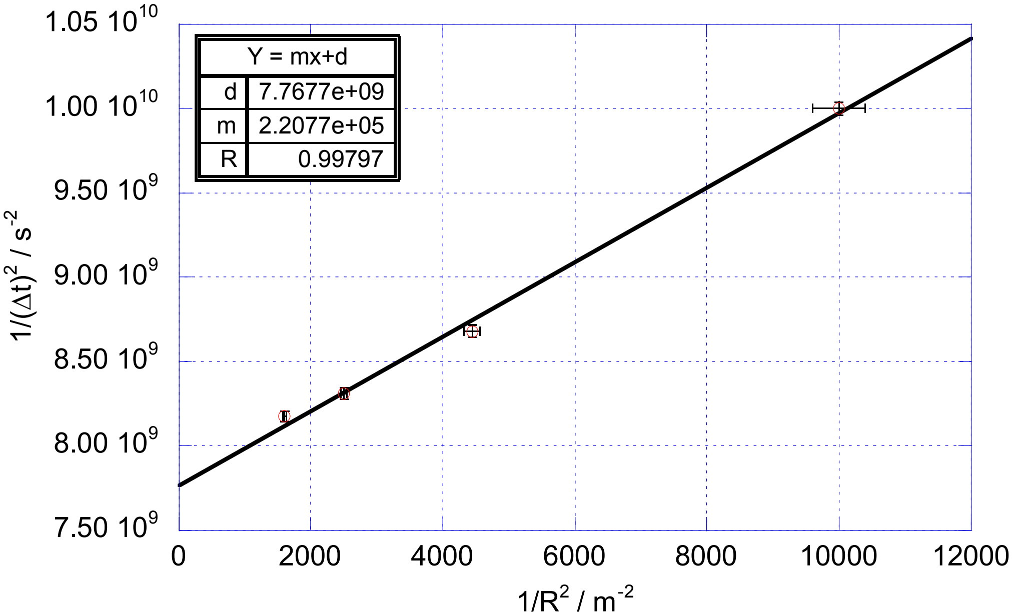

Figure 5.21 The photo-acoustic beam deflection calibration for air.

From Equation 5.28, we see that the y intercept of Figure 5.21 is given by:

$$y\,\text{intercept} = \frac{c_0^2}{(\Delta x)^2} = 7.7677 \text{ x } 10^9 \tag{5.34}$$

The speed of sound in dry air at a temperature t °C is well known [93 - 97], and to an uncertainty of less that 0.05% is given by:

$$c_0(t) = a_0 + a_1 t + a_2 t^2 \tag{5.35}$$

with

$$a_0 = 331.5024\,\text{ms}^{-1}$$
$$a_1 = 0.603055\,\text{ms}^{-1}{}^\circ\text{C}^{-1}$$
$$a_2 = -0.000528\,\text{ms}^{-1}{}^\circ\text{C}^{-2}$$

The mean air temperature during the tests was 18.51 °C. At this temperature, the speed of sound is 342.484 ms^{-1}. Making use of Equation 5.34 gives our probe beam separation as:

$$\Delta x = \frac{342.484}{\sqrt{7.7677 \text{ x } 10^9}} = 0.0038859\,\text{m} \pm 0.0000078\,\text{m} \tag{5.36}$$

We have already established the invariance of the probe beam separation in a typical flame environment (§5.3.2) and use the result given by Equation 5.36 in the subsequent determination of the speed of sound in the flame.

The flame measurements for an equivalence ratio of $\phi = 1$ and various airflow rates are shown in Figure 5.22. For each different airflow rate (and hence temperature) we have fitted Equation 5.28.

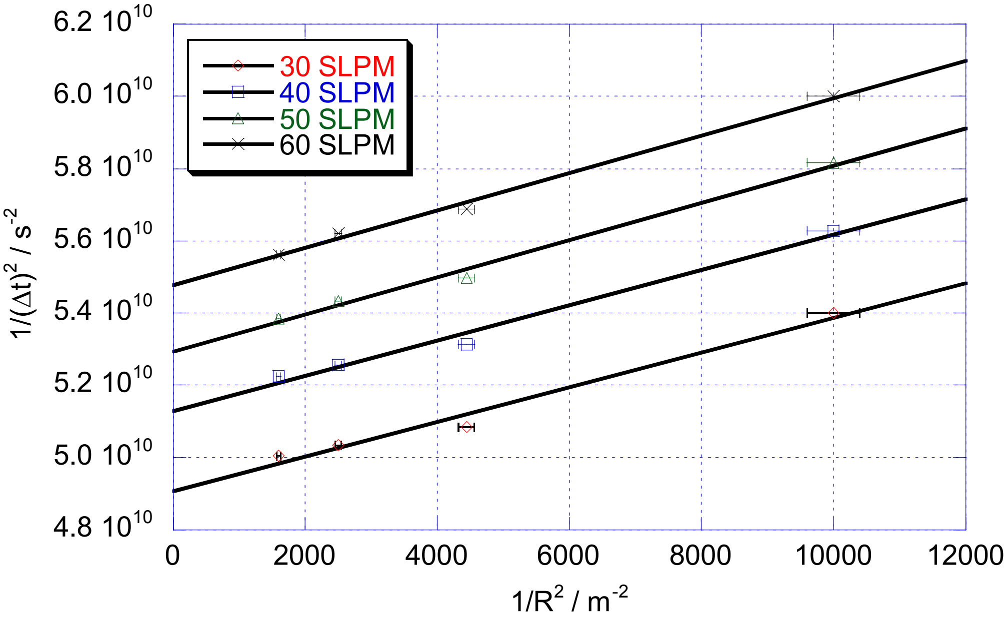

Figure 5.22 The photo-acoustic beam deflection measurements for propane/air combustion at an equivalence ratio of $\phi = 1$, various airflow rates.

Rearranging Equation 5.34 allows us to determine the small amplitude speed of sound, c_0, from the y intercept values shown in Figure 5.22:

$$c_0 = \Delta x \sqrt{y \text{ intercept}} \tag{5.37}$$

Table 5.3 shows the y intercept values and the speed of sound for the measurements shown in Figure 5.22.

Airflow rate / SLPM	***y* intercept (Equation 5.30) / x 10^{10} s^{-2}**	**c_0 / ms^{-1}**
30	4.90814	860.917
40	5.12883	880.059
50	5.29491	894.172
60	5.47795	909.496

Table 5.3 Fitting parameters and calculated speed of sound for propane/air combustion at an equivalence ratio of $\phi = 1$ for various airflow rates.

Applying the same procedure to the rest of the flame measurements, Figure 5.23 shows the small amplitude speed of sound, c_0, versus equivalence ratio and airflow rate.

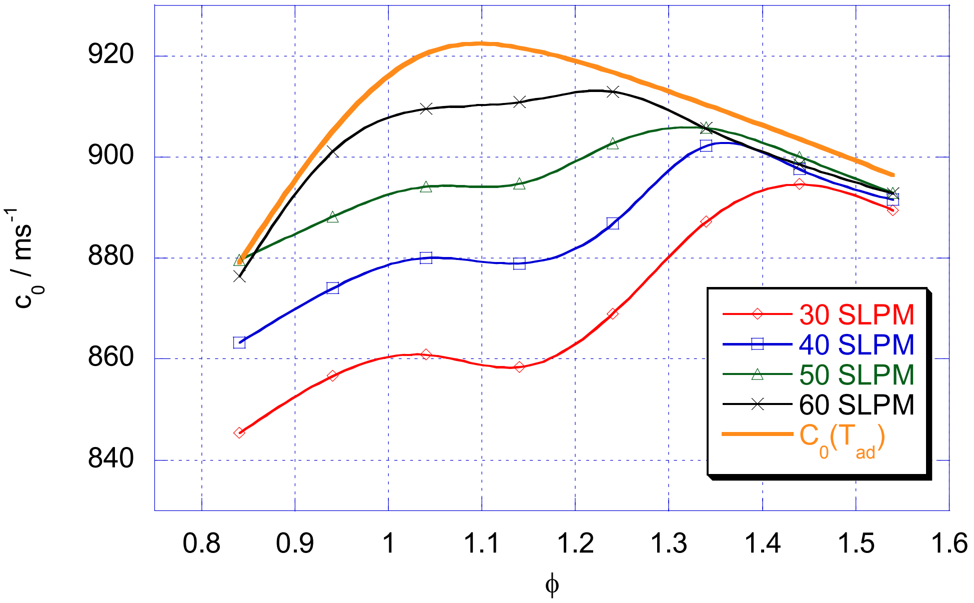

Figure 5.23 The small amplitude speed of sound, c_0, versus the equivalence ratio (ϕ) for various airflow rates (propane/air combustion). The speed of sound at the theoretical adiabatic flame temperature, $c_0(T_{ad})$ is also shown.

To convert these speed of sound values to temperatures we make use of Equation 5.9:

$$T = \frac{c_0^2}{C_a} \tag{5.9}$$

Gaseq [67] chemical equilibrium software was used to perform this calculation. We saw earlier (Figure 5.1) that the acoustic constant, C_a, was a monotonic increasing function of temperature for a given equivalence ratio (ϕ). This means that the flame temperature can be adjusted in *Gaseq* [67] until the desired speed of sound is recovered and it will be unique. Figure 5.24 shows our main result of the measured flame temperature versus equivalence ratio for propane/air combustion for various airflow rates.

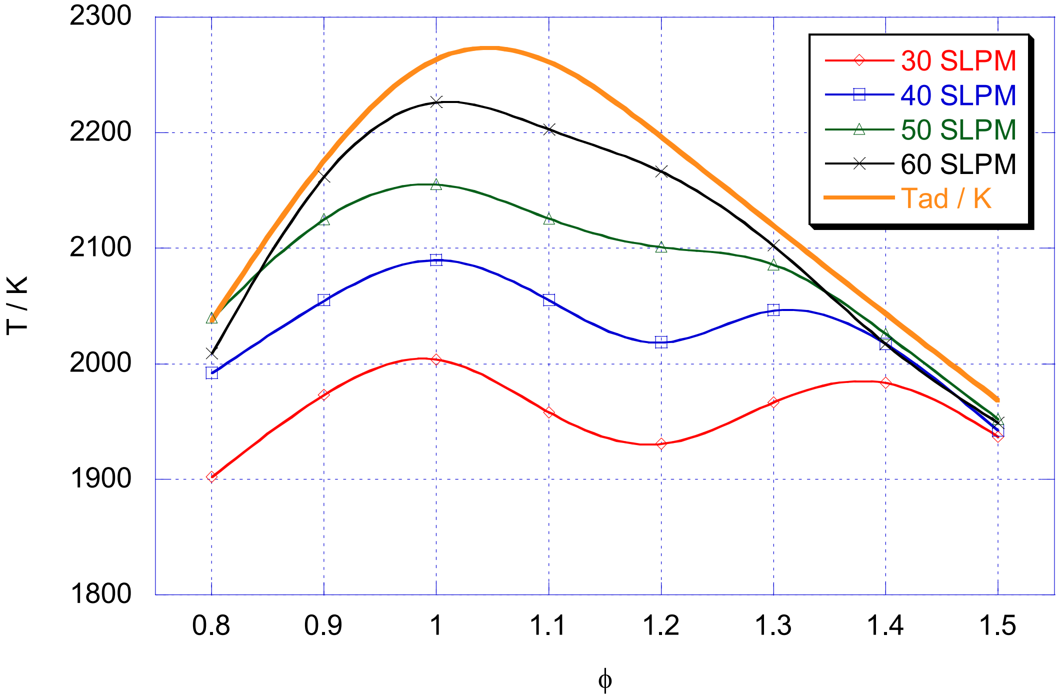

Figure 5.24 The photo-acoustic flame temperature vs equivalence ratio for propane/air combustion for various airflow rates. The adiabatic flame temperature is also shown (T_{AD}).

These results are very similar to the Rayleigh thermometry results and the reader is directed to §4.3.4 for an interpretation of the main features of the figure above. An uncertainty budget for the photo-acoustic thermometry measurements is presented in Table 5.4 showing that the estimated total uncertainty in the temperature measurements is approximately 0.5% at one standard deviation.

Source	Size (1σ)	Type
Acoustic constant Ca	0.1%	B
Flow-meter uncertainty	0.3%	B
Chemical equilibrium assumption	0.2%	B
Probe beam to spark distance	0.2%	A/B
Probe beam separation (difference from air cal. to flame)	0.1%	A
Timing resolution of digitiser (10ns)	0.2%	A
Inlet air/water temperature	0.2%	A/B
Atmospheric pressure	0.1%	A/B
Gas purity	0.0%	B
Combined uncertainty (in quadrature)	**0.5%**	**(A/B)**
Flame temperature reproducibility (measured)	**0.4%**	

Table 5.4 Uncertainty budget for the photo-acoustic thermometry measurements.

5.6 COMPARISON OF THE PHOTO-ACOUSTIC AND RAYLEIGH TEMPERATURE MEASUREMENTS

The Rayleigh scattering and photo-acoustic thermometry systems have now both been used to measure the temperature of the propane/air McKenna burner flame. Figure 5.25 shows the comparison of the flame temperatures measured by the two independent techniques for equivalence ratios (ϕ) from 0.8 to 1.5 and for airflow rates from 30 to 60 SLPM. The percentage difference in temperatures as measured by the two methods:

$$\Delta T(\%) = \frac{(T_{PAS} - T_{RAY})}{T_{RAY}} * 100 \qquad (5.38)$$

is shown in Figure 5.26.

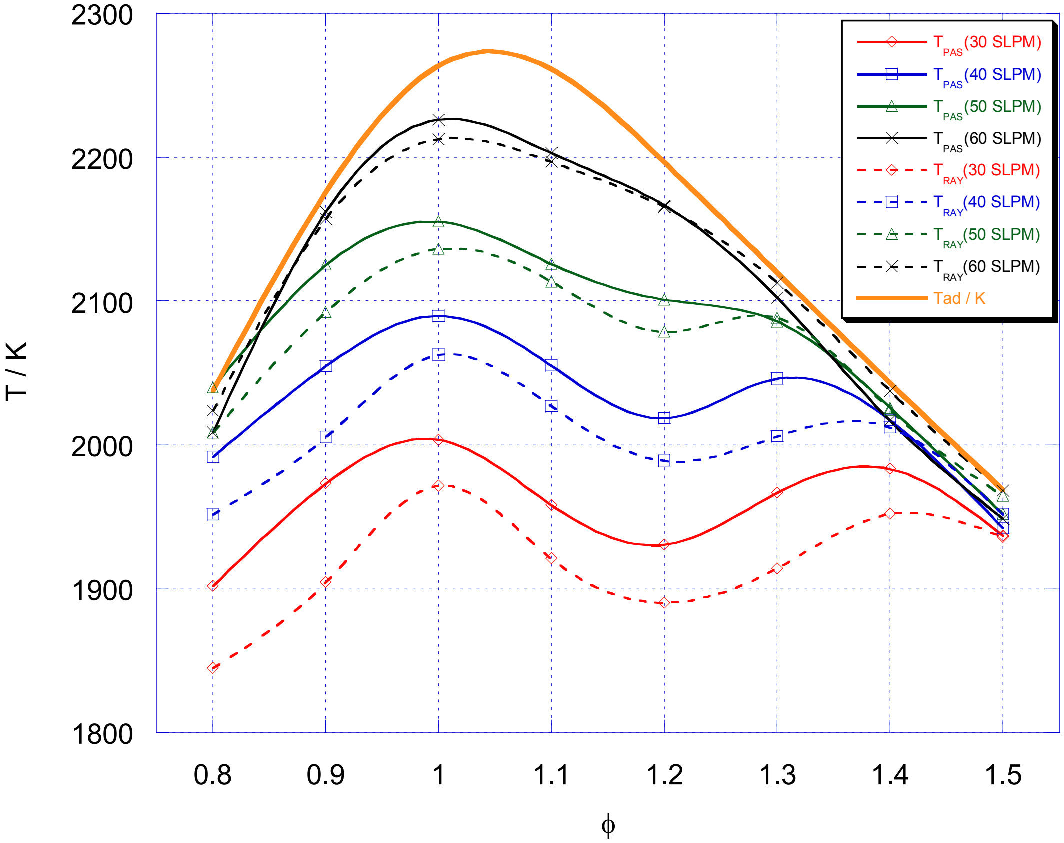

Figure 5.25 Comparison of temperature of the propane/air McKenna burner flame measured by Rayleigh scattering thermometry (T_{RAY}) and Photo-acoustic beam deflection thermometry (T_{PAS}) versus equivalence ratio (ϕ) for various airflow rates.

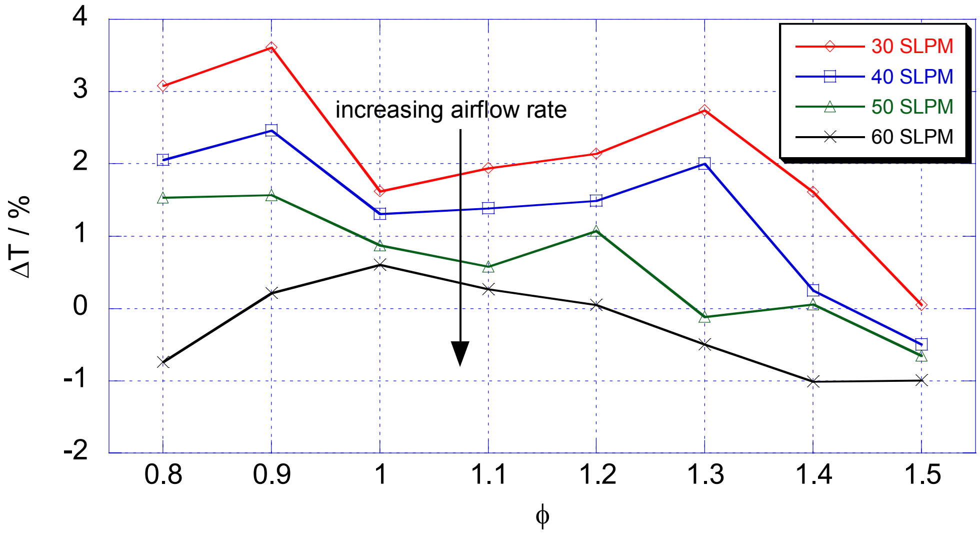

Figure 5.26 Percentage difference between T_{PAS} and T_{RAY} versus equivalence ratio (ϕ) for various airflow rates (propane/air McKenna burner flame).

The key points to note from Figures 5.25 and 5.26 are:

- The change in the photo-acoustic temperature with equivalence ratio (ϕ) follows the same trend as the Rayleigh temperatures.
- Systematically, the photo-acoustic temperatures are higher than the Rayleigh temperatures for a majority of equivalence ratios and airflow rates.
- As the airflow rate increases, the photo-acoustic temperatures tend towards the Rayleigh temperatures.
- The percentage difference between the two temperatures decreases from approximately 3.6% for an airflow rate of 30 SLPM to less than 1% for an airflow rate of 60 SLPM. The latter is within the 1% uncertainty estimated for each technique.
- All temperatures are confined beneath the adiabatic temperature curve (representing the maximum possible flame temperature for no heat losses).

Potential reasons for the difference in temperatures between the two methods for low airflow rates could be connected with assumptions of local thermodynamic equilibrium (LTE), or the validity of the blast wave model.

The flame species may not be in local thermodynamic equilibrium (LTE) and therefore we may not have the species concentrations calculated by the equilibrium software that are needed to convert from the measured signals to actual temperatures. The lack of LTE would apply to both the Rayleigh and photo-acoustic temperatures but literature suggests that the sensitivity of the Rayleigh scattering cross-section to species concentrations is greater than for the photo-acoustic acoustic constant [90]. This implies that the Rayleigh temperatures may have a larger uncertainty than the photo-acoustic temperatures. The fact that the agreement between the temperatures determined by the two methods improves as the airflow rate increases may be due to the fact that the flame temperatures are higher for high flow rates and the mixtures are closer to LTE.

Enhancement of thermal diffusion at higher airflow rates (higher temperatures) may also bring the mixture closer to LTE.

The cylindrical blast wave model used to extrapolate to infinite spark to probe beam distances may not work sufficiently well for the laser-induced spark used in this work. A spherical blast wave model for example may be more appropriate. Any errors in this model would directly relate to the measured small amplitude speed of sound and subsequently on the temperature so determined. It would be interesting to investigate the spherical model at a later date.

5.7 SUMMARY

In summary:

The photo-acoustic beam deflection technique was presented as a method for measuring the speed of sound and hence the temperature of the McKenna burner flame. The variation in the separation of the two probe beams was modelled for typical radially symmetric flame temperature fields and found to be negligible for measurements in the centre of the flame.
The cylindrical blast wave model for laser-induced sparks was presented and found to fit the experimental data well. This allowed for extrapolation to the small amplitude speed of sound, which is the quantity sensitive to the flame temperature.

The beam deflection system including data processing software was developed and found to be stable and reproducible. The temperature of the propane/air McKenna burner flame was successfully measured for various equivalence ratios and airflow rates using the photo-acoustic beam deflection technique. Comparison of the flame temperatures measured by the photo-acoustic and Rayleigh scattering thermometry system has shown good agreement. For low airflow rates photo-acoustic temperatures are approximately 3.6% higher than the Rayleigh temperatures, however, at high airflow rates the agreement is better than 1% of temperature.

Further work is needed to determine the source of the discrepancy between the two thermometry techniques at low airflow rates.

5. SUMMARY AND CONCLUSIONS

An initial survey of extant work on gas and combustion temperature standards, including an assessment of thermometry calibration techniques was undertaken. This survey identified the standard flame as the most suitable candidate for the combustion standard. A McKenna premixed flat flame burner system with associated gas mixing and water-cooling system was commissioned. The burner was operated with propane and air for various equivalence ratios and airflow rates. Within the uncertainty of the measurements, the temperature of McKenna burner flame proved to be highly reproducible over a period of 6 years.

Three non-contact thermometry techniques were identified as suitable for calibration of the standard flame: 1) the Modulated Emission in Gases (MEG) technique, 2) the Rayleigh scattering technique and 3) the photo-acoustic technique. All three of these thermometry techniques have been studied in this thesis. In light of technical difficulties with the Modulated Emission in Gases (MEG) technique, the Rayleigh scattering and photo-acoustic thermometry techniques were developed and comparison made between the temperatures measured by the two techniques. A summary follows:

1) The Modulated Emission in Gases (MEG) technique.

The Modulated Emission in Gases (MEG) thermometry technique has been fully evaluated. Theoretical models and computer simulations have been developed and experiments have been carried out to validate the technique:

- The theoretical basis of the MEG thermometry technique has been described fully.
- The MEG precision analysis has demonstrated that a temperature modulation of 2 K will provide a signal to noise ratio of 10^3 for typical flame parameters.
- The temperature rise due to 5 – 10% absorption of an incident laser beam has been modelled for both a pulse and a modulated continuous wave (CW) laser source. For typical flame parameters, temperature rises of 28 K and >2 K were predicted for pulse and CW laser sources respectively.
- A detailed MEG computer simulation has been written in MATLAB [57] allowing for determination of the uncertainty in the reconstructed MEG temperature for various flame/laser parameters. A propane/air flame operating at an equivalence ratio of 1 was considered in detail. The model introduced shot noise to the detector signals, which was due to the large DC radiance incident on the detectors as a consequence of viewing the flame. In summary:
    - The expected signal to noise ratios for a 2 K temperature modulation agreed with the MEG precision analysis performed earlier ($S/N > 10^3$).
    - The uncertainty in the MEG temperature scales as the square root of the post detection bandwidth with an integration time of 15 minutes shown to provide an uncertainty in the temperature of less than 1%.
    - Determination of the optimum detection wavelength(s) was found to depend on the flame temperature. For temperatures of 1000 K the best signal to noise ratio was obtained for a detection wavelength of 2 μm compared to 1 μm for temperatures of 2000 K. In choosing the optimum wavelength consideration to

absorbing/emitting flame species lead to a superior signal around 4.3 µm due to the strong absorption band of CO_2 at this wavelength.

  - Constraints on the absorption coefficient were needed to successfully recover good signals. If the absorption coefficient was too large, the flame became optically thick with little or no modulated radiation exiting the flame. A value of 1.7 m^{-1} corresponding to 10% absorption across a width of 0.06 m (the width of the McKenna burner flame) were found from spectroscopic synthesis software for CO_2 which was suitable for successful extraction of the MEG signals and hence temperature.
  - Practically, optimisation of the smoothing algorithms used in the processing of the raw signals would be needed to reduce oscillation in the reconstructed MEG temperature.
  - The model demonstrates that in principle it should be possible to recover the true flame temperature with an uncertainty of less than 1%.

- FTIR measurements made on the McKenna burner flame indicated the presence of strong absorption bands of CO_2 at 4.3 µm, 2.7 µm and 10.4 µm with weaker bands of H_2O at 2.9 µm and CO at 4.8 µm. In light of this, a readily available high power C.W. CO_2 laser operating at 10.4 µm was used as the temperature modulation source. A signal detection wavelength around 4.3 µm was chosen to coincide with the strong CO_2 band.
- MEG measurements on a soot-free stoichiometric propane/air McKenna burner flame did not yield any signals. This has been directly attributed to the lack of absorption of the pump laser beam, perhaps due to the weakness of the CO_2 absorption lines at 10.4 µm, the operating wavelength of the laser.
- With the burner operated with an ethane/air flame in the rich limit, it was possible to generate a sooty flame region. By operating the flame in this way, it was found that approximately 10% of the laser energy was absorbed over the length of the flame. A modulated thermal radiance signal (MEG signal) was measured for this type of flame. The sooty flame was very unstable and not well anchored to the burner disk.
- A hot cell apparatus was constructed, providing a clean particle free environment up to 700 °C. With small amounts of ethene added to CO_2 gas it was found that the absorption of the 10.4 µm laser radiation was encouraged thus guaranteeing the thermal modulation required for the MEG technique. For gas temperatures above 600 °C it was found that MEG signals could be measured, following the predicted 1/(modulation frequency). A theoretical spectroscopic model of the hot cell apparatus was also developed to determine the magnitude of the expected signals. Reasonable agreement was obtained between the model and experiment.
- Further analysis of the MEG theory as applied to real flames has since shown that extraction of the temperature information from the MEG signals is technically challenging. The primary reason for this is the spectral nature of the absorption coefficient of gases. Although the theory can predict *average* absorption coefficients to the correct order of magnitude, the sensitivity required to reconstruct accurate temperatures cannot be achieved.
- The use of a high-resolution infrared spectrometer would allow determination of the spectral absorption coefficient and the MEG temperature could then be obtained. A suitable spectrometer would need to resolve the spectral lines of the high temperature gases. Since these lines have a HWHM of 0.05 cm^{-1}, such an instrument

would be very expensive and its utilisation is not regarded as the best approach to meeting the requirements of this work.

2) The Rayleigh Scattering Thermometry Technique

A high accuracy Rayleigh scattering thermometry system has been developed. Corrections to the scattering cross-section to allow for its temperature dependence have been applied and the temperature of the McKenna burner flame has been measured to high accuracy:

- A detailed survey and technical evaluation of the Rayleigh scattering phenomena has been undertaken.
- The total and differential Rayleigh scattering cross-sections have been derived.
- The theoretical evaluation of Rayleigh scattering as an accurate thermometry technique has been undertaken:
    - The differential Rayleigh scattering cross-section for air and major combustion species has been found.
    - The species concentrations in the post flame region of a propane/air flame have been calculated from equilibrium software for various equivalence ratios.
    - The temperature dependence of the differential scattering cross-section has been investigated by considering the contributions of the mean molecular polarisability and the molecular anisotropy.
    - A correction has been developed to provide high accuracy Rayleigh thermometry provided the equivalence ratio is measured precisely.
    - The experimental evaluation of the Rayleigh scattering as an accurate thermometry technique has been undertaken:
- The optimised Rayleigh scattering thermometry system is presented.
- Technical challenges in obtaining the highest accuracy have been described including the reduction of electromagnetic interference and background scattered light, improvement of the detector linearity, optimisation of the Rayleigh signal collection optics and evaluation of the long-term stability of the system.
- The effect of the inlet gas temperature and water content on the flame temperature has been investigated.
- The effect of the ambient pressure on the flame temperature has been explored.
- The effect of the fuel purity on the flame temperature has been investigated.

Detailed measurements on the McKenna burner flame operated with propane and air have been undertaken indicating a long-term temperature reproducibility of better than 0.5% and an absolute accuracy of 1%.

3) The Photo-acoustic Thermometry Technique

A high accuracy Photo-acoustic thermometry system has been developed and temperature measurements have been directly compared with those measured with the Rayleigh scattering thermometry system:

- The relationship between gas temperature and the speed of sound is defined.

- The photo-acoustic beam deflection technique is presented as a method for measuring the speed of sound and hence the temperature of the McKenna burner flame.
- The variation in the separation of the two probe beams is modelled for typical radially symmetric flame temperature fields and found to be negligible for measurements in the centre of the flame.
- The cylindrical blast wave model for laser induced sparks is presented and found to fit the experimental data well. This allowed for extrapolation to the small amplitude speed of sound, which was the quantity sensitive to the flame temperature.
- The beam deflection system including data processing software is developed and found to be stable and reproducible.
- The temperature of the propane/air McKenna burner flame is successfully measured for various equivalence ratios and airflow rates using the photo-acoustic beam deflection technique.

Comparison of the flame temperatures measured by the photo-acoustic and Rayleigh scattering thermometry system show good agreement. For low airflow rates, photo-acoustic temperatures are approximately 3.6% higher than the Rayleigh temperatures, however, at high airflow rates the agreement is better than 1% of temperature. Further work is needed to determine the source of the discrepancy between the two thermometry techniques at low airflow rates.

6. ACKNOWLEDGEMENTS

UK Department of Trade and Industry, National Measurement System Programme in Thermal Metrology, 2004-2007, Prof. Douglas Greenhalgh of Cranfield University, Dr Gordon Edwards, Dr Michael de Podesta and Dr Andrew Levick of The National Physical Laboratory.

7. REFERENCES

[1] G. J. Edwards, S. J. Boyes, *Review of the Status, Traceability and Industrial Application of Gas Temperature Measurement Techniques*, Report CBTM-S1, National Physical Laboratory, 1997.

[2] H. Preston-Thomas, *The International Temperature Scale of 1990, ITS-90*, Metrologia, 27 (1990) 3-10 & 107.

[3] G. J. Edwards, S. J. Boyes, *A transfer standard for gas temperature measurements*, Proceedings of Tempmeko (1996), 457 – 462.

[4] G. J. Edwards, *Report on a feasibility study of the extension of the temperature of the gas temperature standard to 2000 °C* NPL Report CBTM SXX (1998).

[5] J. W. Hahn, C. W. Park, S. N. Park, *Broadband coherent anti-Stokes Raman spectroscopy with a modeless dye laser*, Applied Optics 36 (1997), 27, 6722-28.

[6] S. Prucker, W. Meier, W. Stricker, *A flat flame burner as calibration source for combustion research: Temperature and species concentrations of premixed H2/air flames*, Rev. Sci. Instrum. 65 (1994), 2908 – 2911.

[7] The McKenna Flat Flame Burner, Holthuis & Associates, P.O. Box 1531, Sebastopol, CA 95473, U.S.A.

[8] S. Prucker, W. Meier, I. Plath, W. Stricker, Ber. Bunsenges. Phys. Chem. 96 (1992), 1393.

[9] W. Meier, S. Prucker, W. Stricker, The third international symposium on special topics in chemical propulsion: Non-intrusive combustion diagnostics. Begell House, New York, 1994.

[10] K. Kohse-Höinghaus, U. E. Meier, The Third International Symposium on Special Topics in Chemical Propulsion: Non-intrusive combustion diagnostics. Begell House, New York, 1994.

[11] Yong Suhk Gil, Suk Ho Chug, *Combustion characteristics of a planar flame burner as a calibration source of laser diagnostics.* SPIE, 2778 (1996), Optics for Science and new Technology.

[12] Jun Kojima, Quang-Viet Nguyen, *Development of a High-Pressure Gaseous Burner for Calibrating Optical Diagnostic Techniques*, Glenn Research Centre, Cleveland, Ohio (2003).

[13] R. Devonshire, I. S. Dring, G. Hoey, F. M. Porter, D. R. Williams, D. A. Greenhalgh, *Accurate CARS Measurements and Fluid-Flow Modelling of the Temperature Distribution around a Linear Incandescent Filament*, Chemical Physics Letters, 129 (1986), 2, 191-96.

[14] D. A. Greenhalgh, R. Devonshire, I. S. Dring, J. Meads, H. F. Boysan, *A Temperature Calibration Device for High-Temperature Spectroscopy: CARS Spectrum of N2 Gas in Thermal Equilibrium at 3467 K*, Chemical Physics Letters, 133 (1987), 5, 458-64.

[15] B. Lawton, G. Klingenberg, *Transient Temperature Measurement in Engineering and Science*, Oxford Science Publications (1996).

[16] R. A. Cheville, D. Grischkowsky, *Far-infrared terahertz time-domain spectroscopy of flames*, Optics Letters, 20 (1995), 15, 1646-8.

[17] L. T. Grebenshchikov, V. Ya. Klabukov, E. A. Kosolapov, L. D. Shvartsblat, *A temperature distribution study in cross sections of axially symmetric flames*, Journal of Engineering Physics and Thermophysics, 64 (1993), 3, 251 – 4.

[18] J. H. Miller, S. Elreedy, B. Ahvazi, F. Woldu, P. Hassanzadeh, *Tunable diode laser measurement of carbon monoxide concentration and temperature in a laminar methane-air diffusion flame*, Applied Optics, 32 (1993), 30, 6082 – 9.

[19] K. Wakai, K. Kamiya, S. Sakai, *Instantaneous measurement of two-dimensional temperature and density distributions of flames by a two-band-emission-CT pyrometer*, Proceedings of the SPIE - The International Society for Optical Engineering, 1762 (1992), 564 – 75.

[20] H. A. Pattee, R. B. Peterson, *Flame temperature measurement by monitoring an alkali emission doublet exposed to a selectively filtered background source*, Transactions of the ASME, Journal of Heat Transfer, 114 (1992), 3, 630 – 5.

[21] W. Fischer, H. Burkhardt, *Three-dimensional temperature measurement in flames by multispectral tomographic image analysis*, Proceedings of the SPIE - The International Society for Optical Engineering, 1349 (1990), 96 – 105.

[22] I. A. Vasilieva, L. V. Deputatova, A. P. Nefedov, *Investigating the flame with the aid of self-reversed contours of spectral lines*, Combustion and Flame, 23 (1974), 3, 305 – 11.

[23] A. N. Goyette, W. B. Jameson, L. W. Anderson, J. E. Lawler, *An experimental comparison of rotational temperature and gas kinetic temperature in a H2 discharge*, Journal of Physics D (Applied Physics), 29 (1996), 5, 1197 – 201.

[24] J. F. Behnke, H. Scheibner, *Gas temperature determination from Doppler-broadened spectral lines with self-absorption*, Physica B & C, 124B+C (1984), 1, 85 – 90.

[25] G. Wesselink, D. de Mooy, M. J. C. van Gemert, *Temperature determination of high-pressure optically thick gas discharges by a modified Bartels' method*, Journal of Physics D (Applied Physics), 6 (1973), 4, L27 – 30.

[26] D. Bailly, C. Camy-Peyret, R. Lanquetin, *Temperature measurement in flames through CO2 and CO emission: New highly excited levels of CO2*, Journal of Molecular Spectroscopy, 182 (1997), Iss:1, 10-17.

[27] S. Cheskis, I. Derzy, V. A. Lozovsky, A. Kachanov, F. Stoeckel, *Intracavity laser absorption spectroscopy detection of singlet CH2 radicals in hydrocarbon flames*, Chemical Physics letters, 227 (1997), 423 – 9.

[28] S. Cheskis, I. Derzy, V. A. Lozovsky, A. Kachanov, F. Stoeckel, *Intracavity laser absorption spectroscopy detection of flames: concentration measurements of intermediate species*, Proceedings of the SPIE - The International Society for Optical Engineering, 3172 (1997), 616 – 24.

[29] T. Aizawa, T. Kamimoto, *Measurements of OH Radical Concentration in Combustion Environments by Wavelength-Modulation Spectroscopy with a 1.55-um Distributed-Feedback Diode Laser*, Applied Optics, 38 (1999), 9, 1733 – 1741.

[30] D. M. Sonnenfroh, M. G. Allen, *Absorption measurements of the second overtone band of NO in ambient and combustion gases with a 1.8-mm room-temperature diode laser*, Applied Optics, 36 (1997), 30.

[31] V. Vilimpoc, L. P. Goss, B. Sarka, *Spatial temperature-profile measurements by the thin-filament-pyrometry technique*, Optics Letters, 13 (1988), 2, 93 – 95.

[32] M. Sakami, M. Lallemand, *Futuroscope, france. Retrieval of absorption and temperature profiles in premixed flame by inverse radiative methods*, Laboratoire d'Etudes Thermiques (URA 1403 CNRS),ENSMA 86960.

[33] F. Yousefian, M. Lallemand, *Temperature and species concentration profiles using high resolution infrared transmission data by inverse radiative analysis*, Laboratoire d'Etudes Thermiques, (U.M.R 6608 C.N.R.S),Ecole Nationale Supérieure de Mécanique et Aérotechnique,86960 Poitiers, Futuroscope Cedex, France.

[34] B. Rosier, P. Gicquel, D. Henry, A. Coppalle, *Carbon monoxide concentrations and temperature measurements in a low pressure* $CH_4O_2NH_3$ *flame*, Applied Optics, 27 (1988), 2, 360 – 364.

[35] F. Yousefian, M. Lallemand, *Inverse radiative analysis of high-resolution infrared emission data for temperature and species profiles recoveries in axisymetric semi-transparent media*, J. Quant. Spectrosc. Radiat. Transfer, 60 (1998), 6, 921 – 931.

[36] A. Y. Chang, E. C. Rea Jr., R. K. Hanson, *Temperature measurements in shock tubes using a laser based absorption technique*, Applied Optics, 26 (1987), 5, 885 – 91.

[37] J. Y. Wang, *Laser absorption methods for simultaneous determination of temperature and species concentrations through a cross section of a radiating flow*, Applied Optics, 15 (1976), 3, 768 – 73.

[38] G. J. Edwards, *MEG - Modulated Emission in Gases: a new thermodynamic temperature measurement technique*, private communication, NPL, June 1999.

[39] V. Bergmann, W. Meier, D. Wolff, W. Stricker, *Application of Spontaneous Raman and Rayleigh Scattering and 2D LIF for the characterisation of turbulent* $CH_4H_2N_2$ *jet diffusion flame*, Applied Physics B [Lasers and Optics], 66 (1998), 4, 489-502.

[40] J. A. Wehrmeyer, S. Yeralan, K. S. Tecu, *Linewise Raman-Stokes / anti-Stokes temperature measurements in flames using an unintensified charge-coupled device*, Applied Physics B (Lasers and Optics), 62 (1996), 1, 21 – 7.

[41] J. Haumann, A. Leipertz, *Giant-pulsed laser Raman oxygen measurements in a premixed laminar methane-air flame*, Applied Optics, 24 (1985), 24, 4509 - 15.

[42] G. C. Alessandretti, S. Benecchi, F. Cignoli, *Raman and fluorescence temperature measurements in premixed flames*, Applied Optics, 20 (1981), 16, 2765 – 7.

[43] G. Zikratov, Yueh Fang-Yu, P. Jagdish, O. Singh, P. Norton, R. Arun Kumar, R. L. Cook, *Spontaneous Anti-Stokes Raman Probe for Gas Temperature Measurements in Industrial Furnaces*, Applied Optics, 38 (1999), 9, 1467 – 75.

[44] F. Rabenstein, A. Leipertz, *Two-dimensional temperature determination in the exhaust region of a laminar flat-flame burner with linear Raman scattering*, Applied Optics, 36 (1997), 27, 6989 – 96.

[45] F. Rabenstein, A. Leipertz, *One-Dimensional, Time-Resolved Raman Measurements in a Sooting Flame made with 355-nm Excitation*, Applied Optics, 37 (1998), 21, 4937 - 43.

[46] T. Seeger, A. Leipertz, *Experimental comparison of single-shot broadband vibrational and dual-broadband pure rotational coherent anti-Stokes Raman scattering in hot air*, Applied Optics, Lasers, Photonics, and Environmental Optics, 35 (1996), 15, 2665-2671.

[47] G. Zicak, N. Omenetto, J. D. Winefordner, *Laser-excited atomic fluorescence techniques for temperature measurements in flames: a summary*, Optical Engineering, 23 (1984), 6, 749 – 55.

[48] J. B. Kelman, A. R. Masri, *Quantitative technique for imaging mixture fraction, temperature, and the hydroxyl radical in turbulent diffusion flames*, Applied Optics, 36 (1997), 15, 3506-14.

[49] J. Luque, D. R. Crosley, *Radiative, collisional, and predissociative effects in CH laser-induced-fluorescence flame thermometry*, Applied Optics, 38 (1999), 9, 1423 – 33.

[50] D. L. Peterson, F. E. Lytle, *Determination of flame temperature using the anomalous fluorescence of pyrene*, Optics Letters, 11 (1986), 6, 345 - 47.

[51] K. J. Young, S. N. Ireland, M. C. Melendez-Cervates, R. Stones, *On the Systematic error associated with the measurement of temperature using acoustic pyrometry in combustion products of unknown mixture*, Meas. Sci. Technol., 9 (1997), 1-5.

[52] W. Zapka, P. Pokrowski, A. C. Tam, *Noncontact optoacoustic monitoring of flame temperature profiles*, Optics Letters, 7 (1982), 10, 477 – 79.

[53] D. F. Grosejean, B. Sarka, L. P. Goss, *Time-resolved temperature measurements in a laboratory flame using the optoacoustic beam-deflection method*, Optics Letters, 10 (1985), 7, 324 – 26.

[54] G. J. M. Sutton, *Evaluation of the High temperature Furnace (2000 °C)*, Internal report, NPL, December 1998.

[55] Chell Instruments Ltd, Folgate House, Folgate Road, North Walsham, Norfolk, NR28 0AJ, UK.

[56] G. J. Edwards, *Initial Proposition of the MEG Thermometry Technique*, Private communication, NPL, May 1998.

[57] MATLAB, The Mathworks.

[58] TRANS for Windows, Ver 2.5, 1996, University of South Florida.

[59] L. S. Rothman, R. B. Watson, R. R. Gamache, D. Goorvitch, R. L. Hawkins et al, *HITEMP, the High-Temperature Molecular Spectroscopic Database*, JQSRT, (1998).

[60] R. B. Miles, W. R. Lempert. J. N. Forkey, *Laser Rayleigh Scattering*, Meas. Sci. Technol. 12 (2001) R33-51.

[61] H. C. Van de Hulst, *Light scattering by small particles*, 1957, (New York: Dover).

[62] M. Born, E. Wolf, *Principles of Optics 6th edn*, Oxford: Pergamon, 98, 1980.

[63] G. Sutton, A. Levick, G. Edwards, *A High Temperature Gas Transfer Standard for the Calibration of Optical Diagnostic Techniques*, Proceedings of Tempmeko 2004, Dubrovnik, June 2004.

[64] R. M. Fristrom, A. A. Westenberg, *Flame Structure,* McGraw Hill, 1965.

[65] I. M. Klotz, *Chemical Thermodynamics*, Prentice-Hall Inc, Englewood Cliffs, N.J, 1950.

[66] S. Gordon, B. J. McBride, *Computer Program for the Calculation of Complex Chemical Equilibrium Compositions*, NASA reference publication 1311, NASA Lewis Research Center Cleveland, Ohio.

[67] C. Morely, *A Chemical Equilibrium Package for Windows*, www.gaseq.co.uk, (2004).

[68] *JANAF Thermochemical tables, 2nd Edition, US Standard Reference Data System*, N SRDS-NBS 37, (1971).

[69] R. H. Davies, A. T. Dinsdale, J. A. Gisby, J. A. J. Robinson, S. M. Martin, *MTDATA – Thermodynamics and Phase Equilibrium Software from the National Physical Laboratory*, CALPHAD (2002) 26(2), pp. 229-271.

[70] W. C. Gardiner, JR., Y. Hidaka, T. Tanzawa, *Refractivity of Combustion Gases*, Combustion and Flame 40 (1981) 231-219.

[71] J. Fielding, J. H. Frank S. A. Kaiser, M. D. Smooke, M. B. Long, *Polarized/Depolarized Rayleigh Scattering for Determining Fuel Concentrations in Flames*, Proceedings of the Combustion Institute, 29 (2002), 2703-2709.

[72] U. Hohm, K. Kerl, *Interferometric measurements of the dipole polarisability, α , of molecules between 300K and 1100K: I. Monochromatic measurements at λ = 632.99 nm for the nobel gases and H_2, N_2, O_2 and CH_4*, Molecular Physics, 69 (1990), 5, 803-817.

[73] W. M. Itano, L. L. Lewis, D. J. Wineland, J. Phys. Rev. A, 25B (1982), 1233.

[74] G. W. Ford, J. T. Lewis, R. F. Oconnell, J. Phys. B, 19 (1986), L41.

[75] D. M. Bishop, L. M. Cheung, *Dynamic dipole polarizability of H2 and HeH^+*, J. Chem. Phys. 72 (1980), 9, 5125-5132.

[76] W. Muller, W. Meyer, J. Chem Phys. 85 (1986), 953.

[77] J. Rychlewski, J. Chem. Phys. 78 (1983), 7252-7259.

[78] A. D. Buckingham, J. Chem. Phys, 36 (1962), 3096.

[79] G. Placzek, E. Teller, Z. Phys, 81 (1933), 209.

[80] GSI Lumonics – Laser Group, 22300 Haggerty Road, Northville, MI 48167, USA.

[81] Litron Lasers, 22 Somers Road, Rugby, Warwickshire, CV22 7DH, UK.

[82] National Instruments Corporation, 11500 N Mopac Expwy, Austin, TX 78759-3504.

[83] Stanford Research Systems, Sunnyvale, CA.

[84] K. K. Kuo, *Principles of combustion*, John Wiley and sons, 1986.

[85] L. E. Kinsler, A.R. Frey, *Fundamentals of Acoustics*, second edition, Wiley Eastern Ltd, 1962.

[86] M. B. Ewing, *Thermophysical Properties of Fluids from Acoustic Measurements*, Pure and Applied Chemistry, 65 (1993), 5, 907-912.

[87] W. Zapka, P. Pokrowsky, A.C. Tam, *Noncontact Optoacoustic monitoring of flame temperature profiles*, Optics Letters, 7 (1982), 10, 477-9.

[88] W. Zapka, A. C. Tam, *Noncontact Optoacoustic Determination of Gas Flow Velocity and Temperature Simultaneously*, Appl. Phys. Lett. 40 (1982), 12, 1015-7.

[89] D. F. Grosjean, B. Sarka, L. P. Goss, *Time-resolved Temperature Measurements in a Laboratory Flame Using the Optoacoustic Beam-deflection Method*, Optics Letters, 10 (1985), 7, 324-6.

[90] K. J. Young, S. N. Ireland, M. C. Melendez-Cervates, R. Stones, *On the Systematic Error Associated with the Measurement of Temperature using Acoustic Pyrometry in Combustion Products of Unknown mixture*, Meas. Sci. Technol. 9 (1998), 1-5.

[91] *Visual Basic Professional*, V6.0, Microsoft.

[92] M. Born, E. Wolf, *The Principles of Optics – 7th Edition*, Cambridge University Press. 1999.

[93] G.S.K. Wong, *Speed of Sound in Standard Air*, J. Acoust. Soc. Am. 79 (1986), 1359-1366.

[94] C. L. Morfey, G.P. Howell, *Speed of Sound in Air as a Function of Frequency and Humidity*, J. Acoust. Soc.Am. 68 (1980), 1525-1527.

[95] M. Greenspan, *Comments on "Speed of Sound in Standard Air"*, J. Acoust. Soc. Am. 82 (1987), 370-372.

[96] G. P. Howell, C. L. Morfey, *Frequency Dependence of the Speed of Sound in Air*, J. Acoust. Soc. Am 82 (1987), 375-377.

[97] G. S. K. Wong, T. F. W. Embleton, *Variation of the Speed of Sound in Air with Humidity and Temperature*, J. Acoust. Soc. Am. 77 (1985), 1710-1712.

[98] G. C. Valses, D. L. Jones, *Blastwaves from an Inverse Pinch Machine*, The Physics of Fluids, 9 (1966), 3, 478-85.

[99] D. Jones, *Strong Blastwaves in Spherical, Cylindrical and Plane Shocks*, The Physics of Fluids, 4 (1961), 1183.

[100] D. Jones, *Erratum: Strong Blastwaves in Spherical, Cylindrical and Plane Shocks*, The Physics of Fluids, 4 (1961).

[101] Mells Griot, Sovereign Court, Lancaster way, Huntingdon, UK.

[102] Thorlabs Ltd, 1 Saint Thomas Place, Ely, Cambridgeshire ,UK.

8. REFEREED PAPERS

[1] G. J. M. Sutton, A. P. Levick, G. J. Edwards, *A High Temperature Gas Transfer Standard For The Calibration Of Optical Diagnostic Techniques*, Proceedings of the 9th International Symposium on Temperature and Thermal Measurements in Industry and Science (2004), 2, 1205 – 1210.

[2] G. J. M. Sutton, A. P. Levick, G. J. Edwards, *A Fully Characterised Flame Standard for the Calibration of Optical Diagnostic Techniques*, Proceedings of the 17th Symposium on Air Breathing Engines (2005), paper *ISABE 2005-1261*.

[3] G. J. M. Sutton, A. P. Levick, G. J. Edwards, D. A. Greenhalgh, *A Combustion Temperature And Species Standard For The Calibration Of Laser Diagnostic Techniques*, - accepted for publication in the Combustion and Flame Journal.